

Tracking the nature of neuromuscular disorders via combined proteomics and functional analyses

Inaugural-Dissertation
zur
Erlangung des Doktorgrades
Dr. rer. nat.

der Fakultät für
Biologie
an der

Universität Duisburg-Essen

vorgelegt von
Denisa Hathazi

aus Bistrița, Romania

August 2018

Die der vorliegenden Arbeit zugrunde liegenden Experimente wurden am Leibniz-Institut für Analytische Wissenschaften -ISAS- e.V, Dortmund sowie am „John Walton Muscular Dystrophy Research Centre“ des Institute for Genetic Medicine, Newcastle University, Newcastle upon Tyne (United Kingdom) durchgeführt.

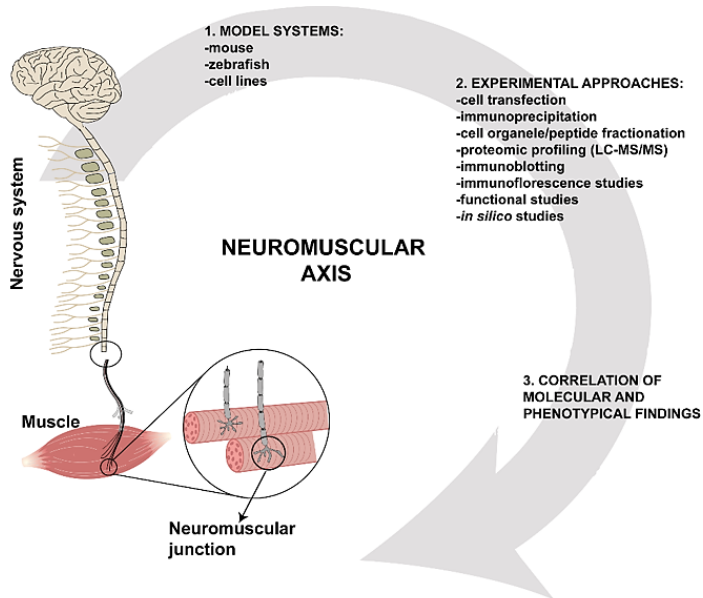
1. Gutachter: Prof. Dr. Kristina Lorenz
2. Gutachter: Prof. Dr. Ruth Grümmer

Vorsitzender des Prüfungsausschusses: Prof. Dr. Andrea Vortkamp

Tag der mündlichen Prüfung: 17.12.2018



Abstract



Due to the vast molecular complexity of skeletal muscle and the nervous system, it is necessary to surmount certain obstacles to carry out systematic explorations and provide significant insights into physiological functions and vulnerabilities. Studies of the etiology of neuromuscular disorders are expanding and have made tremendous progress during the last decade. Multiple technologies have been used to unravel the

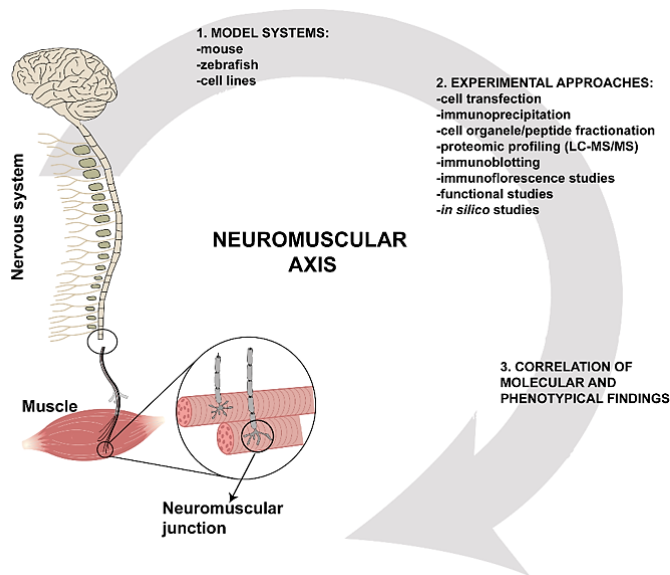
molecular complexity of these (functionally connected) tissues and elucidate the underlying pathomechanisms. In particular, applied proteomic profiling – which enables the simultaneous quantification of thousands of proteins in one experiment – has provided comprehensive molecular information and thus offered a “bigger picture” of molecular processes along the neuromuscular axis in health and disease.

To obtain a broader understanding of general muscle protein composition and gain comprehensive insights into the molecular etiology of different dominant and recessive diseases along the neuromuscular axis, proteomics in combination with further experimental approaches utilizing different model systems including mice and zebrafish, as well as appropriate cell lines were applied. A comprehensive protein catalogue of human primary non-differentiated and differentiated muscle cells as well as of complex muscle tissue was generated based on the combination of different fractionation procedures with LC/MS-MS protein analytics. A new binding partner for Caveolin-3, a protein associated with a dominant form of limb girdle muscular dystrophy (Caveolinopathy), has been identified promoting the understanding of the role of the protein complex at the neuromuscular junction and thus expanding the current understanding of their functional role on a general note.

Furthermore, protein signatures of model systems of Caveolinopathy, INPP5K-related congenital muscular dystrophy complicated by cataracts and mild intellectual disability, GFPT1-related limb girdle muscular dystrophy associated with congenital myasthenia and Charcot-Marie-Tooth neuropathy subtype 4C were determined and results were confirmed by further studies including functional testing in newly generated zebrafish models.

The combined data provide deep insights into the different underlying pathophysiologies and facilitate the defining of a conceptional starting point for (pre-clinical) therapeutic intervention of phenotypes defined by muscular dystrophy, cataracts and intellectual disability.

Zusammenfassung



Die enorme molekulare Komplexität des Skelettmuskels und des Nervensystems bedingt einige Hindernisse, dies es bei der Durchführung von systematischen Forschungsarbeiten zur Erlangung von Einblicken in physiologische Funktionen und Vulnerabilitäten zu überwinden gilt. Im gleichen Kontext nehmen Studien, die auf die Ätiologie neuromuskulärer Erkrankungen abzielen, zu und haben in der

vergangenen Dekade enorme Fortschritte gemacht. Bemerkenswerterweise haben verschiedene Technologien hierbei Einsatz gefunden, verbunden mit dem Ziel, die Herausforderung die die molekulare Komplexität der genannten (funktionell interagierenden) Gewebe an den Forscher stellt, zu überwinden und somit neue Einblicke in die zugrundeliegenden Pathomechanismen zu gewähren. Gerade proteomisch-basierte Analysen, die die simultane Quantifizierung von tausenden von Proteinen in einem Experiment ermöglichen, haben hierbei umfassende molekulare Informationen geliefert und somit zum Verständnis des Gesamtbildes der molekularen Prozesse entlang der neuromuskulären Achse unter gesunden und Krankheitsbedingungen beigetragen. In dieser Arbeit wurde darauf abgezielt, proteomische Analysen in Kombination mit weiteren experimentellen Ansätzen unter der Verwendung von verschiedenen Modellsystemen – darunter Maus- und Zebrafisch- sowie Zellkultur-Modelle – anzuwenden um ein weitreichendes Verständnis der generellen Proteinkomposition des Muskels sowie umfassende Einblicke in die molekulare Ätiologie verschiedener dominant- und rezessiv-erblicher Erkrankungen entlang der neuromuskulären Achse zu erlangen. In diesem Sinne wurde durch die Kombination verschiedener Fraktionierungs-Prozeduren mit LC/MS-MS-basierter Proteinanalytik ein umfassender Proteinkatalog humaner primärer nicht-differenzierter und differenzierter Muskelzellen sowie des komplexen Skelettmuskelgewebes generiert. Es wurde zudem ein neuer Bindungspartner für Caveolin-3, einem Protein das mit einer dominanten Form der Gliedergürtelmuskeldystrophien (Caveolinopathie) assoziiert ist, identifiziert, was das

derzeitige Verständnis der Rolle des Proteinkomplexes an der neuromuskulären Endplatte im speziellen und die biologische Rolle des Komplexes im generellen erweiterte. Darüber hinaus wurde die Proteinsignaturen von Modellsystemen der Caveolinopathie, der INPP5K-bedingten kongenitalen Muskeldystrophie assoziiert mit Katarakten und milder geistiger Behinderung, der GFPT1-bedingten Gliedergürtelmuskeldystrophie assoziiert mit kongenitaler Myasthenie sowie der Charcot-Marie-Tooth Neuropathie Subtyp 4C bestimmt und die erhobenen Resultate wurden durch weiterführende Studien – darunter auch funktionelle Testungen in neu generierten Zebrafischmodellen – verifiziert. Die kombinierten Daten haben tiefe Einblicke in die den verschiedenen Erkrankungen zugrundeliegenden Pathophysiologien gestattet und zudem die Definition eines konzeptionellen Ausgangspunkts für die (prä-klinische) Erprobung eines therapeutischen Interventionskonzepts bei der kombinierten phänotypischen Manifestation von Muskeldystrophie, Katarakten und geistiger Behinderung zugelassen.

Table of Contents

Abstract.....	IV
Zusammenfassung	VI
List of figures.....	XIV
List of tables	XVII
Abbreviations.....	XVIII
1. General introduction.....	20
1.1 Muscle.....	20
1.1.1. Muscle structure: from individual fibers to whole muscle	21
1.1.2 Excitation-Contraction coupling	22
1.1.3 Force generation and movement	22
1.1.4 Heterogeneity of muscle tissue: fiber types	24
1.1.5 Muscle damage and repair.....	26
1.2 Muscle protein composition.....	26
1.3 Muscle disorders	27
1.3.1 Muscular dystrophies	27
1.3.1.1 Duchene and Becker muscular dystrophy	29
1.3.1.2 Limb Girdle muscular dystrophies (LGMDs)	29
1.3.1.3 Congenital muscular dystrophies.....	31
1.3.2 Perturbed muscle innervation.....	33
1.3.2.1 Motor neuron diseases	34
1.3.2.2 Peripheral neuropathies	35
1.3.2.3 Disorders of the neuromuscular junction (CMS) and LGMD-CMS	37
1.4 Proteomics as a powerful tool to study neuromuscular diseases	39
1.4.1 Liquid chromatography coupled with mass spectrometry	40
1.4.2 Label free protein quantification	42

2. Materials and methods	45
2.1 Materials	45
2.1.1 Chemicals and reagents used.....	45
2.1.2 Instruments and disposable consumables.....	47
2.1.3 LC-columns, HPLC and mass spectrometers.....	48
2.1.4 Antibodies	49
2.1.5 Plasmids	50
2.2 Methods.....	51
2.2.1 Cell culture	51
2.2.1.1 Passaging and harvesting the cells.....	52
2.2.1.2 Seeding the cells on coverslips.....	52
2.2.1.3 Cell transfection and generation of inducible HEK 293 T-Rex cells	52
2.2.1.4 Adenovirus transduction.....	53
2.2.1.5 Cell toxicity and viability	53
2.2.2 Clinically affected and unaffected tissues.....	53
2.2.2.1 Human biopsies	54
2.2.2.2 Mouse tissue	54
2.2.3 Cell lysis.....	55
2.2.4 Muscle lysis.....	56
2.2.5 Determination of protein concentration	56
2.2.6 Tandem affinity purification assay.....	56
2.2.7 Proteomic Profiling	57
2.2.7.1 Sample carbamidomethylation	57
2.2.7.2 Sample preparation, proteolysis and cleanup	57
2.2.7.2.1 Filtered aided sample preparation.....	57
2.2.7.2.2 In solution digestion.....	58
2.2.7.2.3 Desalting of proteolytic digests	59

2.2.7.3 High pH reverse phase peptide fractionation	59
2.2.7.4 LC-MS/MS analysis	59
2.2.7.4.1 Protein profiling towards the generation of a muscle protein catalogue	60
2.2.7.4.2 INPP5K fibroblasts	61
2.2.7.4.3 p.P104L CAV3 mouse muscles	61
2.2.7.4.4 Tandem affinity purification products	62
2.2.7.4.5 Gfpt1 ^{tm1d/tm1d} mouse muscles	62
2.2.7.4.6 IQGAP1 overexpressing myoblasts	63
2.2.7.4.7 Sh3tc2 ^{ΔEx1/ΔEx1} mouse muscles	63
2.2.7.5 Data analysis and statistical evaluation	64
2.2.7.5.1 Muscle protein catalogue and TAP assay products	64
2.2.7.5.2 Comparative proteome profiling	65
2.2.7.6 Data plotting and pathway analysis	66
2.2.8 Molecular biology methods	67
2.2.8.1 Protein separation and western blotting	67
2.2.8.2 Co-immunoprecipitation	67
2.2.8.3 Immunofluorescence	68
2.2.8.4 Zebrafish handling and generation of zebrafish models	69
2.2.8.4.1 Zebrafish husbandry and observation	69
2.2.8.4.2 Morpholino knockdown in zebrafish embryos	69
2.2.8.4.3 Dechoriation of embryos at 48 hours post fertilization	70
2.2.8.4.4 Phenotype and motility observation	70
2.2.8.4.5 Rescue experiments	71
2.2.8.4.6 RT-PCR and qRT-PCR experiments	71
2.2.8.4.6.1 RNA extraction	71
2.2.8.4.6.2 cDNA synthesis	71
2.2.8.4.7 RT-PCR	72

2.2.8.4.7.1 qRT-PCR.....	73
2.2.8.4.8 Immunofluorescence staining of whole mount zebrafish	73
2.2.8.5 Microscopy and image analysis.....	74
2.2.8.6 Statistical analysis and data representation	75
3. Subprojects and obtained results	76
3.1 Muscle protein catalogue	76
3.1.1 Known proteomes described from mouse skeletal muscle	76
3.1.2 Identification of 10298 proteins via combined fractionation techniques and LC-MS/MS analysis	77
3.1.3 Myoblasts to myotube transition	83
3.1.4 Myotube to muscle tissue transition.....	85
3.2 Pathophysiology of muscular dystrophies	88
3.2.1 Molecular linkage of rare neuromuscular diseases	88
3.2.1.1 INPP5K as a new gene causing congenital muscular dystrophy.....	88
3.2.1.2 Proteomic signature of INPP5K mutant fibroblasts	90
3.2.1.3 Phenotyping of zebrafish models of Inpp5k-, Sill- and Phgdh-depletion	93
3.2.1.4 Effect of L-serine treatment on inpp5k, sill and phgdh morphants	99
3.2.1.5 Proteome profiling allows a molecular linking of rare neuromuscular diseases and to define common treatment strategies	104
3.2.2 Mutational spectrum and pathophysiology of Caveolinopathies	109
3.2.2.1 Proteomic signature of the CAV3 p.P104L mutant muscle	112
3.2.2.1.1 Discussion.....	115
3.2.2.2 CAV3 missense-mutants: pathogenicity-testing via immunoblot and immunofluorescence studies.....	119
3.2.2.2.1 Discussion.....	123
3.2.2.3 Unravelling new CAV3 functions at the NMJ via identification of IQGAP1 as a new binding partner	126

3.2.2.3.1 Proteins interacting with CAV3 identified using tandem affinity purification coupled with MS	126
3.2.2.3.2 IQGAP1 is required for the proper formation of the NMJ in zebrafish.....	129
3.2.2.3.3 IQGAP1 is co-localizing with the AChR in mouse muscle.....	133
3.2.2.3.4 IQGAP1 presents partial colocalization with CAV3 mutants in the Golgi133	
3.2.2.3.5 The NMJ in the p.P104L CAV3 mouse model is affected	135
3.2.2.3.6 Effects of IQGAP1 overexpression in myoblasts	137
3.2.2.3.7 Discussion.....	143
3.2.3 Molecular pathophysiology in GFPT1-deficient muscles.....	149
3.2.3.1 GFPT1 is a causative factor for LGMD-CMS.....	149
3.2.3.2 GFPT1-deficiency alters the proteomic signature of intercostal muscle.....	150
3.2.3.3 Proteomic profiling of GFPT1-deficient mice improves the knowledge of LGMD-CMS.....	154
3.2.4 Biochemical changes upon muscle denervation in neuropathies	158
3.2.4.1 Proteomic signature of murine gastrocnemius muscle upon neuropathy related short and long-term denervation.....	159
3.2.4.2 Longitudinal proteomic profiling of denervated muscle provides insights into the dynamic molecular processes of neurogenic muscular atrophy	161
4. Final conclusions and remaining challenges.....	166
5. Acknowledgments.....	168
6. References:	170
7. Appendices	189
9.1 Appendix 1	189
9.2 Appendix 2.....	191
9.3 Appendix 3.....	196
9.4 Appendix 4.....	199
9.5 Appendix 5.....	201
9.6 Appendix 6.....	202

8. Curriculum vitae.....	204
9. List of publications and conferences.....	206

List of figures

Figure 1. Muscle fiber organization	21
Figure 2. Schematic representation of the DGC complex	29
Figure 3. Proteomics offers a multitude of tools, aiding the understanding of neuromuscular.	40
Figure 4. Workflow depicting the sample preparation for proteomics.....	44
Figure 5. Venn diagram showing the number of proteins identified in myoblasts, myotubes and muscle.....	77
Figure 6. Proteomap of human muscle resulted from the combination of human primary myoblasts, myotubes and tissue.....	79
Figure 7. Proteomap of the top 500 most abundant proteins found in the muscle protein catalogue.....	81
Figure 8. Comparison of proteomic data obtained from human primary myoblasts, myotubes and muscle tissue.....	82
Figure 9. Overview of the myoblast vs myotubes comparison.	85
Figure 10. Overview of the myotubes vs muscle tissue comparison.....	87
Figure 11. Muscle biopsy from an individual harboring the p.I50T mutation on the INPP5K gene and from a healthy control, matching sex and age.	88
Figure 12. Schematic representation of INPP5K gene and its domains as well as the distribution of mutations identified and immunofluorescence analysis of the INPP5K protein in muscles derived from patients harboring the p.I50T and controls.	89
Figure 13. Comparative proteome profiling of INPP5K derived fibroblasts with control ones.....	90
Figure 14. Pathway analysis of the regulated proteins resulted from the comparative proteome profiling and subcellular localization of altered proteins	91
Figure 15. Schematic representation of the PHGDH increase.	92
Figure 16. Schematic representation of the CDK9 decrease	93
Figure 17. Overview of the <i>inpp5k</i> morphants.....	94
Figure 18. Overview of the <i>sill</i> morphants.....	96
Figure 19. Overview of the <i>phgdh</i> morphants.....	98
Figure 20. Immunoblot analysis of Phgdh in the described zebrafish models.	98
Figure 21. Overview of the rescue experiment.....	100
Figure 22. Effect of L-serine treatment on <i>inpp5k</i> , <i>sill</i> , and <i>phgdh</i> -MO injected	104
Figure 23. Mechanism of L-serine production in the astrocyte.....	105

Figure 24. Caveolin 3 protein domains	109
Figure 25. Immunoblot studies of quadriceps muscle derived from 10 weeks old animals showing a decrease in the amount of CAV3 in the mutant mouse (10 weeks)	111
Figure 26. The volcano plot shows all the proteins identified in the muscles.....	113
Figure 27. Subcellular localization of (A) up regulated proteins and (B) down regulated proteins in the p.P104L mouse	114
Figure 28. Cytoskape network analysis of the regulated proteins and <i>in silico</i> data from different perspectives: gene interrelations revealed by correlation weights, protein interactions as well as functional context given by the GO enrichment analysis.....	114
Figure 29. DGC components are affected by the mislocalization of CAV3	115
Figure 30. Caveolin 3 component domains and the location of the mutations within the protein domains.....	120
Figure 31. Expression of WT CAV3 and CAV3 mutants in RCMH cells which were transiently transfected.....	120
Figure 32. Analysis of RCMH cells transfected with WT CAV3 or different mutant CAV3 constructs.....	121
Figure 33. RCMH transfected cells were fixed and stained against CAV3 and GRP170 at 24 hours post transfection.....	122
Figure 34. Immunoblot analysis of LC3 II in RCMH transiently transfected cell with WT CAV3 and CAV3 mutants.	122
Figure 35. F-actin staining in RCMH transfected cells.....	123
Figure 36. <i>In vitro</i> studies focusing on the proliferation and cytotoxic effect of HEK 293 cell overexpressing the p.P104L in comparison with the cell overexpression the WT or the empty tag	127
Figure 37. Identification of IQGAP1 interacting with CAV3 by tandem affinity purification	128
Figure 38. Overview of the <i>cav3</i> morphants	130
Figure 39. Overview of the <i>iqgap1</i> morphants.....	131
Figure 40. Expression levels of <i>cav3</i> , <i>iqgap1</i> and <i>musk</i> monitored via real time quantitative PCR in the <i>cav3</i> , <i>iqgap1</i> and <i>musk</i> morphants at 48 hpf	133
Figure 41. Immunofluorescence analysis of IQGAP1 and bungarotoxin in mouse muscle....	133
Figure 42. Immunofluorescence analysis in RCMH transfected.....	134
Figure 43. Morphology of the NMJ in the CAV3 transgenic mouse	136

Figure 44. Immunoblotting analysis of quadriceps muscle derived from 24 weeks old p.P104L mice and the respective WT littermates	137
Figure 45. Relative expression of proteins belonging to the post-synaptic area in myoblast and myotubes.....	138
Figure 46. Immunostainings for CAV3 and IQGAP1 were carried out in myoblasts control and transduced with AdV.IQGAP1.....	139
Figure 47. Immunostainings for bungarotoxin and IQGAP1 were carried out in myoblasts control and transduced with AdV.IQGAP1.....	140
Figure 48. Immunostainings for phalloidin in order to visualize the actin cytoskeleton	141
Figure 49. Overview of the proteomics experiment in the IQGAP1 overexpressing myoblasts	143
Figure 50. The box plots depict the distribution of median log ₂ ratio of statistically significant proteins from the proteomics that are crucial for the NMJ.....	143
Figure 51. Schematic representation of the proposed mechanism for the clustering of the AChR receptor where IQGAP1 recruits RAC1 and CDC42 at the sites of MuSK activation.	146
Figure 52. Schematic representation of the GFPT1 domains and the localization of some of the so far identified mutations which spread across the whole domains of the protein	149
Figure 53. Volcano plot of the proteomics findings derived by comparing intercostal muscle from the <i>Gfpt1</i> ^{tm1d/tm1d} with WT littermates	151
Figure 54. Analysis of pathways associated either with up or down regulated proteins revealed by the proteome profiling. and schematic overview of the subcellular compartments and respective proteins	152
Figure 55. Immunoblot analysis reveals that indeed glypcan and MuSK are up regulated in the intercostal muscles of the <i>Gfpt1</i> ^{tm1d/tm1d} mouse	152
Figure 56. STRING network analysis of the statistically significant proteins	153
Figure 57. Immunofluorescence analysis of intercostal muscle derived from control and <i>Gfpt1</i> ^{tm1d/tm1d} 3 months old animals which were stained against IQGAP1 and bungarotoxin-AChR.....	154
Figure 58. Peripheral neuropathy phenotype in the 2 years old CMT4C mouse model and electron micrographs of sciatic nerves isolated from WT and the <i>Sh3tc2</i> ^{ΔEx1/ΔEx1}	158
Figure 59. Volcano plot depicting the proteomics findings derived by comparing gastrocnemius muscle from the <i>Sh3tc2</i> ^{ΔEx1/ΔEx1} (at 3 months-A and 2years old) with WT littermates.	160
Figure 60. Overview of the molecular changes that result upon long and short term denervation in the <i>Sh3tc2</i> ^{ΔEx1/ΔEx1} muscles.	161

List of tables

Table 1. Contractile, metabolic and morphological characteristics of human skeletal muscle ²²	25
Table 2. Selected proteins involved in muscular dystrophies ³³	28
Table 3. Major types of LGMDs ^{41,43-53}	30
Table 4. Major types of CMDs ⁵⁴⁻⁶¹	31
Table 5. Most common forms of CMT neuropathy ^{80,81}	36
Table 6. Chemical and reagents used	45
Table 7. Used laboratory equipment and consumables	47
Table 8. HPLC, columns and mass spectrometers used	48
Table 9. Software used for the MS analysis and acquisition	49
Table 10. Primary antibodies used	49
Table 11. Used algorithms, software for the database searches for the label free experiments	66
Table 12. Employed morpholinos	70
Table 13. PCR primers used	72
Table 14. Regulated proteins with N- and O-glycosylation sites	154

Abbreviations

AChR	acetylcholine receptor
ACN	acetonitrile
ALS	Amyotrophic Lateral Sclerosis
ANNOVA	analysis of variance
ATP	adenosine 5'-triphosphate
BCA	bicinchoninic acid
BMD	Becker muscular dystrophy
BSA	bovine serum albumin
C2C12	mouse skeletal cell line
CCFDN	congenital cataracts facial dysmorphism neuropathy
CID	collision induce dissociation
CMD	congenital muscle dystrophy
CMS	congenital myasthenic syndromes
CMT	Charcot-Marie-Tooth
CNS	central nervous system
CO ₂	carbon dioxide
Da	Dalton
DMD	Duchene Muscular Dystrophy
DMEM	Dubelco's Modified Eagle Medium
DMSO	dimethyl sulphoxide
DNA	deoxyribonucleic acid
dNTP	2'-deoxynucleotide 5'triphosphate
DTT	dithiothreitol
ECM	extracellular matrix
EDTA	ethylenediaminetetraacetic acid
EM	electron microscopy
ER	Endoplasmic reticulum
ERGIC	ER-Golgi intermediate compartment
ERAD	ER-associated degradation pathway
ESI	electrospray ionization
EtOH	ethanol
FA	formic acid
FALS	familial Amyotrophic Lateral Sclerosis
FASP	filtered aided sample preparation
FCS	fetal calf serum
FDR	false discovery rate
GuHCl	guanidine chloride
H&E	hematoxylin and eosin
HCD	high collision dissociation

HEK293	human embryonic kidney cell line 293
HeLa	human cervical epithelium
HPLC	high performance liquid chromatography
IAA	iodoacetamide
IF	immunofluorescence
LDH	lactate dehydrogenase assay
LGMD	limb-girdle muscular dystrophy
m/z	mass-to-charge
MEB	muscle eye brain disease
MgCl ₂	magnesium chloride
MO	morpholino
MRI	magnetic resonance imaging
mRNA	messenger RNA
MS	mass spectrometry
MS/MS	tandem mass spectrometry
MSS	Marinesco-Sjörger syndrome
MW	molecular weight
NAD ⁺	nicotinamide adenine dinucleotide
NADH	reduced nicotinamide adenine dinucleotide
NASF	normalized abundance factor
NMJ	neuromuscular junction
PBS	phosphate buffer saline
Pi	inorganic phosphate
PMA	progressive muscular atrophy
PNS	peripheral nervous system
ppm	parts per million
PTM	post-translational modifications
PVDF	polyvinylidene difluoride
rcf	relative centrifugal force
RNA	ribonucleic acid
SDS-PAGE	sodium dodecyl sulfate-polyacrylamide gel electrophoresis
SKCM	skeletal muscle cell media
TAP	tandem affinity purification
TBS	tris-buffered saline
TBST	tris-buffered saline triton
TCA	trichloroacetic acid
TFA	trifluoroacetic acid
TRIS	tris(hydroxymethyl)aminomethan
UPR	unfolded protein response
WB	western blotting
WT	wild type

1. General introduction

1.1 Muscle

Muscle is a complex tissue playing a crucial function in producing force and motion. Notably, the human body contains three types of muscle, each with overlapping and distinct features:

- Smooth muscle:
 - non-striated
 - involuntary
 - cells are shaped like almonds (tapered ends) with one nucleus per cell
 - can be mostly find in blood vessel walls, hollow organs like the bladder, as well as in the circulatory, reproductive and digestive tracks¹;
- Cardiac muscle:
 - striated
 - involuntary
 - branched, shaped like fibers cross-linked to one another, typically one nucleus per cell
 - exclusively present in the heart
- Skeletal muscle:
 - striated
 - voluntary
 - shaped like long fibers; multinucleated²

Skeletal muscle is one of the most plastic and dynamic tissues in the human body, has a plethora of functions and accounts for approximately 40% of total body mass. This tissue is responsible for locomotion, posture and assists in breathing by converting chemical into mechanical energy. Moreover, skeletal muscle plays a crucial role in glucose metabolism, as it is the main site for glucose turnover thus contributing to the basal energy metabolism³. Also, very important is its contribution to protein metabolism, as muscle serves as a reservoir for amino acids which aid in the maintenance of protein content of certain tissues and organs like skin, brain and heart⁴.

1.1.1. Muscle structure: from individual fibers to whole muscle

The architecture of skeletal muscle is complex and characterized by a very well-defined arrangement of muscle fibers. Each individual muscle is wrapped by a membrane formed out of connective tissue called epimysium. In addition, each muscle contains numerous fascicles which are defined bundles of muscle fibers enclosed by another layer of connective tissue known as the perimysium. This structural organization allows nerves and major blood vessels to penetrate the muscle⁵ (Figure 1). Skeletal muscle fibers (myofibrils) are multinucleated and result from the fusion of mononucleated myotubes. Each single muscle fiber has a width of approximately 100 μM and about 1 cm in length (mammals) and is surrounded by a plasma membrane called sarcolemma. Associated with the sarcolemma are the endoplasmic reticulum, mitochondria and the T-tubule system⁵. The myofibrils have the striated appearance based on their organised sarcomeric composition. These sarcomeres are arranged in a stacked pattern of perfectly arranged structured proteins within each individual muscle fiber. In this context, each individual sarcomere contains parallel arranged actin (thin) and motor myosin (thick) filaments. The sarcomeres are morphologically separated by a Z-disk to which polymerized actin filaments attach. In addition, these filaments contain attached tropomyosin molecules. Thick filaments notoriously do not attach to the Z-disk and are rather situated at the middle of the sarcomere. This myosin filaments contain 2 globular heads and a long tail. The interaction between thick and thin filaments provides the molecular basis of muscle contraction functioning in a calcium-dependent manner^{5,6}.

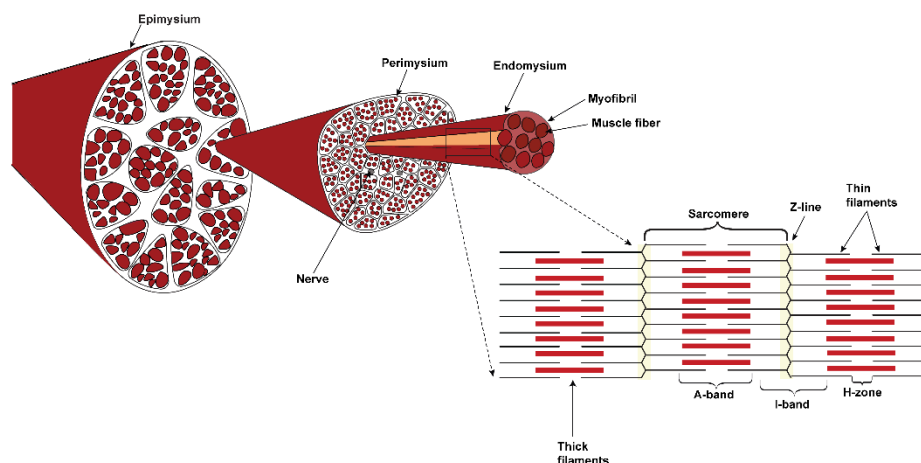


Figure 1. Muscle fiber organization. The epimysium surrounds the whole muscle, then the perimysium divides the fibers up into fascicles and finally each fiber is surrounded by an endomysium. The contractile unit of the muscle fiber is the sarcomere. Z-lines delimitate the boundaries of the sarcomere and provide anchor points for the filaments.

1.1.2 Excitation-Contraction coupling

Excitation-contraction is a complex event that requires the proper coordination of two processes: (i) transmission of the nerve stimulus to the muscle and (ii) the biophysical interaction between actin and myosin leading to a sliding filament mechanism. This complex procedure was first described as a hypothesis in 1954 by Huxley who observed a shortening of the striation upon contraction⁷.

Contraction of the skeletal muscle is achieved by an action potential which arrives from the central nervous system and "travels" within a motor neuron which finally innervates the muscle fiber, hereby, the motor neuron reaches the muscle fiber through a small gap located between the nerve terminal and the muscle fiber called the synaptic cleft. The contraction message stimulates the motor neuron to produce neurotransmitters such as acetylcholine (ACh). Moreover, at the neuromuscular junction (NMJ; the location where the motor neuron "meets" the muscle fiber) the sarcolemma is highly biophysically specialized to receive the signal from the motor neurons (this area is known also as the endplate). After the release of ACh from the endplate, it binds to specific receptors at the postsynaptic membrane stimulating the opening of voltage gated sodium channels thus generating an action potential in the muscle. This potential arrives in the so-called triad where the T tubule is in close proximity to the terminal cisternae of the sarcoplasmic reticulum which stimulates the opening of the dihydropyridine receptors allowing an inward flux of Ca^{2+} . This calcium triggers the opening of the ryanodine receptor leading to the release of large amounts of calcium from the sarcoplasmic reticulum into the sarcoplasm^{3,8,9}. The calcium will then bind to troponin C molecules leading to a structural change causing the tropomyosin molecules which were blocking the active site of actin to be exposed. The heads of the myosin bind to these sites creating cross-bridges and then pivot, which will drawing the actin filament towards the center of the sarcomere¹⁰.

In the presence of ATP, the cross-bridge between actin and myosin disconnects and the myosin head attaches to the next available actin forming a new cross-bridge which pulls the actin towards the center of the sarcomere. The breakage and rearrangement of new cross bridges continues as long as the ATP molecules are present. In order to terminate the contraction, the muscle fiber pumps Ca^{2+} back into the sarcoplasmic reticulum^{10,11}.

1.1.3 Force generation and movement

An important characteristic of the skeletal muscle is its capacity to rapidly modulate the rate of energy production in response to locomotion and movement. This process is powered by the cycling of actin-myosin cross-bridges with immediate energy from ATP¹². Depending on the activity and on the intensity, skeletal muscle has three pathways for energy production: intramuscular stores of CTP and ATP, anaerobic glycolysis and oxidative phosphorylation. The first energy source is notoriously used for high intensity short duration³. The second pathway employs glucose stored in the form of glycogen within the muscle cells or that comes directly from the blood to produce pyruvate and lactate and sustains muscle actions for a few minutes but the secondary products (lactate and H⁺) have unpleasant side effects associated with short term discomfort and muscle fatigue¹³. The energy needed to sustain exercises at high intensity and duration is produced via the oxidative phosphorylation within the mitochondrial network which starts with acetyl-CoA resulted from the carbohydrate (glycolysis) and lipid (β -oxidation) metabolism, which then enters the tricarboxylic cycle (TCA) and coupled with the oxidative phosphorylation from the electron transporter chain. All these pathways are used by the muscle in an overlapping manner in order to produce energy¹⁴.

The "sliding filament" theory explains the basic mechanism by which muscle produces force and movement. The mechanic energy produced by the actin-myosin cross-bridges is transmitted to the Z-disk of the sarcomere with movement occurring if the force reaches the tendons joints and the myotendinous junction. The generation of mechanical energy can be described as a sequential reaction:

- ATP is binding to the myosin active binding site leading to the dissociation from actin
- The ATPase activity of the myosin head hydrolyses ATP to ADP and Pi which remains bound to the myosin
- Then, the myosin head swings over and binds weakly to a new actin molecule with a cross-bridge at 90° relative to the filaments
- The release of Pi triggers a power stroke and the myosin pushes the actin pass it generating mechanical energy
- At the end of this power stroke, ADP is released and myosin remains bound to actin, and a new cycle is ready to begin³

The mechanical energy generated by the muscle is highly depending on several factors including muscle architecture, space between the myofilaments, number of cross-bridges formed and the degree of innervation.

1.1.4 Heterogeneity of muscle tissue: fiber types

Fiber type diversity was first described 40 years ago. The muscle fibers are defined as slow or fast twitch based on their contractile properties and, in accordance with the histochemical staining for the myosin ATPase, as type I (slow-twitch) and type II (fast-twitch)¹⁵.

In 1960, a more complex classification emerged based on studies made at the histochemical and biochemical level as well as using electron microscopy. Important work on this has been performed by Kugelberg and colleagues¹⁶. Their experiments consisted in the stimulation of the single motor axons of tibialis anterior (TA) muscle, then induced glycogen depletion to identify the fibers by periodic acid-Schiff (PAS) staining and SDH activity thus reflecting the oxidative metabolism¹⁶. By performing these experiments, Kugelberg and co-workers demonstrated that motor units were homogeneous, based on the SDH staining and that small SHD positive or large SDH negative fibers were both fast twitch¹⁶. Interestingly, fibers tested as SDH negative underwent a rapid decline in tension under repeated stimulation while the ones that tested positive showed no force-drop for several minutes. Furthermore, few fibers presented with an intermediate SDH staining and resistance to fatigue with a variable mitochondrial content ranging from 5-25 % of total fiber volume¹⁷. Fibers with a higher content of mitochondria presented a considerably developed SR network in contrast to the slow muscle which showed a thin Z-line. Therefore, it was postulated that the structure of the muscle fiber is a process dependent on the speed of contraction, correlated with the development of the SR, the thickness of the Z-line and the mitochondria content¹⁸.

An important step in proving the heterogeneity of muscle fibers was achieved by the discovery of the ATPase staining which revealed two additional fiber populations: type II A and B; both are abundant in fast-twitch muscle and distinct from the type I. In 1988, a further step was done by the discovery of a third type of fiber, the II x fibers which are specific to humans^{19,20}. The contraction and half-relaxation times of the latter fiber type were found to be similar to type 2A and 2B and their resistance to fatigability intermediate to 2A and B units²¹. Notably, each isoform has particular contractile and metabolic properties presented in detail in Table 1.

The fiber types have a different distribution in the mammalian muscles and the proportion depends on species and anatomical site. A good example constitutes the diaphragm, a very active muscle which supports respiration. In large mammals, it is comprised of slow muscle fibers whereas in rats and mice it is comprised of fast muscle fibers¹⁹. In the leg muscle of humans, predominantly slow muscle fiber types are more abundant in the posterior compartment thus aiding with posture¹⁵

Table 1. Contractile, metabolic and morphological characteristics of human skeletal²²

	Type 1	Type II a	Type II x
General properties			
Myosin heavy-chain isoform	MHC1	MHC2A	MHC2X
Contractile and metabolic characteristics	Slow twitch, high oxidative, fatigue resistant	Fast twitch, oxidative-glycolytic, fatigue resistant	Fast twitch, oxidative-glycolytic, fast fatigable
Force production	Weak	Intermediate	Strong
Myoblobin content	High	Intermediate	Low
Time to peak tension (msec)	80	30	
Ca ²⁺ actomyosin ATPase activity (mmol min ⁻¹ mg myosin ⁻¹)	0.16	0.48	
Mg ²⁺ actomyosin ATPase activity (mmol min ⁻¹ g protein ⁻¹)	0.3	0.84	
Glycolytic and oxidative enzymes activity			
Creatine kinase (mmol g ⁻¹ min ⁻¹)	13.1	16.6	
Phosphofruktokinase (mmol kg ⁻¹ min ⁻¹)	7.5	13.7	17.5
Glycogen Phosphorylase (mmol kg ⁻¹ min ⁻¹)	2.8	5.8	8.8
Lactate dehydrogenase (mmol kg ⁻¹ min ⁻¹)	94	179	211
Citrate synthase (mmol kg ⁻¹ min ⁻¹)	10.8	8.6	6.5
Succinate dehydrogenase (mmol kg ⁻¹ min ⁻¹)	7.1	4.8	2.5
3-hydroxyl-CoA dehydrogenase (mmol kg ⁻¹ min ⁻¹)	14.8	11.6	7.1
Morphological properties			
Capillary density (capillaries per fiber)	4.2	4	3.2
Mitochondrial density	High	Intermediate	Low
Fiber size (μm ²)	5310	6110	5600
Percent distribution in whole muscle	54±12.2	32.3±9.1	13.3±7.6
Myonuclear domain size	Small	Intermediate	Large

1.1.5 Muscle damage and repair

Muscle fibers are multinucleated and post-mitotic with a minimal turnover of nuclei. Each nucleus controls the type of protein synthesized in the specific region. Interestingly, muscle has the ability to repair itself in case of damage or injury. The first stage of muscle repair is necrosis which starts with the disruption of the sarcolemma. This in turn will lead to an increase influx of calcium which will activate several proteases. In order to clear up the necrotized tissue, inflammatory processes are activated. Cells like neutrophils and macrophages are mobilized at the site of injury clearing up the debris via phagocytosis^{23,24}. After degeneration, the next stage is regeneration accomplished by muscle satellite cells. Satellite cells represent the stem cells of the skeletal muscle which are located between the sarcolemma and the basal lamina²⁴. One of the signs of muscle damage is the presence of elevated CK in blood, which is released from the fibers after disruption or increased permeability of the sarcolemma²⁵.

1.2 Muscle protein composition

Skeletal muscle is composed of approximately 80% proteins from which more than 50% belong to the contractile apparatus. Hereby, it has been shown that all isoforms of myosin constitute around 18% of the total skeletal muscle proteome thus making it the most abundant protein of this tissue²⁶. Myosin functions as a molecular motor and so far, around eleven sarcomeric myosins have been described (in cardiac and skeletal muscle): embryonic, neonatal, cardiac α , cardiac β or slow type I, fast 2A, fast 2X, fast 2D, fast 2B, extraocular, mandibular or masticatory and slow tonic myosin. The sarcomere and sarcoplasm moreover contain numerous other proteins contributing to the cytoskeletal integrity decisive for excitation coupling and contraction²⁷. In addition, proteins belonging to the thin filament such as actin, which comprises approximately 20% of the myofibril and is expressed in the sarcomere as two isoforms, represent important structural components. Acting in concert with troponin and tropomyosin, actin plays a very important role in mechanisms leading to the generation of force and movement³. Another very highly abundant protein is giant titin which counts for approximately 16% of the total skeletal muscle proteome²⁶. Titin spans half of the sarcomere and the A-band being part of the thick filament. Its C and N-terminus are part of the M-line, respectively of the Z-disk, contributing to the elasticity of the muscle. Additionally, titin also aids the stabilization and alignment of the thick filament by forming flexible connections between the ends of the thick filament and the Z-disk²⁸. Another highly abundant protein is nebulin, an actin binding protein, localized at the thin filament and responsible for regulating its length²⁹.

Another category of highly abundant structural proteins in skeletal muscle are the proteins forming the extracellular matrix (ECM). Those consist of around 10% of the total skeletal muscle proteome. The major structural protein of the ECM is collagen. Several types of collagen such as I, III, IV, VI, XI, XII, XIV and XV are more highly expressed during skeletal muscle development. The skeletal muscle ECM is subdivided in endomysial (around the muscle), perimysial (around groups of cells) and epimysial (around the muscle) regions (Figure 1). The perimysium is primarily composed of type I collagen while the epimysium and endomysium are predominantly composed of equal amounts of collagen I and III. The basal membrane of the muscle primarily consists of type IV collagen, however type VI and XV are also present^{30,31}.

Myoglobin is an oxygen binding heme protein which is found exclusively in striated muscle and constitutes up to 5-10 % of the total cytoplasmic proteins present in skeletal muscle³². Another group of highly abundant proteins accounting for approximately 10% of the total proteome belongs to the energy metabolism. The major sources of energy for muscle are – as mentioned above – lipids and glucose. Glucose is stored in skeletal muscle in the form of glycogen. The main pathways through which energy is produced are: glycolysis, Krebs cycle and oxidative phosphorylation. All the components of this pathways including GLUT1, GLUT4, RAB proteins, 14-3-3 isoforms and AMPK proteins have been recently quantified and described in mouse triceps muscle²⁶. Proteins belonging to the glycolytic pathway alone account for more than 5% of the total skeletal muscle proteome. Abundances of these proteins are continuously changing based on the nutritional state of the person, exercise and disease-manifestation and progression. Lower abundant proteins include skeletal muscle specific translation factors, circadian and immune system related proteins²⁶.

1.3 Muscle disorders

Different inherited or acquired diseases can cause muscle wasting, degeneration and weakness. Muscular disorders can be classified in several categories: muscle dystrophy, inflammatory myopathies, metabolic myopathies, disorders of the neuromuscular transmission, ion-channel disorders, endocrine, iatrogenic and toxic myopathies as well as neurogenic muscular atrophy.

1.3.1 Muscular dystrophies

Muscular dystrophies (MD) are a group of devastating disorders that result in an increase of muscle weakness and wasting over time leading to loss of ambulation and depending on the

respective subtype even premature death. So far, more than 30 inherited forms of MDs have been described. The key features of the dystrophic muscle are centralized nuclei, replacement of muscle with collagen and fatty tissue, fiber splitting and small regenerating fibers. MDs can be either of dominant or recessive mode of inheritance and are in many dominant cases, caused by *de novo* mutations, which are therefore sporadic³³.

Interestingly, some genes can cause more than one phenotype. Hereby, titin represents a good example as different mutations within the corresponding *TTN* gene can lead to a severe limb girdle MD, to a tibial MD depending if the patient has homozygous or a heterozygous mutations³⁴ or to isolated cardiomyopathy³⁵. Clinical and molecular genetic characterization of MDs is even more complicated by the fact that mutations within different genes can cause the same phenotype; here a good example is Emery-Dreifuss MD that can be caused by mutations in two nuclear proteins, laminin or emerin³⁶. There is a vast array of proteins that can cause MD with a heterogeneous subcellular localization, like the sarcolemma, extracellular matrix and nuclei with a few examples described in more detail in Table 2.

Table 2. Selected proteins involved in muscular dystrophy³³

Subcellular localization	Protein	Function	Disease
Extracellular matrix	<i>COL6A1</i> , <i>COL6A2</i> , <i>COL6A3</i>	Provides stability and links proteins from the sarcolemma to the surrounding matrix by forming microfilaments networks	UCMB, BM, AD-LGMD
	<i>LMA α2</i> ,	Links the sarcolemma to the basal lamina	MDC1A
Transmembrane	<i>CAV3</i>	Principal component of the caveolae contributing to the stability of the α-dystroglycan	LGMD1C
	<i>INTα7</i>	Links the ECM to the actin cytoskeleton	CM
	<i>SGC: α</i> , <i>β,γ,δ</i>	Major components of the DGC	LGMD2D, LGMD2E, LGMD2F, LGMD2C
Sarcolemma	<i>DYSF</i>	Muscle repair	LGMD2B, MM
	DMD	Anchors the internal cytoskeleton to the ECM	DMD, BMD

1.3.1.1 Duchene and Becker muscular dystrophy

Duchenne muscular dystrophy (DMD) is one of the most common X-linked inherited disorders and is caused by mutations in the dystrophin gene (*DMD*), the largest gene in the human genome. Symptoms usually manifest in early childhood around the age of 3 years. Patients display late walking, calf pseudohypertrophy, a toe gait and high levels of serum CK and later in disease progression cardiomyopathy and respiratory problems. Cardiomyopathy and

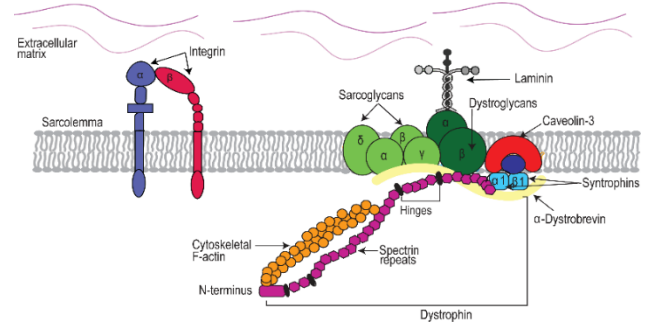


Figure 2. Schematic representation of the DGC complex

muscle weakness may sometimes also manifest in female carriers. *DMD* was the first gene identified to be causative for a form of muscular dystrophy. Approximately 40% of the patients suffering from DMD present point mutations which most of the time result in a premature stop codon or in the expression of a nonfunctional protein. Gene deletions that only disrupt the regular reading-frame of dystrophin are usually associated with the milder phenotype of the disease called Becker muscular dystrophy (BMD)³⁷⁻³⁹. Dystrophin is a central component of the DGC and anchors the sarcolemma to the actin cytoskeleton forming a mechanically strong link. Therefore, this protein has an important role in the maintenance of the sarcolemma stability and in contraction (Figure 2). Muscle biopsies of DMD patients show many myopathic features like myofiber degeneration and regeneration, increased amounts of fatty tissue replacing the muscle, total absence of sarcolemmal dystrophin and lower amounts of components belonging to the DGC⁴⁰. Interestingly, dystrophin is a protein often affected or regulated in other forms of MDs as a secondary consequence.

1.3.1.2 Limb Girdle muscular dystrophies (LGMDs)

LGMDs are a heterogeneous group of muscle dystrophies with the predominant involvement of the shoulder girdle and pelvic muscle. The age of onset, severity, inheritance and features can vary, depending on the subtype of this condition and can be inconsistent even within the same family. Signs and symptoms may appear at any age and generally can get or not worsen with time. Affected individuals can have changes in posture or appearance of the shoulder, back, abnormal curved lower back or to the side. The various forms of limb-girdle muscular dystrophy are caused by mutations in different genes. LGMDs are classified based on their inheritance pattern: type 1 for dominant disorders and type 2 for recessive. An overview of the different LGMD types and the genes which are mutated can be found in Table 3^{41,42}.

Table 3. Major type of LGMD^{41,43-53}

LGMD	Gene	Onset	Muscle affected	Serum CK levels
LGMD1A	<i>MYOT</i>	adult life	hamstring muscles, semimembranous muscle	normal to mildly elevated
LGMD1B	<i>LMNA</i>	fourth decade of life	adductor magnus, semimembranous, soleus and medial half of gastrocnemius	normal to mildly elevated
LGMD1C	<i>CAV3</i>	first decade		moderate to high
LGMD1D	<i>HSP40</i>	first decade to adulthood	gastrocnemius, soleus, tibialis posterior	normal to high
LGMD1E	<i>DES</i>	adulthood	semitendinous, gracilis and sartorius	normal
LGMD1F	<i>TNPO3</i>	variable	proximal muscles	normal to moderate
LGMD1G	<i>HNRNPDL</i>	variable	proximal muscles	normal to moderate
LGMD2A	<i>CALP</i>	early to fourth decade	shoulder girdle, posterior compartments of legs	moderate
LGMD2B	<i>DYSF</i>	second to third decade	gluteal, tensor fasciae, biceps femoris, triceps surae	very high
LGMD2C, 2D, 2E, 2F	<i>SGCA</i>	first decade	thigh and shoulder muscles,	very high
LGMD2G	<i>TCAP</i>	first decade	shoulder girdle; quadriceps femoris, vastus medialis	moderate
LGMD2H	<i>TRIM32</i>	first decade	proximal muscles	normal to moderate
LGMD2I, 2K, 2M, 2N, 2O, 2P, 2T, 2U	<i>DAG</i>	fourth decade	gastrocnemius, soleus, biceps femoris, semimembranous and semitendinosus	moderate to very high
LGMD2J	<i>TTN</i>	first to third decade	mostly cardiac involvement	high
LGMD2L	<i>ANO5</i>	third decade	quadriceps femoris muscles, often with asymmetric involvement	high
LGMD2S	<i>TRAPPC11</i>	first decade	shoulder girdle	high

LGMD2Q	<i>PLEC1</i>	first decade	proximal muscles	high
LGMD2W	<i>LIMS2</i>	first decade	proximal muscles	high

1.3.1.3 Congenital muscular dystrophies

Congenital muscular dystrophies (CMD) are a group of diseases with a very early onset, usually at birth or in the first six months of life. Most children with CMD present with progressive muscle weakness or hypotonia, which can make the baby look “floppy” however, in patients with a milder phenotype, antigravity movements of limbs can be observed and axial muscles of the spine can be more affected as often happens in selenoprotein 1 and laminin A/C related CMDs. Also, patients can develop cardiomyopathy which usually appears particularly during the second decade of life. Usually, CMDs are accompanied by additional neurological features affecting the central nervous system (aDGopathies or to a lesser extent *LAMA2* related CMDs) or the peripheral one (rigid spine seen in patients with defects in *SEPNI*, *LMNA* CMDs). Patients can present with contractures of shoulders, elbows, knees often associated with joint laxity as seen in CMDs due to defects in genes such as like *COL6* or *SEPNI*^{37,54}.

The muscle of CMD patients has a dystrophic appearance depending on the severity and duration of the disease with normal to high levels of serum CK. Immunohistological analysis usually reveals that most of the patients present normal levels of α and β dystroglycans however, the glycosylation of these proteins seems to be highly affected. So far, more than 30 different types of CMD have been described⁵⁴.

Table 4. Major types of CMDs⁵⁴⁻⁶¹

Disease	Gene	Phenotype	Serum CK levels	Muscle Biopsy
CMD with primary laminin- α 2 (merosin) deficiency (MDC1A)	<i>LAMA2</i>	Muscle weakness with a variable severity based on the complete or partial deficiency in <i>LAMA2</i> . Generally normal mental development, epilepsy in about 30%.	high	Complete or partial deficiency of laminin- α 2
CMD with partial merosin deficiency (MDC1B)	Locus: <i>1q42</i>	Variable severity, proximal limb girdle weakness, muscle hypertrophy, early respiratory failure reported.	high	Variable deficiency of glycosylated aDG, secondary reduction of laminin- α 2
LARGE related CMD (MDC1D)	<i>LARGE</i>	Variable. CMD with significant mental retardation, may eventually	high	Variable deficiency of glycosylated aDG, secondary reduction of laminin- α 2

		blend with the MEB/WWS spectrum.		
Fukuyama CMD (FCMD)	<i>FKTN</i>	Frequent in the Japanese population, walking not achieved, mental retardation, epilepsy common, clinical overlap with MEB.	high	Variable deficiency of glycosylated aDG, secondary reduction of laminin- α 2
Muscle-eye-brain disease (MEB)	<i>POMGNT1</i> , <i>FKRP</i> , <i>FKTN</i>	Motor deterioration because of spasticity. Mental retardation, significant ocular involvement (eg, severe myopia, retinal hypoplasia)	high	Variable deficiency of glycosylated aDG, secondary reduction of laminin- α 2
Walker–Warburg syndrome (WWS)	<i>POMT2</i> , <i>FKRP</i>	Often lethal within first years of life because of severe structural CNS involvement. Congenital weakness may be less apparent in the setting of the brain involvement.	moderate to high	Variable deficiency of glycosylated aDG, secondary reduction of laminin- α 2
CMD/LGMD with MR	<i>FKRP</i> , <i>FKTN</i>	Early-onset weakness, ambulation is often achieved, or early-onset LGMD phenotype, with mental retardation and microcephaly.	moderate	Variable deficiency of glycosylated aDG, secondary reduction of laminin- α 2
CMD/LGMD without MR (including MDC1C)	<i>FKRP</i> , <i>FKTN</i>	Early-onset weakness, but ambulation achieved, or early-onset LGMD phenotype, without mental retardation, may have steroid-responsive progression of weakness, cardiomyopathy.	moderate	Variable deficiency of glycosylated aDG, secondary reduction of laminin- α 2
CDG I (DPM3)	<i>DPM3</i>	Cardiomyopathy and stroke-like episode, mild developmental disability.	high	Reduction in glycosylated aDG, variable laminin- α 2 reduction
CDG I (DPM2)	<i>DPM2</i>	CMD with MR and severe myoclonus epilepsy	high	Reduction in glycosylated aDG, variable laminin- α 2 reduction
CDG Ie (DPM1)	<i>DPM1</i>	Initially described as CDG, ie, now emerging evidence of the presence of a dystrophic myopathy with abnormal aDG	moderate	Reduction in glycosylated aDG, variable laminin- α 2 reduction
Collagen VI related, Ulrich (Bethlem)	<i>COL6</i>	Distal joint hyperextensibility, proximal contractures, motor abilities variable, precluding independent	mild elevated	Variable deficiency of COL6 immunoreactivity

		ambulation in severe cases; soft palmar skin.		
Integrin $\alpha 7$	<i>ITGA7</i>	Rare, delayed motor milestones, walking with 2-3 years	mild elevated	Information not available
Rigid spine muscular dystrophy (RSMD)	<i>SEPNI</i>	Delayed walking, predominantly axial weakness with early development of rigidity of the spine, restrictive respiratory syndrome.	normal	No diagnostic immunohistochemical deficiency
Lamin A/C-related CMD	<i>LMNA</i>	Absent motor development in severe cases, more typical: “dropped head” and axial weakness/rigidity, proximal upper and more distal lower extremity weakness, may show early phase of progression.	normal to moderate	No diagnostic immunohistochemical deficiency
CMD merosin-positive	<i>4p16.3</i>	Severe muscle weakness of trunk and shoulder girdle muscles, and mild-to-moderate involvement of facial, neck, and proximal limb muscles. Normal intelligence.	normal	No diagnostic immunohistochemical deficiency.
CMD with adducted thumbs	<i>SYNE1</i>	Rare, adducted thumbs, toe contractures, generalized weakness, delayed walking, ptosis, external ophthalmoplegia, mild MR.	moderate	No diagnostic immunohistochemical deficiency
CMD with cerebellar atrophy	<i>Not known</i>	Delayed motor milestones, mild intellectual impairment.	moderate	No diagnostic immunohistochemical deficiency
Muscular dystrophy, congenital, with cataracts and intellectual disability	<i>INPP5K</i>	Hypotonia at birth, motor developmental delay in the first years of life, early-onset cataracts, muscle weakness, some patients present mild cognitive deficits	high	Nonspecific dystrophic changes: increased fiber size variation, fibrosis, increased adipose tissue, and some internal nuclei

1.3.2 Perturbed muscle innervation

Muscle atrophy is usually a consequence of a certain physiological process like aging, long term immobilization, malnutrition and most often de-innervation^{62,63}. Neuromuscular diseases

normally affect the motor neurons, the neuromuscular junction and the muscle itself⁶⁴. Thus, NMDs encompass of a vast array of different syndromes and diseases. In neurogenic muscle atrophy, protein degradation exceeds protein production thus leading to progressive muscle wasting. Neurogenic muscular atrophies can be the result of motor neuron diseases and peripheral neuropathies^{64,65}.

1.3.2.1 Motor neuron diseases

Motor neuron diseases refer to a group of disorders in which the upper or lower or both motor neurons are affected. The upper motor neuron is comprised of the corticospinal tract and the corticobulbar (lower brain stem) tract controlling the cranial nerve motor nuclei and the anterior horn cells. The severity and prognosis vary amongst the degenerative motor neuron diseases^{64,66,67}.

The one of the most common motor neuron disease is Amyotrophic lateral sclerosis (ALS) with an incidence is of 1 in 100,000. The disease is characterized by progressive loss of the upper and lower motor neurons at the spinal or bulbar level⁶⁸. The most common form of ALS is the sporadic accounting 90 to 95% of the cases. The remaining 5 to 10% cases are due to the genetic dominance inheritance factor (familial-type ALS or FALS)⁶⁹. The onset of the first symptoms is usually between the ages of 50 and 65⁷⁰. Patients usually present with the following phenotype: muscle weakness, twitching and cramping, which leads to muscle atrophy and impairment. In the advanced stages, patients also develop dyspnea and dysphagia⁷¹. The etiology of sporadic ALS is largely unknown; however, a few gene candidates have been proposed such as APEX, ANG, HFE, PON, SMN1, SMN2 and VEGF⁷². The most common cause of FALS is associated with extra non-coding nucleotide repeat expansions (GGGGCC) in Guanine nucleotide exchange C9ORF72 causing the accumulation of toxic aggregates⁷³.

Progressive muscular atrophy (PMA) is a rare, adult onset disease characterized by progressive flaccid weakness, muscle atrophy, fasciculations, and absence of reflexes. PMA is due to the degeneration of the isolated lower motor neuron including anterior horn cells and brainstem motor nuclei. Most of the patients develop later upper motor neuron signs and are considered to have lower motor neuron-onset amyotrophic lateral sclerosis, thus making PMA part of the ALS spectrum rather than a distinct disorder^{74,75}.

Spinal muscular atrophy (SMA) is a group of disorders characterized by the degeneration of motor neurons in the anterior horn of the spinal cord. The most common form of SMA is caused by autosomal recessive mutations in the survival of motor neurons gene (*SMN1*), accounting for

95% of cases⁷⁶. The disorder affects 1 in 10,000 to 60,000 infants and has a carrier concurrency of 1 in 40⁷⁷. Typical clinical findings include lower motor neuron signs of weakness, atrophy, loss of reflexes and fasciculations. The motor impairment predominates usually at the proximal muscles of the torso, pelvis and shoulders. Usually, the intercostal muscles are involved while the diaphragm is spared. So far, five types of SMA have been described based on the age of onset and severity. The most severe one is type 0 which is usually diagnosed antenatal as the fetus shows less mobility and is usually fatal at short term after birth due to flaccid tetraplegia with respiratory impairment⁷⁶⁻⁷⁸.

1.3.2.2 Peripheral neuropathies

Peripheral neuropathies are a heterogeneous group of diseases and often manifest as sensorimotor condition. Broadly, the peripheral neuropathies can be divided into two main categories: myelinopathies and axonopathies. Axonal neuropathy involves the degeneration and loss of axons while myelinopathies lead to a loss of myelin surrounding the axons^{64,79}.

Charcot-Marie-Tooth (CMT) neuropathy is one of the most common neuromuscular disorders with a prevalence of about 40 individuals in every 100,000⁸⁰. The number of gene defects leading to CMT manifestation has expanded rapidly such that more than 100 CMT-associated genes have been described⁸¹. The most common pattern of inheritance in CMT is autosomal-dominant as seen in CMT1, 2 and dHMN. Autosomal recessive mode of inheritance can be an indication of CMT4 and AR-CMT2⁸². *De novo* mutations can also occur and have been seen especially in CMT1A and CMT2A⁸². The affected genes encode for different types of proteins with different subcellular locations in Schwann cells, axons and non-compact myelin. Moreover, the corresponding proteins can be involved in the control of diverse cellular functions, ranging from maintenance of the myelin, cytoskeleton formation, axonal transport to mitochondrial metabolism^{83,84}. Usually, motor symptoms start distally (from the feet), and patients commonly develop high arches and hammer toes. Subsequently, the disease affects the leg and the lower part of the thigh leading to distal atrophy moving on to the hands. Sensory loss follows the same pattern. This disease is also characterized by difficulty in walking, foot drop, steppage gait, reduced or absent deep tendon reflexes, hand tremors and cramps^{82,84}.

CMT disorders are classified in several main groups based on the nerve pathology and conduction. The first type of CMT is the demyelinating form characterized by slow nerve conduction velocities and myelin abnormalities in the nerve biopsy (such as onion-bulb formations). The second type of CMT is the axonal form in which the patients present normal

to mildly reduced nerve velocities but reduced amplitudes, and signs of re/degeneration of the axons. A third group is represented by the patients with only degenerations in the motor neurons characterized by sparing of sensory nerves. These three groups are further subdivided into other categories based on the causative gene and assigned loci (Table7) ^{82,85}.

Table 5. Most common forms of CMT neuropathies^{81,82}

Type	Gene	Frequency	Phenotype
CMT1-autosomal dominant (demyelinating)			
CMT1A	<i>17 p dup.(PMP22), point mutations PMP22</i>	60-90% of CMT1	Classic CMT1
CMT1B	<i>MPZ</i>	<5% of CMT1	Classic CMT1, DSD, CHN
CMT1C	<i>LITAF</i>	<1% of CMT1	Classic CMT1
CMT1D	<i>EGR2</i>	<1% of CMT1	Classic CMT1, DSD, CHN, infantile onset
CMT1F	<i>NEFL</i>	rare	CMT2, with tremor and cerebral ataxia
CMT2-autosomal dominant, axonal			
CMT2A	<i>MFN2</i>	20% of CMT2	Classic CMT2, progressive, optic atrophy
CMT2B	<i>RAB7</i>	rare	Classic CMT2 with sensory complications
CMT2C	<i>TRPV4</i>	rare	Classic CMT2, early onset, involvement of vocal cords
CMT2D	<i>GARS</i>	very rare	Upper limb predominance
CMT2E	<i>NEFL</i>	<2% of CMT	CMT2 with ataxia
CMT2F	<i>HSPB1</i>	very rare	Motor predominant
CMT2I/J	<i>MPZ</i>	5% AD-CMT2	Late onset CMT2
CMT2- recessive, axonal			
CMT2B1	<i>LMNA</i>	very rare	CMT2 rapid progression
CMT2B2	<i>MED25</i>	very rare	Classic CMT2
CMT2H/K	<i>GDAP1</i>	very rare	Mild phenotype, slow progression
CMT4-recessive, demyelinating			
CMT4A	<i>GDAP1</i>	rare	CMT1 or CMT2, early onset
CMT4B1	<i>MTMR2</i>	rare	Severe CMT1, focally folded myelin
CMT4B2	<i>SBF2/MTMR13</i>	rare	Severe CMT1

CMT4C	<i>SH3TC2</i>	rare	Severe CMT1, scoliosis, cytoplasmic inclusions
CMT4D	<i>NDRG1</i>	rare	Severe CMT1
CMT4E	<i>EGR2</i>	rare	CMT1, DSD, CHN phenotype
CMT4F	<i>PRX</i>	rare	Severe CMT1, sensory, focally folded myelin
CMT4G	<i>HK1</i>	rare	Severe early onset CMT1
CMT4H	<i>FGD4</i>	rare	CMT1, predominantly motor
CMT4J	<i>FIG4</i>	rare	CMT1, cataracts
CMTX, X-linked dominant			
CMTX1	<i>GJB1</i>	7-12% of all CMT	Males CMT1; females CMT2
CMTX6	<i>PKD3</i>	rare	CMT2
CMTX, X-linked recessive			
CMTX2	<i>unknown</i>	rare	CMT2, infantile onset
CMTX3	<i>unknown</i>	very rare	early inset, pain and paresthesias
CMTX4	<i>AIFM1</i>	rare	CMT2, infantile onset
CMTX5	<i>PRPS1</i>	rare	CMT2, deafness

1.3.2.3 Disorders of the neuromuscular junction (CMS) and LGMD-CMS

The neuromuscular junction (NMJ) offers unique insights into the molecular biology of synaptic transmission in mammals as it is an easily accessible synapse even in humans and separated anatomically from other synaptic structures and processes allowing its detailed study. Like other synapses of the nervous system, the NMJ is organised through a multitude of signaling pathways which are essential for all steps in its normal development, maturation and maintenance⁸⁶. These interactions exist not only between the presynaptic nerve terminal and postsynaptic apparatus, but also between extracellular, transmembrane and cytoplasmic proteins which have structural and signaling roles⁸⁷. Studies in model organisms such as *Xenopus*, *Torpedo*, *Drosophila* and mice have revealed genetic, structural and functional mechanisms required for neuromuscular transmission such as the presynaptic synthesis and release of neurotransmitters and the receptor binding, ion channel opening and propagation of signals post-synaptically.⁸⁷⁻⁹⁰ However, many pathways critically important for mammalian neuromuscular transmission remain undiscovered or poorly understood, as evidenced recently by the discovery of sympathetic input into the NMJ.

At the NMJ, neural excitation, in the form of motor nerve impulses, is transmitted from the nervous system to the appropriate muscle fibers, thus triggering their contraction⁸⁷. Collectively,

diseases which cause impairment or failure of neuromuscular transmission (CMS, mitochondrial disorders, Charcot-Marie-Tooth neuropathies and myasthenia gravis) have an estimated combined prevalence of 1 in 1200 and lead to varying degrees of muscle weakness or paralysis which may, in extreme cases, be life-threatening⁹¹⁻⁹³. The known range of these disorders is increasingly diverse, including not only ‘acquired’ autoimmune conditions such as myasthenia gravis (MG) but also the many inherited forms⁹⁴. However, for many of these conditions, our understanding of the disease mechanism is incomplete and therapeutic options are often inadequate. A more profound understanding of the functional interplay of proteins altered by impaired neurotransmission will improve the current understanding of the complex biochemical processes maintaining the proper cross-talk between nerve and muscle, define further functional (modifying) candidate genes in patients with NMJ dysfunction, and is crucial for the identification of novel therapeutic targets.

Neuromuscular transmission involves two distinct events. The first is the release from the presynaptic motor nerve terminal of multimolecular ‘quanta’ of the chemical transmitter, acetylcholine (ACh), by exocytosis from membrane-bound synaptic vesicles (SVs), in response to the nerve impulse. The second is the response of the muscle fibre to that transmitter, an electrical depolarisation of the surface membrane, triggered by current flow through the ligand-gated cation channels of the ACh receptor (AChR) opened by ACh binding. ACh action is terminated by its hydrolysis by acetylcholine esterase (AChE), present in the space between nerve and muscle. These events depend on a proper quality control and transport as well as on the interaction of a large number of core proteins, including several gated ion channels and a highly sophisticated evoked exocytosis complex in the nerve. The speed of the process, which takes only a few milliseconds, requires a proper function and precise localisation of a diversity of proteins involved in this process to permit rapid and effective signal transmission. Impaired neuromuscular transmission is a feature of an increasingly diverse group of diseases, including congenital myasthenic syndromes (CMS), mitochondrial disorders and distal axonopathies^{86,87,95}.

Congenital myasthenic syndromes (CMS) are a diverse group of disorders caused by a set of mutations in genes encoding various proteins involved in neuromuscular transmission. In recent decades, mutations in more than 20 genes have been identified as causative in about 80% of patients with inherited impairment of neuromuscular transmission expressing in early life (CMS), indicating that not all responsible genes have been identified⁹⁶⁻⁹⁸. Many of the genes involved encode ‘core’ NMJ proteins mediating the immediate events of neuromuscular

transmission. Foremost among these are the genes which code for core postsynaptic proteins, including the acetylcholine receptor (AChR) subunits and the scaffolding proteins that regulate the specialization of the motor end-plate - agrin, muscle specific receptor tyrosine kinase (MuSK), rapsyn, low density lipoprotein receptor related protein-4 (LRP4) and Dok-7⁹⁹⁻¹⁰². Another group of CMS genes encode proteins in, or likely to be in, the nerve terminal, including choline acetyltransferase (ChAT), synaptotagmin 2 (SYT2) and the recently identified unconventional myosin MYO9A and the choline transporter SLC5A7^{103,104}.

1.4 Proteomics as a powerful tool to study neuromuscular diseases

The study of neuromuscular disorders is an expanding field that has progressed tremendously during the last decades. The vast complexity of the nervous system and of the skeletal muscle has impinged the systematic explorations. Multiple technologies like *in situ* hybridization, NMR, EM, emission tomography, WB, diverse staining and imaging techniques, transcriptomics and genomics have tried to overcome the complexity of these tissues and shed some light in the underlying pathomechanisms. However, the discovery of proteomic-tools offered a more biochemical approach and allowed the study of proteins in an unbiased, quantitative and sensitive manner¹⁰⁵. MS based techniques have a wide toolbox for the investigation of proteomes (Figure 4). Firstly, it offers the opportunity to identify and quantify “whole” proteomes sometimes even with the detection of different protein isoforms and spliced variants. These kind of studies are helpful as they offer wide catalogues of proteins and pathways associated with the disease. Secondly, MS-based correlation via isotopic labelling together with imaging can show and capture the dynamic translocation of proteins from a cellular compartment to another under certain conditions¹⁰⁶. Crosslinking MS or XL-MS is nowadays a very valuable tool for the determination of conformational aspects for individual complexes but also for the whole proteome¹⁰⁷. Proteins interact with other proteins, DNA or small molecules for structural and functional reasons. MS based proteomics allows the identification of this kind of interactions on a very precise manner¹⁰⁸. Post translational modifications or PTMs play crucial roles in cell signaling thus regulating most of the cellular processes. Unfortunately, PTMs have a very high dynamic nature changing their stoichiometry and position during different cellular processes. However, there has been great progress in the enrichment and detection of PTM using MS. Multiple signaling events can now be described in the same sample by the survey of multiple PTMs: phosphorylation, acetylation, ubiquitination, N-termini enrichment, palmitoylation, nitrosylation, glycosylation and oxidative PTMs^{105,109-112}. However, there are still some limitations due to the high amount of

starting material needed (which is generally in the milligram range). Last, imaging MS or IMS offers the possibility of direct analysis of tissue sections with high spatial resolution eliminating the step of samples preparation³¹.

Recent papers have highlighted the important contribution of proteomics in studying muscle under exercise, atrophy, aging, as well as in diseases like inclusion body myositis, myofibrillar myopathy, Bethlem and Ullrich muscular dystrophies, FHSD, metabolic myopathies as well as neurodegenerative diseases such as ALS, Huntington's and Alzheimer's¹¹³. Moreover, the great benefit of the intersection of genomics and proteomics (proteogenomics) to “solve the unsolved” in neuromuscular diseases has recently been pointed out¹¹⁴.

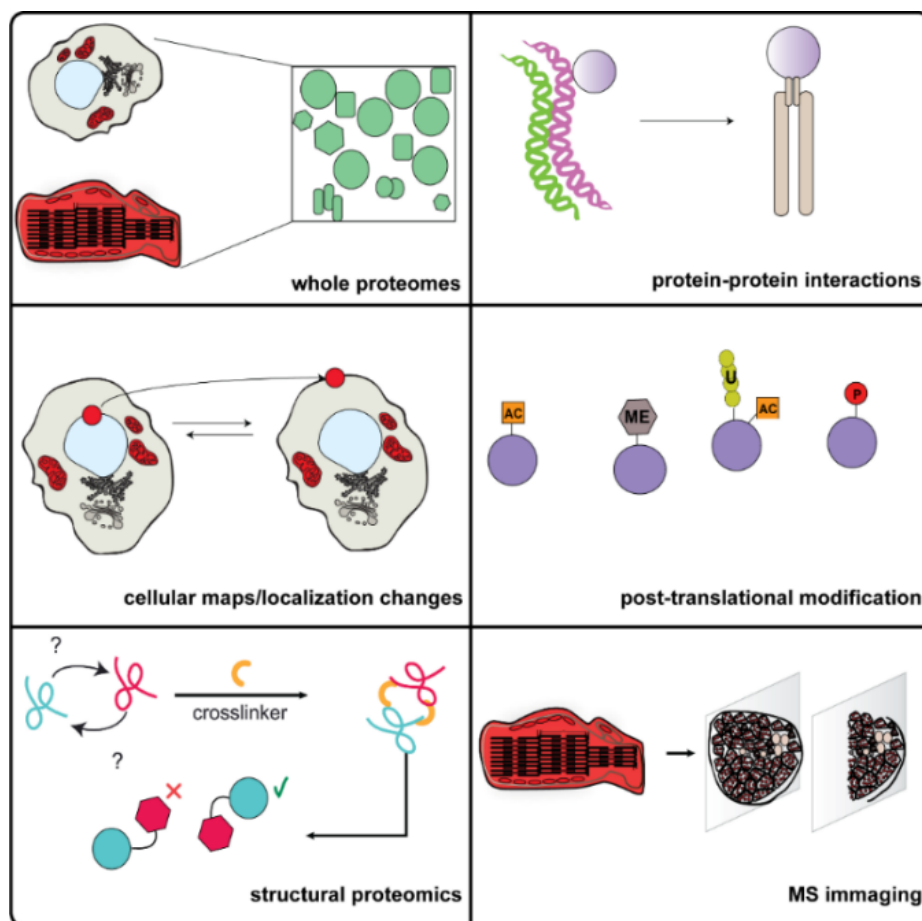


Figure 3. Proteomics offers a multitude of tools, aiding the understanding of neuromuscular processes and associated diseases.

1.4.1 Liquid chromatography coupled with mass spectrometry

Mass spectrometry is a sensitive and selective technique allowing to gain structural information and the molecular weight of a compound. Mass spectrometers are capable of producing ions and

separate them according to their mass-to-charge ratio. Electric fields are applied inside the instrument thus, influencing the trajectory velocity and direction of the ions. The mass of an ion is usually directly proportional to the electric charge in inversely proportional to its mass. Additionally, to avoid the collision between accelerated ions and air molecules, ion separation must be done under vacuum. Despite the advantages of MS, this technique was seldom applied to study proteins until, the early 1990. The discovery of soft ionization techniques allowed the conversion of large molecules into gas phase by slowly reducing the hydration layer surrounding the peptides and without affecting their integrity. This ionization methods were electrospray ionization (ESI) and matrix-assisted laser desorption ionization (MALDI)¹¹⁵.

In order to generate ions via ESI a high voltage current is applied to a liquid passing through a narrow capillary (an ESI emitter), with a potential difference of ± 1.5 -4.5 kV between the emitter and the counter electrode. This forms a strong electric field and small charged drops with a diameter smaller than 10 μm locate at the tip of the emitter. Then the accumulated charged drops are attracted to the counter electrode due to the electrostatic repulsion from the emitter. When the voltage reaches a threshold value the liquid surface changes rapidly changes its shape to a rounded cone, known as the Taylor cone. Liquid is then sprayed from the tip of this cone causing the charge droplets to evaporate quickly until the number of charges on their surface surpasses the Rayleigh limit (the surface tension cannot withstand the charge repulsion). As a consequence, they explode (“Coulombic explosion”) and multiple charged droplets are formed. This process is usually repeated until ionizable analyte escape the liquid droplets. The ions are further desolvated by passing through a heated capillary or with a warm nitrogen counter current depending on the source. Notably, in ESI multiple charge states can be observed based on the size of the peptide or on the solvents used. In order to improve the sensitivity in the ESI, the spraying capillaries are reduced to several microns $< 1\mu\text{m}$. Coupling the miniaturized ESI sources to a high-pressure liquid chromatography (HPLC) with columns smaller than $< 100\mu\text{m}$ can further increase the sensitivity¹¹⁵⁻¹¹⁸.

In “bottom up proteomics”, MS analysis is done at the peptide level so proteomes are first digested using a protease, typically trypsin. In order to reduce the complexity of these big proteomes, a fractionation step prior to MS is usually necessary¹¹⁹. Usually the separation of peptides prior to MS is done using reversed phase (RP) chromatography. In the RP, peptides are separated based on their hydrophobicity by interacting with a non-polar stationary phase in a polar mobile phase. The stationary phase of the column is usually made from a porous silica material on which long alkyl groups are bonded (usually 8 carbons long). The mobile phase is

made out of water, formic acid, methanol or acetonitrile. The more hydrophobic the peptides are the stronger their interaction with the stationary phase. The elution of the peptides from the column is done by gradually changing the composition of the mobile phase.

As proteomes can be very complex, tandem mass spectrometry is usually performed. This provides information about the sequence of the peptide. The sequencing of the peptides involves a two-step process. Firstly, peptides and ions (precursors) from a specific m/z window are selected and then dissociated. Various fragmentation techniques but the most common one used for peptides is collision induced dissociation or CID¹²⁰. In CID the precursor ion is activated by the collision with an inert gas (usually nitrogen or argon) resulting in a conversion of the kinetic energy into internal energy, finally leading to the cleavage of the weakest bond. The complete fragmentation is achieved by hundreds of weak collisions. Other types of fragmentation include also high collision induced dissociation which is suitable for the fragmentation of peptides bearing different tags (TMT, iTRAQ). In the final step of the tandem MS the resulting m/z values are analyzed^{120,121}.

1.4.2 Label free protein quantification

Label-free quantification is used to determine the relative amounts of protein in two or more biological samples. Unlike other methods used for protein quantification, the label-free approach offers a few advantages: 1) it does not require expensive labelling agents, 2) it requires less biological samples, which is very important when analyzing human derived material, 3) it can be applied to any biological material coming from eukaryote, prokaryote or plants and 4) the complexity of the sample is not increased since it is not necessary to mix different proteomes, in addition ,5) no ratio compression occurs¹²². Usually, in label-free precursor, ion peaks are integrated and used as a measure of quantitation. This method is based on the principle that the area of the peak in the MS 1 level is a measure of abundance of the protein (an increase in the signal should reflect an increase of the protein abundance). The areas under the peaks across different samples are calculated, and the abundances of peptides belonging to each protein are summed up. The summed peak areas are compared across different samples resulting in relative protein quantification^{122,123}. All the steps involved in this kind of quantification are often carried out in software like Progenesis.

The workflow most often employed for label free quantification is described in Figure 4. After samples are lysed, peptides are usually generated using a proteolytic enzyme (in most cases,

trypsin is the enzyme of choice due to its high specificity in cleaving peptides after arginine and leucine residues). Then the peptides are subjected to LC-MS/MS analysis and the obtained spectra is interpreted. The first step in data analysis is usually the import of the raw data in Progenesis. Afterwards, the spectra are aligned by choosing one run as the alignment reference and then aligning the retention times of all other runs to this chosen reference. This allows for the correction of any drift in retention time, giving adjusted retention times which are equivalent across all runs. In the second step, a run is selected as a reference and then, for each feature, the software calculates a quantitative abundance ratio between the run being normalized and the reference run. The idea behind this is that many proteins (and therefore peptide ions) won't be changing in the experiment and so the quantitative abundance ratio should be equal to 1. Due to experimental (or technical) variations such as differences in the quantity of protein loaded into the instrument, differences in ionization etc., the actual ratio will not be 1. In order to correct all these experimental variations, the distribution of all ratios is determined. The second step involves the mapping of peptides to proteins. This is usually done using different databases and algorithms. These algorithms usually correlate an experimental tandem MS spectra with a theoretical one predicted for each peptide contained in a protein. After this step, data is re-imported in Progenesis for matching abundances to peptides and proteins respectively. The abundance of each peptide is calculated from all its constituent peptide ions. For each protein, the N most abundant peptides (N being set according to the user selection) have their abundances averaged to provide a reading for the protein signal. The ranking of peptide abundance is based on the values from across all the runs thus giving confidence in the peptide selection by taking all runs into account. This averaged reading allows a relative quantitation of the same protein across runs¹²⁴.

Another way of quantifying proteins using label free profiling is summing up the MS/MS spectra (spectral counting). The relative quantification is done by comparing the sum of PSM for a given protein across multiple samples (a higher abundance will correspond to a higher number of PSM)¹²². The spectral counting methods used to relatively quantify proteins are APEX (absolute protein expression index), emPAI (exponentially modified protein abundance index and NASF (normalized spectral abundance factor)¹²⁵⁻¹²⁷.

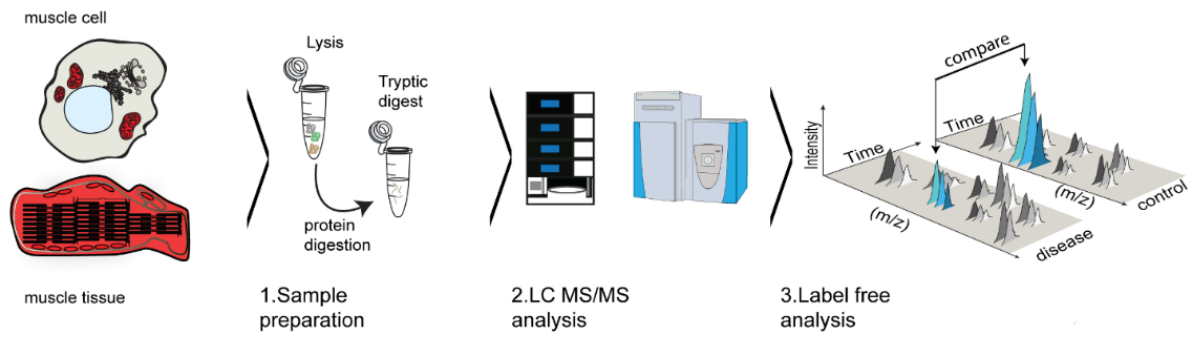


Figure 4. Workflow depicting the sample preparation for proteomics. Proteins are extracted either from cultured cells or from complex tissue and then are lysed and enzymatically digested using a proteolytic enzyme like trypsin. Peptides are afterwards measured and the obtained spectra are further analyzed.

2. Materials and methods

2.1 Materials

2.1.1 Chemicals and reagents used

Table 6. Chemical and reagents used

Name	Supplier
1Kb DNA ladder	Fermentas
24Kb DNA ladder	Fermentas
2-Mercaptoethanol	Sigma-Aldrich
Acethone	Biosolve BV
Acetone	Sigma-Aldrich
Acetonitrile	Biosolve BV
Acrylamide/Bis solution (30%)	Biorad
Agarose	Roche Applied Sciences
Ammonium acetate	Fluka, Sigma-Aldrich
Ammonium bicarbonate	Fluka, Sigma-Aldrich
Ammonium hydroxide 25% (v/v)	Fluka, Sigma-Aldrich
Amoniumpersulfate	Sigma-Aldrich
Amplitaq Gold DNA polymerase	Applied Biosystems
Benzonase Nuclease	Merk Chemicals GmbH
Bicinchoninic acid assay kit	Pierce, Thermo Scientific
BioTaq™ DNA polymerase	Bioline
Bovine Serum Albumin	Sigma-Aldrich
Bromphenol blue	Sigma-Aldrich
Calcium chloride	Merk KgaA
Calmodulin-Sepharose® 4B	GE Healthcare
Clorhidric acid	Sigma-Aldrich
Comassie Brilliant Blue	BioMol Feinchem
Complete mini EDTA-free	Roche
Dithiothreitol	Roche Applied Sciences
DMSO (molecular biology grade)	Sigma-Aldrich
DNA-free™ DNA Removal Kit	Thermo Scientific
dNTP	Bioline
Doxycycline	Sigma-Aldrich
Dubelco's Modified Eagle Medium(DMEM)	PAN-Biotech
Dubelco's Phosphate Buffer Saline	PAN-Biotech
EDTA	Sigma-Aldrich

EGTA	Sigma-Aldrich
Ethanol	Merk KgaA
Ethidium bromide	Merk
Film	Fuji
Foetal bovine serum	Gibco
Foetal calf serum	Gibco
Formic acid	Biosolve BV
Glycerol	Merk
Guanidine hydrochloride	Sigma-Aldrich
High-Capacity cDNA Reverse Transcription Kit	Thermo Scientific
Hybond-P PVDF membrane	GE Healthcare
Hygromycin B	Invitrogen
Iodoacetamide	Sigma-Aldrich
Isopropanol	Biosolve BV
L-glutamine	Gibco
Lipofectamine	Thermo Scientific
Magnesium chloride	Sigma-Aldrich
Methanol	Merk
Mili-Q water	Milipore
Milk powder	BioChem
MS-Compatible Magnetic IP Kit, protein A/G	Thermo Scientific
N,N,N,N-tetramethylethylene	Sigma-Aldrich
Name	Supplier
NP-40	AppliChem
PageRuler™ Prestained Protein Ladder, 10 to 250 kDa	Thermo Scientific
Paraformaldehyde	Sigma-Aldrich
BCA protein assay kit	Thermo Scientific
Penicilin/Streptomycine solution	PAN-Biotech
Phosphate buffer saline tablets	Sigma-Aldrich
Prolong Diamond with DAPI	Invitrogen
Rnase Zap	Ambion
Skeletal muscle cell growth medium	PromoCell
Sodium chloride	Merk KgaA
Sodium dodecylsulfate	Sigma-Aldrich
Sodium hydroxide	Merk KgaA
Supper Signal West Pico Chemiluminiscent Substrate	Thermo Scientific
SYBR green jump start Taq ready mix	Invitrogen
TEV protease	Invitrogen
Thiourea	Sigma-Aldrich

Trifluoroacetic acid	Biosolve BV
Tris (hydroxymethyl)aminomethane base	Applichem GmbH
Triton X-100	Roche Diagnostics GmbH
Triton-X	Sigma-Aldrich
TRIzol kit	Invitrogen
Trypsin (T-1426)	Sigma-Aldrich
Trypsin EDTA	PAN-Biotech
Trypsin Gold	Promega
Tween-20	Sigma-Aldrich
Urea	Sigma-Aldrich
WST1 cytotoxicity detection	Roche Applied Sciences
Zeocin	Invitrogen

2.1.2 Instruments and disposable consumables

Table 7. Used laboratory equipment and consumables

Name	Supplier
384-qPCR plates	Invitrogen
50 and 10 ml falcon tubes	Greiner
96-well plate covering foils (RNase/DNase free)	Capitol Science
96-well plates	Eppendorf
Analytical balance	Sartorius Lab Instruments
Axioplan 2iE Light Microscope	Carl Zeiss
Biological Safety cabinet (HERASAFE KSP18), built in UV-Lamps	Thermo Electron LED
Cell incubator	Heraeus
Cellstar tissue culture flask (25 and 75 mm ³)	Greiner
Centrifuge (5417R, 5424, MiniSpin Plus)	Eppendorf
Confocal laser scanning microscope Leica TCS SP8	Leica
Coverslips (22x22mm, 22x40mm, 22x50mm)	Merck
Electrophoresis chambers	BioRad
Eppendorf pipettes (P1000, P200, P100, P20, P10, P2.5)	Eppendorf
Graduated filter tips	Greiner
Infrared Imaging System Odyssey	Licor
Microcentrifuge tubes (Protein LoBind)	Eppendorf
Microcentrifuge tubes (Safe Lock)	Eppendorf
Microscope slides	Merck

Microtiterplate reader	Thermo Scientific
NanoDrop 2000 UV-Vis Spectrometer	Thermo Scientific
Nanospet Centrifugal Devices with Omega Membrane-30KDa	Pall
Nikon A1R confocl microscope	Nikon
OMIX C18 pipete tips	Agilent
PCR thermocycler	BioRad
PCR tubes	Biogene
pH test strips	Macharey Nagel
pH-electrode (Blue line14)	Schott Intruments
QuantStudio 7 Flex System	Invitrogen
Thermomixer	Eppendorf
Ultrasonic bath	Banderlin Electronic
Ultrasonic processor (Vibracell 75022)	ACIL Sarl
Vacuum centrifuge (Savant SPD 121P)	Eppendorf
Vacuum manifold system	Agilent
Vortex mixer (Genie-2)	Scientific Industries
Water purification system	ELGA LabWater
Western Blot Chamber	BioRad

2.1.3 LC-columns, HPLC and mass spectrometers

Table 8. HPLC, columns and mass spectrometers used

Name	Supplier
Acclaim PepMap C18 75µm ID, 15/25/50 cm length, 3µm particle size, 100 Å pore size	Thermo Scientific
Acclaim PepMap C18 100µm IDx2 cm length, 5µm particle size, 100 Å pore size	Thermo Scientific
Kinetex C18 0.5 mm ID, 15 cm length, 2.6 µm particle size, 100 Å pore size (bulk material)	Phenomenex
Biobasic C18 0.5 mm ID, 15 cm leght, 5 µm particle size 300 Å pore size	Thermo Scientific
PepSwift Monolithic trap column, 200 µm ID, 5 mm length	Thermo Scientific
PepSwift Monolithic capillary column, 200 µm ID, 5 cm length, PS-DVB	Thermo Scientific
Ultimate U3000 HPLC	Thermo Scientific
Ultimate U3000 HPLC nano rapid separation liquid chromatography	Thermo Scientific
LTQ Orbitrap Elite	Thermo Scientific
Q Exactive and Q Exactive Plus	Thermo Scientific
Orbitrap Lumos Fusion Tribrid	Thermo Scientific

1.1.3 Software used for LC-MS/MS acquisition, control and data analysis

Table 9. Software used for the MS analysis and acquisition

Software	Version (s)
Chromeleon	6.8 (SR 8-11)
Mascot ¹²⁸	2.6
MS GF+ ¹²⁹	
OMSSA ¹³⁰	2.1.9
Peptide Shaker ¹³¹	1, 1.0, 1.2, 1.4, 2.0
Progenesis ¹³²	4.1
Proteome Discoverer	1.4, 2.2
SearchGUI ¹³³	1.18, 2.0
Sequest ¹³⁴	
STRING	10
Xcalibur	2.2
Cytoskape ¹³⁵	3.4.0
ClueGO ¹³⁶	2.5.1
CluePedia	1.5.1
X!Tandem	Jackhammer (15.06.2013)

2.1.4 Antibodies

The list of primary antibodies and their corresponding dilution are shown below.

Table 10. Primary antibodies used

Primary antibody	Description	Company	Use	Dilution
GAPDH	Mouse monoclonal	Sigma-Aldrich	WB	1:2000
anti-FLAG	Mouse monoclonal	Sigma-Aldrich	WB	1:2000
anti-HA	Mouse monoclonal	Sigma-Aldrich	WB	1:2000
α -actinin	Mouse monoclonal	Sigma-Aldrich	WB	1:2000
F319	Mouse monoclonal	Developmental Studies Hybridoma Bank, Iowa	IF	1:200
F59	Mouse monoclonal	Developmental Studies Hybridoma Bank, Iowa	IF	1:50
SV2	Mouse monoclonal	Developmental Studies Hybridoma Bank, Iowa	IF	1:200
CAV3	Mouse polyclonal	BD Biosciences	IF	1:200
CAV3	Rabbit polyclonal	Abcam	WB	1:2000
Golgi 97	Rabbit polyclonal	Gene Tex	IF	1:200
HYOU 1	Rabbit polyclonal	Thermo Scientific	IF	1:200
LC3	Rabbit polyclonal	Novus	WB	1:2000
IQGAP1	Rabbit polyclonal	Abcam	WB	1:2000
IQGAP1	Rabbit polyclonal	Abcam	IF	1:200

MuSK	Rabbit polyclonal	Abcam	WB	1:2000
CDC42	Rabbit polyclonal	St. Johns	WB	1:2000
RAC-GAP1	Rabbit polyclonal	St. Johns	WB	1:2000
Rac1/2/3/CDC42	Rabbit polyclonal	St. Johns	WB	1:2000

The secondary antibodies used for immunofluorescence were conjugated to Alexa Flour 488 or 594 (Invitrogen). Anti-mouse and anti-rabbit HRP-conjugated as well as florescence-conjugated secondary antibodies were obtained from Invitrogen. Florescence-conjugated secondary antibodies used in this study include anti-mouse 680 and anti-rabbit 680 as well as for the actin cytoskeleton or F-actin Phalloidin Alexa 546 or 488. For the AChR receptor alpha-bungarotoxin 594 also obtained from Invitrogen was used.

2.1.5 Plasmids

Full-length CAV3 coding DNA (cDNA) was obtained by PCR on reverse transcribed RNA extracts from mouse skeletal muscle. Forward and reverse primers contained adaptors with restriction sites for *KpnI* and *EcoRI*, respectively. The PCR product was subcloned into the pCRXL-TOPO vector (Invitrogen). For the synthesis of CAV3-CTAP-pcDNA5/FRT/TO expression vector, the coding sequence of CAV3 was amplified by PCR from CAV3_pCR-XL-TOPO. A pair of primers was constructed, containing adapters with restriction sites for *HindIII* and *KpnI* that allowed in-frame cloning in the pcDNA5/FRT/TO-C-TAP vector. The p.P104L, p.E34K, p.W58R, p.G56R, p.C72W, p.Y72C, p.T78M, p.T78K and p.A93T mutant expression constructs were generated by site-directed mutagenesis (Stratagene) according to the manufacturer's instructions utilizing the WT construct as a template. For the construction of an "empty FLAG vector" called pcDNA5/FRT/TO-empty-FLAG-tag, the plasmid pcDNA5/FRT/TO-Sil1-TAP was digested with enzymes *HindIII* and *XhoI*, then ligated with double stranded *HindIII*-overhang triple FLAG *XhoI*-overhang oligo (ds *HindIII*-FLAG-*XhoI*) composed of annealed oligos empty FLAG-tag-Oligo sense and empty FLAG-tag-Oligo anti-sense. All of these constructs were generated in ISAS by Dr. Raffael Kettler.

Additionally, a CAV3 WT-FLAG construct was generated from the pcDNA5/FRT/TO-mmCaveolin3-P104-TAP (wildtype) which was digested with the restriction enzymes *Acc65I* and *NotI*, in order to remove the C-terminal TAP-tag. The "vector-band" was then isolated using agarose gel electrophoresis and ligated with double stranded *Acc65I*-overhang triple FLAG

NotI-overhang oligo (ds *Acc65I*-FLAG-*NotI*) composed of annealed oligos FLAGAcc65INotIF and FLAGAcc65INotIR.

The pRP[Exp]-Puro-CMV>hIQGAP1[NM_003870.3]/HA was purchased from Vector Builder.

2.2 Methods

2.2.1 Cell culture

Human cervical epithelium (HeLa) and human embryonic kidney cells (HEK293) were grown in DMEM (containing L-glutamine) supplemented with 10% fetal bovine serum, 100 U/ml penicillin-streptomycin, at 37°C in a 5% CO₂ and humidified atmosphere. Human skeletal muscle cells (RCMH) were grown in DMEM, F-12-HAM supplemented with 12.5% fetal bovine serum, 0.1% sodium bicarbonate, and 100 U/ml penicillin-streptomycin at 37°C in a 5% CO₂ and humidified atmosphere¹⁰⁸.

The human primary myoblasts used in the experiments were set up by Dr. Mojgan Reza at the biobank of the MRC Centre for Neuromuscular Diseases, Newcastle, United Kingdom. Cells were then grown in Skeletal Cell Muscle Media (PromoCell), supplemented with 10% fetal calf serum, 1.5% L-glutamine, 0.06% gentamicin at 37°C in a 5% CO₂ and humidified atmosphere. Next, myoblasts were differentiated into myotubes by changing to a medium with reduced serum content. When myoblasts were about 80% confluent the SKCM media was removed and the cells washed in PBS. Following this, 15 ml of differentiation media (composed of 95% DMEM and 5% horse serum) was added to the flask which was then returned to the incubator. After five days cells were about 80% fused and myotubes were visible (multinucleated cells that appear to line up alongside each other).

The human primary fibroblasts used for the experiments described in chapter 3.2.1 were obtained from skin biopsies that were taken from three clinically affected (and genetically proven; c.149T>C; p.Ile50Thr) INPP5K patients⁵⁵. Fibroblasts were grown in DMEM medium supplemented with 10% fetal bovine serum, 50 units/ml penicillin, 50 µg/ml streptomycin, 0.4% (v/v) amphotericin B (250 µg/ml), and 1 mm sodium pyruvate at 37 °C in a 5% CO₂ atmosphere. Cells were grown to 80% confluence prior to harvesting for proteomic profiling. All INPP5K fibroblasts were grown and collected by Dan Cox from the MRC Centre Biobank for Neuromuscular Diseases, Newcastle, United Kingdom¹³⁷. Control fibroblasts were also obtained from the Newcastle Biobank and cultured in the same conditions as the diseased ones. All donors matched in sex and age.

2.2.1.1 Passaging and harvesting the cells

When cells reached about 80% confluence, the media was discarded and the cells were washed with 5 ml of PBS in order to remove all traces of FCS. The PBS was then removed and trypsin was added (accordingly to the size of the flask or plate) and incubated at 37 °C in a 5% CO₂ atmosphere. HeLa and RCMH cells were incubated for 2 minutes, while for all the primary cells it was necessary to incubate for 5 minutes. Following this procedure, 5 ml of serum containing media was added to the flask to quench the trypsin and the cells were transferred to a 10 ml universal tube. Then, cells were centrifuged at 160g for 5 minutes. Following this, the supernatant was discarded and cells were washed with 10 ml of PBS. Cells were then either frozen at -80°C or lysed immediately.

2.2.1.2 Seeding the cells on coverslips

To perform the immunofluorescence studies, cells were seeded on coverslips: autoclaved circular cover slips were placed into each well of a six well plate. After harvesting, cells were re-suspended in 3ml of medium. To the centre of each cover slip, 500 µl of cell-containing medium was pipetted, together with 1ml of normal media before placing the plate back into the incubator to allow the cells to adhere to the cover slip and to proliferate.

2.2.1.3 Cell transfection and generation of inducible HEK 293 T-Rex cells

For DNA transfection experiments, HeLa and RCMH cells were seeded in 6 well or in 10 cm² plates one day before being transfected with the indicated DNA (1 µg for the 6 well plates or 4 µg for the 10 cm² plates) using Lipofectamine 2000 following the manufacturer's protocol. At 48 hours post transfection, cells were either harvested as described above or further prepared for immunofluorescence.

HEK 293 Flp-In T-Rex 293 cells were selected for the generation of stable CAV3 (WT and p.P104L)-inducible *in vitro* systems. The Flp-In T-Rex construct was transfected into HEK 293 cells and a culture medium containing 100 mg/mL Zeocin™ and 15 mg/mL blasticidin (Invitrogen) was used to select the cells that incorporated the construct. Preparation of the HEK T-REX cells was carried out by Dr. Andreas Roos at the RWTH Aachen University Hospital, Institute of Neuropathology. Next, Flp-In T-Rex HEK cells that stably express the inducible CAV3 (WT and p.P104L)-TAP fusion proteins were generated according to the manufacturer's instructions (Invitrogen). For the selection of stable clones, hygromycin B at a concentration of 10 mg/mL was added to the culture media. To induce the expression of CAV3 (WT and

p.P104L), doxycycline was administered to cell culture media at a final concentration of 1 mg/mL.

2.2.1.4 Adenovirus transduction

The *Adv.IQGAP*, *Adv.GFP* and a control adenovirus were purchased from Vector Builder and supplied at a concentration of $>10^{10}$ PFU/ml (plaque forming units). Primary myoblasts were seeded on coverslips in a 24 well plate one day before they were transduced. Next, cells were infected with a concentration of 100 PFU/ml of the corresponding adenoviruses. After 24 hours, the cell media containing the virus was replaced with normal growth media and cells were incubated for an additional 72 hours at 37 °C in a 5% CO₂ atmosphere in skeletal muscle growth media.

2.2.1.5 Cell toxicity and viability

To determine the cell toxicity upon the stable expression of empty TAP, CAV3 WT and CAV3 p.P104L, the WST1 assay was performed. Cells were cultured on a 96 well plate at a density of 4000 cells/well in 100 µL of DMEM. 24 hours prior to the experiment, some of the cells were induced using doxycycline. All cells were seeded in triplicate. To correctly assess the release of LDH several controls were prepared: 1-spontaneous LDH activity (10 µL of water were added to non-induced cells); 2-maximum LDH activity (10 µl of lysis buffer added to the induced cells). Next, to all the controls and induced samples, the reaction mixture was added and cells were further incubated for 45 minutes at 37 °C in a 5% CO₂ atmosphere after which 50 µL of stop solution was added to the mixture and the absorbances at 490 and 690 nm were recorded. To determine the LDH activity, the 680 nm absorbance was subtracted (background values) from the 490 nm before the calculation of the cytotoxicity. For the calculation of the % Cytotoxicity the following formula was used:

$$\%Cytotoxicity = \frac{\text{Induced cells LDH activity} - \text{Spontaneous LDH activity}}{\text{Maximum LDH activity} - \text{Spontaneous LDH activity}}$$

Cell proliferation was measured with the help of CASY cell counter. HEK293 T-REX cells stably expressing WT and p.P104L CAV3 and the empty TAP were cultured in six well plates at a density of 5×10^5 cells/well. Cells were kept induced for the duration of the experiment and were collected in 2 ml of PBS and counted at 24, 48 and 72 hours post expression of the protein of interest in 10 ml of the “CASY-Ton”. Only viable cells were taken into consideration.

2.2.2 Clinically affected and unaffected tissues

2.2.2.1 Human biopsies

The skeletal muscle biopsy (*quadriceps femoris*) derived from a healthy donor utilized for the generation of the muscle protein catalogue was provided by Prof. Dr. Werner Stenzel (Institute of Neuropathology, Charité Berlin).

Skeletal muscle biopsies derived from three index patients (mid portion of *vastus lateralis*) harboring the c.149T>C; p.Ile50Thr on the *INPP5K* gene were obtained from Dr. Rita Barresi and Dr. Richard Charlton from the Muscle Immunoanalysis Unit (Medical School, Newcastle University; United Kingdom) and used for immunofluorescence studies.

2.2.2.2 Mouse tissue

p.P104L CAV3 transgenic mouse model

The transgenic mouse model expressing p.P104L CAV3 was kindly provided by Prof. Yoshihide Sunada (Department of Neurology, Kawasaki Medical School, Okayama, Japan). Positive transgenic mice were identified as described previously^{138,139}. To generate offsprings, several founder mice were bred with the wt littermates. For the proteomics studies, *quadricep* muscles derived from 10 weeks old animals (3 transgenic and 3 wt littermates) were used. All procedures were approved by the Uniklinik RWTH Aachen Institutional Animal Care and Use authorities.

GFPT1 mouse model

The *Gfpt1*^{tm1d/tm1d} mutant mouse was generated by Dr. Yasmin Issop at the John Walton Muscular Dystrophy Research Centre for Neuromuscular Diseases, Newcastle, United Kingdom. The generation of the mouse model, genotyping and phenotypical features have been described in detail¹⁴⁰. For the unbiased proteomic profiling, intercostal muscle derived from 3 months old animals was used (3 muscles derived from the *Gfpt1*^{tm1d/tm1d} and 3 muscles from the wt littermates). All procedures were approved by the Home Office and were carried out in accordance to the Animals Scientific Procedures Act of 1986 under license 70/8538.

Sh3tc2^{ΔEx1/ΔEx1} mouse model

The *Sh3tc2*^{ΔEx1/ΔEx1} mouse model represents a suitable animal model for Charcot-Marie-Tooth neuropathy subtype 4C (CMT4C) and was a generous gift from Dr. Roman Chrast from the Karolinska Institutet, Department of Neuroscienc (Stockholm, Sweden). The generation of this mouse model was described by Arnaud and colleagues in detail¹⁴¹. Homozygous affected

animals as well as wild-type littermates were obtained by mating heterozygous males with heterozygous females and the genotyping was performed as previously described¹⁴¹. All experiments with animals followed protocols approved by the veterinary office of the Canton of Zurich, Switzerland. For the proteomics experiments, *gastrocnemius* muscle derived from 2 years and 3 months old animals were used (3 muscles derived from the Sh3tc2 KO animal and 3 muscles derived from the wt littermates were used).

2.2.3 Cell lysis

For the proteomic profiling, lysis of cells was performed using a buffer comprised of: 1% SDS, 150 mM NaCl, 50 mM Tris-HCl at the pH of 7.8 and a protease inhibitor cocktail (Complete mini). Cell lysis was performed on ice under a sterile laminar hood. For every million cells, a volume of 100 μ l of lysis buffer was added. Cell homogenization was carried out by pipetting the mixture up and down until the complete solubilization of the pellet was achieved. To degrade the nucleic acids, benzonase (25 U/ μ L) together with 2 mM MgCl₂ was added to the lysate and incubated at 37°C for 30 minutes. Next, samples were centrifuged at 4°C for 30 minutes at 8000 g to separate cell debris from the protein extract. Finally, the supernatant containing the extracted proteins was collected and either used immediately or stored at -80°C until further use.

For western blotting, protein extracts were prepared using a buffer composed out of 150 mM NaCl, 1% NP40, 0.1% SDS and 10 mM Tris-HCl, pH 7.8 and a cocktail of protease inhibitors. For homogenization, cells were pipetted up and down a few times. Aliquots of the protein extracts were then mixed with Lämmli-buffer in a ratio of 1:1 (100 mM Tris-HCl, pH 6.8, 10% SDS, 25% glycerol, 0.2% (w/v) bromophenol blue, and 5%(w/v) 2-mercaptoethanol) and heated for 5 minutes at 95 °C.

2.2.4 Muscle lysis

To ensure the proper homogenization of the muscle tissue a two-step lysis procedure was employed. The first step consisted in the mechanical grinding of the tissue in a buffer composed of 1% SDS, 150 mM NaCl, 50 mM Tris-HCl at the pH of 7.8 supplemented with a protease inhibitor cocktail, using a glass mortar and pestle. The grinding procedure lasted between 2 and 4 minutes, depending on the size of the tissue. The amount of lysis buffer added to the tissue depended on the amount of muscle that was aimed to be lysed: e.g. for 1mg of tissue, 200 μ L of buffer was added. In the second step, the lysates were transferred into LoBinding Eppendorf tubes and subjected to two ultrasonication cycles (30 seconds, amplitude 30 and pulse 1 s/1 s). Then, debris were separated from the protein extracts by centrifugation at 4°C for 10 minutes at 3000 g. The supernatant was collected in a LoBind Eppendorf tube and stored at -80°C until further use.

2.2.5 Determination of protein concentration

For the correct determination of the protein concentration in the cell and tissue lysates, the calorimetric bicichoninic acid assay was performed according to the manufacture's protocol. Three serial dilutions, in triplicate, per sample were prepared using ultra-pure water. Afterwards, samples were pipetted into a 96-well plate. To each well, 200 μ L of the BCA solution was added, and plate incubated for 30 minutes at 60°C. As a calibrator, bovine serum albumin was used (a calibration standard curve was created using a five points-concentration range of BSA between 5-250 μ g/ml). After incubation, the absorbance at 570 nm was measured using a microtiter plate reader.

2.2.6 Tandem affinity purification assay

The "TAP method" involves the fusion of the protein of interest (in this case CAV3) with the TAP tag which consists of 2 IgG binding domains of *Staphylococcus aureus* protein A and a calmodulin binding peptide, which are separated by the tobacco virus (TEV) cleavage site. This type of tag allows the purification of a protein of interest and its binding partners in a two-step procedure, making it to a very efficient method for the elimination of contaminants or unspecific bound proteins¹⁴².

For the tandem affinity purification assay (TAP), cells stably expressing the WT and mutant forms of CAV3 in an inducible fashion were used. HEK293 TREX cells were grown in

suspension in 1 litre of cell media using bioreactors in order to ensure sufficient starting material. Afterwards, cells were pelleted, washed 3 times with ice cold PBS and lysed gently on ice for 3 hours, using the TAP lysis buffer composed of 100 mM Tris-HCL pH 8.0, 150 mM NaCl, 10 mM KCl, 1.5 mM MgCl₂, 0.5 mM DTT, 1% glycerol, 0.1% NP-40 and protease inhibitor cocktail. The extract was centrifuged at 10000 g and the pellet representing the cellular debris was subsequently discarded. The supernatant was transferred to an Eppendorf tube which contained 100 µL of IgG Sepharose beads (previously washed 3 times with 200 µL of TAP lysis buffer) corresponding to 200 µL of bead suspension. The mixture was incubated at 4°C under rotation at 15 rpm overnight. Afterwards, the supernatant was discarded and the beads were washed thrice with 500 µL of TAP lysis buffer and one time with TEV buffer cleavage buffer (10 mM Tris-HCl, pH 8, 150 mM NaCl, 0.5 mM EDTA and 1 mM DTT). The cleavage from the protein A motive was achieved with 100 units of TEV protease at room temperature for 4 hours. To facilitate the binding to the calmodulin beads, 3 ml of the calmodulin buffer (Tris-HCl 10 mM, pH 8, 150 mM NaCl, 1 mM Mg(CH₃COO)₂, 1 mM imidazole, 2 mM CaCl₂, 10 mM 2-mercaptoethanol) and 3 µL of 1M CaCl₂ were added to the eluate recovered after TEV cleavage. The supernatant was then transferred into a new Eppendorf tube containing 100 µL of calmodulin beads (previously washed with calmodulin binding buffer) and incubated for a minimum of 3 hours at 4°C under continuous shaking. The supernatant was discarded and the beads washed thrice with 500 µL of calmodulin binding buffer. Finally, the precipitated proteins were eluted with 500 µL of calmodulin elution buffer (Tris-HCl 10 mM, pH 8, 150 mM NaCl, 1 mM Mg(CH₃COO)₂, 1 mM imidazole, 2 mM EGTA).

2.2.7 Proteomic Profiling

2.2.7.1 Sample carbamidomethylation

Prior to carbamidomethylation, the disulfide bonds, which stabilize the quaternary and tertiary structure of proteins, were reduced by incubating the cell or tissue protein extracts with 10 mM DTT at 56°C for 30 minutes. Next, the free thiol groups were alkylated using IAA (30 mM, 30 minutes at room temperature in the dark).

2.2.7.2 Sample preparation, proteolysis and clean-up

2.2.7.2.1 Filtered aided sample preparation

For a proper clean-up of the samples and for proteolysis, filters containing a weight cut off membrane of a certain molecular weight were employed^{143,144}. This method is widely used for

the removal of contaminants like SDS which are contained by the lysis buffer. The FASP protocol consists of a centrifugal device with a membrane of a nominal MW cutoff (MWCO). The size of the MWCO pores is usually chosen based on an approximation of the non-denatured proteins and can be 10, 30 or 50 kDa. For all the experiments, FASP was performed with filters having a MWCO of 30 kDa.

After oxidation and alkylation of the lysate, 100 µg of protein, was diluted with a solution containing 8 M urea and 100 mM Tris-HCl pH 8.5, so that the final concentration of SDS in the solution reaches 0.1% and the UREA 7 M. Next, the samples were placed on the spin filter and the device centrifuged at 13500 g at room temperature for approximately 15 minutes. This allowed the proteins to be trapped on the membrane while the contaminants such as salts, SDS or low molecular components passed through the filter. For an efficient elimination of all contaminants, the filter was washed 3 times with 100 µL of the 8 M urea buffer. For the buffer exchange, the membrane was washed three times with 100 µL of 50 mM NH₄HCO₃ pH 7.8. Next, 100 µL of the proteolysis buffer (trypsin-1:25 w/w of enzyme to substrate, 1 mM CaCl₂ and 0.1 mM GuHCl) was added to the filter and incubated at 37°C overnight. Finally, peptides were recovered by centrifugation followed by two consecutive washing steps with 50 µL of the 50 mM NH₄HCO₃ pH 7.8. To ensure a better recovery of peptides, the final washing step was performed with 50 µL of ultrapure water. The FASP filter will retain any high molecular weight material such as partially or completely undigested proteins. The obtained tryptic peptides were acidified to a pH < 3.0 with 10% TFA and stored at -80°C until further use.

2.2.7.2.2 In solution digestion

The amount of proteins obtained from certain experiments, such as immunoprecipitation, is mostly lower than 5 µg, thus making FASP unsuitable for sample preparation. Additionally, the components used in the buffers required for the IP are mostly incompatible with the membrane of the FASP filters. For these reasons, ethanol precipitation was used as a clean up method. The amount of protein in the samples was roughly estimated as being 5 µg. The protein solution is first diluted 10-fold (ratio of 1:10) with an ice cold ethanol solution, and then stored at -40°C for 60 minutes followed by centrifugation at 4°C for 30 minutes at 18000 g. Afterwards, the supernatant was discarded and the pellet washed thrice with 100 µL of ice cold acetone. After washing, the pellet was dried under a laminar flow hood and then solubilized with a solution containing 1 M GuHCl, 50 mM NH₄HCO₃ pH 7.8 and proteins were reduced and alkylated as described in section 2.2.6.2.1. Next, samples were diluted with 50 mM NH₄HCO₃ pH 7.8 until a concentration of 0.2 M GuHCl was attained. Proteolysis was performed by adding trypsin to

the sample in a ratio of 1:20 of enzyme to substrate followed by sample incubation for a minimum of 12 hours at 37°C.

2.2.7.2.3 Desalting of proteolytic digests

Desalting of tryptic peptides was carried out with the help of C18 material in the form of commercially available tips. Depending on the amount of digested peptides, either C18 pipette tips suitable for 10 and 100 µL (Omix) or in house generated C18+oligoR3 tips were used. Prior to utilization, the tips were activated by using 100% ACN followed by equilibration with 0.1% TFA. All volumes used were assessed based on the size/capacity/type of the tip used. After the resin was equilibrated, the peptide mixture was loaded onto the tips and the flow through passed two times onto the tip was then discarded. The column was washed 3 times with 0.1%TFA to ensure proper elimination of contaminants. Finally, peptides were eluted from the resin with 60% ACN in 0.1%TFA. The eluates were dried in the SpeedVac and then resuspended in 0.1% TFA.

2.2.7.3 High pH reverse phase peptide fractionation

To reduce the complexity of the samples by a simultaneous increase of the analytical dynamic range and proteome coverage, a high pH reverse phase fractionation of the tryptic peptides was performed. 50 µg of the desalted and dried peptides were resuspended in 10 mM ammonium formate, pH 8 and fractionated on a C18 column with a binary buffer system: buffer A-10 mM ammonium formate, pH 8 and buffer B-10 mM ammonium formate, 84%ACN, pH 8. The sample was loaded onto the column with buffer A at a flow rate of 12.5 µL/minute and separation was carried out using the following gradient: 3% B for 10 minutes, 3-50% B in 75 minutes, 95% B hold for 10 minutes, 95%-3% B in 10 minutes and finally column re-equilibration for with 3% B for 20 minutes. Twenty fractions were collected in LoBind Eppendorf tubes at 60 seconds intervals. After the 20 fractions were collected, the process was repeated starting with the first tube in a concatenated mode. Finally, all the collected fractions were dried in a SpeedVac and then resolubilized in 0.1%TFA and stored at -80°C until further analysis. These fractionations were performed on an UltiMate 3000 HPLC.

2.2.7.4 LC-MS/MS analysis

Peptide separation prior to MS analysis was conducted on C18 reverse phase columns using either a nano-flow U3000 HPLC or U3000 RSLC HPLC system from Thermo Scientific. The commercial column used was a C18 Acclaim PepMap (Thermo Scientific) with the following specifications:

- trapping column: 100 μm inner diameter x 2 cm length, 5 μm particle size, 100 \AA pore size,
- main column: 75 μm inner diameter x 50 cm length, 2 μm particle size and 100 \AA pore size.

For certain samples, an in-house packed column was employed which was filled with Kinetex C18 material with a 2.6 μm particle size for the main column and 0.75 μm for the trapping column, 100 \AA pore size. All the separations were carried out with a binary gradient: buffer A-0.1%FA and buffer B-84%ACN in 0.1%FA, pH 2.7. Peptides were prepared in 15 μL of loading buffer (0.1%TFA) and were first preconcentrated on the trapping column using 0.1%TFA followed by separation on the main column using the binary system described above.

For the MS/MS analysis the following mass spectrometers were employed:

- LTQ Orbitrap Velos (Thermo Scientific)
- Orbitrap Elite (Thermo Scientific)
- Orbitrap Fusion (Thermo Scientific)
- Orbitrap Lumos Fusion (Thermo Scientific)

As an interface between the MS and the LC, electrospray ionization was used. All MS measurements were acquired in data dependent manner. All the MS parameters (number of MS scans, ACG target, and injection times) were adjusted according to the complexity of the sample and the capacity of the instruments.

2.2.7.4.1 Protein profiling towards the generation of a muscle protein catalogue

Peptides obtained from myotubes, myoblasts and muscle tissue were fractionated using high pH system as described above (Section 2.2.6.1, 2.2.6.2.1, 2.2.6.3). Each fraction obtained from the myotubes and myoblasts (total of 40 fractions) was analysed using an Ultimate 300 HPLC system coupled with a qExactive HF. All the samples were measured and processed by Dr. Rene Zahedi (ISAS). The peptides were preconcentrated on a trapping column for 10 minutes using 0.1% TFA at a flow rate of 20 $\mu\text{L}/\text{min}$ followed by the separation on the commercial main column with a 120 minutes gradient ranging from 3 to 35% B at a flow rate of 250 nL/min . The full MS scan was acquired from m/z 300 to 1500 at a resolution of 60000 using the polysiloxane ion at 371.101236 as lock mass¹⁴⁵ with an AGC target value of 3×10^6 ions and a maximum injection time (IT) of 120 ms. Isolation of the precursor was done by the quadrupole with a window of 1.2 m/z . The top 15 most intense ions were fragmented in the HCD (NCE 35%) cell

with an AGC target value of 5×10^4 . MS/MS scans were acquired at a resolution of 15000 and a dynamic exclusion of 20 s.

To gain increased sensitivity, the fractions obtained from the muscle tissue were measured using a Lumos Fusion mass spectrometer with the detection in the ion trap. Peptides (20 fractions) after fractionation were preconcentrated and separated employing the same method and instrument as described above. The MS survey scans were acquired in the Orbitrap from 300 to 1500 m/z at a resolution of 120000 using the polysiloxane ion at m/z 445.12002 as lock mass¹⁴⁵, and AGC target of 2×10^5 and maximum IT of 50 ms. Top speed most intense signals were selected for HCD fragmentation (collision energy 30%) and the MS/MS spectra were acquired in the Iontrap using an AGC target of 2×10^3 , maximum IT 300 ms and a dynamic exclusion of 15 s and an isolation window of 1.2 m/z .

2.2.7.4.2 INPP5K fibroblasts

The workflow employed for sample preparation has been previously described in the 2.2.6.1 and 2.2.6.2.1 chapter. In total 6 samples (3xINPP5K fibroblasts and 3x control fibroblasts) were processed independently. 1 μg of each sample was measured using an Ultimate 3000 nano RSLC system coupled to an Orbitrap Fusion Lumos mass spectrometer. Peptides were separated as described above using a 120 min LC gradient ranging from 3-35 % of 84 % ACN, 0.1 % FA (v/v) at a flow rate of 250 nL/min. MS survey scans were acquired in the Orbitrap from 300 to 1500 m/z at a resolution of 120000 using the polysiloxane ion at m/z 445.12002 as lock mass, with an AGC target of 2.0×10^5 and maximum IT of 50 ms. Next, top speed most intense ions were subjected to HCD with a normalized collision energy of 35% at a resolution of 120000, taking into account a dynamic exclusion of 15s and an isolation window of 1.2 m/z . The ACG target and maximum injection times were set to 2.0×10^3 300 ms respectively.

2.2.7.4.3 p.P104L CAV3 mouse muscles

Six quadriceps muscles, i.e. three derived from 10 weeks old p.P104L CAV3-transgenic animals and three from wt littermates were collected, snap-frozen in liquid nitrogen at -80°C and processed independently as described in sections 2.2.6.1 and 2.2.6.2.1. A total of 1 μg of peptides were analysed using an Orbitrap Elite mass spectrometer coupled with an Ultimate 3000 nano RSLC system. Peptides were separated as described above using a 210 min LC gradient ranging from 3-42 % of 84 % ACN, 0.1 % FA (v/v) at a flow rate of 230 nL/min. The MS survey scans were acquired in the Orbitrap from m/z 300 to 1500 at a resolution of 60,000 using the polysiloxane ion at m/z 371.101236 as lock mass. Then, the ten top most intense ions

were subjected to collision induced dissociation (CID) in the ion trap, taking into account a dynamic exclusion of 30 s. CID spectra were acquired with a normalized collision energy of 35%. AGC target values were set to 10^6 for MS¹ and 10^4 for ion trap MS² scans, and maximum injection times were set to 100 ms for both full MS and MS² scans.

2.2.7.4.4 Tandem affinity purification products

For the tandem affinity purification, 3 biological replicates for each cell line were analysed and tryptic peptides were obtained as described in sections 2.2.6.1, 2.2.6.2.2 and 2.2.6.3. For the tandem affinity purification assay, inducible stable expressing cells were prepared as described in section 2.2.1.3 and the tandem purification was performed as described in section 2.2.1.6. In total, six samples (3x CAV3-WT HEK293-TREX and 3x CAV3-p.P104L HEK293) were subjected to tryptic digested. The samples were analysed using an Orbitrap Elite mass spectrometer coupled with an Ultimate 3000 nano RSLC system. Peptides were separated as described above using a 115 min LC gradient ranging from 3-45 % of 84 % ACN, 0.1 % FA (v/v) at a flow rate of 230 nL/min. The full MS scans were acquired in the m/z 300 to 1500 at a resolution of 60,000 using the polysiloxane ion at m/z 371.101236 as lock mass. Next, the ten top most intense ions were subjected to collision induced dissociation (CID) with a NCE of 35% in the ion trap, taking into account a dynamic exclusion of 30 s. AGC target values were set to 10^6 for MS¹ and 10^4 for ion trap MS² scans, and maximum injection times were set to 100 ms for both full MS and MS² scans

2.2.7.4.5 *Gfpt1*^{tm1d/tm1d} mouse muscles

In total, six samples – three intercostal muscle samples derived from the GFPT1 mouse model and three derived from wildtype littermates – were prepared as described in sections 2.2.6.1 and 2.2.6.2.1. Samples were analysed using an Ultimate 3000 nano RSLC system coupled to an Orbitrap Fusion Lumos mass spectrometer (both Thermo Scientific). Briefly, peptides were pre-concentrated on a trapping column and separated on the main column using a 120 min LC gradient ranging from 3-35 % of 84 % ACN, 0.1 % FA (v/v) at a flow rate of 230 nL/min. MS survey scans were acquired in the Orbitrap from 300 to 1500 m/z at a resolution of 120000 using the polysiloxane ion at m/z 445.12003 as lock mass, an automatic gain control target value of 2.0×10^5 and maximum injection times of 50 ms. Top speed most intense signals were selected for fragmentation by HCD with a collision energy of 30 % and MS/MS spectra were acquired in the Iontrap at a resolution of 1200000 and taking into account a dynamic exclusion of 15s. The ACG target for MS² was set at 2.0×10^3 ions, a maximum injection time of 300 ms.

2.2.7.4.6 IQGAP1 overexpressing myoblasts

In total, six samples – three controls (transfected with the *Adv.Gfp*) and three overexpressing *Adv. IQGAP1* – were prepared as described in sections: 2.2.6.1 and 2.2.6.2.1. Samples were analysed using an Ultimate 3000 nano RSLC system coupled to an Orbitrap Fusion Lumos mass spectrometer (both Thermo Scientific). Briefly, peptides were pre-concentrated on a trapping column and separated on the main column using a 90 min LC gradient ranging from 3-35 % of 84 % ACN, 0.1 % FA (v/v) at a flow rate of 230 nL/min. MS survey scans were acquired in the Orbitrap from 300 to 1500 *m/z* at a resolution of 120000 using the polysiloxane ion at *m/z* 445.12003 as lock mass, an automatic gain control target value of 2.0×10^5 and maximum injection times of 50 ms. Top speed most intense signals were selected for fragmentation by HCD with a collision energy of 30 % and MS/MS spectra were acquired in the iontrap at a resolution of 1200000 and taking into account a dynamic exclusion of 15 s. The ACG target for MS² was set at 2.0×10^3 ions, a maximum injection time of 300 ms.

2.2.7.4.7 *Sh3tc2*^{ΔEx1/ΔEx1} mouse muscles

In total, 12 gastrocnemius muscles – three derived from 2 years and three derived from 3 months old *Sh3tc2*-deficient animals and six respective wild-type littermates (corresponding to three months and 2 years old animals) – were surgically removed, snap-frozen in liquid nitrogen at -80°C and processed independently. 1 μg of peptides out of each condition were analysed using an Orbitrap Elite, Orbitrap Lumos or Orbitrap Lumos Fusion mass spectrometer all coupled with an Ultimate 3000 nano RSLC system. In all measurements, samples were analysed in a randomized order to minimize systematic errors. Peptides were pre-concentrated on a trapping column for 10 min using 0.1 % TFA (v/v) at a flow rate of 20 μL/min followed by separation on a 75 μm x 50 cm C18 main column (both Pepmap, Thermo Scientific) with: 1) a 230 min (OrbiElite)/ 150min (Lumos Fusion) gradient ranging from 3-42 % or 3-30% of 84 % ACN, 0.1 % FA (v/v) at a flow rate of 230 nL/min. For samples measured on OrbiElite MS, survey scans were acquired in the Orbitrap from *m/z* 300 to 1500 at a resolution of 60,000 using the polysiloxane ion at *m/z* 371.101236 as lock mass¹⁴⁶. The ten most intense signals were subjected to collision induced dissociation (CID) in the ion trap, taking into account a dynamic exclusion of 30 s. The spectra were acquired with a normalized collision energy of 35 %. AGC target values were set to 10^6 for MS¹ and 10^4 for ion trap MS² scans, and maximum injection times of 100 ms for both full MS and MS² scans. For the samples measured on the Orbitrap Fusion, full MS scans were acquired in the Orbitrap from 300 to 1500 *m/z* at a resolution of 120000 and the

m/z ion signal of $\text{Si}(\text{CH}_3)_2\text{O}_6\text{H}$ 445.12003 m/z was used as lock mass. Top speed most intense signals (with an isolation window of 3 s) were further fragmented using CID, taking into consideration a dynamic exclusion of 60 s. A normalized collision energy of 35 % was used and AGC target values were set to 4.0×10^5 for MS^1 and 10^4 for MS^2 scans with maximum injection times of 50ms for full MS and 40 ms for the MS^2 scans. The data from the Lumos Fusion was acquired with similar parameters as described for the Fusion data with some modifications: top speed most intense signals were fragmented using HCD with an NCE of 30%, ACG target values of 2.0×10^3 ions, a maximum injection time of 300 ms.

2.2.7.5 Data analysis and statistical evaluation

2.2.7.5.1 Muscle protein catalogue and TAP assay products

The database search for these two data sets was performed using Proteome Discoverer (PD) from Thermo Scientific. The raw MS data is directly imported into PD and analysed using a user-defined workflow. The muscle protein catalogue raw files were analysed in PD 2.2.0388 (Thermo Scientific). Database searches were conducted in a target/decoy manner against a concatenated protein sequence database (*Homo sapiens*, 20,226 target sequences, downloaded from UniProt in October 2017 and a common contaminant database comprising 247 target sequences). For myotube and myoblast samples, three search algorithms (Sequest HT, MS Amanda, Mascot 2.6.1 (Matrix Science)) were used and the precursor and fragment mass tolerances were set to 10 ppm and 0.02 Da, respectively. In the case of the data belonging to the muscle tissue fractions, search algorithms were used (Sequest HT, Mascot 2.6.1) and the fragment mass tolerance was adjusted to 0.5 Da. For this dataset, MS Amanda was not employed as the acquired data is low resolution. Thus, this search engine would not improve the number of identified proteins and would increase the duration of the search considerably. For all searches, enzyme specificity was set to fully tryptic with a maximum number of 2 missed cleavages allowed. Carbamidomethylation of Cys (+57.02146 Da) was defined as fixed, while oxidation of Met (+15.99491 Da) and acetylation of protein N-termini (+42.01056 Da) were allowed as variable modifications. False discovery rate (FDR) estimation was performed by the percolator node and all data were filtered to meet a 1% FDR-level for PSMs as well as peptides. To obtain the most comprehensive proteome catalogue, all searches (myoblasts, myotube and muscle tissue) were combined with the multi consensus feature of Proteome Discoverer and the resulting dataset was further filtered for 1% FDR on the protein level, additionally excluding proteins without uniquely assigned peptides and ones not marked as ‘master’ proteins. The

abundances of the identified proteins was given by the calculation of the NASF for each protein using the following formula:

$$(\text{NASF})_k = \frac{\left(\frac{\text{SpC}}{L}\right)_k}{\sum_{i=1}^N \text{SpC}/L)_i}$$

where NASF-normalized abundance factor, k-protein, SpC-total number of MS/MS spectra identifying a protein, L-length of the protein, N-number of proteins in an experiment.

The raw files resulted from the TAP assay experiment were analysed using PD 1.4 (Thermo Scientific). Databases searches were conducted as well in a target/decoy manner against the sequence database. Two algorithms were used for searching the data (Sequest and Mascot 1.4) and the precursor mass tolerance and fragment mass tolerance were set to 10 ppm and 0.02 Da, respectively. Parameters like enzyme specificity, dynamic and fixed (except the acetylation of N-termini) were fixed as described above. False discovery rate (FDR) estimation was performed by the percolator node and all data were filtered to meet a 1% FDR-level for PSMs as well as peptides, search engine rank 1 and a minimum of 2 unique peptides.

2.2.7.5.2 Comparative proteome profiling

For the INPP5K fibroblasts, CAV3 muscles, GFPT1 muscles CMT4C muscles and for the IQGAP1 overexpressing myoblasts label free was performed. This comparative proteome profiling allowed insights to be gained into the major differences between healthy and diseased tissue or cells. The quantitative analysis of the acquired MS data was performed using the Progenesis software from Nonlinear Dynamics. The raw data was imported into the software which automatically selects one of the LC-MS files and automatically aligns all the runs according to this reference file. After peak picking, only features which were within the set retention times, m/z widows and with a charge state of +2, +3, and +4 were considered for peptides statistics, analysis of variance (p-ANNOVA). In order to maximize the number of identified proteins, spectra were exported and lists were searched against the mouse or human database using at least three search algorithms Mascot, X!Tandem Jackhammer and MS-GF with the help of SearchGui^{129,130,133,134}. For each dataset, the software versions, search engines and databases used are illustrated in Table 13. Carbamidomethylation of Cys was set as fixed and oxidation of Met was selected as variable modification. MS and MS/MS tolerances were set to 10 ppm and 0.5 Da, respectively. To interpret and fuse the data from multiple search engines and also to validate the data, FDR (1%) on the PSM and protein level Peptide Shaker¹³¹ was

used. The features of this software also allowed the direct re-import of the quality-controlled data back into Progenesis. Peptide searches containing oxidized Met were excluded from further analysis. Only proteins with unique peptides were exported and considered for further analysis. Also, for each protein identified, using the normalized abundance (given by Progenesis), the ratio was calculated.

Table 11. Used algorithms, software for the database searches for the label free experiments

Experiment name	Search algorithms	Software	Protein database	Nr. of entries
INPP5K fibroblasts	Mascot 2.4, MSGF+ v10282 (19.12.2014), X!Tandem (15.12.2015)	Search Gui 3.2.2.0	<i>Homo sapiens</i> , 22.07.2015	20273
CAV3 mouse muscles	Mascot 2.4, MSGF+ Beta v10024 (05.09.2014), X!Tandem Sledgehammer(01.09.2013)	Search Gui 1.21.0	<i>Mus musculus</i> , 11.12.2013	16649
IQGAP1 overexpressing myoblasts	Mascot 2.6, MSGF+ Beta v10282 (19.12.2014), X!Tandem Vengeance(15.12.2015)	Search Gui 3.3.3	<i>Homo sapiens</i> , 20.11.2017	20226
GFPT1 mouse muscles	Mascot 2.4, MSGF+ Beta v10282 (19.12.2014), X!Tandem Vengeance(15.12.2015)	Search Gui 2.8.6	<i>Mus musculus</i> , 22.07.2015	18669
SH3TC2 mouse model (2 years)	Mascot 2.4, MSGF+ Beta v10024 (05.09.2014), X!Tandem Sledgehammer(01.09.2013)	Search Gui 1.21.0/1.25.6	<i>Mus musculus</i> , 11.12.2013	16649
SH3TC2 mouse model (3 months)	Mascot 2.4, MSGF+ Beta v10282 (19.12.2014), X!Tandem Vengeance(15.12.2015)	Search Gui 3.2.18	<i>Mus musculus</i> , 22.07.2015	18669

2.2.7.6 Data plotting and pathway analysis

All data was plotted using Origin 6.0 and Adobe Illustrator. For pathway analysis, the GO ontology, KEGG and Reactome were used^{147,148} and data were finally manually filtered for relevant pathways. For network analysis, STRING 9.1 and Cytoscape 3.2.0 including the plugin ClueGo and GO-term analysis¹³⁶ were used. In STRING, the confidence score with a cutoff at 0.5 was set while in Cytoscape the network significance was set between global and medium by showing only significant pathways with a p-value of 0.05. Proteomaps were created based on a defined hierarchy tree from certain datasets using the online tool available (<https://www.proteomaps.net/>). The annotation of these proteomaps are based on the KEGG database platform and each protein is shown by a polygon and functionally relevant proteins

are arranged as neighbours. Additionally, polygon areas represent protein abundances weighted by protein size.

2.2.8 Molecular biology methods

2.2.8.1 Protein separation and western blotting

For protein separation, polyacrylamide gel electrophoresis (SDS PAGE) was employed. The lysed samples, as described in section 2.2.3, were mixed with 2x laemmli buffer (900 μ L of the commercial laemmli buffer + 100 μ L of beta-mercaptoethanol) and boiled at 90°C for 5 minutes in order to facilitate protein denaturation. Samples were then resolved either using precast commercial gels (with an acrylamide concentration ranging from 4-12%) or self-made gels (usually 10 or 12% acrylamide) with Tris-Glycine running buffer (25 mM TRIS-HCl, 192 mM glycine and 0.1% SDS), at 120 V for up to 60 minutes in a mini gel tank. As a size marker, a pre-stained protein standard from Invitrogen was used.

For subsequent antibody probing, the separated proteins were first transferred onto a methanol activated Hybond-PVDF membrane using a transferring solution made up of 5 mM Tris-HCl, 192 mM glycine and 30% methanol. Next, the membrane was incubated either in 5% non-fat milk or 3%BSA, prepared in TBST (10 mM TRIS-HCl pH 7.4, 150 mM NaCl, 2.7 mM KCl and 0.1%Tween 20) at room temperature for a minimum of 2 hours. Primary antibodies were diluted in 3%BSA in TBST at the desired concentration (Table 12). The blocked membrane was then incubated with the primary antibody overnight at 4°C. To remove the excess of primary antibody after incubation, the membrane was washed thrice with TBST with gentle agitation at room temperature. The membrane was incubated afterwards with the desired secondary antibody for at least 2 hours at room temperature under gentle agitation. To remove excessive secondary antibody and to avoid background staining, the membrane was washed at least 3 times in TBST at room temperature. Based on the secondary antibody, the membrane was either blotted using a chemiluminescence substrate (ECL) and exposed to X-Ray film, or the protein bands were visualized by densitometry scanning using the Odyssey Infrared Imaging System (LiCOR).

2.2.8.2 Co-immunoprecipitation

For the co-immunoprecipitation (co-IP), at least 3×10^6 HeLa cells were grown in 10cm tissue dishes and co-transfected with the respective constructs as described in section 2.2.1.3. At 48 hours post transfection, cells were collected and lysed in TAP lysis buffer as described in

section 2.2.5.1. The cell lysate was first incubated with the antibody that would act as a bait under continuous agitation at 4°C overnight. Meanwhile protein A/G magnetic beads were prepared by washing 3 times in 1 mL of TAP lysis buffer. Afterwards, beads were re-suspended in TAP lysis buffer and an appropriate amount (usually around 20 µL of pure beads) was added to the lysate and incubated for a minimum of 3 hours at room temperature or overnight at 4°C rotating at 15 rpm. To recover the bound protein, the beads were separated from the supernatant using a magnetic rack. The supernatant was discarded, and the beads washed gently three times with 1 mL of TAP lysis buffer. To release the protein from the beads 100 µL of Lämmli buffer was added to the beads and incubated for another 15 minutes at room temperature. Finally, the mixture was boiled at 90°C for 5 minutes and the beads were discarded. The resulting solution, including the precipitated proteins, was then subjected to the usual SDS PAGE and subsequent western blotting.

2.2.8.3 Immunofluorescence

For immunofluorescence (IF) cells were grown on coverslips as described in section 2.2.1.2 and then fixed with 4% formaldehyde for 15 minutes at room temperature. Excessive formaldehyde was removed, and samples washed thrice with PBS before permeabilising with 0.5% Triton-x in PBS for 10 minutes at room temperature and then blocked with 1% BSA for one hour at room temperature. Next, cells were washed thrice with 1 mL of PBS and then incubated at 4°C overnight with the desired primary antibody. Excessive primary antibody was removed by washing 3 times with 1 mL of PBS. Fluorescence-labelled antibodies or phalloidin or bungarotoxin diluted in BSA were added to the samples and incubated at room temperature for at least one hour. Finally, samples were washed three times with PBS and once very briefly with water and mounted onto microscope slides.

Freshly dissected tissue was carefully frozen in isopentane cooled with liquid nitrogen and then sectioned in thin slices of 10 µm using the cryostat. Sections were left outside to dry and then either stored at -20°C or stained immediately. A hydrophobic pen was used to draw around the sections to stop solutions from dispersing around the slide. The sections were then washed thrice in PBS and afterwards blocked for 30 minutes in 1% normal goat serum. In the following step, the samples were incubated with the respective antibodies in a humidified chamber at 4°C overnight. The next day, slides were washed thrice with PBS and the secondary antibody was applied for 1 hour. The secondary antibody was washed off with PBS and samples were mounted. For formalin fixed paraffin embedded tissue (FFPE), the sections were first de-waxed in xylene for 10 minutes and re-hydrated by washing in

decreasing concentration of ethanol. Antigen retrieval was performed by boiling the sections in pre-heated Tris-HCl pH 8, 1 mM EDTA buffer in a pressure cooker for 30 minutes. Samples were then left to cool at room temperature and then rinsed in water and PBS. The staining and blocking procedure was then performed exactly as described for the frozen tissue.

2.2.8.4 Zebrafish handling and generation of zebrafish models

2.2.8.4.1 Zebrafish husbandry and observation

All zebrafish experiments presented in this thesis were performed at the Institute of Genetic Medicine, University of Newcastle, UK. All animals used for these experiments were processed according to the UK Home Office regulation (Guidance on the Operation of animals, Scientific Procedures Act 1986). The zebrafish strains used in this thesis were the Golden (slc24a5b1/+) *Danio reiro* strain obtained from ZIRC, OR, USA and transgenic (islet-1: GFP) *Danio reiro* strains¹⁴⁹. Zebrafish and larvae were raised and staged according to standard procedures described by Kimmel¹⁵⁰. All specimens were sacrificed by the administration of an anesthetic overdose (Tricaine).

2.2.8.4.2 Morpholino knockdown in zebrafish embryos

For the knockdown of certain proteins, anti-sense morpholino oligonucleotides (MO) were designed based on the zebrafish targeted protein, or their sequence was used as previously published^{55,99,151} and purchased from Gene Tool (Pilomath, OR). All the morpholinos employed as well as the injected amount are summarized in table 14. The Gene Tool standard control Mo targeting a human β -haemoglobin gene was used as a negative control. The knockdown was performed always on one-cell stage embryo of the AB strain of zebrafish.

Zygotes were injected following the standard procedures. Briefly, the microinjection of early stage (one to two-cell stage embryo) was carried out manually, without a micromanipulator due to the easy access into the embryos (no hard shell or envelopes). The injection of the MO was carried out through the chorion into the cytoplasm or into the unsegregated ooplasm. The embryos were lined out on a petri dish and immobilized by the removal of the medium and then injected using a nitrogen gas injector. The MO solutions were prepared as follows: the MO is delivered as a powder and is diluted with Danieau buffer (58 mM NaCl, 0.7 mM KCl, 0.4 mM MgSO₄, 0.6 mM Ca(NO₃)₂, 5 mM HEPES, pH 7.6) to 5 mM, followed by the dilution of the stock solution to 1 mM with injection buffer and 0.05% phenol red. Prior to use, the 1 mM MO stock solution was heated to 65°C for 5 minutes in order to resuspend any precipitated MO.

Table 12. Employed morpholinos

MO	Target	Effect	Sequence	Concentration (ng)
<i>phgdh</i>	exon 2	translation blocking	5'- GCCATTATTATCGTGGACTTGCGGA -3'	20
<i>sill</i>	exon 2	splice blocking	5'- GGTGACTGTGTAAACAGAACAAAT C-3'	6, 8
<i>inpp5ka*</i>	intron 4	splice blocking	5'- CAGACTGAAGAGGAGCAGCATTCA A-3'	5
<i>inpp5kb*</i>	intron 4	splice blocking	5'- TAGACTGGGACACATTTGCTCAGGT -3'	2.5
<i>cav3</i>	exon1	translation blocking	5'- GTTAGTGTTGTACTIONGGTCCGCCATA -3'	3
<i>iqgap1</i>	exon 2	splice blocking	5'- GATCTGGACTCTTACCGTTTAGCCT- 3'	15
<i>musk</i>	exon 2	translation blocking	5'- GTAGAGGATTACCGTATTGCCGTT- 3'	5
<i>control</i>			5'- CCTCTTACCTCAGTTACAATTTATA- 3'	20, 6, 8, 5, 2.5, 3, 15

2.2.8.4.3 Dechoriation of embryos at 48 hours post fertilization

The dechoriation of embryos was performed by pronase digestion (1 g powder dissolved in 100 mL of Danieau buffer). 1 mL (10 mg/mL) of pronase was added to each petri dish containing zebrafish and placed back into the incubator for another 10 minutes and then vigorously shaken until most fish left the chorion.

2.2.8.4.4 Phenotype and motility observation

To determine the effect on mobility and movement upon the knockdown of certain proteins in zebrafish, tail twists in chorion at 24 hpf were measured. The embryo was observed for 60 seconds while counting the total number of complete twists. A total of 10 embryos per condition were observed. For 48 hpf fish, the touch-evoked swimming response was followed by gently touching the head or tail of the fish with a pipette tip. Unusually, normal zebrafish will swim

away from the stimulus while the abnormal fish would present circling movements, twitching, or no movement at all. At least 10 embryos for each category were recorded.

2.2.8.4.5 Rescue experiments

The phenotypic rescue of the Islet-1 zebrafish embryos was performed by supplementing the E3 embryo medium (5 mM NaCl, 0.17 mM KCl, 0.33 mM CaCl₂ and 0.33 mM MgSO₄) with L-Serine to a final concentration of 100 µM. At 24 hpf, the movements inside the chorion were examined and at 48 hpf the central nervous system was imaged.

2.2.8.4.6 RT-PCR and qRT-PCR experiments

2.2.8.4.6.1 RNA extraction

RNA was prepared using the TRIzol Reagent. This method can be used to simultaneously extract DNA and protein besides RNA from the same sample. The extraction of RNA was carried out according to the manufacturer's protocol for tissue. Briefly, the fish samples were homogenized in 1 mL of TRIzol with a pestle and then incubated at room temperature for 5 minutes in order to allow complete dissociation of the nucleoprotein complexes. Next, 200 µL of chloroform was added to the homogenate and the tube vigorously shaken and left to incubate at room temperature for 3 minutes, followed by centrifugation at 12000 g for 15 minutes at 4°C. After centrifugation, the aqueous phase within the upper layer contains the RNA. The RNA was precipitated from the aqueous phase by using 500 µL of isopropanol after which the solution was centrifuged at 12000 g for 10 minutes at 4°C. The supernatant was removed and the pellet which contains the RNA was washed with 1 mL of 75% ethanol. The suspension was centrifuged again at 7500 g for 5 minutes at 4°C and the pellet dried and re-suspended in 20 µL in RNAase free water. The quality of the RNA was examined using an agarose gel and the concentration determined using a NanoDrop spectrophotometer.

2.2.8.4.6.2 cDNA synthesis

Given that RNA is usually quite unstable and has a short shelf life even at -80°C, immediately after purification the RNA was transcribed into cDNA by using a reverse transcriptase. For this procedure, the cDNA transcription kit from Applied Biosystems was used. A master mix containing 2 µL of 10xRTbuffer, 0.8 µL 25x dNTP (100Mm), 2 µL 10x random primers, 4.5 µL of water and 1 µL of the RT enzyme. In a PCR tube, the master mix was added to the RNA template and the resulting mixture was incubated at 25°C for 10 minutes, 37°C for 120 minutes and finally 5 minutes at 85°C in a BioRad Thermocycler.

2.2.8.4.7 RT-PCR

The efficient gene knockdown in zebrafish was confirmed by RT-PCR. The nucleic acid sequences of interest were amplified by using the cDNA obtained as described above as a template. The standard mixture for the PCR reaction was composed out of 5 μ L 10x Buffer, 4 μ L enhancer, 1 μ L forward primer (from a stock solution of 50 mM), 1 μ L reverse primer (from a stock solution of 50 mM), 2 μ L dNTP mix (from a 10 mM stock solution), 0.5 μ L Taq polymerase. All reagents used were included in the MolTaq kit from Molzyme. Reactions were carried out in PCR tubes where 2 μ L of cDNA together with 50 μ L of the standard mix were added. The annealing temperature was specific to each pair of primers, which are listed in table 15. In general, the reactions were performed by using the following cycling parameters: 1) initialization step: 2 minutes 95°C; 2) denaturation step: 15 seconds 95°C; 3) annealing step: specific temperature for primers; 4) elongation step: 2 minutes 72°C; repeat of steps 2-4 for 40 cycles, 5) final extension step: 5 minutes 72°C.

Table 13. PCR primers used

Gene	Forward	Reverse
<i>phgdh</i>	5'-GCTGAACTCACCTGTGCTCT-3'	5'-ATGACCCGATCACTCCTCCA-3'
<i>sill</i>	5'-ACCCACAGACAAGTGGCAA-3'	5'-AGCTCATCCATTGGCCGAAA-3'
<i>inpp5ka</i> *	5'-GATGAGGCCAATGAGGAAGTG-3'	5'-TCTCTGTCCCAAAGCAGGTT-3'
<i>inpp5kb</i> *	5'-GAAGGCAAACGACAAGGCTTT-3'	5'-CTCCTGTTGTTTTTCTGGCTCT-3'
<i>cav3</i>	5'-CCCCAAGCAAATCAACGAAG-3'	5'-AAGGTGTGGATGCAGAGAG-3'
<i>iqgap1</i>	5'-GAACAGAATGCACCCGGAGA-3'	5'-AGCAGGTCATCCTGGTAGGT-3'
<i>musk</i>	5'-TGACCAGATGCTCAAATCTGGT-3'	5'-ATTAAGCTAGCGGTGAGGTCGCCCTA-3'
<i>efla</i>	5'-CTGGAGGCCAGCTCAAACATGG-3'	5'-CTTGCTGTGTCCAGCCACATTAC-3'

The results of the PCR were visualized using gel electrophoresis and a 1% agarose gel. Briefly, 1 g of agarose was mixed with 100 ml of 1x TAE buffer and with 1 μ L ethidium bromide. The mixture was heated in a microwave and casted into the specific shape. To each well, 5 μ L of the PCR mixed with 0.5 μ L of the loading dye was added and the gel was ran for 30 minutes at 70 V in 1x TAE buffer. The bands were visualized on the UV gel documentation system.

2.2.8.4.7.1 qRT-PCR

To determine the amplification of the targeted DNA during the PCR in real time, the SYBR green reagent was used according to the manufacture's protocol. SYBR green is a fluorescence dye that binds to all double bonded DNA formed, allowing the variance in fluorescence to be recorded. The primers chosen are represented in table 15 (Cav3, Iqgap1, MusK and Efl α) and are at a concentration of 50 μ M (stock solution). All reactions were set up in a UV-sterilised hood. The master mix consisted of 5 μ L of the SYBR Green qPCR Super Mix, 0.5 μ L of the reverse and forward primer and 2 μ L water. This mixture was then vortexed and dispensed into the designated wells on a 384-well plate. Next, 2 μ L of the cDNA was added to the master mix in each well except to the no-template control. All samples were run in triplicate and data was recorded using a QuantStudio 7 thermal cycler from Invitrogen. Cycling conditions consisted of: 10 minutes hold at 95°C followed by 40 cycles of 95°C 15 seconds, 60°C 1 minute followed by a 0.05°C/second gradual increase of the temperature up to 95°C. The results of the run were exported using Microsoft Excel. The data were analysed using the $\Delta\Delta C_q$ method and the relative expression ratio was determined using the formula:

$$RER = \frac{2^{-\Delta C_t \text{ target}(KD-ctrl)}}{2^{-\Delta C_t \text{ ref}(KD-ctrl)}}$$

where ΔC_t is the difference in crossing points, ref is the value corresponding to the reference gene and KD refers to the MO injected fish.

2.2.8.4.8 Immunofluorescence staining of whole mount zebrafish

Whole mount immunofluorescence of zebrafish was performed as previously described^{99,152}. Briefly, after dechoriation and euthanasia, zebrafish were fixed in 4% paraformaldehyde/PBS overnight at 4°C followed by washing in PBS. Next, the fish were permeabilized by incubating them with ice cold acetone at -20°C for 7 minutes. After removing the acetone, samples were washed with 10 ml of PBS/Tween-20, embryos were blocked for 1 hour at room temperature in 5% horse serum prepared in PBS and then incubate with the corresponding primary antibody overnight at 4°C under gentle agitation. The following day, the embryos were washed thrice with 2 ml of PBS and then incubated in the secondary antibody for at least 2 hours at room temperature. Finally, the fish were washed 5 times in 5 ml of PBS and then mounted correspondingly onto the microscope slide.

2.2.8.5 Microscopy and image analysis

RCMH and HeLa Cells were visualized using a Nikon A1R laser scanning confocal microscope with oil-immersion 60x objectives, while for the myoblasts the measurements were performed with a Leica TCS 8 with an APE picoEmerald as a laser source and a water-immersion 60x objective. All confocal settings were optimized to obtain the best compromise between image quality and acquisition rate. All tissue images were recorded on an Axio Imager Z1 microscope from Zeiss using either a 5x or 10x magnification. All image analyses was performed on maximum intensity projections of the z-stacks by using the ImageJ software (Binary Connectivity Plugin). To quantify the florescence intensity of the INPP5K and control human derived muscle, Fiji ImageJ was utilized. Average fluorescence and area of each fiber was measured together with regions without muscle fibres in to establish a mean background florescence. Next, the total corrected fluorescence was calculated by extracting the background florescence from the total intensity of each individual fibre.

The morphology of the postsynaptic NMJ was analysed using the NMJ-morph platform¹⁵³ with tools implemented in ImageJ. Briefly, images were opened using maximum intensity projection and after the threshold was set (“Huang method”), thus obtaining an accurate binary image. Self-explanatory parameters such as perimeter or area were measured using standard ImageJ functions. The compactness of the AChR at the endplate was defined as:

$$\text{compactness} = \left(\frac{\text{AChR area}}{\text{endplate area}} \right) * 100$$

The number of clusters was determined by utilizing the segment particles function in ImageJ to properly resolve the endplate into easy countable clusters. Finally, the fragmentation index was calculated using the formula:

$$\text{fragmentation} = 1 - \left(\frac{1}{\text{nr. of AChR clusters}} \right)$$

where a solid plaque-like endplate has an index of 0 and a highly fragmented one an index close to 1.

All the immunofluorescence images of zebrafish were recorded on a Nikon A1R confocal microscope and the Z-stack images were obtained by scanning one half of the myotome of the trunk. All Islet-1 zebrafish were imaged live using with an Axio Imager Z1 microscope from Zeiss using a 10x magnification. At 24hpf and at 48 hpf the tail movements within the chorion

and the touch evoke response of zebrafish embryos were recorded using a Canon Legria Hf R76 camera coupled to a Leica stereomicroscope.

2.2.8.6 Statistical analysis and data representation

To assess the statistical significance of the presented data, the two-sample t-test was performed using graph pad where a $t \leq 0.01$ was considered as very statistically significant and $t \leq 0.05$ as statistically significant. All data was plotted using Origin 6.0 and Adobe Illustrator.

3. Subprojects and obtained results

3.1 Muscle protein catalogue

3.1.1 Known proteomes described from mouse skeletal muscle

To gain a deeper understanding into different physiological and pathological processes that affect a tissue during disease, it is necessary to have a comprehensive view of its protein composition. Muscle proteomics is a particularly challenging field, mainly due to the high dynamic range of the tissue but also due to its proteome composition, as 50% is composed of just 10 proteins. Peptides derived from these proteins are in such abundance that they mask the other neighbouring proteins, which will not be picked up for fragmentation, thereby reducing the overall number of identifications. So far, several protein catalogues attempting to achieve a very deep proteome coverage in different cell lines have been published including RCMH, (a human skeletal muscle cell line)¹⁵⁴, C2C12 (mouse skeletal muscle cell line) and muscle tissue derived from mouse²⁶. Attempts have also been made to describe the proteome composition of distinct fiber types^{155,156}.

The most comprehensive muscle proteome was described for mouse skeletal muscle by Mann and colleagues²⁶. This catalogue comprises 10281 proteins and projects the identification of peptide and proteins done in the C2C12 myotubes, an immortalized cell line, onto mouse muscle. However, when their analysis focused on muscle samples alone, the number of proteins identified was 5887, while in the C2C12 myotubes 9642 proteins were identified. Interestingly, their analysis revealed that 18% of the total muscle proteome is composed of myosin (including all the isoforms), while titin accounts for 16%. When comparing C2C12 myotubes with muscle tissue, 4310 proteins were found to be differentially regulated, pinpointing the major functional differences. Proteins involved in glucose metabolism, mitochondria, contraction, and calcium signalling were enriched in the muscle, while in the C2C12 myotubes proteins associated with DNA replication, protein processing and control were enriched²⁶. Although this protein catalogue is very comprehensive, identifying even low abundant circadian clock proteins, it does not completely reflect the proteome composition of human muscle due to the structural and biochemical differences (different fiber typing, gait kinematics and sarcomere length) between the two species of muscle¹⁵⁷. Despite C2C12 being a widely used cell line to study muscle

disorders, due to their immortality and transformations, they are prone to genetic instability and thus losing tissue specific function of their mortal parental population¹⁵⁸.

3.1.2 Identification of 10298 proteins via combined fractionation techniques and LC-MS/MS analysis

Due to recent advances in MS-based proteomics, multiple complex cell proteomes have been extensively described^{159,160}. Despite this, analysis of tissue proteomes and particularly of skeletal muscle remains challenging due to their molecular complexity. This intricacy arises from proteins involved in contraction and muscle fibre structure as well as from a large number of complex internal membranes structures such as triad junctions, transverse tubules, and cisternae furthermore complicating the proteomic analysis and more precisely the definition of the protein catalogue of skeletal muscle¹⁶¹.

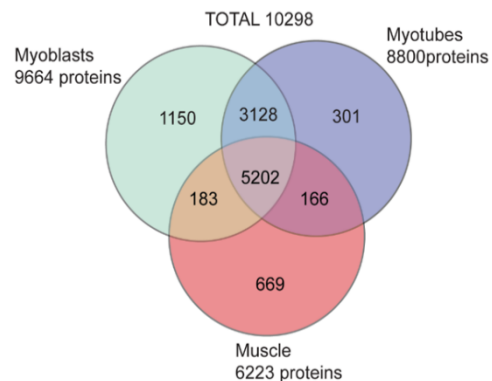


Figure 5. Venn diagram showing the number of proteins identified in myoblasts, myotubes and muscle

To overcome the limitation in muscle proteomics caused by the high dynamic range of the tissue, human primary myoblasts, myotubes and complex tissue were fractionated using two techniques: (1)

high pH fractionation at peptide level and (2) organelle fractionation. Afterwards, fractions were analysed via liquid chromatography coupled to tandem mass spectrometry. To generate a comprehensive protein catalogue, results from all investigated fractions were searched against the database (UniProt) and then combined using the multi consensus feature. Following this, proteomic signatures obtained from myoblasts, myotubes and muscle tissue were combined at the data analysis level, allowing the increase in numbers of identified proteins by about 40%, compared with the number obtained from muscle tissue alone. This approach resulted in the identification of 10298 different proteins (Figure 5) with a FDR $\leq 1\%$ at protein level. A total of 9664 proteins were identified in myoblasts, 8800 in myotubes, while in muscle tissue 6223 proteins were identified (Figure 5). This lower identification rate in the tissue compared to the *in vitro* systems is most likely caused by the large dynamic range of skeletal muscle, as structural proteins are in great abundance. Notably, 5202 of proteins were found to be common for myoblasts, myotubes and muscle.

NASF values were determined for all proteins. These values correlate with the relative expression of a protein within the respected cell line or tissue. To depict the protein composition of the entire catalogue, a proteomap was created (Figure 6). This facilitates quantitative mapping of proteomes to a pathway. Maps were automatically generated based on the proteomic data (accession and NASF number) and the pathway was then assessed based on the KEGG database¹⁶². The content of the proteome is presented hierarchically by grouping proteins into pathways and then into their higher categories. Proteins are displayed in circles or polygons and the ones belonging to the same category share similar colours and subcellular localizations. For the generation of this map, a unique annotation was chosen for each protein. This *in silico*-based visualization of the proteomic findings shows the “big picture” of the human muscle proteome (Figure 6), wherein proteins belonging to muscle fibre structure, to the contractile apparatus and to metabolic processes (especially those involved in glycolysis and TCA) seem to dominate the human skeletal muscle proteome. Furthermore, proteins involved in energy metabolic processes, such as those involved in oxidative phosphorylation, are also highly abundant in the muscle protein catalogue (Figure 6). This molecular observation accords with the knowledge that skeletal muscle is a tissue with a very high ATP-demand and the largest site for glucose disposal¹⁶². Given that the excitation-contraction coupling, and thus sarcomere-based muscle fibre contraction represents a process highly controlled by Ca^{2+} , the predominance of pathways controlled by Ca^{2+} signalling in the complex muscle tissue is expected. Another dominating pathway is the mitogen-activated protein kinase MAPK signalling cascade. The MAPK signalling pathway activation originates at the cell membrane/sarcolemma, where small GTPases and various protein kinases phosphorylate and activate MAPKKKs towards fibre specialization, muscle mass maintenance and fibre regeneration¹⁶³.

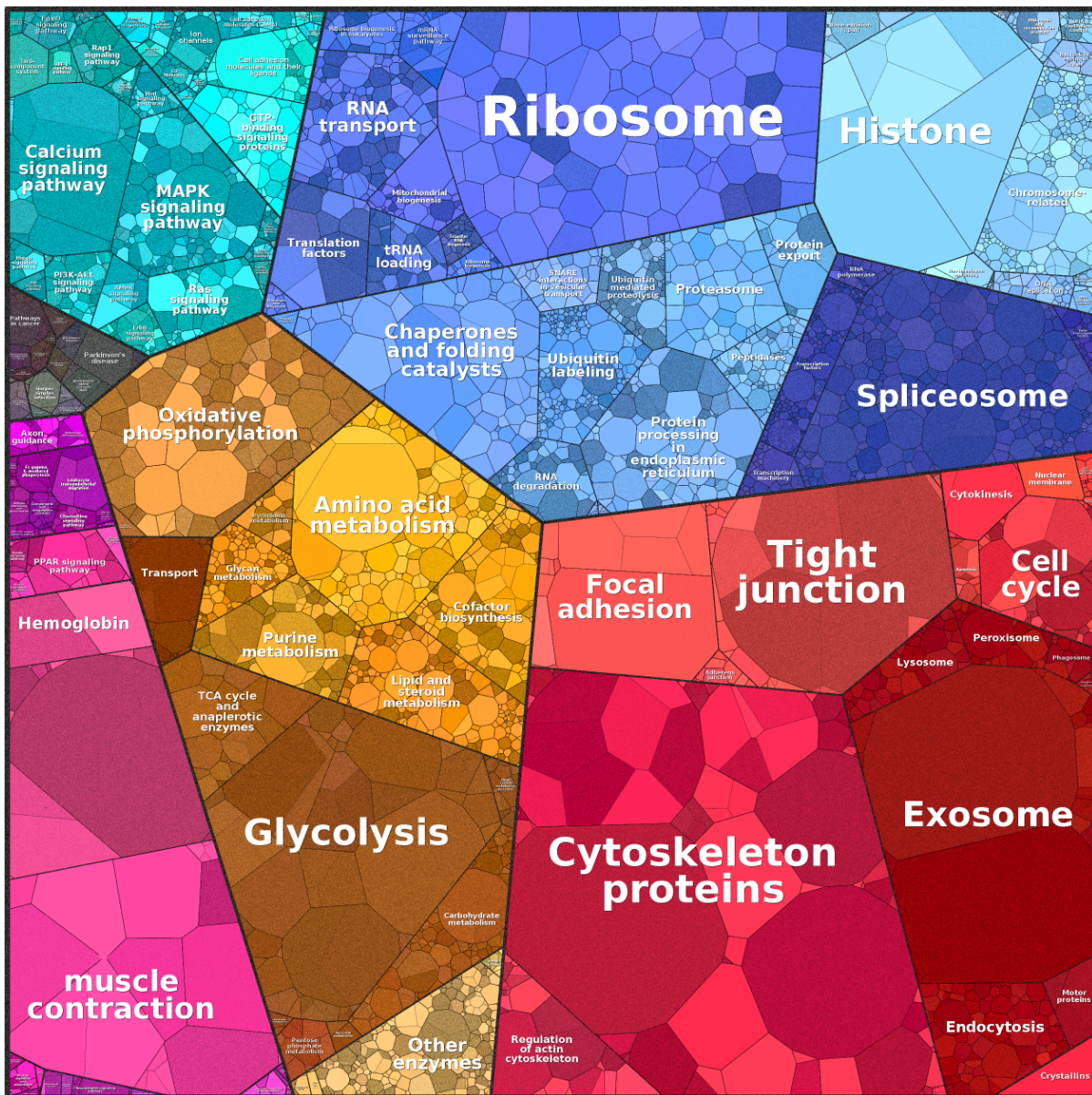


Figure 6. Proteomap of human muscle resulting from the combination of human primary myoblasts, myotubes and skeletal muscle tissue. Every polygon or circle represents a protein, the size of which is given by the NASF number multiplied by protein chain lengths. The proteins are then grouped in functional categories based on the KEGG database. The proteomap shows five main hierarchy levels, which are further divided into sub-pathways. Colour code: brown-metabolism, pink-muscle homeostasis and contraction, dark blue-cellular processes, light blue-signalling and red-ECM, cytoskeleton.

Additionally, a proteomap of the most 500 abundant proteins was generated (Figure 7). This map showed that the muscle proteome is predominated by structural proteins (~ 30% of the top 500) such as components of the sarcomere, the contractile unit of the muscle⁵, and by further proteins involved in cytoskeleton like intermediate filaments which are aiding the excitation-contraction coupling. This group of proteins is followed by metabolic proteins belonging to the

glycolysis or to the amino acid metabolism with a very high abundance of CKM, a known marker for muscle fiber damage¹⁶³ (Figure 7). Interestingly, 19% of the top 500 proteins are ribosomal proteins (Figure 7). In general, skeletal muscle is very sensitive to nutritional status as protein synthesis following nutritional ingestion is necessary for muscle growth and maintenance. Muscle protein synthesis is mainly determined by the cellular content of ribosomes, thus it is expected that 19% of the top 500 most abundant proteins belong to this category (Figure 7). Furthermore, ribosomal proteins also modulate the immune responses and (muscle) cell development and are very likely to contribute to muscle fibre repair¹⁶⁴. In the context of protein synthesis, approximately 15% of the top 500 proteins are involved in splicing and ER/SR-based protein processing as well as sarcoplasmic chaperones. As chaperones (protein folding factors) are required for the function of contractile proteins as well as the assembly of the sarcomere, their high abundance among the top 500 proteins accords with the predominance of structural/sarcomeric proteins as described above¹⁶⁵. Besides modulating sarcomere integrity, chaperones and the proteasome system (~ 5% of the top 500) have evolved to regulate general protein turnover and to play pivotal roles in the regulation of skeletal muscle mass and metabolic function in multiple conditions. Both systems have also been found to be activated in muscle cells under catabolic states, sarcopenia as well as degenerative muscle disorders. Mutations of different proteins belonging to these systems have been directly linked to the manifestation of myopathic diseases¹⁶⁶. Some of the most abundant proteins related to processing and folding have been also associated with pathophysiological processes in a variety of neuromuscular disorders: BiP/HSPA5, VCP, CALR, CANX, HSPA1A and P4HB¹⁶⁷ (Figure 7).

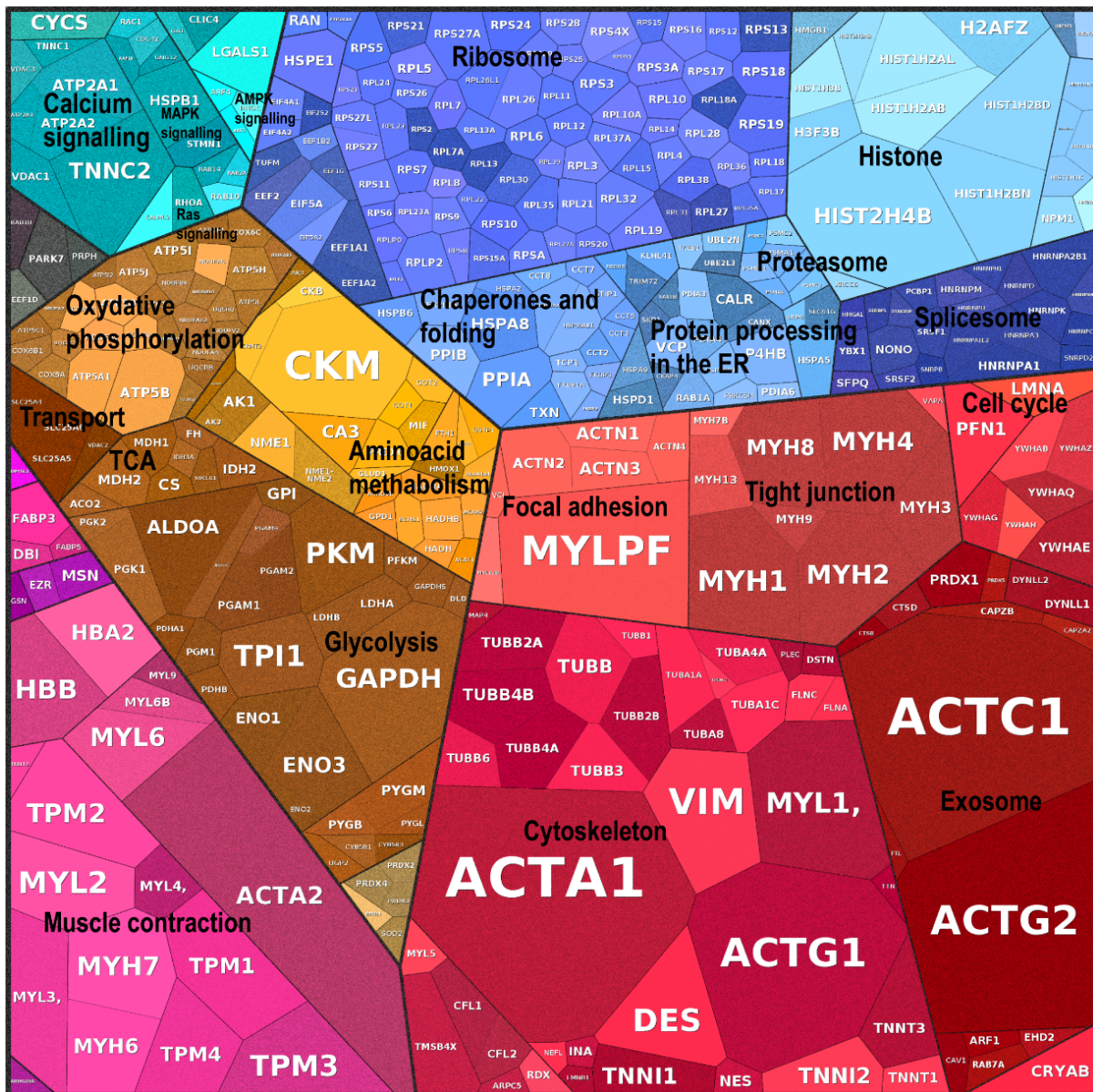


Figure 7. Proteomaps of the top 500 most abundant proteins found in the muscle protein catalogue. Every polygon or circle represents a protein, the size of which is given by the NASF number multiplied by protein chain lengths. The proteins are then grouped in functional categories based on the KEGG database. The proteomaps show five main hierarchy levels, which are further divided into sub-pathways. Color code: brown-metabolism, pink-muscle homeostasis and contraction, dark blue-cellular processes, light blue-signaling and red-ECM, cytoskeleton

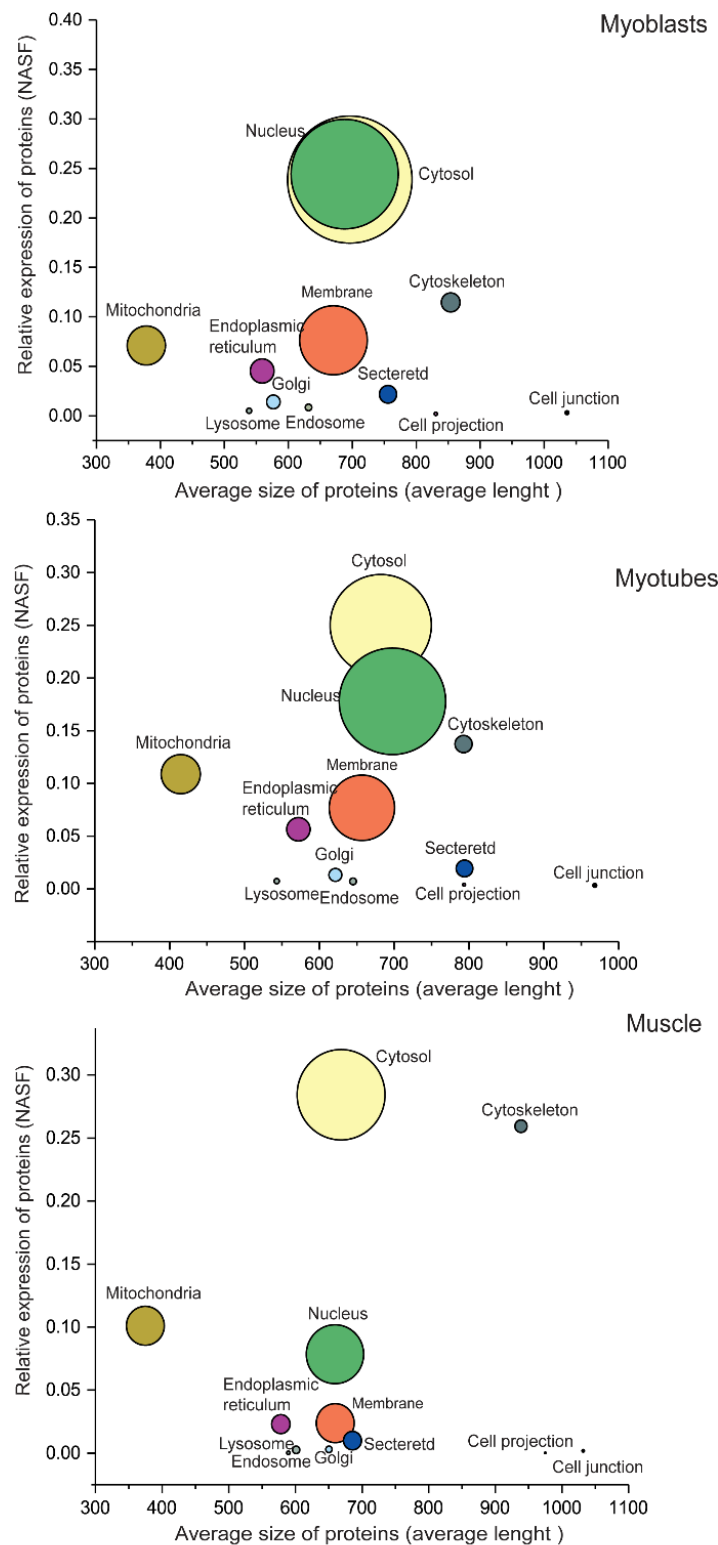


Figure 8. Comparison of proteomic data obtained from human primary myoblasts, myotubes and muscle tissue. Each protein was assessed using a subcellular localization and the following parameters were determined: 1) the sum of individual NASF values of these proteins; 2) the average length of the proteins included in each sublocalization and 3) the size of the circle, representing the number of proteins for organelle.

For all proteins identified, the subcellular localization was determined using Uniprot KB and then for each organelle the relative expression and size (average amino acid length) was assessed. All information was plotted taking the number of proteins identified for each compartment (represented by the size of the circle) into consideration (Figure 8). In line with the previous findings, the most abundant proteins in muscle are those belonging to the cytoskeleton and sarcomere function. Mitochondria play a crucial role in muscle fibre function as they provide the needed energy in the form of ATP. Consequently, the abundance of mitochondrial proteins is increased in myotubes and muscle tissue compared to myoblasts (Figure 8). However, this might also result from an increased number of overall mitochondria in myotubes and muscle tissue rather than represent a “pure” increase of mitochondrial proteins. RNA synthesis and DNA replication are processes which dominate the activity of myoblasts. Therefore, nuclear proteins are very likely highly abundant in proliferating myoblasts. While the most of RNA synthesis in myotubes is in accordance with a high protein turn-over rate in differentiated muscle, high abundance of nuclear proteins modulating DNA-replication in myotubes as post-mitotic represents an interesting molecular observation which accords with the findings of recent publications describing the high expression of proteins involved in DNA replication and processing in myotubes, although at lower levels compared to myoblasts^{26,168}. However, this does not fully exclude that possibility that this molecular observation is in fact caused by incomplete differentiation or further cytological processes.

The development of the muscle fibres depends on a series of complex cellular events which begin with the fusion of myoblasts into multi-nucleated cells called myotubes. This process takes place in stages and begins with the exit from the cell cycle, concomitant with the expression of certain genes, followed by the alignment of myoblasts which fuse to form myotubes¹⁶⁹. By focusing on proteins exclusively expressed in one of the *in vitro* systems of the muscle tissue, we sought for proteins important in the different phases of muscle cell function and differentiation:

3.1.3 Myoblasts to myotube transition

During differentiation, myoblasts undergo a well-characterized sequence of morphological and transcriptional events which result in the formation of myotubes. This transition is initiated by well-known myogenic regulatory factors like MyoD, MYF5, MGN and MRF¹⁷⁰. The individual protein catalogues of myoblasts and myotubes grant insights into the biological differences between molecular signatures of the distinct differentiation status of these cells. Examination of

these two proteomes revealed that 8342 proteins are commonly expressed, while 1321 were found solely in myoblasts and 431 in myotubes (Figure 9A). Next, the subcellular localization and pathways of these exclusive myoblast or myotube expressed proteins were analyzed (Figure 9-B and C). Then the protein abundances were calculated (NASF sum) for each organelle and pathway. As expected, a high percentage of proteins found solely in myoblasts are localized in the myonucleus and are involved in cell cycle and gene expression (Figure 9B and C). Activation of the myogenic program is tightly coupled with a series of signal transduction pathways that either suppress or stimulate cell proliferation and differentiation (Figure 9C). Consequently, proteins involved in cell proliferation like EGFR (that blocks differentiation¹⁷¹) or negative regulators of differentiation like TGF- β /BMP proteins¹⁷²⁻¹⁷⁴ are more abundant in myoblasts compared to myotubes. Proteins involved in Rho GTPase modulated pathways, in turn controlling the commitment to differentiation through the regulation of activity of factors such as Rac1, CDC42 and JNK^{175,176}, were also found to be expressed in myoblasts. Similarly, proteins modulating cytokine signalling seem to be more abundant in myoblasts. This molecular finding accords with the fact that cytokines are essential for efficacious skeletal muscle stem-cell function, augmenting regeneration and strength¹⁷⁷. Moreover, proteins involved in cilium assembly are more abundant in myoblasts compared to myotubes. The primary cilium acts as a cellular antenna, transducing diverse signalling pathways (according with higher expression of signalling proteins in myoblasts than myotubes) and cilia are assembled during the initial stages of myogenic differentiation but disappear as cells progress through myogenesis¹⁷⁸. In myotubes, cytoskeletal proteins and elements of the contractile apparatus seem to be highly expressed coinciding with the fusion and maturation of myotubes (Figure 9B and C). Furthermore, myotubes express more proteins involved in signalling pathways that control metabolism and organization of the ECM and the cytoskeleton (GCPR signalling)¹⁷⁹ or involved in the formation of the neuromuscular junction (WNT signalling)¹⁸⁰ compared to myoblasts (Figure 9C).

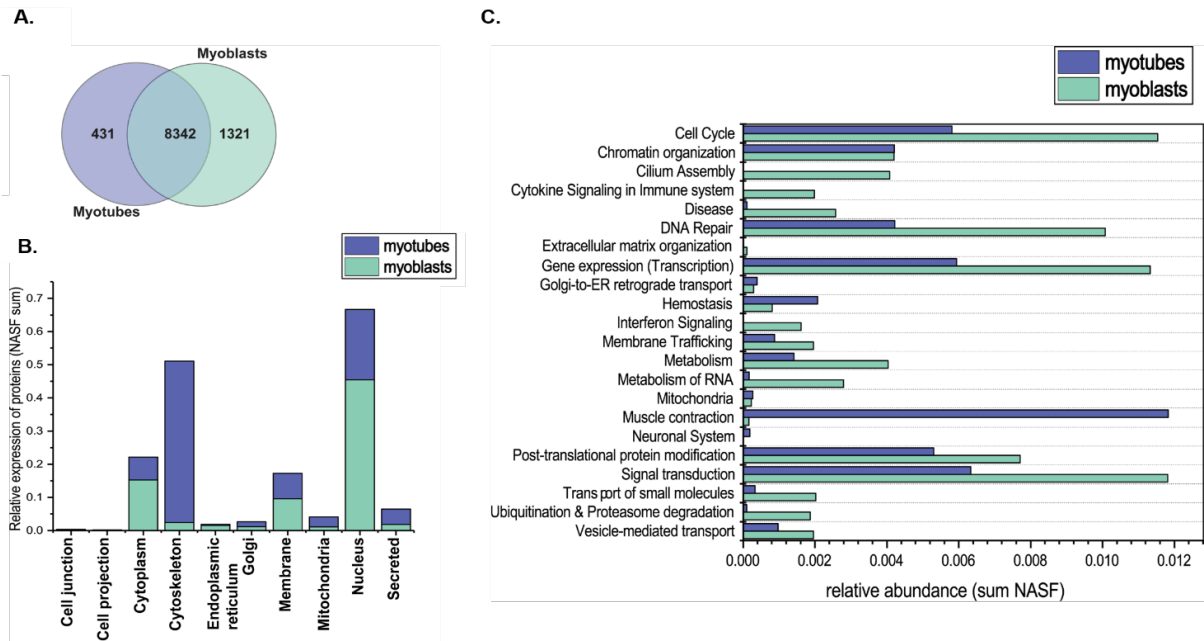


Figure 9. Overview of the myoblast vs. myotubes comparison. (A) 431 proteins are found solely in myotubes while 1321 are found solely in myoblasts, as seen in the Venn diagram. (B) Subcellular localization and C-pathway analysis of the proteins found just in myoblast and myotubes.

3.1.4 Myotube to muscle tissue transition

Similarly to the previous section the functional differences between myotubes and muscle were assessed. Interestingly, 3429 proteins were found exclusively in myotubes, whereas 851 were found only in muscle and 5368 were common for both (Figure 10-A). The high numbers of proteins found only in myotubes is most likely due to the known complexity of muscle which hinders the MS analysis and protein discovery. For these exclusive proteins, cellular localization and pathway analysis were performed and results subsequently plotted based on protein abundances. This approach revealed that proteins expressed solely in muscle tissue but not in myotubes mostly belong to the cytoskeleton, sarcoplasm but surprisingly also to DNA repair (Figure 10B and C). DNA damage (for instance induced by reactive oxygen species) is present in muscles as controlled or transient DNA damage. The latter appears to be essential for muscular differentiation and homeostasis, while uncontrolled and/or chronic DNA damage negatively affects muscle function¹⁸¹. Thus, higher expression of proteins involved in DNA repair might reflect the higher demand of controlled correction of DNA damage in complex tissue compared to myotubes. Interestingly, Circadian Clock proteins are also enriched in complex muscle tissue compared to myotubes (Figure 10C). Circadian regulation of transcriptional processes has an important impact on muscle cell metabolism and it was showed

that a more extensive rhythmic transcription is present in human skeletal muscle tissue compared to *in vitro* cell culture¹⁸². This conclusion was made, as a large part of the *in vivo* mRNA rhythmicity was lost *in vitro* suggesting an essential role for the circadian coordination of skeletal muscle metabolism (particularly glucose and lipid homeostasis) in humans¹⁸³. Consequently, this previous study supports the findings of the human skeletal muscle protein catalogue presented here. In addition, signal transduction related proteins seem to be more abundant in complex muscle tissue than in myotubes. The same molecular observation holds true for proteins involved in the transportation of small molecules (Figure 10C) which can be low molecular weight species that include lipids, monosaccharides, second messengers, other natural products and metabolites. Thus, enrichment of proteins modulating their proper transportation in muscle tissues is in accordance with the high metabolic activity and Ca²⁺ signalling in muscle tissue. Given that the immune system is relevant to the muscle regeneration, higher abundance of related proteins are present in complex tissue (Figure 10C), compared to *in vitro* systems and most likely facilitates effective regenerative strategies in muscular homeostasis¹⁸⁴. A recent publication highlighted the need of post-translational modifications of structural components of the sarcomere such as of critical myofilament proteins in the fast-twitch skeletal muscle which are necessary for proper function and contraction¹⁸⁵. Thus, enrichment of related proteins in muscle tissue compared to myotubes (Figure 10C) accords with higher abundance of structural proteins in the tissue and might reflect a tight control of sarcomeric components via post-translation modifications towards proper contraction which is in turn controlled by transmission of signals from the peripheral nervous system. Similarly, proteins controlling axon guidance (also called axon pathfinding) are also more abundant in muscle tissue compared to myotubes (Figure 10C). This molecular finding might be caused by the presence of nerve fibres in the muscle tissue as the expression of these proteins in tissue enables communication between muscle and nerve cells. The heterogeneity of the tissue compared to differentiated cells is not only mirrored by the higher abundance of proteins involved in axon guidance but also by proteins involved in coagulation and platelet signalling and oxygen transport (Figure 10C) most likely corresponding to the presence of capillaries in the muscle tissue. In accordance with the high demand of proper proteostasis in muscle tissue, proteins belonging to the protein processing machinery and to cellular stress defence mechanisms (chaperones) as well as to protein clearance (particularly the proteasome) are enriched in the tissue compared to myotubes (Figure 10C).

The muscle normally has quiescence satellite cells which are the myogenic cells that accumulate at the site of damaged tissue and are known to re-activate and re-enter the cell cycle, having increased nuclear proteins¹⁸⁶. Interestingly, proteins involved in cell cycle, chromatin organization and transcription seem to be more highly expressed in myotubes than in muscle tissue (Figure 10C). Although muscle tissue harbours satellite cells with mitogenic potential, these muscle stem cells seem to be less abundant to be covered in the proteomic signature of muscle tissue.

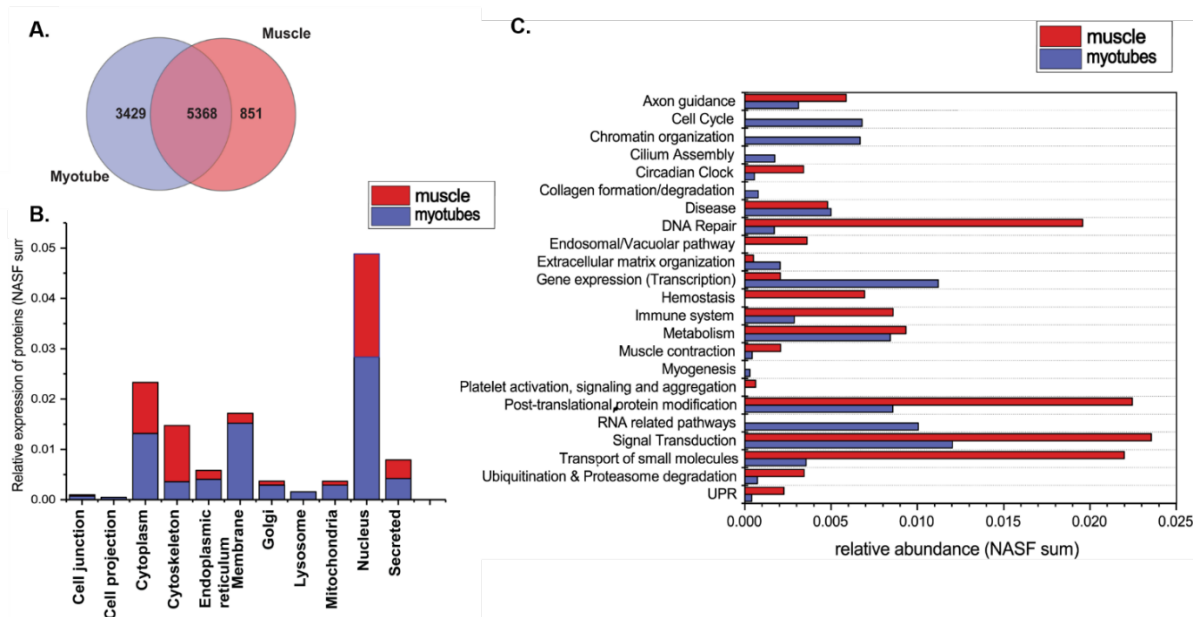


Figure 10. Overview of the myotubes vs. muscle tissue comparison. (A) Venn diagram representing the distinct and overlapping proteins when comparing myotubes with muscle tissue. (B) and (C) Comparison of protein abundances that were identified either in muscle or in myotubes. Selected proteins were either grouped based on their subcellular localization or on their biological function.

3.2 Pathophysiology of muscular dystrophies

3.2.1 Molecular linkage of rare neuromuscular diseases

3.2.1.1 INPP5K as a new gene causing congenital muscular dystrophy

INPP5K is a skeletal muscle and kidney enriched inositol polyphosphate phosphatase (SKIP) and has a 5-phosphatase activity towards trisphosphate inositol and phosphatidylinositol (PtdIns) in positions 3, 4 or 5¹⁸⁷. The resulting phosphoinositides are involved in the generation of new signal molecules (diacylglycerol and inositol) which mobilize Ca^{2+} stores and activate protein kinase C. Additionally, PtdIns, through their phosphorylated head groups, recruit other proteins to the inner plasma membrane thus regulating processes like vesicle formation, actin and microtubule dynamics and transport of ions^{187,188}. Mutations in INPP5K have recently been associated with congenital muscular dystrophy associated with early onset cataracts and mild intellectual impairment⁵⁵. Affected individuals also presented with high levels of creatine kinase (up to 14 times higher than normal values) and the electromyography results showed a progressive myopathic process^{55,189}. Muscle biopsies were heterogeneous and displayed typical dystrophic features such as internalized nuclei, variable range of muscle fibers, fibrosis as well as substitution of muscle fibers with fat and collagen (Figure 11A and D). Muscle fiber distribution (Figure 11B and C) is highly uneven, with no clear fiber grouping and with some fascicles displaying type 1 or 2 predominance. Additionally, it was reported that components of the DGC are not necessarily affected in the INPP5K morphology^{189,190}.

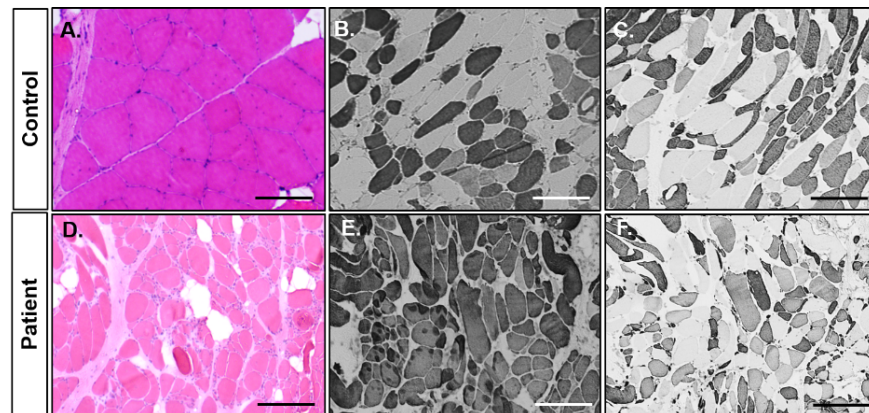


Figure 11. Muscle biopsy from an individual harbouring the p.I50T mutation on the INPP5K protein and from a healthy control, matching sex and age. (A) H&E stain revealing variation in fiber size, rounding of fibers, increased endomysial collagen and some degree of fatty degeneration compared with the normal control (D).

(B, E) Immunohistochemical analysis of the slow fibers using the ATP-ase staining while in (C, F) the fast myosin is depicted. Scale bars: 50 μ M.

So far, several mutations affecting the 5-phosphatase (catalytic active domain) and one affecting the SKITCH (responsible for the translocation of the protein to the membrane) domain have been described in some patients (Figure 12A). Mutations that are located in the 5-phosphatase domain of INPP5K impinge on the catalytic function of INPP5K leading to a decrease in the phosphoinositide phosphate activity especially in the case of the p.T300C missense mutation. Interestingly, these mutations do not lead to a subcellular mis-localization of the protein with the exception of the p.I363T mutation affecting the SKITCH domain. Immunoblot-studies revealed that the levels of the mutant INPP5K are fairly stable, a molecular observation which was also confirmed via IF (Figure 12B).

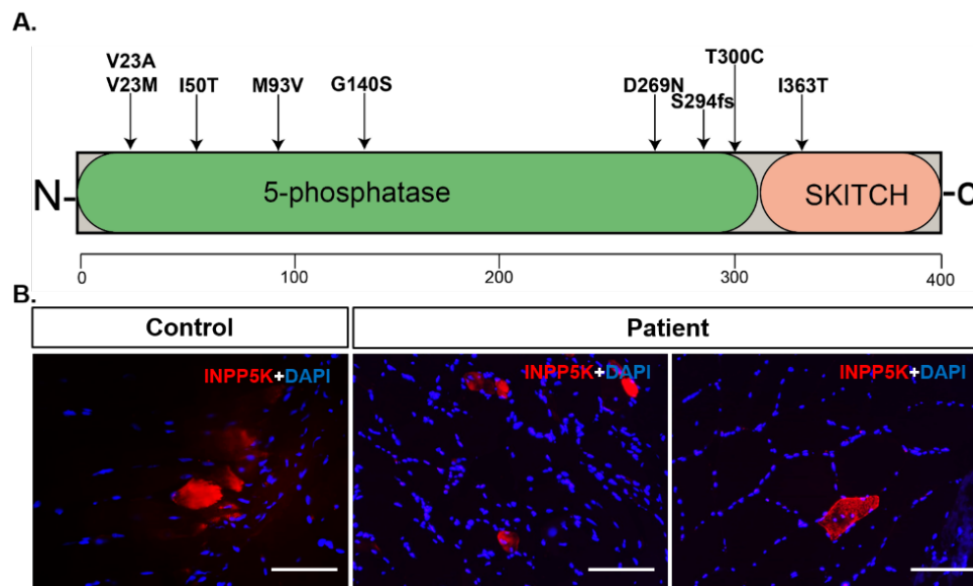


Figure 12. (A) Schematic representation of INPP5K protein and its domains as well as the distribution of mutations identified so far in families presenting with cataracts and congenital muscular dystrophy associated with mild intellectual disability. (B) Immunofluorescence analysis of the INPP5K protein in muscles derived from patients harbouring the p.I50T and controls, showing that the protein is stable.

Interestingly, the muscle, eye and brain phenotype caused by INPP5K mutations are clinically overlapping with other rare multisystemic neuromuscular disorders such as Marinesco-Sjögren syndrome (MSS) and congenital cataracts, facial dysmorphism and neuropathy syndrome (CCFDN). MSS is an autosomal recessive disorder with infantile onset. Patients present with progressive muscle weakness due to a vacuolar myopathy, cataracts, cerebral atrophy and intellectual disability^{191,192}. MSS is caused by mutations in

the *SIL1* gene which encodes for a protein responsible for the efficient cycling of ADP and ATP for BiP, a major chaperone of the ER¹⁹³. CCFDN is caused by a recurrent mutation in the *CTDP1* gene, encoding an RNA polymerase II subunit A C-terminal domain phosphatase. Remarkably, further similarities between INPP5K-CMD and MSS were observed¹⁹⁴: Morphological examinations of the muscles showed vacuoles as well as electron-dense material surrounding degenerating myonuclei and both proteins are known binding partners of the major ER-resident chaperone called BiP^{55,193}. The clinical and ultra-morphological overlap of these two diseases implies that common cellular cascades are affected. Discovery of these cascades would lead to a better understanding of the molecular aetiology of the disorders and, more importantly, to the definition of common therapeutic targets.

3.2.1.2 Proteomic signature of INPP5K mutant fibroblasts

In order to identify key molecular players that contribute to the INPP5K related phenotype, proteomic signature of fibroblasts derived from 3 patients harbouring the p.I50T missense mutation were compared with the signature of control fibroblasts. Proteomic profiling lead to the identification of 3018 proteins with a minimum of 2 unique peptides. Approximately 8% (232 proteins) of the identified proteins were found to be statistically significant (p-Anova ≤ 0.05) and hereby 44 were statistically significant altered in abundance (22 were up regulated while 22 were down regulated; see Figure13).

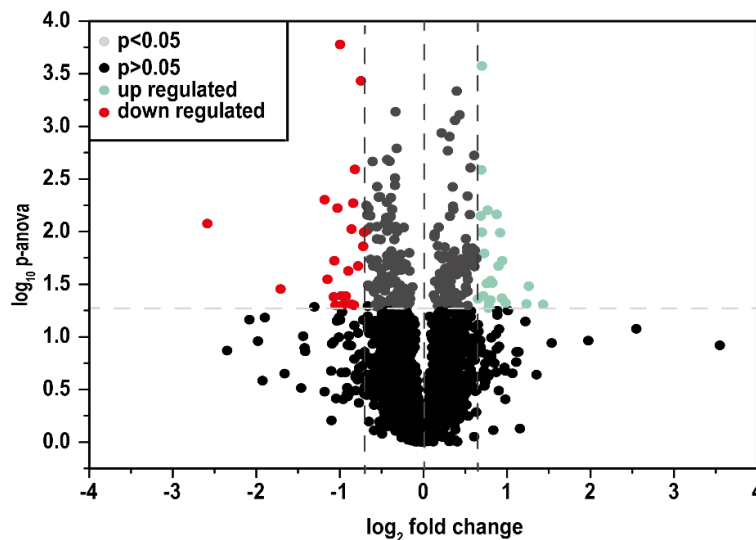


Figure 13. Comparative proteome profiling of INPP5K derived fibroblasts with control ones. The volcano plot depicts all the proteins identified in fibroblasts, making a clear delimitation between the proteins with a p-Anova < 0.05 -statistically significant (horizontal line). Proteins which are decreased are represented in red while the up regulated ones are in green.

Altered proteins were further studied *in silico* using KEGG, DAVID and Reactome pathway analysis platforms and found to be involved in various pathways including cell death and aging, protein folding and aggregation, gene expression as well as cell proliferation and differentiation (Figure 14A). Proteins involved in actin cytoskeleton and cell adhesion seem also to be affected by the INPP5K mutation, a molecular observation which accords with the function of INPP5K as a negative regulator of the actin cytoskeleton. The subcellular localization of altered proteins was assessed using Uniprot. The organelle most affected by the p.I50T-INPP5K mutation seems to be the plasma membrane (10 proteins out of 44) followed by the cytoskeleton/cytoplasm (9 proteins) and the nucleus (6 proteins) (Figure 14 B).

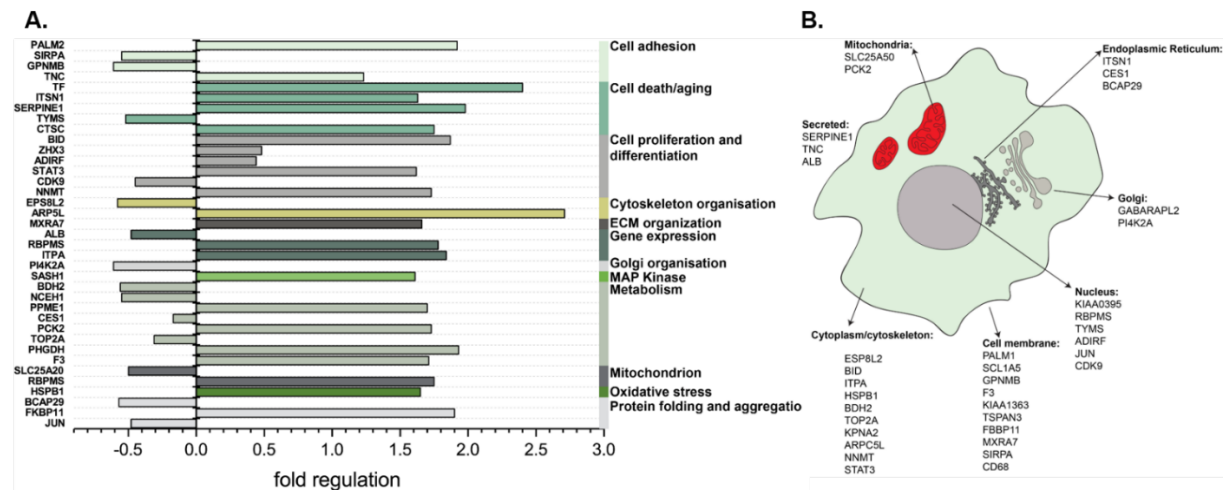


Figure 14. *In silico* analyses of proteomic findings. (A) Pathway analysis of the regulated proteins resulted from the comparative proteome profiling. All proteins were searched using KEGG, DAVID and Reactome databases for protein pathway annotation. (B) Subcellular localization of altered proteins.

After proteomic profiling was performed, obtained INPP5K-data were intersected with the already published proteome profiling data of MSS-patient derived lymphoblasts¹⁹⁵ and existing but unpublished data of MSS-patient derived fibroblast to identify common pathomechanisms linking these rare phenotypically overlapping diseases also at molecular level. This approach allowed for the identification of D-3-phosphoglycerate dehydrogenase (PHGDH) as a metabolic protein downregulated in MSS-patient derived cells but increased in the INPP5K-patient derived fibroblasts (Figure 15A)^{190,193}. The increase of PHGDH was also confirmed in the INPP5K-patient derived fibroblasts via immunoblotting (Figure 15B). Additionally, muscle biopsies derived from 3 patients carrying the p.I50T mutation in INPP5K were stained utilizing an antibody against PHGDH (Figure 15C). The overall

quantification of fluorescence intensity revealed that in 2 of the 3 investigated patients PHGDH shows a statistical significant increase.

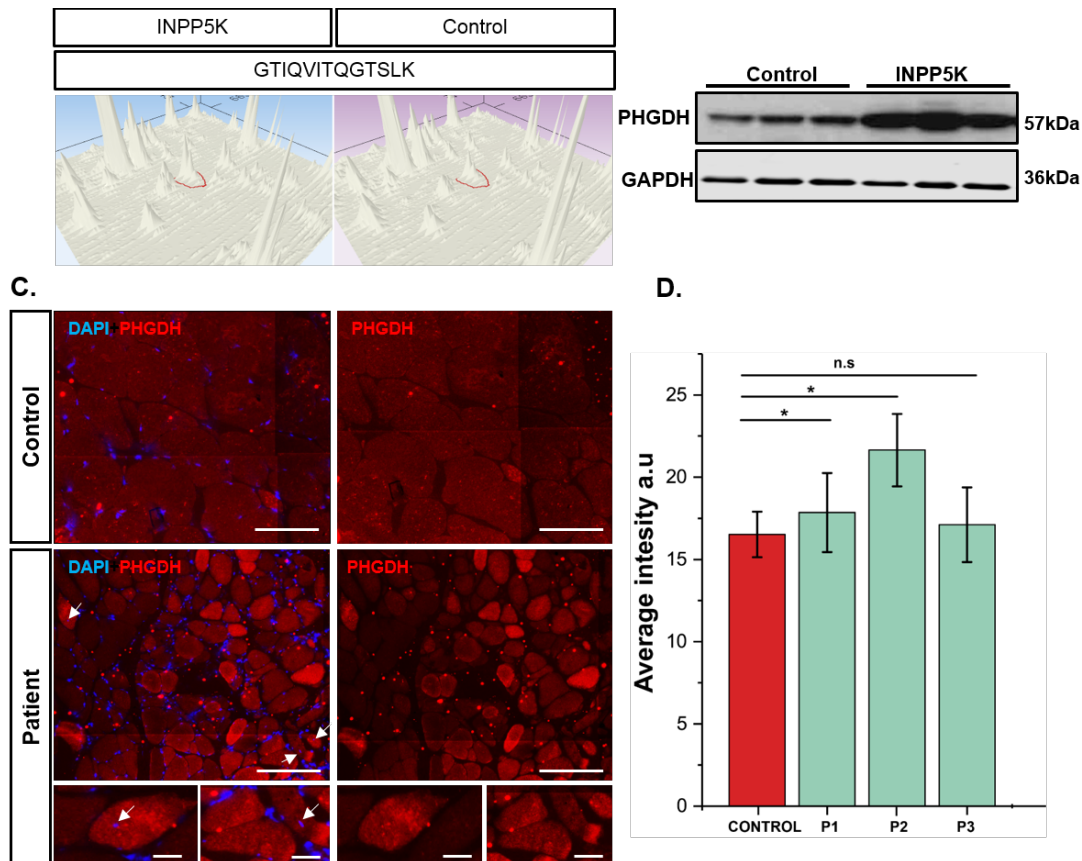


Figure 15. Schematic representation of the PHGDH increase in INPP5K-patients. (A) The increase of PHGDH in INPP5K-patient derived fibroblasts seen in proteomics depicted via a 3D montage. This montage shows an increase in the PHGDH tryptic peptide GTIQVITQGTSLK. (B) The proteomics data were verified via immunoblotting confirming an increase in PHGDH. GAPDH was used as a loading control. (C) Immunofluorescence analysis of PHGDH in *vastus lateralis* muscle derived from INPP5K patients and controls. (D) By quantifying INPP5K abundance in three patient muscles, an up-regulation of PHGDH compared to controls can be observed for two patients; *-t-test<0.05. Scale bars: 200 μ m.

In addition, proteomic analysis of INPP5K-patient derived fibroblasts revealed a decrease of cyclin-dependent kinase 9 (CDK9) (Figure 16A). CDK9 modulates the activity of RNA polymerase II subunit A, C-terminal domain phosphatase (CTDP1)¹⁹⁶ thus linking INPP5K-CMD to the pathophysiology of CCFDN as a clinically overlapping disease. Further immunofluorescence studies on CDK9 in muscle specimen biopsies from controls revealed an enrichment of the protein at the sarcolemma while in samples obtained from INPP5K patients, CDK9 does not show any staining in the sarcolemma region and reduced immunoreactivity in the myonuclei (Figure 16B). The 3D-structural representation of CDK9

distribution in muscle fibers shows that CDK9 is mainly localizing within the cytoplasm in accordance with previous research in which CDK9 was found to shuttle between the nucleus and cytoplasm upon the expression of cyclin T1 in different cell models¹⁹⁶ (Figure 16 B and C).

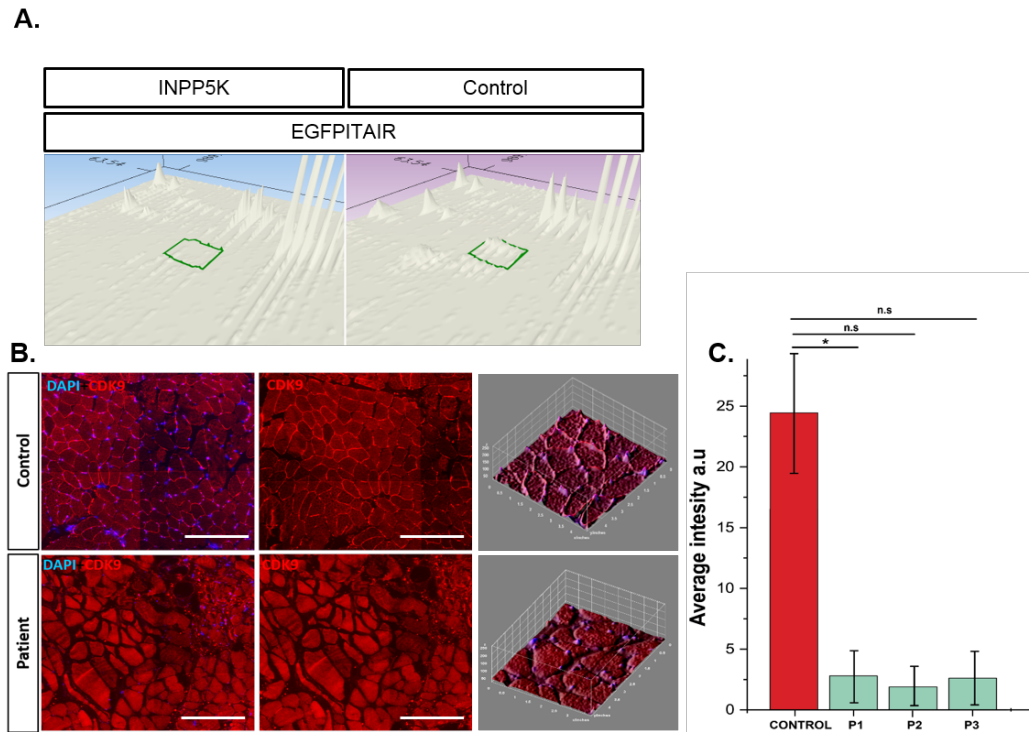


Figure 16. CDK9 protein abundance in INPP5K patients. (A) EGFPITAIR, a tryptic peptide of CDK9 shows a decrease in patient derived fibroblasts as visualized in the 3D montage presented here. (B) Immunofluorescence analysis of CDK9 in *vastus lateralis* muscle derived from INPP5K-patients and controls and 3D montages of the fluorescence distribution in the muscle fibers. (C) Fluorescence intensity quantification revealed that the sarcolemma- and myonuclear-resident CDK9 is increased in the control muscles compared with the diseased ones, *-t-test<0.05. Scale bars: 200 μ m.

3.2.1.3 Phenotyping of zebrafish models of *Inpp5k*-, *Sill*- and *Phgdh*-depletion

Although mice are evolutionary more similar to humans, zebrafish are considered excellent model organisms for the study of vertebrate biology and genetics, drug screening and disease etiology¹⁹⁷. To further assess the phenotypical consequences of *Inpp5k*-, *Sill*- and *Phgdh*-depletion *in vivo*, zebrafish models were generated by morpholino induced knockdown (KD) of the respective genes (Table 15). The choice of zebrafish as an *in vivo* system was prompted by the recent generation of *inpp5k* and *sill* KD fish models, both displaying features of the human pathology^{55,151}. Notably, generation of a *phgdh* knockdown fish model is described here for the first time.

Two orthologues of *inpp5k* (a and b) were identified in zebrafish which were addressed with specific morpholinos that reduced the expression of *inpp5ka* and *inpp5kb* at 48hpf as described previously¹⁸⁹ (Figure 17A). Fish presented with a high rate of death (Figure 17B) upon the KD of both orthologues. Surviving embryos macroscopically presented with an altered tail morphology (Figure 17C) and histologically with abnormalities of the skeletal muscle (wavy fibers, disruption of the somites and absent myosepta) (Figure 17D) as visualized via phalloidin staining. NMJ and the brain development at 48 hpf seem to be mostly unaffected by depletion of *inpp5k* (Figure 17D and E). For the visualization of the hindbrain, a transgenic zebrafish was used in which a GFP-tagged *Isl1* protein is expressed in somatic and visceral neurons¹⁴⁹. In line with the human phenotype, *Inpp5k*-depleted fish showed no hindbrain-abnormalities also confirming the previously published phenotype of the fish model¹⁸⁹.

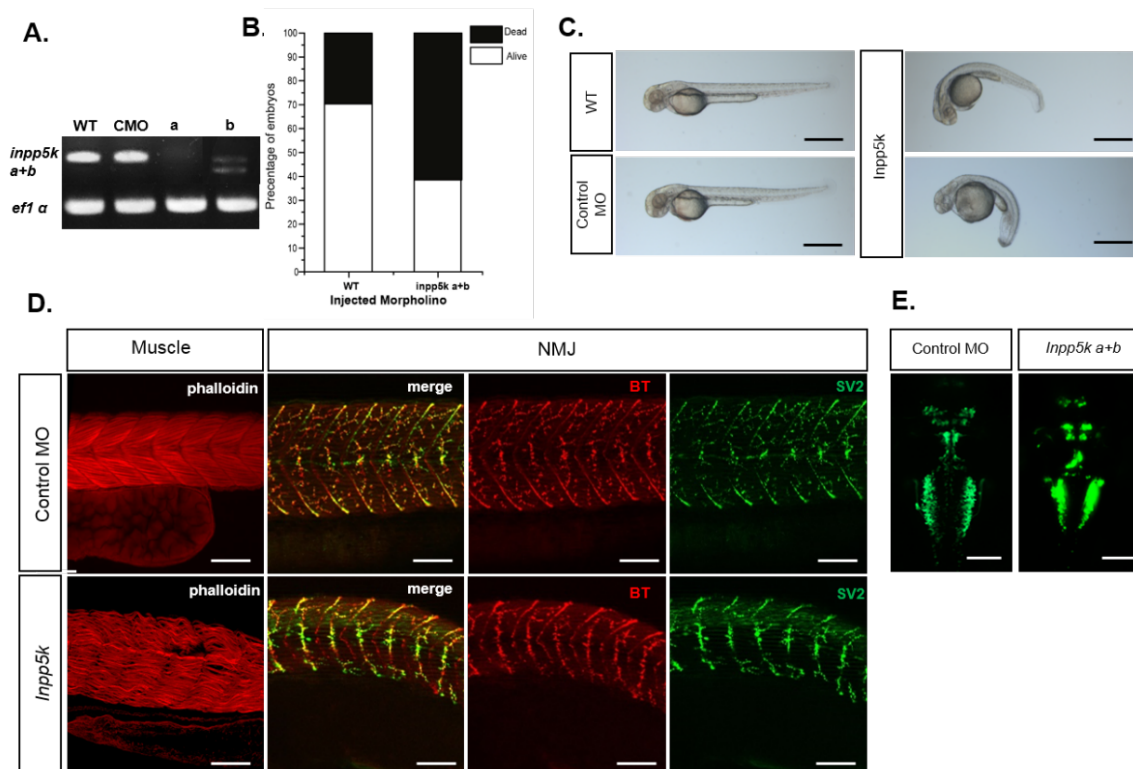


Figure 17. Overview of the *inpp5k* morphants. (A) The anti-sense morpholinos designed for the knockdown of *inpp5k* disrupt the splice donor site of intron 4 of *inpp5ka* and *inpp5kb*. RT-PCR analysis of *inpp5k* transcripts (400 bp) from 48hpf double knockdown embryos shows a down regulation of *inpp5ka* and a mis-spliced *inpp5kb*. *Efl1 alpha* was used as an internal RT-PCR control to exclude variations in cDNA quality. (B) Graph depicting the survival rates in the control MO and *inpp5k* and *b* morpholino injected fish. At least 100 injected embryos were counted. (C) Live embryos images of non-injected, control MO and *inpp5k a+b* injected zebrafish at 48 hpf showing a vulnerability of the tail. Scale bars: 500 μ M. (D) Whole mount immunostainings of 48hpf

zebrafish using antibodies against the actin cytoskeleton, postsynaptic AChR (α -bungarotoxin, red staining) and presynaptic nerve endings (SV2 antibody, green staining). Scale bars: 50 μ M. (E) Live fluorescent imaging of *inpp5k* morphant mid and hindbrain in *isl1*: GFP transgenic strain of zebrafish. Dorsal view of the midbrain and hindbrain of CMO embryos and *inpp5k* morphants at 48hpf (Tg (*isl1*:GFP) line). Scale bars: 100 μ m. Figure 17A and C as well as the NMJ staining was adapted from a previous publication of Wiessner and co-workers¹⁸⁹.

The zebrafish model for MSS was recently described by Kawahara and colleagues¹⁵¹. The exact splice blocking morpholino targeting the splice acceptor site of exon 2 was employed for the generation of the *sill* depleted zebrafish described in this study. Embryos were injected with 6 ng of the morpholino, which reduced the expression of *sill* compared with the controls, and their phenotype was subsequently assessed¹⁵¹ (Figure 18). Macroscopically, the *sill* KD display an abnormal shape following de-chorination including a curved tail resulting in abnormal swimming behaviour (Figure 18-B). Interestingly, *sill*-depleted muscle fibres display almost no abnormality at 48hpf upon phalloidin staining most likely due to the low concentration of injected morpholino. Although, Kawahara and colleagues stated that at a concentration of 6 ng of the morpholino they observe a disturbed pattern of muscle fiber integrity, this finding could not be confirmed upon careful inspection of their birefringence assay which solely revealed a very mild muscle phenotype. Additionally, NMJ and brain morphology were investigated. Although, the muscle presents no remarkable alterations, the NMJs of MSS zebrafish show disruption of synapse formation along the myosepta, particularly at the presynaptic part of the NMJs (Figure 18C). This finding accords with affected NMJs in both MSS patients and woozy mice (mouse model of MSS)¹⁹⁸ Live imaging of the cranial motor neurons using the transgenic *Isl1* fish showed an altered brain morphology with nerves III (oculomotor), IV (trochlear), VI (abduces) VII (facialis) and X (vagus) being the most affected by the reduction of *Sill* levels (Figure 18D).

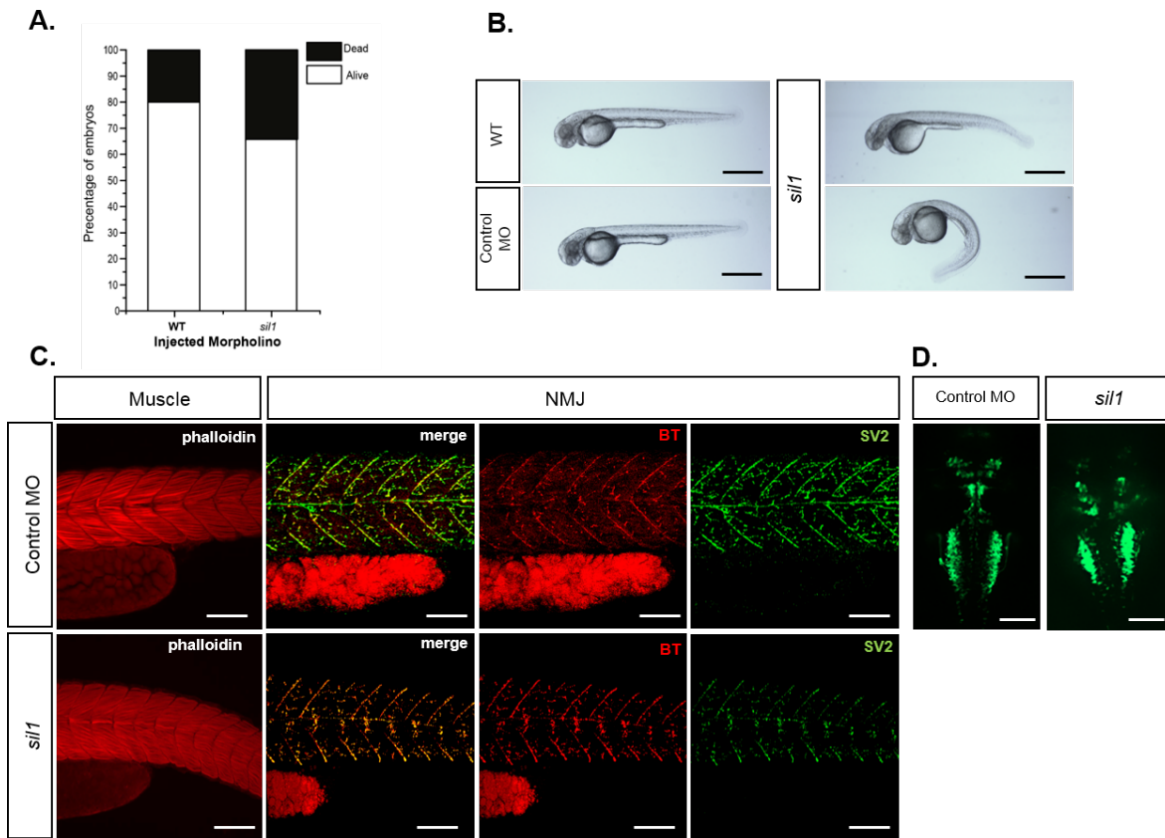


Figure 18. Overview of phenotypical findings in the *sil1* morphants. The anti-sense morpholinos designed for the knockdown of *sil1* disrupt the splice donor site of exon 2 of *sil1*. (A) Graph depicting the survival rates in the control and *sil1* morpholino injected fish. At least 100 injected embryos were counted. (B) Live embryos images of non-injected, control MO- and *sil1* MO-injected zebrafish at 48 hpf showing mild alterations of the tail. Scale bars: 500 μ m. (C) Whole mount immunostainings of 48hpf zebrafish using antibodies against the actin cytoskeleton, postsynaptic AChR (α -bungarotoxin, red staining) and presynaptic nerve endings (SV2 antibody, green staining). Scale bars: 50 μ m. (D) Live fluorescent imaging of *Sil1* morphant mid and hindbrain in *is11:GFP* transgenic strain of zebrafish. Dorsal view of the midbrain and hindbrain of control embryos and *sil1* morphants at 48hpf (Tg (*is11:GFP*) line). Scale bars: 100 μ m.

PHGDH-deficiency in humans has been associated with an autosomal recessive disorder in which patients present with a very severe phenotype defined by congenital microcephaly, seizures and psychomotor retardation¹⁹⁹. The clinical significance of this enzyme has so far been demonstrated solely in PHGDH knockout mice and no report of a zebrafish model has been described so far. The complete KO of the protein leads to embryonic lethality and the null PHGDH embryos were poorly developed, with apparent brain and limb abnormalities, mild exencephalic phenotype, dorsal closure failure, absence of the olfactory bulb, ganglionic eminence and cerebellum^{200,201}. For the generation of the fish model, a translation blocking morpholino targeting exon 2 was designed and injected into embryos. At 48hpf, the decreased

expression of *phgdh* in injected zebrafish was confirmed via RT-PCR (Figure 19A). Injection of the *phgdh*-MO led to 10% more embryos dying compared to CMO; however, the overall survival rates were higher than in the *Inpp5k* fish and showed similar rates to the *MSS* fish (Figure 19B). Histologically, the *phgdh*-MO fish presented with abnormalities of skeletal muscle morphology and immunostainings of the actin cytoskeleton (phalloidin) showed disruption of the regular chevron shape of somites, wavy fibers and in some of the cases absent notochord (Figure 18-D). NMJ-development is highly disrupted in the *phgdh*-MO injected embryos as seen by the staining of the AChR and SV2 (Figure 18-D). The depletion of Phgdh leads to a striking reduction of neuromuscular synapses in the dorsal region of the myotome segment. In contrast, the pre-patterning of the AChR clusters seems to be mostly unaffected. PHGDH has a strong expression in radial glia/astrocyte lineage and in olfactory ensheathing glia of the mature brain while in neurogenesis is mostly expressed in neuroepithelial stem cells thus being crucial for brain development¹⁹⁹. Live imaging of the MO injected *Isl1* zebrafish showed a strong effect of Phgdh KD on the development of the hindbrain; with a similar effect being observed in the *Phgdh* deficient mouse model (Figure 19C), thus confirming the suitability of the here generated and new introduced Phgdh fish model.

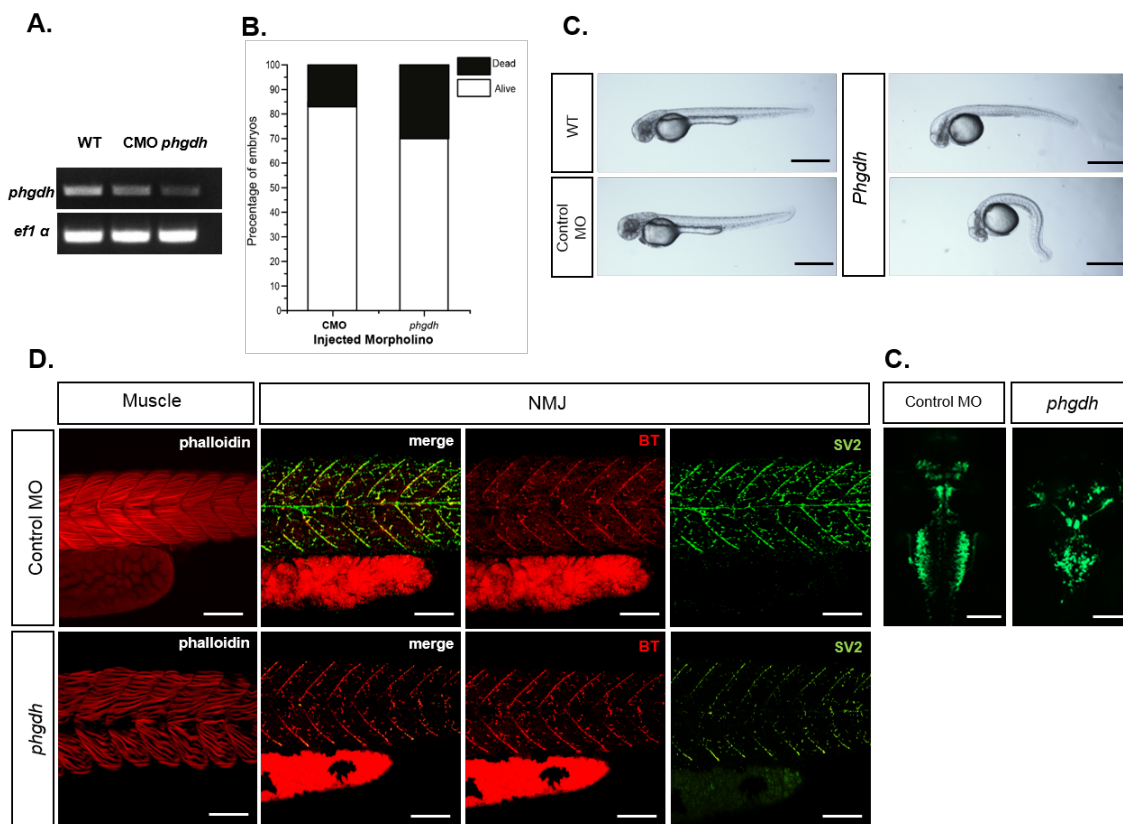


Figure 19. Overview of the phenotypical findings in *phgdh* morphants. (A) The anti-sense morpholinos designed for the knockdown of *phgdh* disrupt the splice donor site of exon 2. The RT-PCR analysis of *phgdh* transcripts (400 bp) from 48hpf embryos shows a down-regulation of the transcript in the *phgdh*-MO injected fish compared with the CMO or the non-injected ones. *Efla* was used as an internal RT-PCR control to exclude variations in cDNA quality. (B) Survival rates were assessed in the control and *phgdh* morpholino injected fish. At least 100 injected embryos were counted. (C) Live embryos images of non-injected, control and *phgdh* MO injected zebrafish at 48 hpf showing a modified morphology. Scale bars: 500 μ M. (D) Whole mount immunostainings of 48hpf zebrafish using antibodies against the actin cytoskeleton, postsynaptic AChR (α -bungarotoxin, red staining) and presynaptic nerve endings (SV2 antibody, green staining) showing a clear vulnerability of both muscle and NMJ in the Phgdh KD fish. Scale bars: 50 μ M. (E) Live fluorescent imaging of *phgdh* morphant mid and hindbrain in *isl1*:GFP transgenic strain of zebrafish. Dorsal view of the midbrain and hindbrain of CMO embryos and *Inpp5k* morphants at 48hpf (Tg (*isl1*: GFP) line). Scale bars: 100 μ m.

Next, the protein abundances of Phgdh were examined in all 3 described zebrafish models via WB. This analysis revealed that Phgdh is increased in the *inpp5k* morphant (Figure 20), result being in accordance with the findings obtained in the fibroblasts and muscle derived from patients harbouring the p.I50T mutation. In contrast, Phgdh seems to be decreased in the *sil*-MO injected embryos (Figure 20), a molecular observation also detected in the fibroblasts and lymphoblasts of MSS patients¹⁹⁵. The protein levels are also decreased in the *phgdh*-MO injected embryos, thus confirming the successful knockdown of *phgdh* and serving as a proof-of-principle (Figure 20).

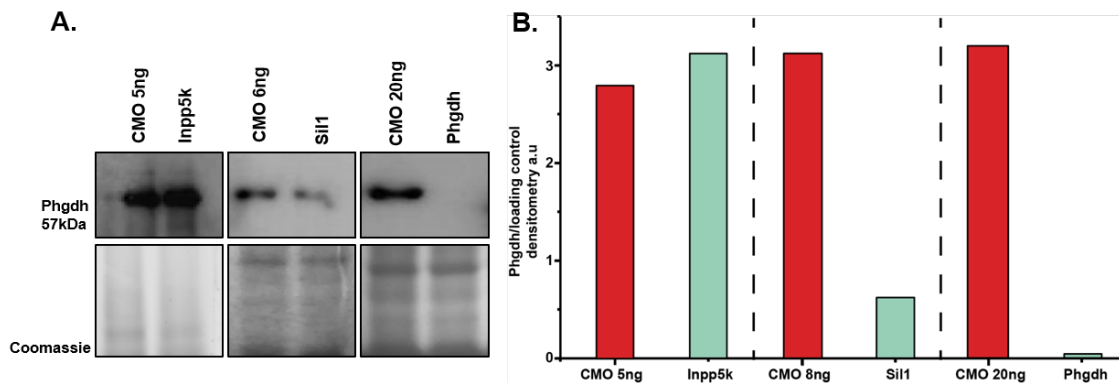


Figure 20. Analysis of Phgdh abundances: (A) Immunoblot analysis of Phgdh in the described zebrafish models, showing a decrease Phgdh levels in the *sil*- and *phgdh*-morphants while in the *inpp5k*-MO injected fish, the levels are increasing. An appropriate control was employed for each zebrafish model. As a loading control, Coomassie of proteins was used. (B) Phgdh protein level were normalized to overall protein abundances represented by the respective Coomassie staining. This revealed a slight increase in the *Inpp5k* fish whereas in *Sil1* and *Phgdh* fish, a remarkable decrease could be observed.

3.2.1.4 Effect of L-serine treatment on *inpp5k*, *sill* and *phgdh* morphants

PHGDH is an enzyme involved in the *de novo* synthesis of L-serine via oxidation of 3-phosphoglycerate, a product of glycolysis²⁰². This amino acid is classified as non-essential and plays crucial roles in cell homeostasis and survival²⁰³. Numerous publications have underlined the importance of L-serine in the development of the central nervous system (CNS)¹⁹⁹ and supplementation of L-serine was found to have a beneficial effect on neurodegeneration in CNS disorders²⁰⁴.

Zebrafish are a suitable animal model for the pre-clinical drug testing, as small molecules have the capacity to surpass the chorion fact demonstrated by the 65 molecules so far tested successfully²⁰⁵. Additionally, different studies demonstrated that these molecules have the capacity to pass further physiological boundaries, such as the blood brain barrier²⁰⁶. As PHGDH was found to be a common molecular denominator for MSS and INPP5K-CMD, rescue experiments in which L-serine was supplemented in the growth media were performed. The dosage of L-serine was determined using the non-injected and CMO-injected fish as previous reports of D-serine showed that a concentration of 1000 ppm has a detrimental effect on muscle and NMJ²⁰⁷. To study the exposure time and dosage effects on zebrafish embryos, L-serine at concentrations ranging from 75 to 200 μ M were added to the growth media of the non-injected and CMO fish. Next, the skeletal muscle phenotype and survival rates were assed at 48 hpf. These studies revealed no differences between the 75 and 100 μ M L-serine concentrations, (Figure 21A and B), whereas at 200 μ M the death rates amongst the fish were close to 100%. In order to determine the potential beneficial effect of L-serine supplementation on *inpp5k*-, *sill*-, and *phgdh*-MO injected embryos, the amino acid was added to the growth media. A final dosage of 100 μ M was chosen for further utilization as the mean survival rates showed that *sill*- and *phgdh* morphants increased by 19% and 18% respectively when compared to the mock-treated group (Figure 21-B). In contrast, the survival rates remain mostly unchanged in the *inpp5k* treated and untreated morphants (Figure 21B).

Given that the *sill*-MO injected embryos did not present a proper muscle phenotype when a concentration of 6 ng of oligos was applied, a possible improvement of myopathology upon L-serine treatment would be difficult to pinpoint. Despite the injection of 8 ng impacting the survival rates, rescue experiments were carried out with the higher concentration of *sill*-MO, as at this injected concentration a phenotype more similar phenotype to MSS was induced (Figure 21C).

Zebrafish movement within the chorion can be indicative of neuronal development and be measured by counting the repetitive tail movements²⁰⁸. To quantify this in our different fish models, 24hpf embryos were recorded for 2 minutes and the normal tail movements (tail thrashes) were counted. Non-injected zebrafish moved on average 4.7 times per minute and the injection of the control MO reduced this to 4.1 while a combination of CMO and serine slightly decreased the movements to 3.8 tail thrashes/minute as shown in figure 21D. No movements were recorded in the *inpp5ka+b* morphants, however the supplementation of L-serine seems to increase the movements to 2.4/ minute. *sil1* morphants treated with L-serine presented with 4.1 movements/ minute, similar to the CMO embryos while in the mock-treated *Sil1* embryos the movements were reduced to 50% (Figure 21D). Presumably due to a severe brain phenotype, the *phgdh* morphant embryos presented exclusively with abnormal tail movements catalogued as alternating side tail thrash (Figure 21D).

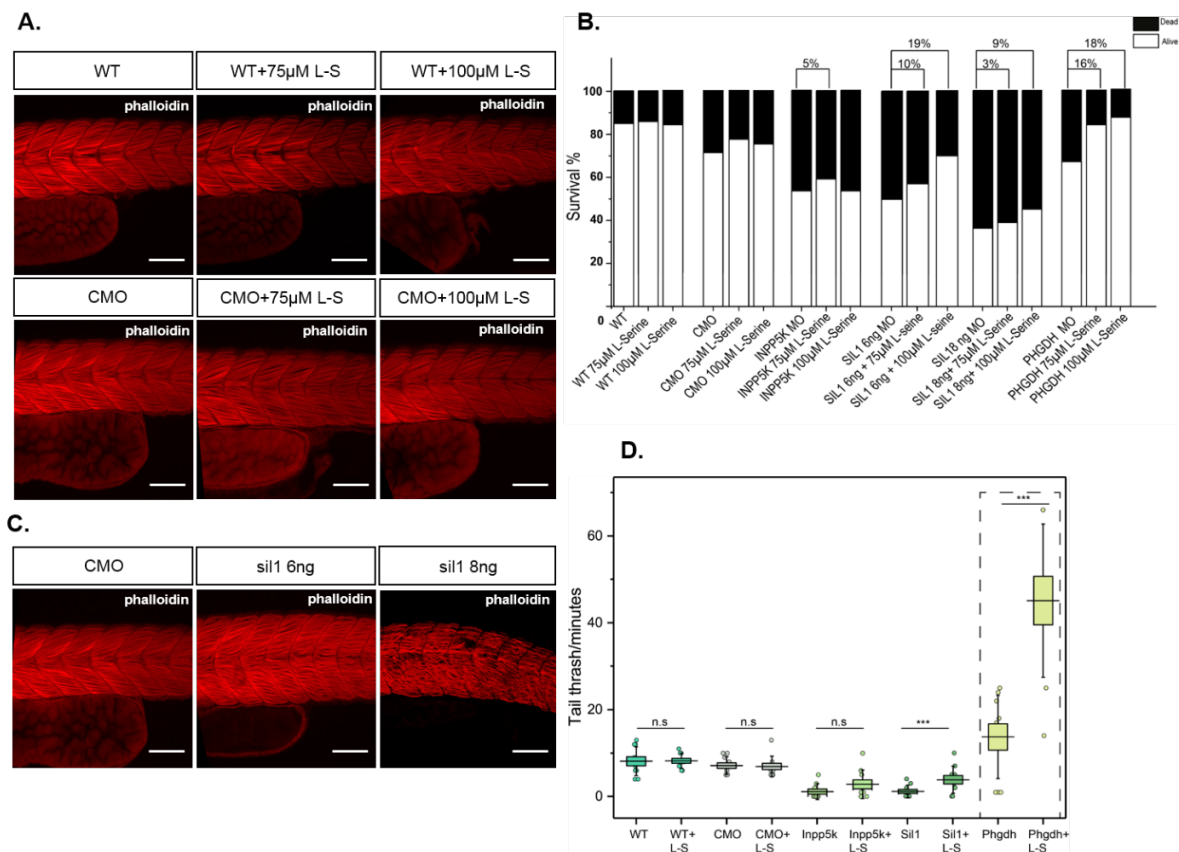


Figure 21. Overview of the findings obtained in the L-serine based rescue experiment. (A) Immunofluorescence staining of 48hpf non-injected and CMO-injected embryos, treated with different amounts (75 and 100 µM) of L-serine, in order to visualize the effect of this amino acid on the muscle fiber. The integrity of the fiber seems to be unaffected by the L-serine treatment. Scale bars: 50 µM. (B) Survival rates were assessed in the WT, CMO, *inpp5k*-MO, *sil1*-MO and *phgdh*-MO injected fish treated or not treated with L-serine at 48hpf. An

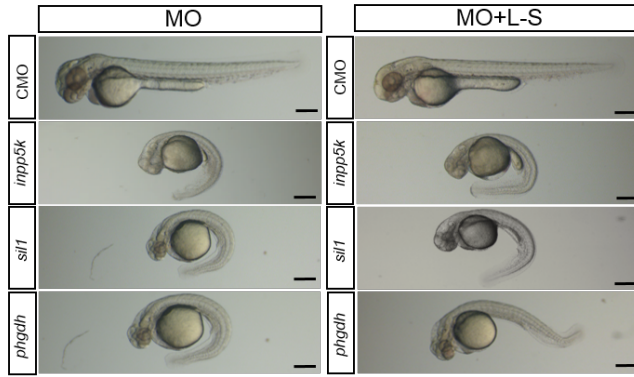
increase in survival rates can be observed in the *pill* and *phgdh* morphants. A minimum of 250 embryos were counted per condition. (C) Whole mount immunofluorescence analysis of the actin cytoskeleton (phalloidin staining) showing the detrimental effect of increasing the amount of *sil*-MO injected. Scale bars: 50 μ M. (D) Movements performed by zebrafish within the chorion at 24hpf in 2 minutes showing the changes upon L-serine treatment. Unpaired t-test was performed to determine the statistical significance: n.s. = not significant, *** = $t \leq 0.01$, ** = $t \leq 0.03$ and * = $t \leq 0.01$.

To verify potential beneficial effects upon L-serine treatment, morphological changes of the brain, NMJs and skeletal muscle were further investigated. Macroscopically, *inpp5k*-, *sill*- and *phgdh*-MO injected fish treated with L-serine for 48 hours presented no differences in comparison with the respective mock-treated fish models (Figure 22A). The morpholino injected embryos still present an abnormal shape following de-choriation, characterized by a shortened and curved tail. (Figure 22A). Histologically, the skeletal muscle phenotype does not seem to be ameliorated by the L-serine treatment as the chevron shape of the somites remains disrupted and fiber still have a wavy appearance (Figure 22B). The NMJ integrity was assessed via staining for the postsynaptic (AChR receptor) and the presynaptic (Synaptic vesicle protein 2) parts of the NMJs. In the WT and CMO, L-serine treated and non-treated zebrafish presented numerous synapses on motor branches within the myotome and motor axons extended along the lateral myosepta (Figure 22C). In contrast, the *sill*- and *phgdh*-MO injected embryos show a similar NMJ-phenotype with a reduction in motor axon extension along the myospeta and a dramatic decrease in the number of intramuscular synapses due a failure of motor axon branches to extend from the medial nerve into the lateral muscle (Figure 22C). Upon treatment of the disease models with L-serine, the motor axon growth seems to be slightly improving, together with synaptogenesis. This is also mirrored in the Pearson's coefficient which shows an increase in co-localization of the SV2 with the BT (Figure 22B and C). As expected upon treatment with L-serine *Inpp5k* zebrafish present no changes in NMJ morphology (Figure 22C).

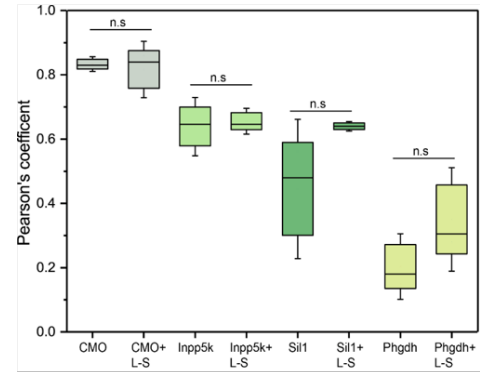
For tracking the development of motor neurons in the hindbrain upon L-serine treatment of the *inpp5k*, *sill* and *phgdh* morphants, transgenic fish expressing the Isl1-GFP in the cranial motor neurons were utilized. As shown in the previous chapter, the depletion of *sill* impinges on the brain: fish presented with no florescence in the III, IV, VI and VII nerves corresponding to the oculomotor, trochlear, abduces and facialis nerves. The phenotype seen in the *phgdh* morphants is more severe than the one in the *sill* morphants as the brain seems to be severely underdeveloped. In contrast, the brain of *inpp5k* morphants is similar to the one of the CMO with just a mild decrease in florescence in the area corresponding to the

oculomotor and trochlear nerve (III and IV) (Figure 22C). By supplementing the media with L-serine, brain improvements could be observed in all morphants, especially in the *Sil1* and *Phgdh* KD fish models (Figure 22C, nerves which showed an improvement are marked in red).

A.



B.



C.

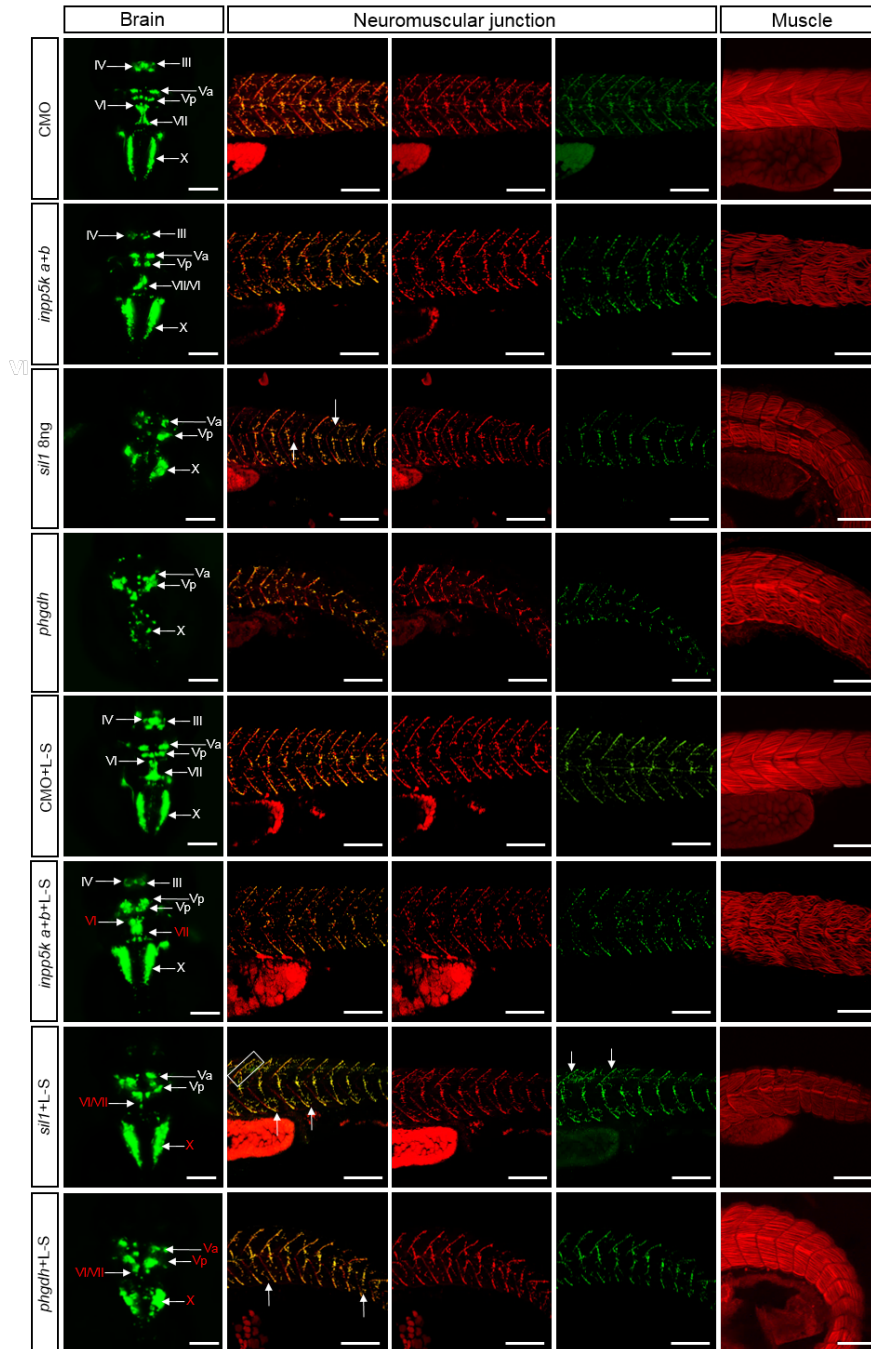


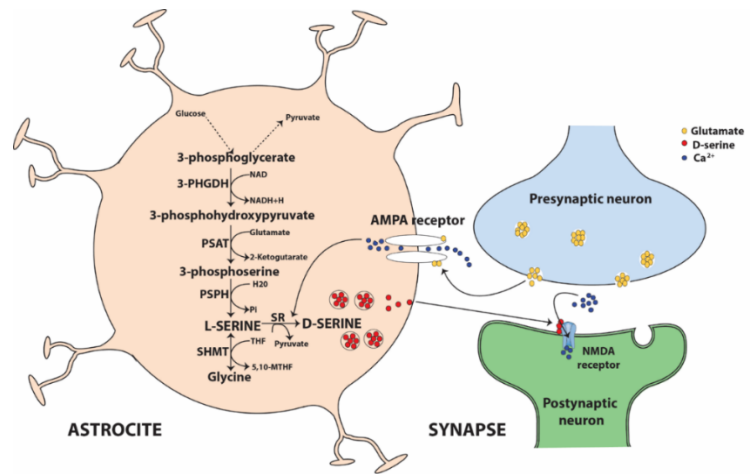
Figure 22. Effect of L-serine treatment on *inpp5k*, *sill*, and *phgdh*-MO injected. (A) Live embryo images of control MO and *inpp5k a+b-*, *sill-* as well as *phgdh*- MO injected zebrafish treated and non-treated with L-serine at 48 hpf showing a modified morphology and no clear macroscopical differences between the treated and the mock group. Scale bars: 500 μ M. (B) The colocalization coefficient between the AChR (BT) and SV2 was determined and plotted for the different fish models. For the evaluation, Pearson's coefficient was used where a number of 1 corresponds to a perfect colocalization. An unpaired t-test was performed to determine the statistical significance: n.s. = not significant. (C) Whole mount immunofluorescence studies of the morphants in order to track the changes occurring in muscle fiber integrity, NMJ and brain morphology upon L-serine treatment. For the assessment of the muscle fibers, antibodies against the actin cytoskeleton (phalloidin) were employed, showing no clear difference between the treated and untreated. For the NMJ visualization, the postsynaptic AChR (α -bungarotoxin, red staining) and presynaptic nerve endings (SV2 antibody, green staining) were stained, showing a clear vulnerability of NMJs but also a mild but statistically non-significant improvement upon the L-serine treatment. Scale bars: 50 μ M. For the brain visualisation live fluorescent imaging of the morphant and CMO injected zebrafish mid and hindbrain in *isl1:GFP* transgenic strain of zebrafish was used. Dorsal view of the midbrain and hindbrain of CMO embryos and morphants at 48hpf in the (Tg (*isl1:GFP*)) line in the treated and untreated groups of the respective disease models. Cranial nerves were represented with roman numbers: III-oculomotor, IV-trochlear, V_a-anterior nuclei of the trigeminal nerve, V_p-posterior nuclei of the trigeminal nerve, VI-abducens, VII-facialis and X-vagus. Scale bars: 100 μ m.

3.2.1.5 Proteome profiling allows a molecular linking of rare neuromuscular diseases and to define common treatment strategies

Similarities between MSS and INPP5K-CMD go beyond the clinical phenotype which involves the so-called “clinical triad” consisting of skeletal muscle, eye and brain abnormalities. Previous studies have also highlighted a molecular link between the two disorders as SIL1 and INPP5K interact with BiP, a major chaperone of the ER. MSS is a disease of the ER as the loss of functional SIL1 impacts BiP, leading to a massive build-up of protein aggregates in the vulnerable tissues²⁰⁹. On the other hand, INPP5K missense-mutants seem to still bind to BiP without triggering a massive cellular stress response as no toxic aggregates containing BiP were present in the cells⁵⁵. This might suggest that INPP5K is not an essential binding partner of BiP or that possible compensatory mechanisms are able to manage the BiP related processes in the presence of mutant forms of INPP5K.

To gain further insights into the molecular connection between the two diseases, INPP5K fibroblasts derived from 3 patients harbouring the p.I50T missense-mutation were analyzed via unbiased proteomic profiling and compared with the proteomic signature of control fibroblasts. The obtained data revealed that multiple biological processes including cell adhesion, death and proliferation as well as metabolic processes, are affected in patient-

derived fibroblasts (Figure 14). Additionally, this data set was intersected with the already published proteome of MSS lymphoblastoid cells¹⁹⁵ and with unpublished data obtained from MSS-patient derived fibroblasts, allowing the identification of PHGDH as a common denominator that is up regulated in the INPP5K fibroblasts/muscle and down regulated in the MSS samples. PHGDH is an enzyme that catalyzes the first step of L-serine synthesis via the oxidation of 3-phosphoglycerate to 3-phosphohydroxypyruvate, a product resulting from glycolysis (Figure 23). Proper serine homeostasis was demonstrated to be crucial for the survival,



development and maintenance of the central nervous system²⁰³. So far two potential mechanisms by which PHGDH deficiency is disturbing CNS integrity and function have been postulated. The first one implies that cell cycle progression presents significant disturbances, as seen in the *Phgdh* KO mouse model, thus perturbing neurogenesis which is tightly connected with cell cycle regulation^{201,210}. The second postulated mechanism involves D-serine, a molecule obtained from L-serine via racemization (Figure 23) and glycine obtained by serine-hydroxymethyltransferases¹⁹⁹. These two amino acids are crucial for the neuronal migration to their mature positions and for the activation of the N-methyl-D-aspartate (NMDA) receptor^{199,203}. Additionally, L-serine together with glycine were shown to be an astroglia-derived trophic factor for Purkinje neurons, a population highly affected by the loss of *SIL1*^{211,212}. Mutations in *PHGDH* were linked to L-serine deficiency and patients present with serious neurological symptoms, including congenital microcephaly, slight cerebellar ataxia, psychomotor retardation, white matter lesions and cataracts, features found also in MSS^{192,203,213}. In contrast, individuals with bi-allelic *INPP5K* mutations present a normal

cerebellum and only mild intellectual disability⁵⁵ probably due to the presence of compensatory mechanisms driven by the overexpression of PHGDH.

Although, no proper muscle phenotype has been explicitly described in PHGDH deficient humans or mice, genes involved in muscle development were found to be down regulated in the PHGDH knockdown mouse model²⁰¹. This observation accords with the above described *Phgdh*-zebrafish phenotype which actually presents a vulnerability of the skeletal muscle (Figure 19) and a phenotype similar to the one observed in the *Sill* morphants (Figure 18 and 17) thus suggesting that the muscle is actually vulnerable to the reduction of levels of this enzyme. Moreover, PHGDH was found to be increased upon the treatment with the β -adrenergic agonist Ractopamine thus linking the genes associated with the serine synthesis pathways with the coordination of lean muscle growth²¹⁴. Hence, in this context the increase of PHGDH also identified in the skeletal muscles of the INPP5K patients, most likely represents a cellular attempt to compensate muscle degradation.

Prompted by the hypothesis that PHGDH-increase in INPP5K-patients might contribute to the milder brain phenotype and by the fact that L-serine was successfully applied in humans to ameliorate the PHGDH phenotype²¹⁵, experiments were designed in order to examine if the compensation with L-serine can also improve the phenotype of MSS patients. To address this assumption, the well characterized zebrafish models of *Inpp5k*⁵⁵ and *Sill*¹⁵¹ deficiency (Figure 17 and 18) were treated with L-serine. The *Phgdh* depleted zebrafish were included in this study as a proof-of-principle. Upon the treatment with L-serine, the *Sill* morphants showed an improvement in the vagus (X), facialis (VII) and abducens (VI) cranial nerves (Figure 22). The *Phgdh* morphants displayed a more severe phenotype than the *Sill*-depleted fish, with regions of the brain completely absent. Remarkably, treatment with L-serine partially rescued the brain phenotype as improvements in the vagus (X), facialis (VII), abducens (VI) and anterior/posterior nuclei of the trigeminal nerve (V_a and V_b) (Figure 22C) were observed. *Inpp5k*-depletion in fish led to a very mild brain phenotype and upon treatment with L-serine cranial nerves III, VI, VII (oculomotor, abducens and facialis) are morphologically improving (Figure-22-C). In addition, the NMJ phenotype of both fish models showed a slight improvement in the presynaptic NMJ structures, confirmed by an increase in the motor axon extension along the lateral myosepta (Figure 22C). Additionally, the *sill* morphants showed a slight improvement in motor axon branching (Figure 22C). On a general note, the mechanism by which L-serine acts as a neuroprotective molecule is still elusive and further research is needed to fully understand this process on the precise

molecular level. One of the current theories suggests is that this small molecule may function as an ER-proteostasis regulator thus making the cell alert to a possible neurotoxic insult via the reprogramming of the UPR to favour the removal of protein aggregates and accumulating proteins²¹⁶. Unfortunately, no improvement in the muscle phenotype was observed upon L-serine treatment, most likely because the mechanism by which PHGDH is involved in muscle homeostasis is tightly connected to other signalling cascades which need to be simultaneously activated.

The proteomic profiling of INPP5K patient-derived fibroblasts revealed that CDK9, a regulator of the transcriptional elongation, phosphorylating the carboxyl-terminal domain (CTD) of the large subunit of the RNA polymerase II, is decreased¹⁹⁶. This finding obtained in fibroblasts was consistent with the immunofluorescence-findings obtained in the skeletal muscle of INPP5K-patients showing a decrease of the protein at the sarcolemma and in myonuclei. CDK9 was recently described also to be crucial for muscle cell differentiation as it acts as a coactivator of MyoD²¹⁷. Notably, CTFP1 (RNA polymerase subunit A-C terminal domain phosphatase), the protein affected in CCFDN, dephosphorylates serine motifs in the carboxyl-terminal domain of the large RNA polymerase subunit II, enhancing its activity¹⁹⁴. Hence, perturbations in phosphorylation of the large RNA polymerase II subunit might be a signature process in INPP5K-CMD and CCFDN. Moreover, both disorders share muscle, brain and eye vulnerabilities presenting as a “clinical triad”. Although CCFDN is a clinical differential diagnosis for MSS²¹⁸ due to the striking phenotypical similarities, CDK9 was not identified in the MSS lymphoblasts or wozy muscle. Thus, no further conclusions regarding the molecular interconnection of these 2 diseases can be drawn.

In conclusion, this study allowed the molecular linkage of three rare neuromuscular disorders, beyond the clinical phenotype. PHGDH was identified as a protein altered in abundance in both INPP5K and MSS patients; however, with opposing regulation in the two diseases. A therapeutic potential of this new acquired knowledge was further pursuit and demonstrated via the utilization of zebrafish models. This approach suggested that a simple yet crucial component for the CNS in the form of L-serine might alleviate the brain and neuromuscular phenotype of the MSS patients and might also explain the rather milder affection of the CNS and the NMJs in the INPP5K-disease model. Additionally, impairments in phosphorylation of the RNA polymerase subunit II might link INPP5K-CMD and CCFDN. Unfortunately, no tissue or cells from patients suffering from CCFDN were

available for this study, thus some questions still remain open regarding the molecular puzzle of these three diseases.

3.2.2 Mutational spectrum and pathophysiology of Caveolinopathies

Caveolins are integral membrane proteins and represent the major coat proteins of caveolae which are flask-shaped plasma membrane invaginations found in numerous cell types such as fibroblasts, adipocytes, epithelial cells and smooth/ striated muscle^{219,220}. Typically, these caveolae are lipid rafts enriched in cholesterol, sphingolipids and glycosyl phosphatidylinositol-anchored proteins²²¹. So far, three types of caveolin proteins have been described from which caveolin-3 (CAV3) is expressed predominantly in skeletal and cardiac muscle^{222,223}. However, there is also evidence for CAV3 expression in Schwann cells and a patient suffering from a limb girdle muscular dystrophy complicated by signs of perturbed myelination has been described²²⁴. CAV3 is 151 amino acid sized protein and divided separate domains: the N-terminal-, the scaffolding, the transmembrane and the C-terminal domain²²⁵ (Figure 24). The scaffolding segment is responsible for the homo-oligomerization of CAV3 which starts in the endoplasmic reticulum where in a first step detergent-resistant caveolar complexes are formed. These complexes are transported to the Golgi and exit bearing different lipids. Then, these molecules fuse with the plasma membrane or sarcolemma forming a hair pin loop²²⁶. In mature myofibers, CAV3 is present through the T tubule system where it clusters at the necks of the tubule thus facilitating the transmission of the contractile impulse²²⁷. Within the plasma membrane, CAV3 associates with the dystrophin-glycoprotein complex (DGC) providing a link between the cytoskeleton and the extracellular matrix thus stabilizing the sarcolemma²²². CAV3 was shown to have many other different functions in the maintenance of the muscle fiber homeostasis by regulating signal transduction, lipid metabolisms, insulin signalling and vesicle trafficking²²⁸⁻²³².

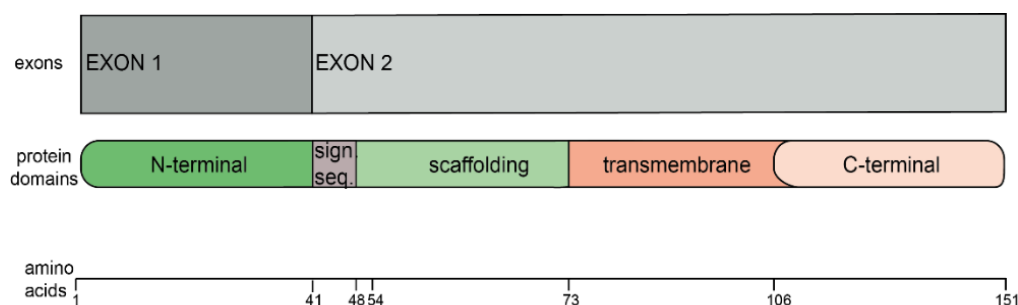


Figure 24. Gene structure of *CAV3* and Caveolin 3 protein domains.

Muscle disorders caused by mutations in the *CAV3* gene are called Caveolinopathies and so far, more than 40 pathogenic *CAV3* mutations have been described. Caveolinopathies are usually

transmitted with an autosomal dominant inheritance and only 6 autosomal recessive *CAV3* mutations have been described so far^{232,233}. Mutations in the *CAV3* gene can lead to a deficiency of the CAV3 protein and can result in four distinct, sometimes overlapping phenotypes: limb girdle muscular dystrophy (LGMD), rippling muscle disease (RMD), distal myopathy (DM) and hyperCKemia (HCK)²³².

LGMD-1C describes a childhood or adult onset MD characterized by muscle weakness and wasting affecting mostly the limb and proximal musculature. Muscle biopsy specimens usually show variable fiber size, degenerating/regenerating muscle fibers, centralized myonuclei and a very mild substitution of muscle with connective tissue associated with reduced levels of CAV3. Several mutations affecting either the N-terminal (p.N33K, p.V43E), scaffolding (p.T63P, p.G56S, p.C72W, p.W58R), or the membrane spanning domain (p.A93T, p.P104L, p.T78M, p.T78K) have been described^{232,234,235}. RMD is a muscle disorder with a variable age of onset characterized by increased muscle irritability. Muscle biopsy presents with an increase in muscle fiber size variability, mild type I fiber predominance and internalized nuclei. Patients present with the following symptoms: increased fatigability, tiptoe walking, myalgia and muscle stiffness. Several *CAV3* mutations associated with RMD, affecting the N-terminal (p.R27Q, p.P28L, p.E46K) scaffolding (p.S52G, p.W70X,) or the membrane spanning domain (p.L85P, p.F103_F104del) have been described in the literature²³⁶. Patients with a distal myopathy phenotype experience muscle wasting and weakness, mostly in the small muscles of hands and feet but hypertrophy of the calf muscles can also occur. Muscle biopsy specimen present with a mild variation in fiber size and centralized nuclei with a severe decrease in CAV3 expression²³⁷. Some *CAV3* mutations have been identified in patients affected by hyperCKnemia. Usually, they present plasma levels of CK four to ten times higher than normal and histological muscle analysis typically reveals no abnormalities. A transgenic animal model which expresses an additional copy of the *CAV3* harboring the p.P104L mutation was described by Sunada and colleagues⁴¹. Transgenic mice show poor growth and were significantly smaller than their littermates. They also present with kyphosis and spine paralysis of the hind limbs as well as severe progressive muscle wasting. The hematoxylin and eosin (H&E) staining of the muscles shows clear myopathic features such as fibers with a variable size, centralized nuclei and replacement of muscle with connective tissue. The phenotype of the transgenic mice is considered to be a good phenocopy of the human disorder^{139,238}. Previously published *in vitro* studies have shown that homo-oligomers of the WT protein are translocated via the ER-Golgi network to the plasma membrane whereas the p.P104L does not target the plasma membrane

and displays a mis-localization to the Golgi apparatus²³⁹. Although, in this transgenic mouse model there is a co-expression of both mutant and WT protein (mimicking the dominant condition of the disease), CAV3 levels are

lower in the transgenic animals compared to WT littermates (Figure 25A). This deficiency of CAV3 results from the fact that the mutant protein displays a dominant negative effect on the WT protein as the homo-oligomers formed by the p.P104L-mutant and the WT CAV3 are less stable and degraded via the proteasome. In addition, prior to degradation, these aggregates are retained within the Golgi and thus most likely also influence proper functions of this subcellular compartment playing a major role in protein processing^{138,139} (Figure 25B). Under physiological conditions, the WT CAV3 protein forms oligomers of 400 kDa soon

after it is synthesized in the ER and afterwards targeted for transportation to the sarcolemma. However, the p.P104L oligomers retained in the Golgi cause ER stress which leads to the activation of the UPR¹³⁸. This pathological process has been already described by Kuga and colleagues¹³⁸. Their study showed that the UPR is activated by this toxic aggregates. Notoriously, the UPR-activation leads to prolonged ER/Golgi stress which may result in the build-up of protein aggregates.

Interestingly, CAV3 was found to be enriched at the NMJ where it is associated with the AChR and directly interacts with the MuSK receptor upon agrin stimulation²³⁰. Additionally, in mice lacking CAV3, the postsynaptic part of the NMJ is severely affected²³⁰. The exact underlying mechanisms by which CAV3 regulates NMJ-integrity are still elusive but it is thought that besides concentrating the AChR receptor at the NMJs due to its scaffolding properties, CAV3 is also activating MuSK in a Rac1 depended manner²³⁰. In addition, it is suggested that the activation of MuSK via self-phosphorylation is decreased in myotubes lacking CAV3^{230,240}.

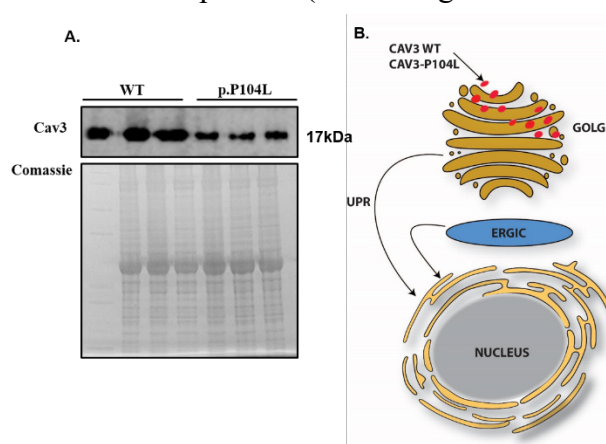


Figure 25. CAV3 abundance in wildtype and p.P104L CAV3 mutant animals. (A) Immunoblot studies of quadriceps muscles derived from 10 weeks old animals reveal a decrease in the amount of the CAV3 protein in the mutant animals; Coomassie staining was used as a loading control. (B)-Under physiological conditions CAV3 is transported via de ER-Golgi network to the plasma membrane while in the transgenic mouse model the oligomers formed by the mutant and the wildtype protein are retained within the Golgi.

Moreover, in patients suffering from Myasthenia Gravis, CAV3 was found to have a patchy distribution in skeletal muscle along with altered expression levels²⁴¹.

3.2.2.1 Proteomic signature of the CAV3 p.P104L mutant muscle

To gain molecular insights into the changes that occur upon the expression of the p.P104L mutant form of the CAV3 protein, liquid chromatography coupled with mass spectrometry was employed. For this experiment, quadriceps muscles from three transgenic animals were compared with respective muscles from three WT littermates at the age of 10 weeks (muscles were from the right leg of male animals). A number of 120 proteins with an altered abundance was identified from which 77 were increased and 43 were decreased (with a log₂ ratio of 0.3>for up regulated and >-0.26 for down regulated) (Figure 26A). All quantified proteins had a minimum of two unique peptides and a FDR of 1%. Pathway analysis revealed that several important cellular processes were altered in the skeletal muscle of transgenic mice compared with the control animals (Figure26B). Interestingly, the proteomic data revealed that proteins belonging to the UPR are also affected thus confirming the previous results published by Kuga and co-workers¹³⁸.

It is known that CAV3 plays a major role in the modulation of the energy metabolism by regulating the expression of the insulin receptor at the sarcolemma (translocation of GLUT4 from the cytoplasm to the plasma membrane), as well as by translocating phosphofructokinase, an enzyme involved in glycolysis²⁴². Additionally, caveolae facilitate the uptake of free fatty acids²⁴³. Pathways involving glycogen breakdown, sugar and lipid metabolism as well as insulin signalling cascades seem to be affected in the muscle of p.P104L transgenic mice. The obtained proteomics results moreover suggest that processes controlling the organization of the cytoskeleton, muscle contraction and extracellular matrix organization are also hindered (Figure 26B).

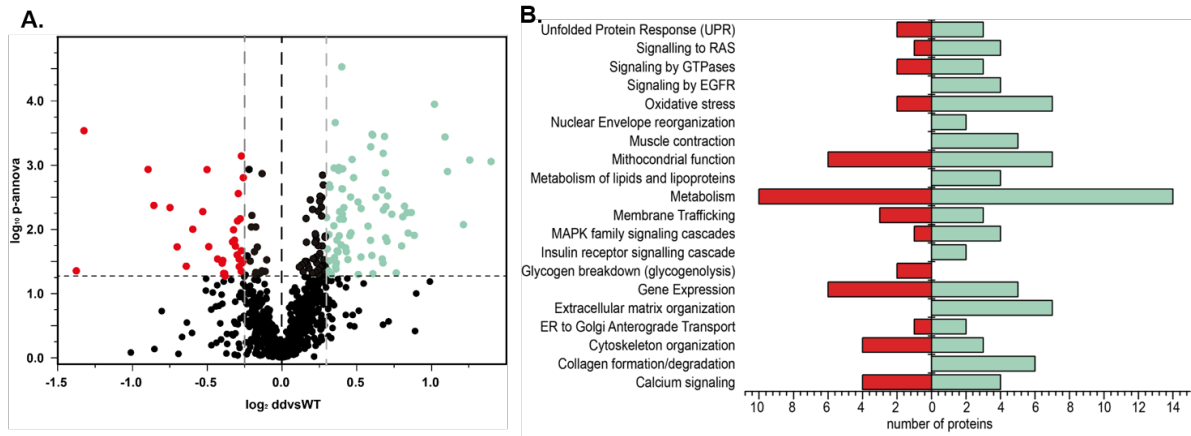


Figure 26. *In silico* analyses of proteomic findings obtained in the Caveolinopathy mouse model. (A) The volcano plot presents all proteins quantified in the analysed muscles, making a clear delimitation between the proteins with a p-Anona of <0.05 (giving statistically significant results; horizontal line). Proteins which are decreased are represented in red while the up regulated ones are in green. (B) Pathway analysis of all proteins altered in abundance towards the identification of cellular process perturbed upon expression of p.P104L mutant CAV3 in skeletal muscle.

Subcellular localization of proteins which were altered in abundance is presented in Figure 27. Affected proteins localize to the Golgi-ER network including proteins belonging to the secretory pathway. In line with the subcellular localization of CAV3 at the DGC, structural proteins belonging to the cytoskeleton and ECM organization seem to be perturbed in the skeletal muscle of p.P104L transgenic mice (Figure 27).

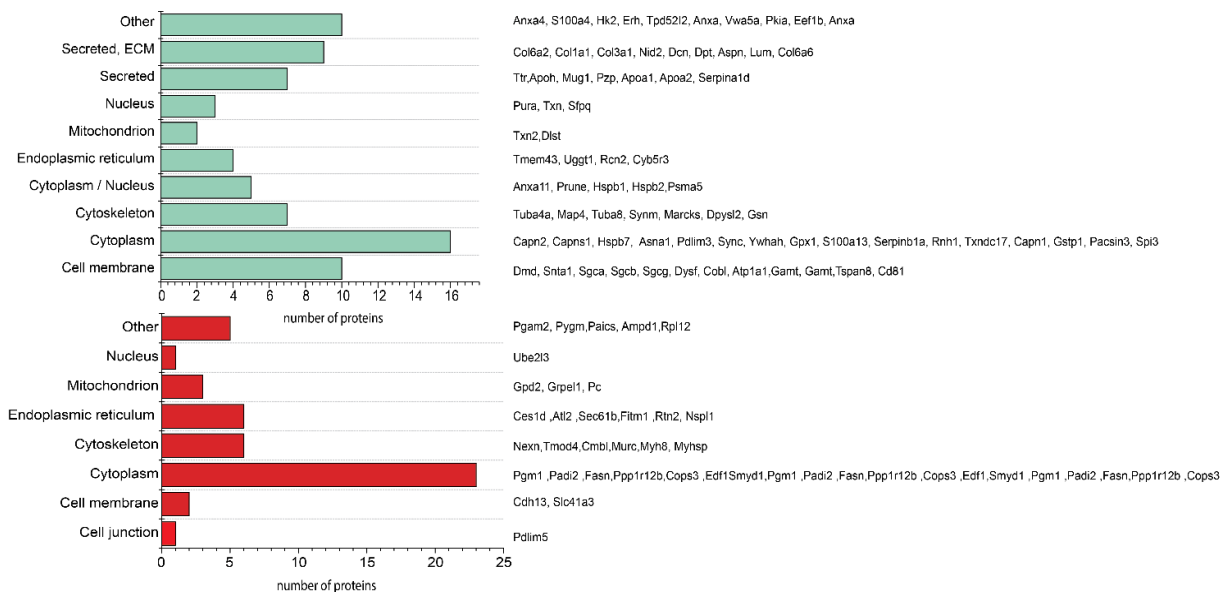


Figure 27. Subcellular localization of (A) up regulated and (B) down regulated proteins in p.P104L_CAV3 diseased quadriceps muscle.

Using Cytoskape along with the ClueGO and CluePedia app, a functional grouped network with pathways and genes belonging to the proteins altered in abundance was created. In this network, the node colour reflects a functional group (GO ontology) and cluster distribution. CluePedia automatically calculated the linear and non-linear statistical dependencies from the experimental data as well as the significance of the terms and groups. The strings describe the relationship between the altered proteins resulting from the proteomic experiment¹³⁶ (Figure 28).

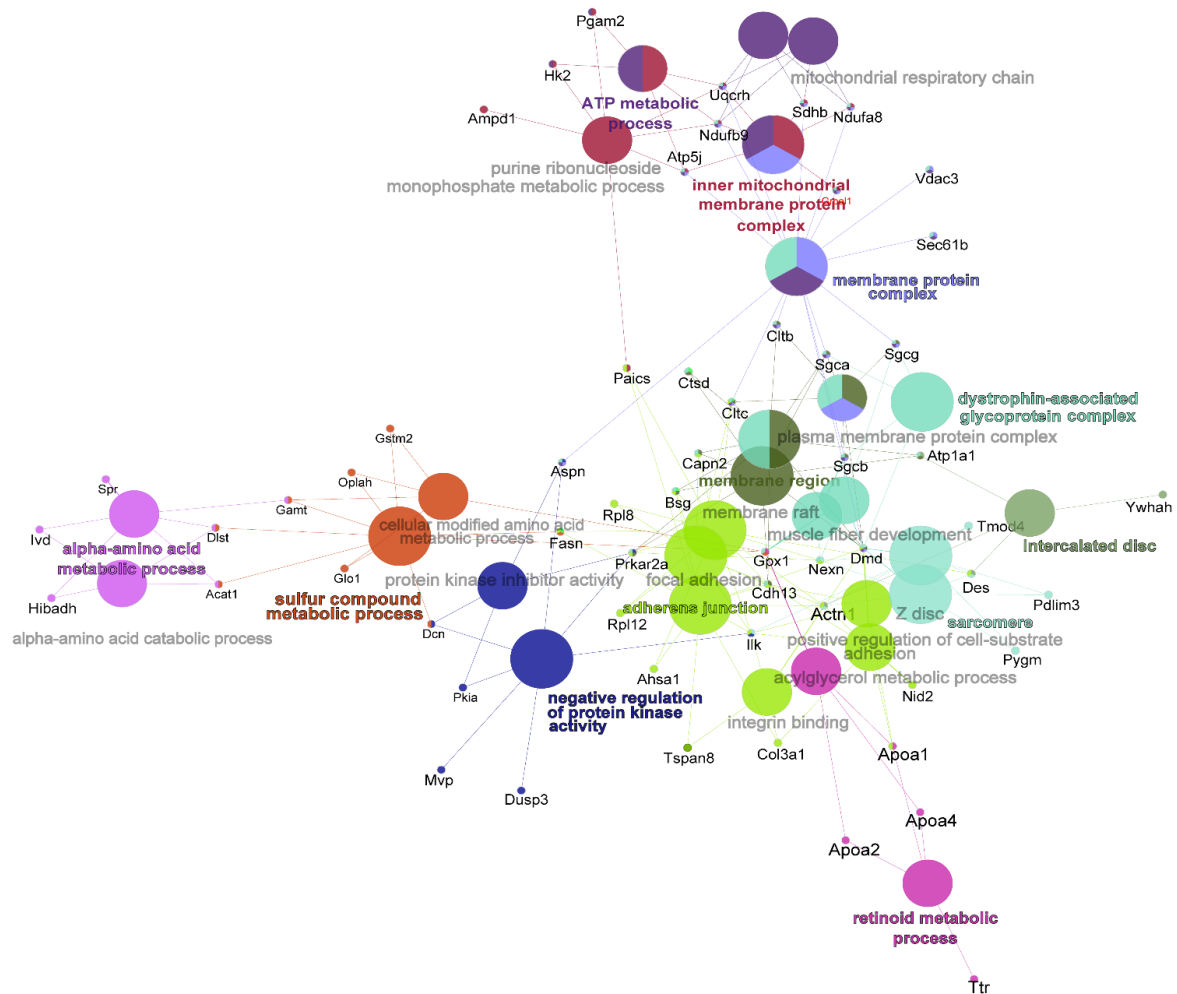


Figure 28. Cytoskape network analysis of the regulated proteins and *in silico* data from different perspectives: gene interrelations revealed by correlation weights, protein interactions as well as functional context given by the GO enrichment analysis. The nodes are linked based on their kappa score level (≥ 0.3), where only the label of the most significant term per group is shown. The node size represents the term enrichment significance. Functionally related groups partially overlap.

Remarkably, components belonging to the dystrophin-associated glycoprotein complex (DGC) are increased in the quadriceps muscle of p.P104L transgenic mice and, due to the mislocalization of CAV3 to the Golgi, the integrity of the DGC is presumably compromised. Paradigmatic proteomic findings were also confirmed by immunoblot analysis, validating the findings and showing an increase in further components of the DGC (Figure 29). These immunoblot experiments were performed at the Institute of Neuropathology University Hospital RWTH-Aachen (Dr. José Andrés González Coraspe).

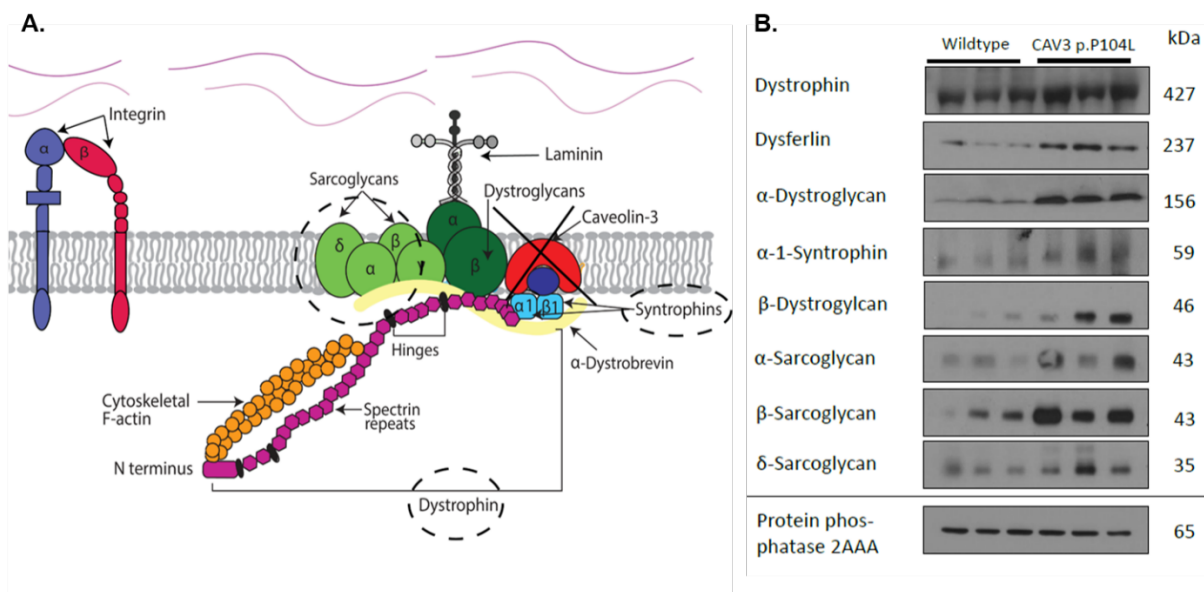


Figure 29. DGC components are perturbed by the mislocalization of CAV3 to the Golgi. (A) Immunoblot analysis of the DGC showing an increase in dystrophin, dysferlin, α and β dystroglycan, α -1-syntrophin, as well as the sarcoglycans. (B) Representation of the DGC. CAV3 is localized at the plasma membrane where it is directly interacting with β -dystroglycan and NOS. Additionally, CAV3 interacts indirectly with other components of the DGC such as syntrophin and dystrobrevin. Proteins circled with a dotted line were increased in the proteomic analysis.

3.2.2.1.1 Discussion

Previous experiments revealed that WT CAV3 forms oligomers of about 400 kDa soon after the protein is synthesized in the ER and then these oligomers are targeted for the plasma membrane/sarcolemma¹³⁸. The p.P10L mutant proteins form aggregates which are over 400 kDa in size and are retained in the Golgi¹³⁸. This accumulation within the Golgi leads to the activation of UPR as a cellular attempt to restore cellular homeostasis²⁴⁴. The precise molecular consequences of the disturbed ER-Golgi system is still elusive and were not properly understood in Caveolinopathies. To gain a better understanding of the molecular events taking place in

Caveolinopathies, quadriceps muscle derived from the CAV3 p.P104L transgenic mouse model, (a well-established model for this Caveolinopathies) was investigated^{139,238}. Morphological investigations of the ER-Golgi system, described by González Coraspe and colleagues are consistent with prolonged ER stress which leads to perturbations of the ER-Golgi machinery²⁴⁵. Results of the proteomic analysis also support this pathomorphological finding as altered abundances of proteins involved in the maintenance of the organelle structure were found (EF1B, ASNA1, RCN2, UGGT1 and TMEM43). Along this line, González Coraspe and colleagues identified that these animals present a build-up of vacuoles and an increase in abundance of ubiquitinated proteins²⁴⁵. The proteome profiling backs up this data as proteins that inhibit the proteasome (ANT3, ILEUA, SPB6, MUG1 and A1AT4) were shown to be altered in abundance. The accumulation of misfolded proteins also leads to an increase in expression of some heat shock proteins (HSP70, HSPB2, and HSPB2) which are responsible for the refolding and degradation of stress damaged proteins²⁴⁶, a molecular finding which accords with the presence of ER-stress and the build-up of protein aggregates. CAPN, a caspase involved in the breakdown of misshaped proteins²⁴⁷, was also increased in the muscles of p.P104L animals further supporting the concept of perturbed proteostasis as a pathomechanism in p.P104L Caveolinopathy.

Within the sarcolemma CAV3 is part of the DGC, stabilizing the plasma membrane and linking the cytoskeleton to the ECM. Thus, changes in CAV3 expression leads to the disruption of the DGC which hinders the sarcolemma²²². Interestingly, in the proteome profiling components of the DGC such as DYSF, DMD, SGCG and SGCB were found to be up-regulated, most likely as a cellular attempt to antagonize the loss of CAV3 and sarcolemma disruption. Moreover, DGC proteins are known substrates processed within the ER-Golgi compartments, thus alterations of this complex can lead to protein accumulation which are retained in the ER, recognized by the quality control, re-transported into the cytoplasm to be degraded by the ubiquitin-proteasome system²⁴⁸. This, in turn, would lead to a vulnerability of the sarcolemma, further supported by the proteomic data, which show that proteins involved in cell adhesion (costameres) and motility (CAD13, SLC41A3 and PTRF) were down-regulated^{249,250}. Moreover, the data suggest that diverse mechanisms antagonizing sarcolemmal vulnerability are activated. This is shown by an increase in abundance of DERM (regulating cell-cell adhesion) and ATP1A1 (controlling the exchange of sodium and potassium ions, a process affected in Duchenne)^{251,252}. DGC also spans the muscle-cell membrane and links the actin cytoskeleton to the surrounding basement membrane. Thus, altered abundance of ECM and cytoskeleton

proteins is in accordance with the pathophysiological effects of Caveolinopathies²³². Proteins involved in the remodelling and binding of the actin filaments (NEXN, MYH8 and MURC) were decreased thus suggesting an alteration of the cytoskeleton. In contrast, an increase in proteins like COBL, HSPB7, TUB4A, TUBA8, MAP4 and PDLIM, which are involved in actin cytoskeleton and homeostasis, gross muscle mass formation and myogenesis suggests activation of antagonizing mechanisms to avoid muscle fiber break-down²⁵³⁻²⁵⁵. Secreted proteins belonging to the ECM, in particular collagens, were found to be elevated, most likely due to an increase in fibrosis /ECM accumulation, which is a pathophysiological hallmark of intermediate to late stages of muscular dystrophies²⁵⁶.

Additionally, annexin proteins (ANXA4, ANXA7, ANXA11 and ANXA5) were altered in abundance in the quadriceps muscle of the transgenic mouse model. These proteins are not only dysferlin-interacting factors but they also modulate the migration of satellite cells thus controlling cell differentiation and membrane fusion²⁵⁷. Given that ANXA5, a modulator of inflammatory processes and membrane repair in muscle cells, also shows an increase, an attempt of regeneration of the diseased muscle fibers can be speculated²⁵⁸. This hypothesis is further supported by increased levels of CD81, protein required in normal muscle regeneration by tightly controlling cell fusion²⁵⁹.

The p.P104L CAV3 mutant also affects pathways involved in the glucose/glycogen processing, insulin receptor cascade as well as lipid metabolism. CAV3 regulates the insulin expression and is required for the membrane targeting of PFK (enzyme involved in glycolysis)^{232,260}. An up-regulation of PANC3 impairs the internalization of proteins like GLUT1 and TRPV4 increasing the sarcolemmal levels, while an increase in YWHAH can affect the translocation of GLUT4 to the plasma membrane²⁶¹. Other proteins altered in abundance that suggest disordered glucose metabolism are PGM1, HK2 and RTN2. Finally, CAV3 facilitates free fatty cellular uptake. The proteomic findings support the role of CAV3 in lipid homeostasis by increased levels of FITM1 and CES1D. Other pathways affected are related to impaired energy production via mitochondrial alteration and oxidative stress protection (GSTP1, TXN2, GPX1 and TX).

In conclusion, the LC-MS/MS analysis of muscle derived from the transgenic p.P104L mouse model confirmed the previously reported ER-Golgi pathology and add further knowledge to this topic. Interestingly, this study could show that components of the DGC are actually up-regulated upon CAV3 loss and are also substrates of the ER-Golgi machinery secondarily affecting the ECM and cytoskeleton. Hence, our findings add p.P104L-related Caveolinopathy to the growing

list of secondary Chaperonopathies, an important aspect with potential relevance for the development of new therapeutic concepts for Caveolinopathies as UPR can be addressed with molecular chaperones and other drugs promoting ER-protein folding capacity and/or protein clearance. However, further pre-clinical therapeutic intervention studies utilizing the investigated mouse model would be needed to confirm this assumption.

3.2.2.2 *CAV3* missense-mutants: pathogenicity-testing via immunoblot and immunofluorescence studies

A new *CAV3* mutation was found segregating in a three-generation family with multiple members affected. This mutation is a point mutation (c.218A>G) affecting the highly conserved amino acid tyrosine at position 73 (p.Tyr73Cys) and displays an autosomal dominant inheritance. Family members presented with a variable phenotype: muscle hypertrophy, a history of rippling, exercise intolerance, toe gait and mild increase in CK. Muscle MRI revealed hypertrophy with the involvement of the gastrocnemius particularly the medial aspect and a mild involvement of the hamstrings. One patient (hereafter called the index patient) was diagnosed in his second year of life with a history of neonatal hypotonia, gross motor delay, exercise intolerance and eight times higher levels of CK. Immunohistochemistry studies showed an absence of *CAV3* from the sarcolemma. Molecular genetic testing of the *CAV3* gene revealed the presence of a second *CAV3* mutation in this patient on the c.100G>A (p.Glu34Lys) which was inherited from his unaffected parent. To assess the pathogenicity of these mutants located in different functional domains, we made use of myoblastic RCMH cells transiently transfected with expression constructs for different mutant forms of *CAV3* including those segregating in the family. Hereby, two important parameters were examined: (i) subcellular localization of the mutant forms of *CAV3* protein in comparison with the wildtype protein (utilization of a Golgi and ER makers as well as focusing on-actin cytoskeleton integrity) and (ii) comparative study of the molecular behaviour utilizing the immunoblot-technique. The amino acid exchanges included in the subcellular localization and immunoblot studies target all the domains of the *CAV3* protein: scaffolding region (p.G56S, p.W58R, p.C72W, p.Y73C), transmembrane domain (p.T78M, p.T78C and p.A93T, p.P104L) and N-terminal domain (p.E34K) -Figure 30.

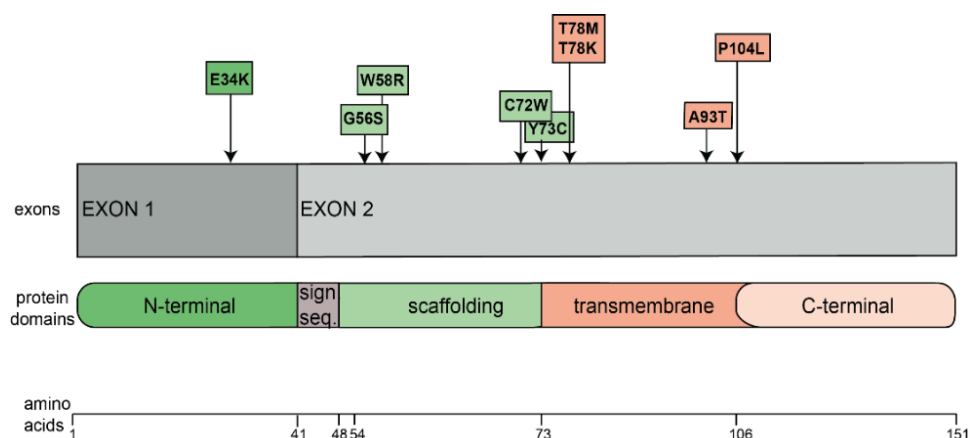


Figure 30. Caveolin-3 protein domains and the localization of the mutations investigated within the different protein domains.

To compare the expression of the CAV3 wildtype proteins to the mutant forms of CAV3, RCMH cells were transiently transfected, using same plasmid concentrations, with the constructs harbouring different missense mutations. As indicated in Figure 31, immunoblot analysis of these cells revealed a higher abundance of p.W58R, p.T78K, p.T78M, p.G56S and p.C72W CAV3 compared to the WT protein. The CAV3 protein carrying the p.E34K mutation showed a downward shift in terms of its electrophoretic mobility. In the case of p.P104L and p.Y73C the expression of the protein seems less abundant probably due to the fast degradation while the p.A93T mutation seems to induce a cleavage of the protein.

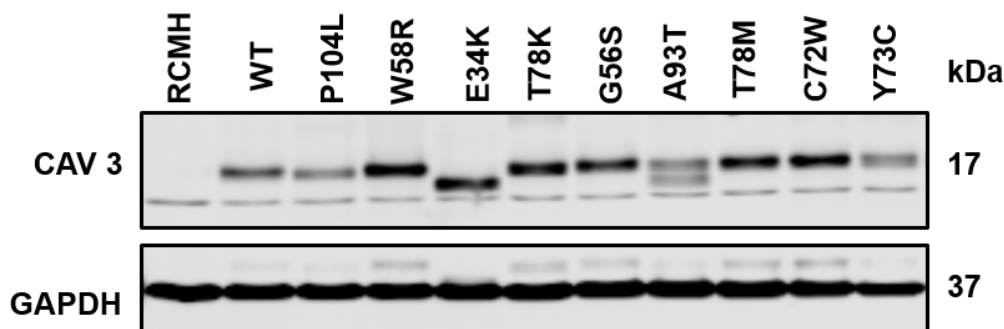


Figure 31. Expression of WT CAV3 and CAV3 missense mutants in RCMH cells which were transiently transfected with constructs encoding either the WT CAV3 or constructs carrying different mutations point mutations. GAPDH was used as a loading control.

To examine the subcellular localization of the different CAV3 mutants when compared with the WT, RCMH cells transiently transfected with the respective constructs were stained against CAV3 and GOLGA1, a marker of the Golgi compartment (Figure 32). The immunofluorescence-based analysis revealed the presumed localization of the WT CAV3 protein at the plasma membrane while p.W58R, p.C72W, p.T78K, p.A93T and p.P104L, completely associated with the Golgi. Notably the p.G56S CAV3 which is a modifier for the manifestation of a muscle disease rather than a Caveolinopathy causing mutation²⁴⁴ presents immunoreactivity just in the plasma membrane while, p.T78M (one of the rare recessive variants)²³⁵ present immunoreactivity both in the plasma membrane and in the Golgi, confirming previous results^{235,244}. The p.Y73C CAV3 mutant form presents a co-staining with the Golgi but also with the plasma membrane where the mutant protein seems to accumulate in (irregular) clusters, while p.E34K co-localizes like the other above mentioned mutants with the Golgi (Figure 32).

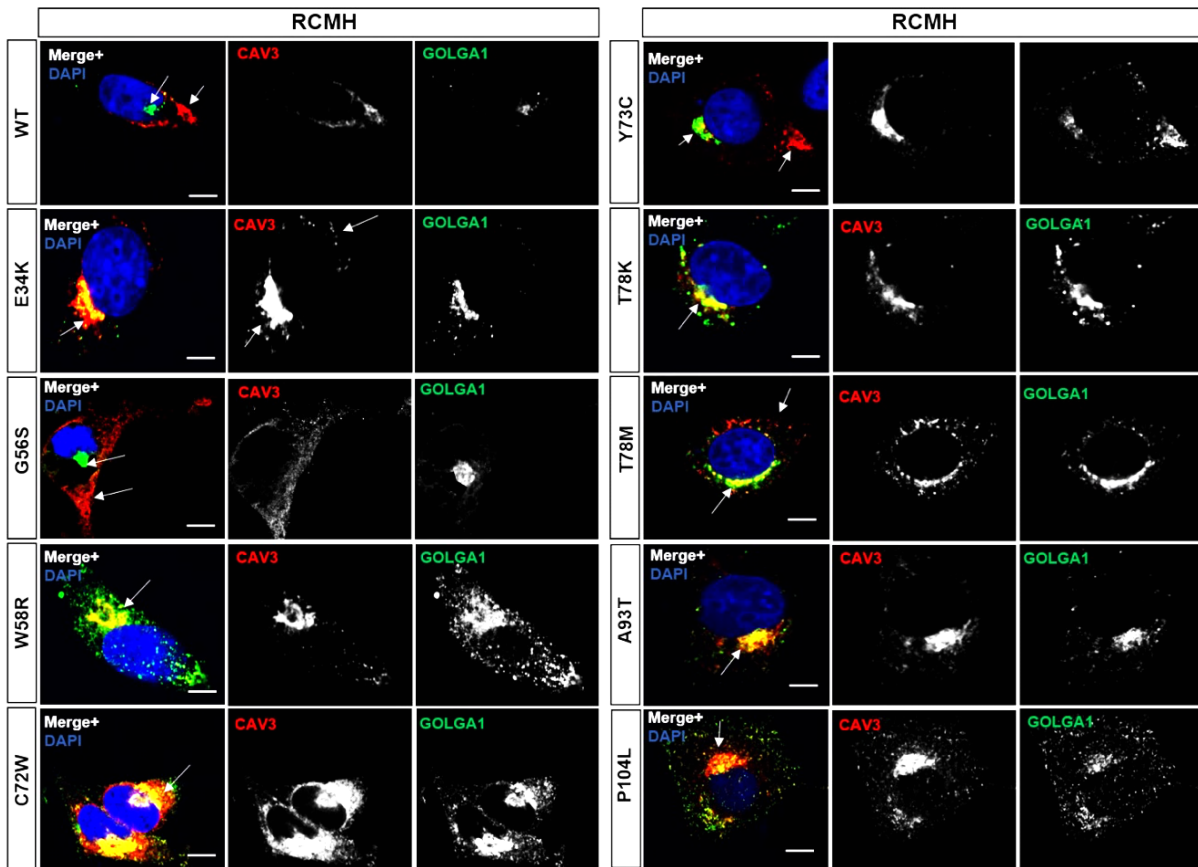


Figure 32. Analysis of RCMH cells transfected with WT CAV3 or different mutant CAV3 constructs. 24 hours post transfection cells were fixed and stained against CAV3 (red), GOLGA1 (green) and DAPI (blue). CAV3 is retained in the Golgi compartment in the case of all mutants except p.Y73C, p.T78M and p.G56S where CAV3 localizes partially at the plasma membrane. Scale bars: 20 μ m.

CAV3 mutants have been described to induce ER stress due to the mislocalization to the Golgi. So far, a potential mislocalization of the mutant forms of CAV3 to the ER has not been addressed in a systematic way as has been done for the mislocalization to the Golgi apparatus. In this context, RCMH transiently transfected cells were further co-stained for GRP170 (a co-chaperone of BiP, marker protein of the endoplasmic reticulum with a crucial role in protein folding) and CAV3 (Figure 33). Most of the mutant CAV3 proteins tended to also co-localize with GRP170 thus suggesting a partial mislocalization to the ER (Figure 33). Notably, the p.G56S and p.T78M only partially co-localized with the ER marker most likely due to their low pathogenicity^{235,244} (Figure 33). It has been described previously that in myoblastic cells transfected with different CAV3 mutants autophagic vacuoles can be found²⁴⁴. In some RCMH cells transfected with mutant forms of the CAV3 protein, the presence of structures resembling vacuoles (Figure 33, indicated by white arrows) was also observed. Additionally, an increase in

autophagic vacuoles was additionally confirmed via immunoblotting which showed alterations in LC3 II (protein involved in the formation of the autophagosomes²⁶²) (Figure 34).

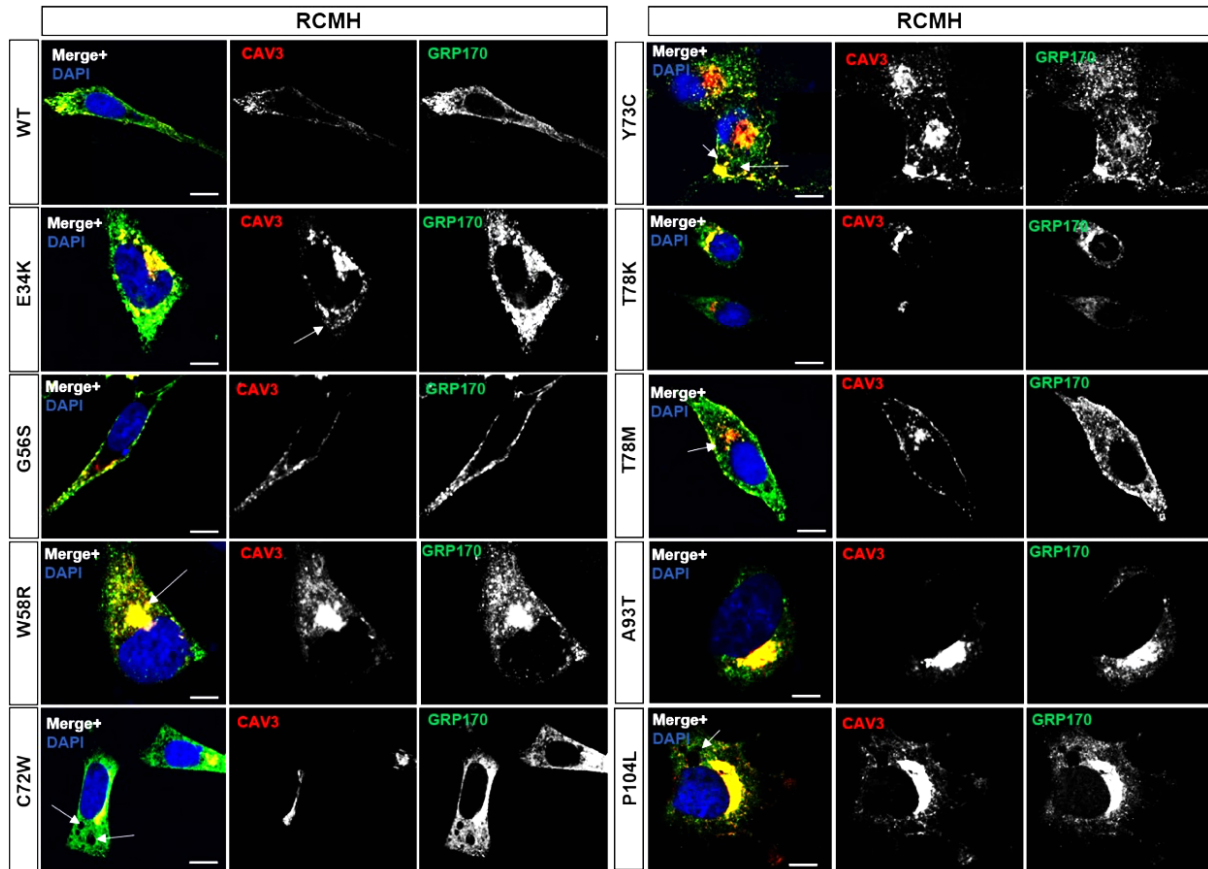


Figure 33. RCMH transfected cells were fixed and stained against CAV3 and GRP170 at 24 hours post transfection. Majority of the mutants show a co-localization as well with an ER marker protein. Arrows depict vacuolar like structures. Scale bars: 20 μ m.

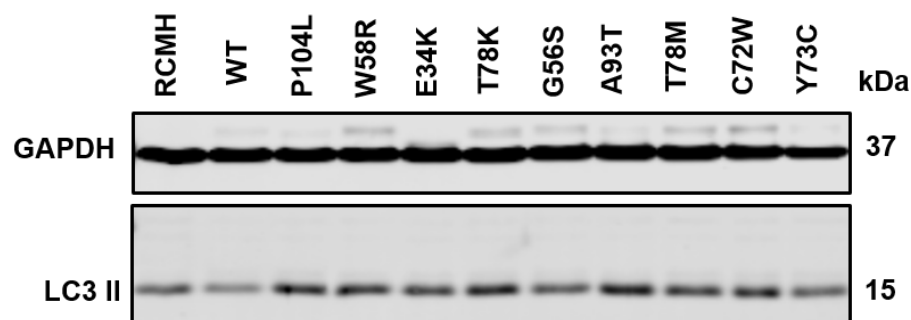


Figure 34. Immunoblot analysis of LC3 II in RCMH transiently transfected cell with WT CAV3 and CAV3 mutants, indicating an increase in autophagosomes. GAPDH was used as a loading control.

Caveolae have been described as sites for actin tail formation which are then anchored at the surface of the sarcolemma by apical actin²⁶³. In order to examine the effect of CAV3 mutants

on proper cytoskeleton, phalloidin staining (a mushroom toxin that binds specifically to F-actin) was performed. This immunofluorescence-based analysis indeed showed that the actin cytoskeleton was highly perturbed in cells expressing the mutant forms of the CAV3 protein where the actin accumulates and polymerizes towards the margins of the cell with a tendency for the microfilaments or bundles to display a more feathery and curvilinear appearance compared to the cells transfected just with the WT CAV3 (Figure 35).

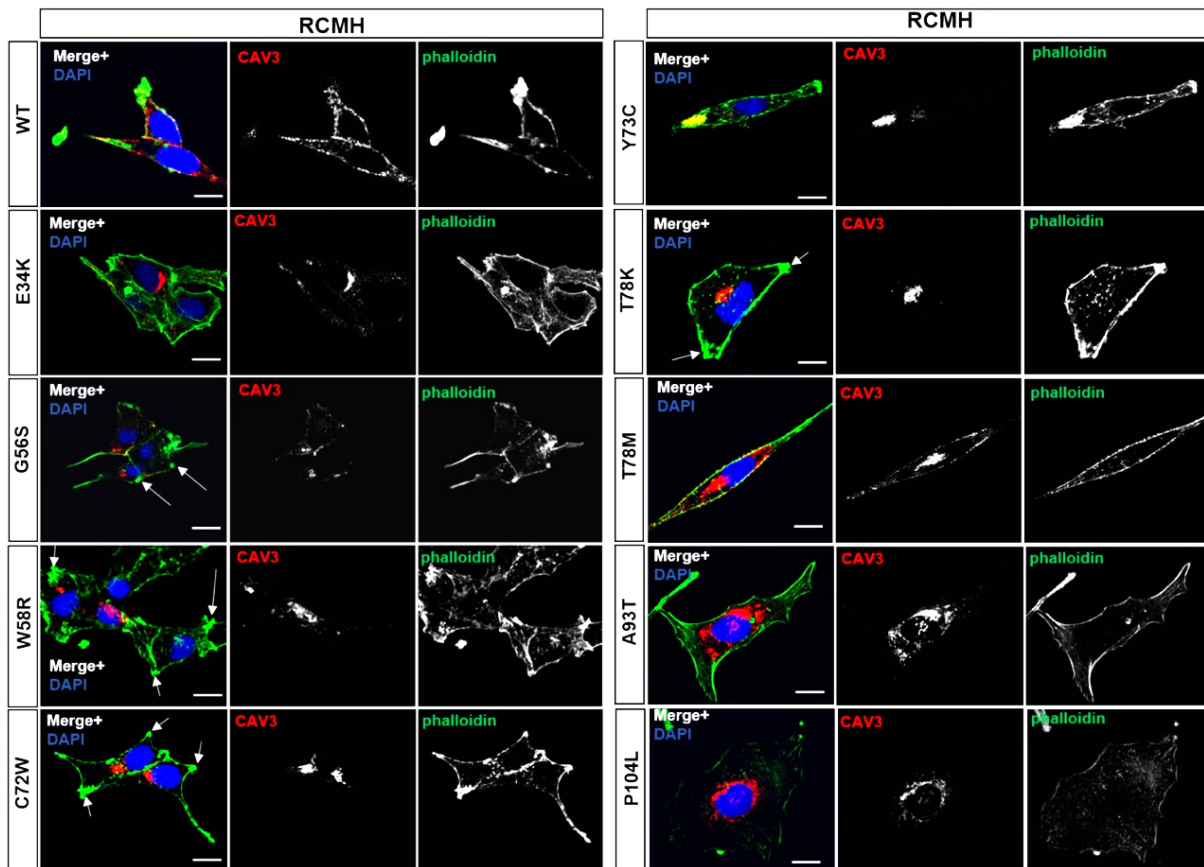


Figure 35. F-actin staining in RCMH cells transfected with different CAV3 expression constructs. Cells were fixed and then stained against CAV3 (in red) and phalloidin (in green). All CAV3 mutants show alterations in the actin cytoskeleton. Arrows depict actin ruffles localized at the cell membrane. Scale bars: 20 μ m.

3.2.2.2.1 Discussion

The main focus of this chapter was to characterize and test the potential pathogenic effect of the two new mutations segregating in the family using functional testing. Several parameters including colocalization with the Golgi (showing the retention of the CAV3 mutant protein in the ER), with GRP170 (modulation of the unfolded protein response), and the integrity of the actin cytoskeleton as well as activation of autophagy via LC3-II accumulation were assessed.

Mutations in CAV3 cause various muscle phenotypes ranging from clinically asymptomatic to severe myopathies. To assess the pathogenicity of the CAV3 mutants segregating in the above mentioned family, we compared them with well described mutants which affect different regions of the protein and which are either pathogenic (p.W58R, p.C72W, p.T78K, p.A93T, p.P104L) or polymorphisms as they do not dramatically change either the localization or the expression of the protein (p.G56S, p.T78M)^{138,224,244,264}. Tyrosine 73 is a highly conserved amino acid residue located in the scaffolding domain and at the proximity of the transmembrane domain^{232,265}. This region has an important role in the homo-oligomerization of CAV3 and thus in the formation of CAV3 oligomers²³². The substitution of this amino acid with cysteine, which is a polar and more hydrophobic than tyrosine²⁶⁶, might promote the formation of bigger CAV3 homooligomers which are unstable and are rapidly degraded. This fact is also mirrored in the SDS-PAGE analysis where the abundance of p.Y73C mutant CAV3 seems to be less compared to the other mutants, however with a similar pattern like p.P104L, a very well know pathogenic mutant which forms these degradation-prone aggregates with the WT protein¹³⁸. The p.E34K mutation led to an alteration in the apparent molecular weight. This phenomenon is most likely due to the replacement of glutamic acid – acidic at neutral pH – with a lysine, a basic amino acid at neutral pH. In turn this leads to an increase in the overall positive charge of the protein and in might increase the binding of the SDS molecules to the protein making it migrate faster through the gel (Figure 31).

The subcellular localization of mutant forms of CAV3 within Golgi and ER can also be used to describe the pathogenicity of the newly identified mutants. As described previously, most of the mutant CAV3 proteins accumulate within the Golgi due to their failure to target the plasma membrane except p.T78M and p.G56S which are less pathogenic and still present within the membrane. Interestingly, p.Y73C forms aggregate-/ dot-like structures which are still localizing to the muscle cell plasma membrane, most likely due to the increased hydrophobicity associated with the amino acid exchange. Also, in the case of overexpression of all the mutant CAV3 forms, the Golgi has a disperse appearance compared to the WT protein in which the staining shows a compact organelle situated perinuclear. The apparent fragmentation of this organelle might result from the recycling of Golgi enzymes back to the ER which then can emerge from the ER as distal Golgi elements²⁶⁷. Most of the CAV3 mutants show a further co-localization with a marker of the ER, GRP170, except for the p.G56S and p.T78M forms of the CAV3 protein. This fact might constitute an attempt for the cells to re-establish homeostasis by allowing the CAV3 mutant proteins to either re-fold or undergo degradation by the ER quality control system²⁶⁸.

Finally, remodelling of the actin cytoskeleton was also used to evaluate the pathogenicity of the mutant CAV3 proteins. CAV3 is a component of the DGC which links the ECM with the actin cytoskeleton²³². The mislocalization of CAV3 mutant proteins to the Golgi leads to the destabilization of this complex which in turn affects the cytoskeleton, a fact also mirrored in this study by the results of the phalloidin staining (Figure 35). In almost all these mutants, an improper organization and a concentration of the actin at the periphery of the cell can be observed. Here, the p.Y73C mutant form of CAV3 showed an interesting co-localization and clustering with actin underneath the plasma membrane. The p.P104L is the only CAV3 mutant that shows a drastic reduction in fluorescence which indicates an affection of the cytoskeleton, a fact also seen and confirmed in the *in vivo* model described and characterized in the previous chapter using proteomics. This detrimental effect, seen only in the p.P104L mutant, can be due to the probable affection of the C-terminal domain of the protein which is crucial for the interaction of CAV3 with the components of the DGC as it is spanning into the sarcoplasm²⁶⁹.

In conclusion, the two CAV3 mutations identified in the above-mentioned family display a variable phenotype. The index's early onset and severity of the disease is most likely caused by the inherited second CAV3 mutation for which a pathogenic behaviour has been demonstrated within this study. One might speculate that the p.E34K mutation is one of the rare recessive CAV3 mutations and thus does not cause a phenotype in the father but in combination with the p.Y73C mutation on the second allele triggers pathophysiological processes leading to an earlier manifestation of the disease as observed in the index patient. Although double-trouble for CAV3 mutations in association with other defects within other genes have been presented previously²⁷⁰, this is the first family described with pure CAV3 double trouble.

The cellular phenotype presented by all the mutations is quite variable however some patterns still emerge so that molecular tools can be used to assess their pathogenicity. Firstly, the very mild mutations (p.G56S and p.T78M) described seem to have no or little co-localization with the Golgi while the pathogenic ones present a total overlap with this organelle (Figure 32). Secondly, in the case of severe mutants, GRP170 is completely recruited to the Golgi together with CAV3 aggregates while for the milder mutations GRP170 has a mostly cytoplasmic (ER/SR) distribution. However, no proper correlation between the actin cytoskeleton and the gravity of the CAV3 mutations *in vivo* can be properly established. The inclusion of further mutants, or the creation of *in vitro* models for these mutations could further expand the knowledge in this area and facilitate the demonstration of a proper correlation.

3.2.2.3 Unravelling new CAV3 functions at the NMJ via identification of IQGAP1 as a new binding partner

3.2.2.3.1 Proteins interacting with CAV3 identified using tandem affinity purification coupled with MS

Although immunoprecipitation of protein complexes coupled to subsequent MS became a gold standard in the identification of new protein interaction partners, a relatively high amount of starting material is needed for this procedure. In general, transient transfected cells can be used for the pull-down of protein complexes, however this approach harbours several disadvantages, as transfecting higher amounts of cells would require higher amounts of transfecting agents which in turn can be toxic and thus trigger apoptotic cascades within the cells. To overcome this problem for this experiment, Flp-In T-Rex 293 cells which stably express CAV3 WT-TAP or p.P104L CAV3-TAP or solely the TAP-tag in an inducible fashion were generated (Figure 36). Then the effect of short and long-term over-expression of these (fusion-) proteins in the respective cell lines was tested by measuring the toxicity (LDH assay) and cell numbers (via CASY) (Figure 36). Notably, a higher cytotoxic effect caused by the overexpression of the p.P104L missense mutant form of CAV3 was observed in the HEK293 cells when compared with the cells expressing the WT CAV3 or solely the TAP-tag. An effect on cell numbers could be seen only upon prolonged expression of the p.P104L missense mutant CAV3. However, combined results confirm the pathologic effect of the p.P104L mutant and thus suggest that our *in vitro* model is suitable for further studies, such as the search for new binding partners under wildtype and mutant conditions.

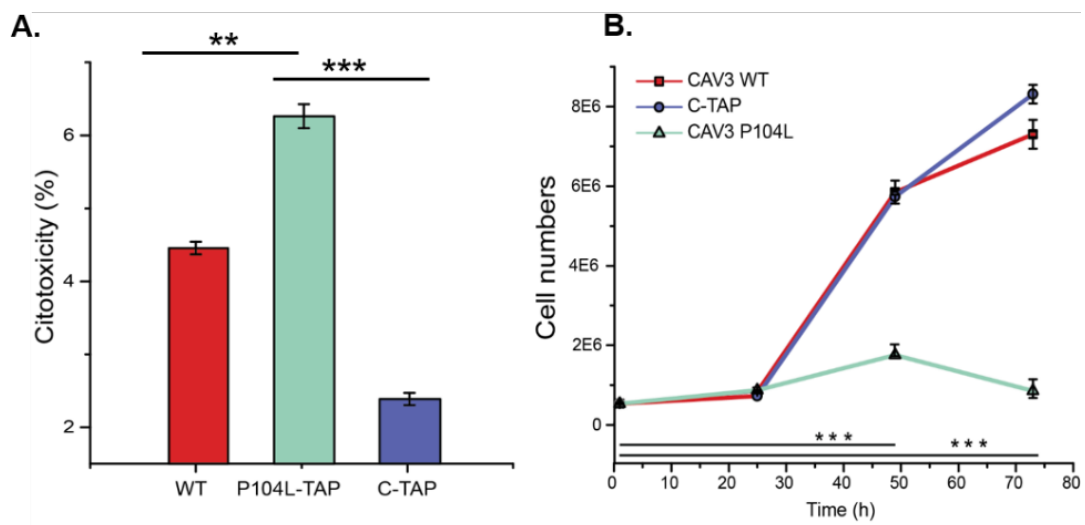


Figure 36. *In vitro* studies focusing on the proliferation and cytotoxic effect in HEK293 cells overexpressing the p.P104L mutant form of CAV3 in comparison with cells overexpressing the WT protein or the empty tag. (A) The cytotoxic effect was measured using the LDH assay and could be demonstrated for the mutant form of the CAV3 protein. (B) Cell numbers indicative for proliferation were determined with the help of CASY at three different time points. Cells overexpressing the missense mutant protein shows a statistically significant reduction in cell proliferation compared with the cells overexpressing the WT or the empty tag. Unpaired t-test was performed and ***- $t \leq 0.01$, **- $t \leq 0.03$ and *- $t \leq 0.01$.

To identify intracellular protein binding partners of CAV3, tandem affinity purification followed by MS analysis was performed (for the TAP assay see section 2.2.5.1) (Figure 37A). First, three independent experiments were performed and among all the proteins identified as potential CAV3 binding partners, only those with a minimum of 2 unique peptides were further considered. Then, proteins presented in the negative control (TAP-tag only) were excluded from further consideration. Amongst, other proteins, IQGAP1 a Ras GTPase-activating-like protein, was identified as a novel binding partner of the CAV3 WT protein (Figure 37B). To confirm the results of the interaction screening described above, WT CAV3-FLAG and IQGAP1-HA were transiently overexpressed in HeLa cells and immunoprecipitation was performed in both directions. In addition to the co-precipitation of WT CAV3-FLAG along with IQGAP1-HA, immunoprecipitation in the other direction showed that IQGAP1-HA can be co-precipitated with WT CAV3-FLAG (Figure 37C). As control conditions, HeLa cells transiently expressing either only the HA- or the FLAG-Tag were used. Moreover, by using the FLAG-tagged version of CAV3 (fusion protein), results of the co-IP confirm that the TAP-tag used in the previous screening, it is not modulating the interaction between the two proteins. Previously, caveolins have been described to preferably bind to other molecules which carry the following amino acid motives: $\Phi X \Phi X X X X \Phi$, $\Phi X X X X \Phi X X \Phi$, or $\Phi X \Phi X X X X \Phi X X \Phi$, where Φ represents an aromatic amino acid like: phenylalanine, tyrosine and tryptophan and X represents any other amino acid²³⁰. However, these amino acid sequences were not present in the IQGAP1 protein and the exact region of binding cannot be determined based on the results of this study. Utilization of protein fragments of WT CAV3 and/or IQGAP1 for further co-IPs would possibly provide more detailed information regarding the exact binding sites of both proteins.

Next, the co-localization of the two proteins was investigated in HEK293 and RCMH cells. Since these two cell lines do not express CAV3 endogenously, they were transiently transfected with the WT CAV3-FLAG construct. Remarkably, the localization of the WT CAV3-FLAG and IQGAP1 proteins overlapped in the plasma membrane of both cell lines (Figure 37D). This observation is in accordance with the known subcellular localization of the two proteins^{232,271}.

A.

Gene	Description	Coverage	Unique Peptides	MW [kDa]
IQGAP1	Ras GTPase-activating-like protein	24.28	8	187.7
CAV3	Caveolin-3	18.48	2	22.7

B.

CAV3-FLAG	+	+			+	+
Empty-FLAG			+	+		
IQGAP1-HA	+	+			+	+
Empty-HA						+
Input	+	+			+	+

189kDa					IQGAP1
18kDa					CAV3
	FLAG-beads		HA-beads		

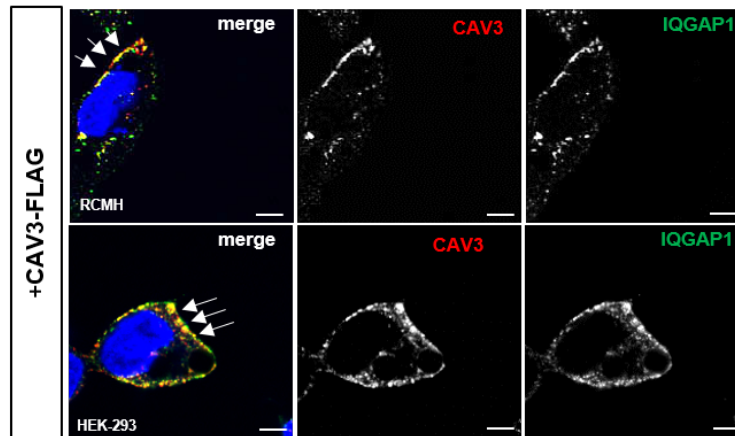
C.


Figure 37. Identification of IQGAP1 interacting with CAV3 by tandem affinity purification. (A) WT CAV3-TAP and empty TAP were purified from stably transfected Flp-In T-Rex HEK 293 cells and the complex identified via MS and confirmed via immunoblotting. (B) Co-immunoprecipitation of WT CAV3-FLAG and IQGAP1-HA. HeLa cells were transiently transfected with the two constructs and cells expressing either empty-HA or empty-FLG were used as a control. Beads decorated either with the HA or FLAG were used for the pulldown. Proteins were separated on SDS-PAGE gel and then transferred to PVDF membrane. Proteins were detected by using a CAV3 respectively an IQGAP1 antibody followed by a fluorescence secondary antibody. (C) HEK293 and RCMH cells were transiently transfected with WT CAV3-FLAG while IQGAP1 was analysed endogenously. Immunofluorescence analysis revealed that these two proteins co-localize at the plasma membrane. Scale bars: 50 μ m.

3.2.2.3.2 IQGAP1 is required for the proper formation of the NMJ in zebrafish

Zebrafish models were designed to further examine the molecular purpose of the CAV3-IQGAP1 interaction via comparing the potential similarity of phenotypes resulting from knock-down of the respective gene expression. Firstly, one orthologous of the *cav3* gene was identified in zebrafish and embryos were then injected with a translation blocking morpholino targeting the start codon (Table 15) thus reducing the CAV3 expression at 48 hours post fertilization (Figure 38B). The concentration of the injected morpholino was adjusted so that a suitable range of phenotypes could be obtained. Macroscopically, the *cav3* MO-injected zebrafish show blocky somites, altered tail morphology (curved and an undulated notochord; Figure 38A). The *cav3* morpholinos exhibit either no escape response or uncoordinated moves in response to tactile stimulus (touch-evoked escape response) whereas the control MO-injected ones displayed no abnormalities (Figure 38C). Histologically, the *cav3*-MO injected fish presented with abnormalities of skeletal muscle morphology: immunostainings of the actin cytoskeleton (phalloidin) and of the fast muscle (F310) show disruption of the regular chevron shape of somites, wavy fibers and in some of the cases absent notochord. These findings are also in accordance with an already well described *Cav3* KO zebrafish model²⁷² (Figure 38D) thus proving the suitability of this model. Previously, it has been described that NMJs in CAV3 deficient mice are highly disturbed and the clustering of the AChR is absent suggesting a profound role of the CAV3 protein in NMJ function and integrity²³⁰. To investigate the NMJ morphology in the *cav3*-MO injected fish, AChR localization was traced by labelling the receptor with bungarotoxin, while the motor axons were stained with synaptic vesicle protein 2 (SV2) antibody. The NMJ of the *cav3*-MO injected fish shows a disruption of the synapse and a disorganization of the pre- and post-synaptic branching compared to the CMO fish. Additionally, in the *Cav3* KO fish, the AChR clusters have a reduced density and size of the distributed synapses at 48 hpf. Interestingly, in the mild *cav3* morphants, a slight increase of the AChRs localized at the myosepta, similar to the pattern seen in the *Dok7* KO fish was observed⁹⁹ (Figure 38-D-arrows). *Dok7* was demonstrated to be crucial for the AChR clustering and formation of NMJs as it interacts with MuSK and activates the receptor kinase and mice deficient in *DOK7* show neither muscle pre-patterning of AChRs nor NMJ formation²⁷³.

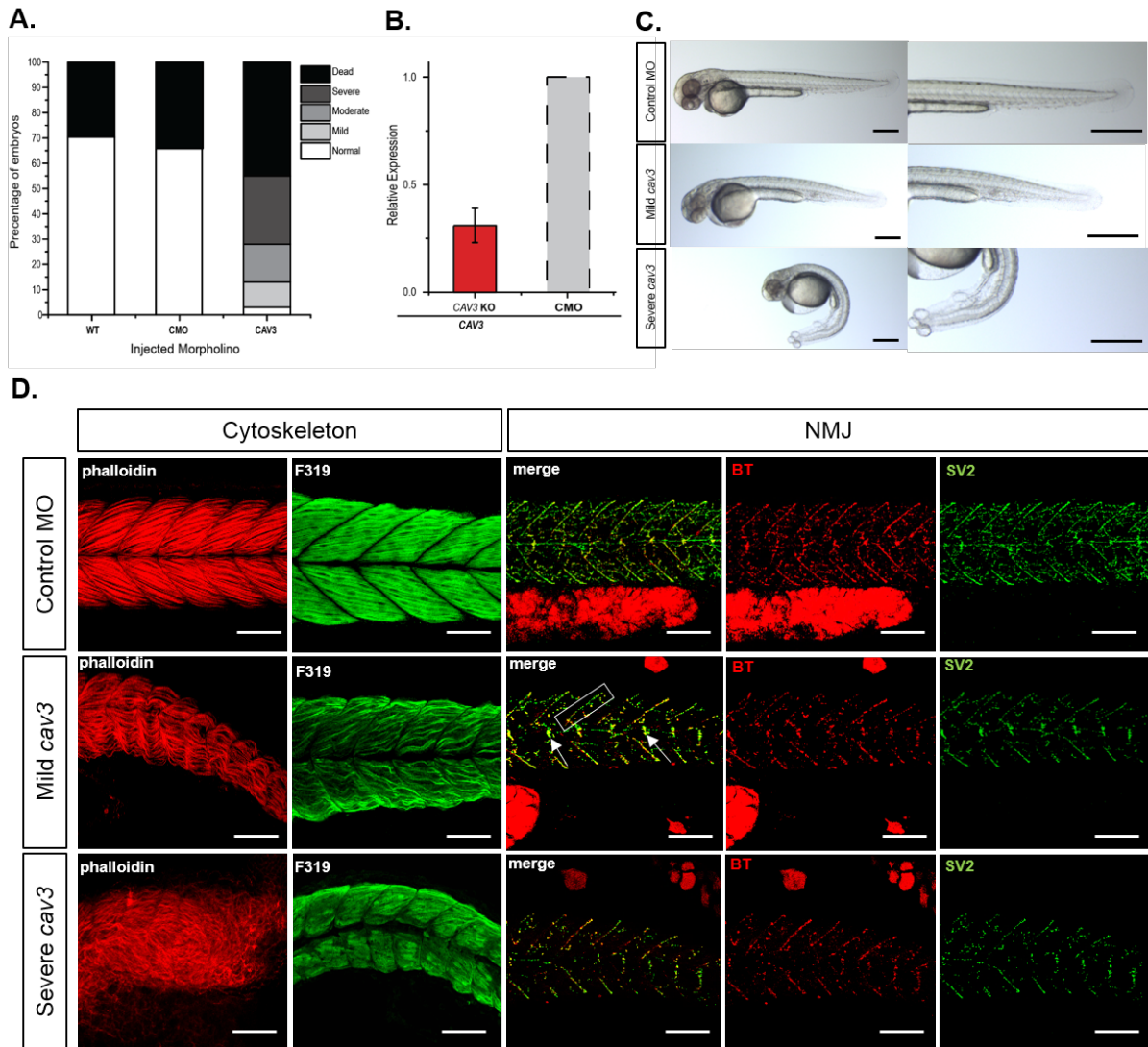


Figure 38. Overview of phenotypical findings in the *cav3* morphants. (A) Survival rates and phenotype distribution in the *cav3*-MO injected fish compared to the CMO and the non-injected fish. (B) qRT-PCR analysis of *cav3* transcripts from 48 hours post fertilization embryos injected with the translation blocking MO, showing a reduction in the expression level of *cav3*. (C) Living embryos injected with *cav3*-MO or CMO were imaged. Approximately, 5% of the *cav3* KD fish presented a mild phenotype while around 20% presented with a severe phenotype and defects in terms of tail morphology. Scale bars: 500 μm. (D) Whole-mount immunostainings of zebrafish embryos at 48 hpf using phalloidin for the visualization of the actin cytoskeleton and F319 for the fast muscle myosin heavy chain (fastMyHC). The presynaptic motor nerve endings were visualized using a synaptic vesicle protein 2 antibody while for the AChR was used bungarotoxin. Scale bars: 50 μm.

Given that CAV3 seems to play a crucial role in NMJ function and integrity, an *iqgap1* zebrafish KO model was generated to address the potential functional role of the new CAV3 binding partner also in NMJ maintenance. One orthologus for the *iqgap1* gene was identified in zebrafish and a splice blocking morpholino was designed and zebrafish were injected with 15 ng of

morpholino which reduced the expression of *Iqgap1* and yielded the best range of phenotypes (Figure 39A). After decorination, the touch evoke test was performed on the *iqgap1* morphants which demonstrated an abnormal response to touch stimuli, similar to the *cav3* morphants. Macroscopically the fish presented at 48 hpf an altered tail morphology, depicted here by the curly tail. The effect of *Iqgap1* depletion on muscle fiber integrity was assessed by immunofluorescence. The *iqgap1* morphants present a muscle phenotype similar to the one observed in the *cav3* morphants: disturbed actin cytoskeleton with abnormal alignment of fibers which appear wavy and have gaps in between (as seen in the slow twitch fibers; Figure 39C arrows) and as well loss of myosepta. (Figure 39C).

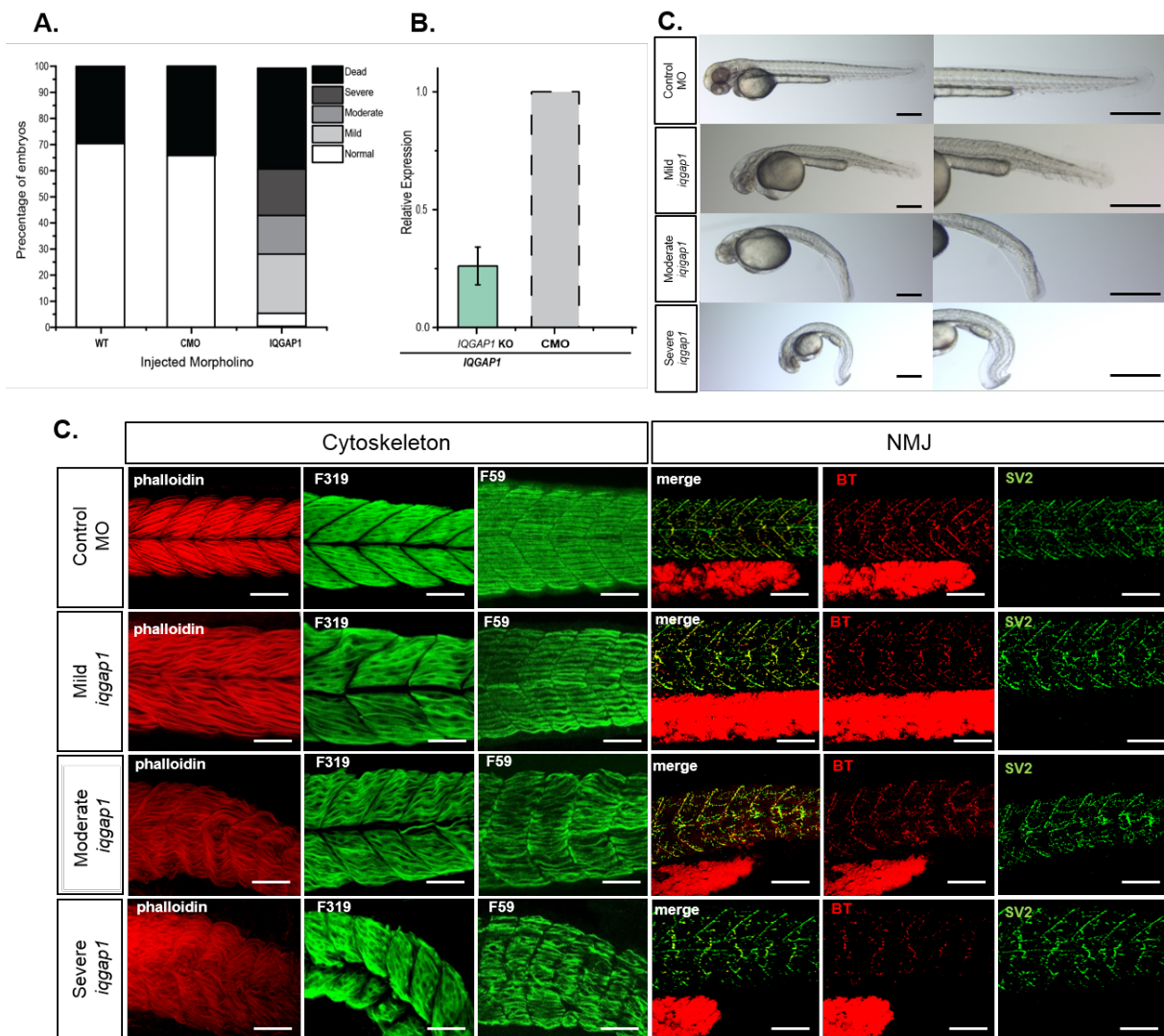


Figure 39. Overview of the phenotypical findings in the *iqgap1* morphants. (A) Survival rates and phenotype distribution in the *iqgap1*-MO injected fish compared to the CMO and the non-injected fish. (B) qRT-PCR analysis of *cav3* transcripts from 48 hours post-fertilization embryos injected with the translation blocking MO, showing a

reduction in the expression level of *iqgap1*. (C) Living embryos injected with *iqgap1*-MO or CMO were imaged. Approximately, 5% of the *Iqgap1* KD fish presented a mild phenotype while around 20% presented with a severe phenotype and defects in terms of tail morphology. Scale bars: 500 μ m. (D) Whole-mount immunostainings of zebrafish embryos at 48 hpf using phalloidin for the visualization of the actin cytoskeleton and F319 for the fast muscle myosin heavy chain (fastMyHC). The presynaptic motor nerve endings were visualized using a synaptic vesicle protein 2 antibody while for the AChR was used bungarotoxin. Scale bars: 50 μ m.

Notably, immunofluorescence studies of the *iqgap1* morphants also revealed disturbed NMJ structures with disorganization of the pre- and post-synaptic branching across the muscle fiber, a phenotype similar to the one observed in the *Cav3* KD zebrafish (Figure 39C). During early development acetylcholine receptors accumulate at the centre of the muscle fibers, navigated by the motor growth cones. The postsynaptic differentiation requires agrin to initiate the clustering of the AChR receptor and MuSK for promoting AChR clustering and activate gene expression^{240,274}. Given that CAV3 has been described as a direct binding partner of MuSK, modulating the clustering of the AChR and that IQGAP1 interacts with CAV3 (having a crucial role in the formation of NMJ), we next focused on the molecular interplay of the transcripts corresponding to these three proteins in the above described zebrafish models. Consequently, the *Musk* KD zebrafish described previously was also included²⁷⁵ and the expression levels of each transcript in the respective zebrafish model was monitored by real time quantitative PCR. Interestingly, it could be observed that in the *cav3* morpholino injected fish, levels of *iqgap1* and *musk* are decreased. A similar effect was seen in the *Iqgap1* KD fish where the expression of *cav3* and *musk* were drastically decreased. Moreover, the decreased levels of *musk* due to its knockdown in zebrafish, impinge on the *cav3* and *iqgap1* levels (Figure 40). Hence, our combined data suggest a molecular interplay of the three NMJ-factors already at the transcript level.

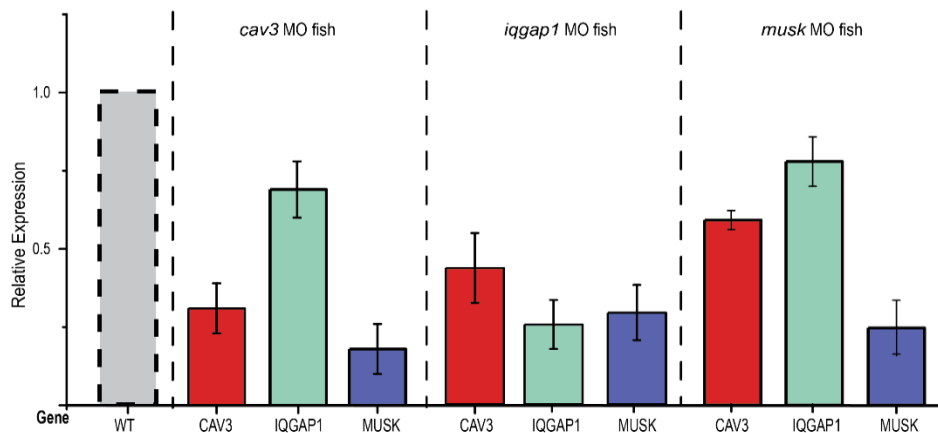


Figure 40. Expression levels of *cav3*, *iqgap1* and *musk* were monitored via real time quantitative PCR in the *cav3*, *iqgap1* and *musk* morphants at 48 hpf showing a molecular linking between the three proteins.

3.2.2.3.3 IQGAP1 is co-localizing with the AChR in mouse muscle

CAV3 was previously described to co-localize with AChR and play a crucial role in the clustering of the receptor. IQGAP1 also seems to be involved in the stability of the NMJ as seen in the generated knockdown zebrafish model. Next, immunofluorescence on murine muscles was performed and muscle derived from WT animals was stained using bungarotoxin (for the AChR) and against IQGAP1 (Figure 41). For this purpose, 32 NMJ from 4 different WT animals were analyzed. Strikingly, 24 of the 32 analyzed NMJs showed a clear colocalization of bungarotoxin with IQGAP1 (Figure 41).

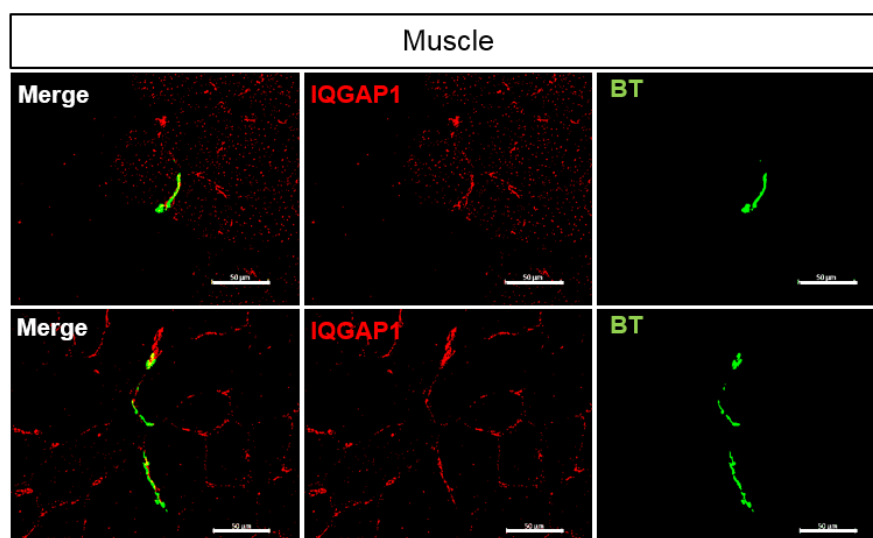


Figure 41. Immunofluorescence analysis of IQGAP1 (stained in red) and bungarotoxin (stained in green) in skeletal muscle of wildtype mice. Images show a co-localization of the two proteins at the sarcolemma. Scale bars: 50 µm.

3.2.2.3.4 IQGAP1 presents partial colocalization with CAV3 mutants in the Golgi

Mutations in CAV3 have been described in the previous chapter as affecting the subcellular localization of the protein with the exception of milder mutants like p.G56S and p.T78M which partially localize at the plasma membrane/sarcolemma. To shed light on the question of whether IQGAP1 is affected by the mistargeting of mutant forms of CAV3 to the Golgi apparatus, further immunofluorescence experiments were performed: myoblastic RCMH cells were transiently transfected with equal amounts of constructs harbouring different mutations in different domains of the CAV3 protein (see section 3.2.3.3) and stained against IQGAP1 and CAV3. Some pathogenic mutants like p.E34K, p.A93T and p.P104L seem to have a negative dominant

effect on endogenous IQGAP1 in terms of mislocalizing in a perinuclear compartment (probably within the Golgi) together with CAV3 (Figure 42). In contrast, in the mutations affecting the scaffolding region of CAV3 (p.G56S, p.W58R, p.C72W and p.Y73C), IQGAP1 is still partially or almost entirely localizing at the plasma membrane (Figure 42). This suggests that not all CAV3 missense mutations have a dominant negative effect on IQGAP1 and that this protein can escape from forming protein aggregates in the case of CAV3 mutations affecting the scaffolding domain. It is important to note that for some of these CAV3 missense variants (p.G56S and p.C72W) only a mild pathogenic or modifying effect has been described concomitant with a solely partial mislocalization of the missense variants to the Golgi²⁴⁴.

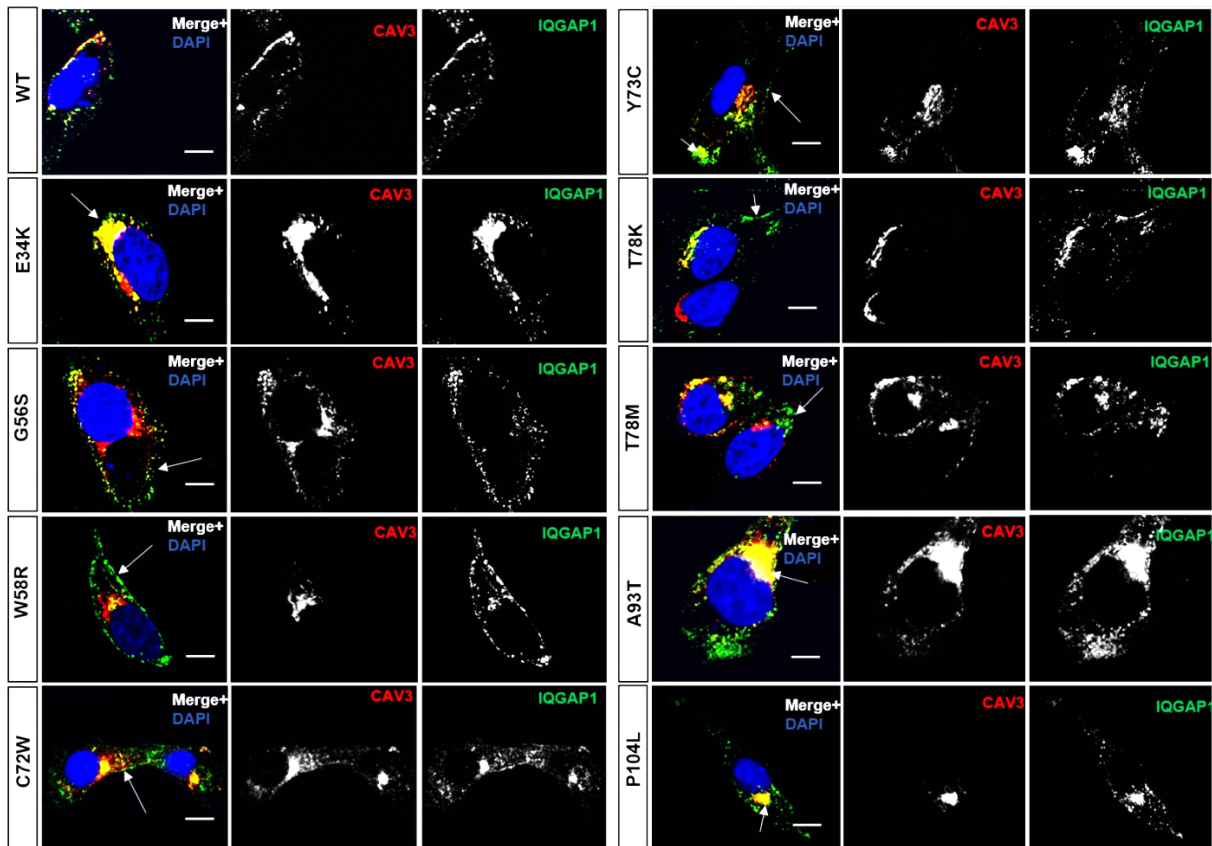


Figure 42. Immunofluorescence analysis of IQGAP1 distribution in RCMH cells transfected with different CAV3 expression constructs. Cells were fixed and then stained against CAV3 (in red) and endogenous IQGAP1 (in green). IQGAP1 seems to be co-localizing with the most pathogenic CAV3 mutants within the Golgi. Arrows depict IQGAP1 either still localizing at the plasma membrane or together with the CAV3 in a perinuclear compartment most likely corresponding to the Golgi. Scale bars: 20 μ m.

3.2.2.3.5 The NMJ in the p.P104L CAV3 mouse model is affected

Previously, it has been described that CAV3 is enriched at the NMJ and is associated with the AChR and MuSK proteins. Furthermore, a CAV3 KO mouse model showed an impairment in the AChR clustering²³⁰. Interestingly, Pratt and colleagues described postsynaptic changes in dystrophic muscles where apparently the lack of dystrophin impacts the endplate maintenance²⁷⁶. Dystrophin forms a complex together with a series of dystrophin-associated glycoproteins including CAV3 which stabilize the sarcolemma and links the ECM with the intracellular cytoskeleton²⁷⁷. So far, the disturbances in the NMJs of dystrophic patients have been under looked and underestimated as they actually might contribute to the phenotype seen in patients.

The disturbances of the NMJs caused by mutant CAV3 were further checked in the quadriceps muscles from the well described transgenic p.P104L mouse model¹³⁸. Muscles were stained against the AChR receptor with bungarotoxin and then analyzed based on the NMJ-morph protocol¹⁵³. The quantitative results showed major differences in the AChR area and perimeter as well in the cluster size and numbers in the p.P104L transgenic mouse model compared to the WT littermates (Figure 43). The amount of the AChR receptor, reflected here in the compactness parameter, is significantly reduced in the transgenic animals. The fragmentation of the endplate seems to be higher in the p.P104L mouse model compared to the WT littermates, however this difference is not statistically significant. In the *mdx* mice, a mouse model for Duchenne muscular dystrophy, a high degree of fragmentation was also observed²⁷⁶.

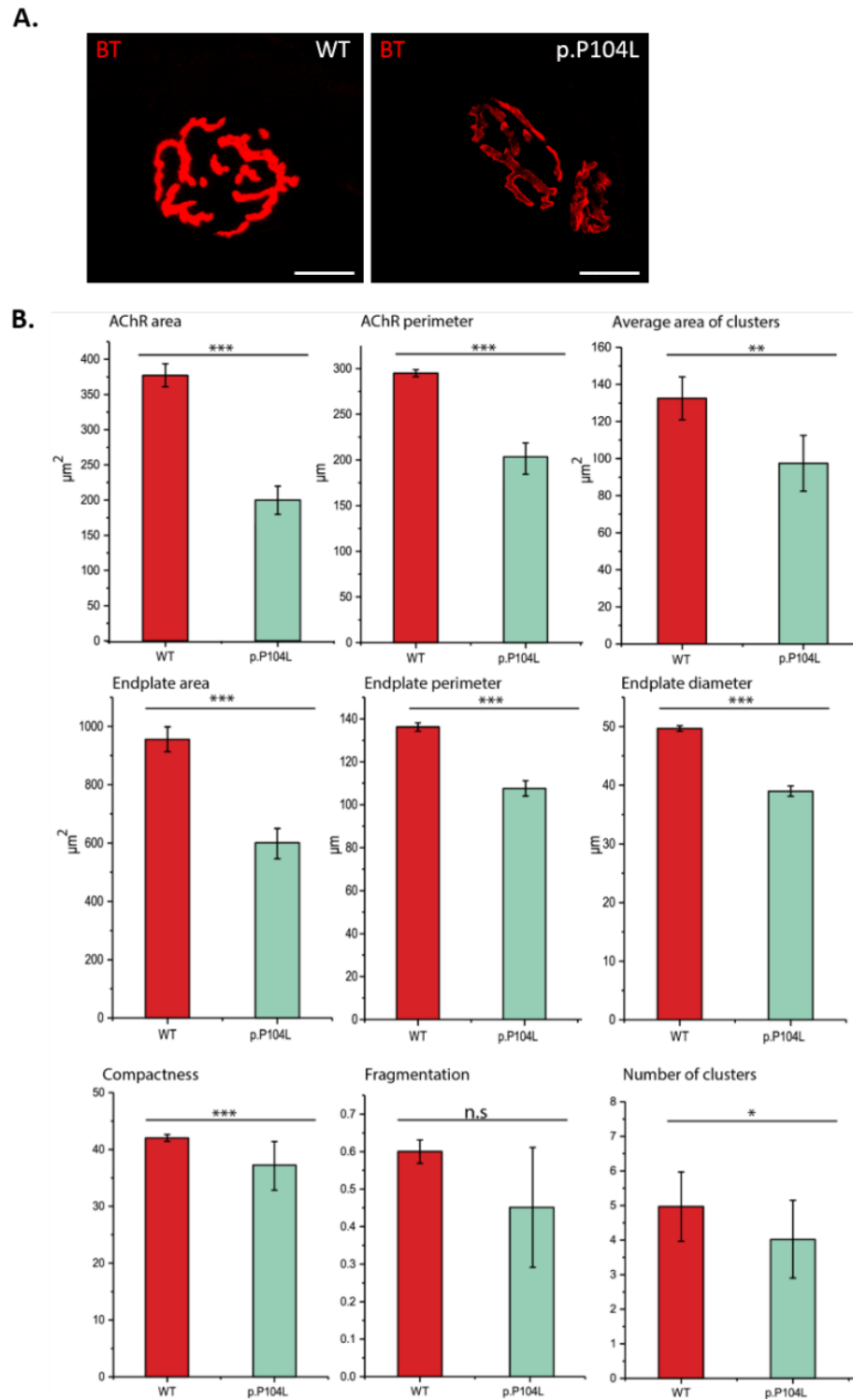


Figure 43. Morphology of the NMJs in the p.P104L_CAV3 transgenic mouse model. (A) Representative confocal micrographs from quadriceps muscles in the WT and transgenic mice. Scale bars: 50 μm . (B) Bar charts showing the differences between the WT and the p.P104L transgenic animals across a range of postsynaptic variables. Each bar represents the mean (\pm SEM) of >150 NMJs from 2 distinct animals. Unpaired t-test was performed and ***- $t \leq 0.05$, **- $t \leq 0.03$ and *- $t \leq 0.01$.

Next, the levels of IQGAP1 were investigated in the quadriceps muscles of the transgenic p.P104L CAV3 mouse model via immunoblot analysis in order to see if the mutant CAV3 exerts an effect on IQGAP1 also in a mammalian *in vivo* model of Caveolinopathy (Figure 44). This biochemical investigation showed that the levels of IQGAP1 are decreasing upon CAV3 mislocalization and degradation²⁴⁵, in accordance with the immunofluorescence analysis performed on multiple CAV3 missense mutants (Figure 42). IQGAP1 acts as a small GTPase scaffolding platform recruiting both, GTPase regulators and effectors²⁷⁸. In this context, the levels of CDC42 and RAC1-GAP, were also examined in the muscles of the CAV3 animals (p.P104L_CAV3 transgenic animals versus wildtype littermates). The immunoblotting analysis revealed that RAC1-GAP was increased while the levels of CDC42 remain unchanged (Figure 44).

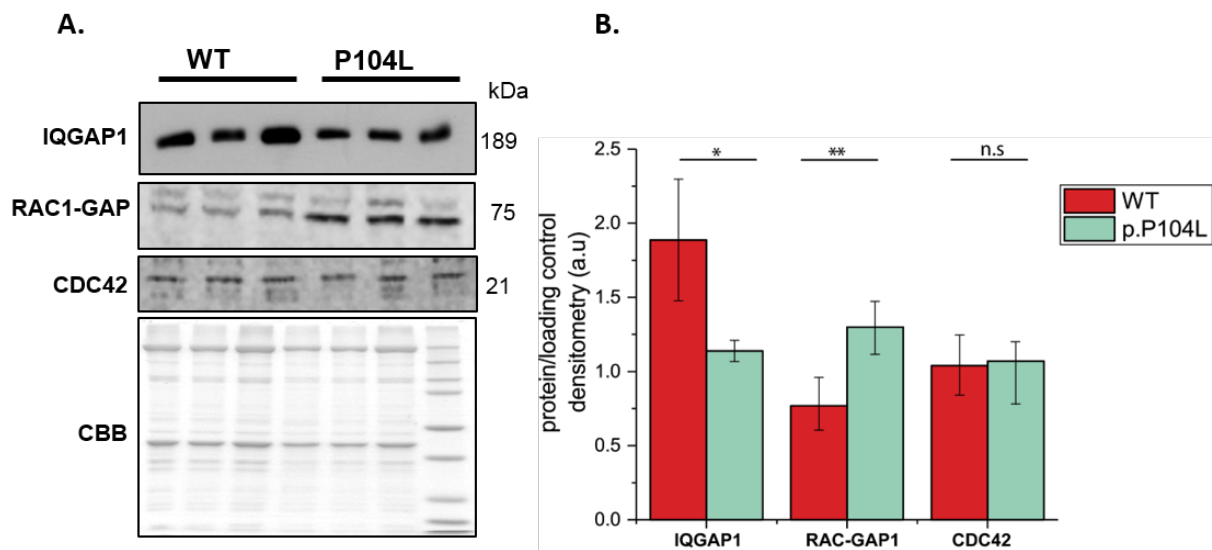


Figure 44. Biochemical study of IQGAP1 and related proteins in a mouse model of Caveolinopathy. (A) Immunoblotting analysis of quadriceps muscle derived from 24 weeks old p.P104L_CAV3 mice and the respective WT littermates, showing alterations in cytoskeleton related proteins like IQGAP1, CDC42 and RAC1-GAP1. Commassie gel was used as a loading control. (B) Results of quantification and statistical analysis of the obtained immunoblot results.

3.2.2.3.6 Effects of IQGAP1 overexpression in myoblasts

To further study the muscular role of IQGAP1 and potentially gain further molecular insights into its role in NMJ integrity, the effect of IQGAP1 overexpression in primary muscle cells was investigated. Thus far it has been described that only differentiated muscle cells possess most of the proteins necessary for agrin induced clustering of the receptor with the exception of some AChR receptor units²⁷⁹. It has been stated that CAV3 is expressed only in differentiated

myoblasts²⁸⁰. As undifferentiated muscle cells show significantly better rates of viral-based transfection²⁸¹, the muscle protein catalogue described in the chapter 3.1 was employed to see whether myoblasts also express the NMJ-relevant proteins and thus might already serve as a suitable model for these studies. All proteins necessary for the clustering of the AChR receptor such as subunits of the AChR, MuSK and its further binding partners as well as CAV3 were confirmed to be already expressed in human primary myoblasts. Thus, making these cells suitable for studying the effect of IQGAP1 on AChR receptor clustering (Figure 45).

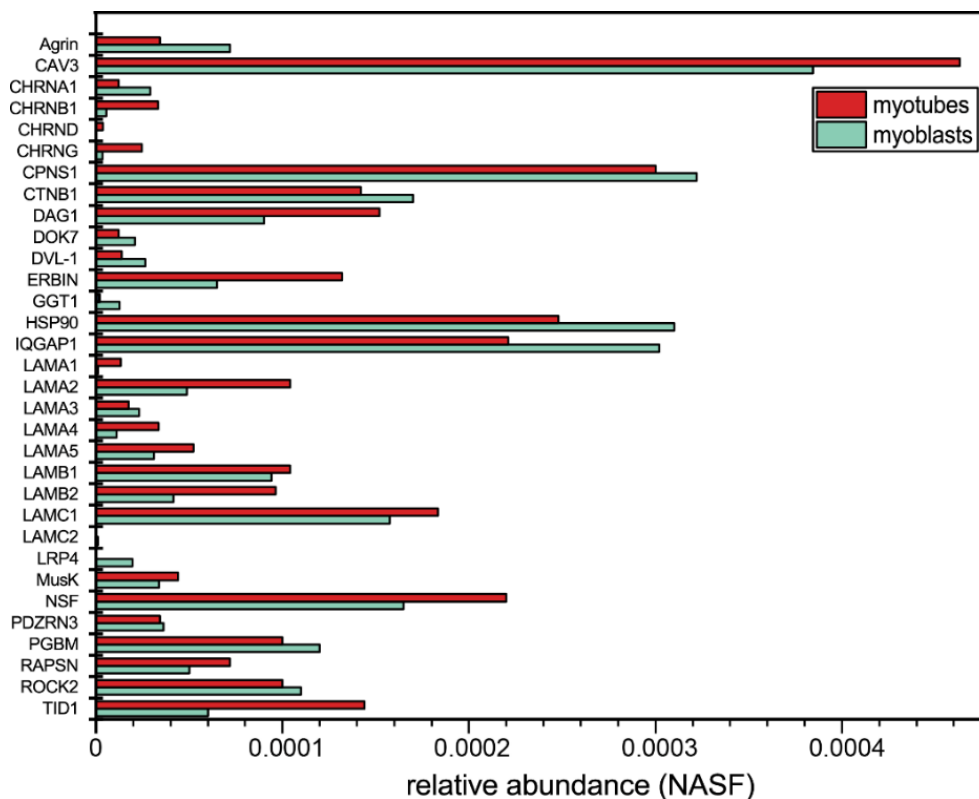


Figure 45. Relative expression of proteins belonging to the post-synaptic area in myoblast and myotubes. The relative expression is given by the NASF (normalized spectral abundance factor) number.

Human primary myoblasts were infected at 100 MOI with *AdV.IQGAP1* and transduced for 48 hours. To verify the efficiency of viral infection and transduction, further cells were transfected with an *AdV.GFP* and used as a control. To trigger the clustering of the AChR receptor, transduced and non-infected cells were treated with 200 nM of NT-1654 for 3 hours. This drug is a water soluble 44 kDa fragment of neuronal agrin. Notably, NT-1654 has been successfully used as a therapeutic compound in mouse and zebrafish models of CMS^{282,283}. Here, cells were fixed and different stainings were performed to assess the changes upon IQGAP1 overexpression.

The distribution of IQGAP1 and of CAV3 in *Adv.IQGAP1* cells was verified (Figure 46) and control myoblasts indeed presented a plasma membrane staining against CAV3 and IQGAP1 which was particularly enriched at the cell-cell junction (Figure 46, left panel). The overexpression of IQGAP1 leads not only to a sarcolemma staining which is co-localizing with CAV3 but also to a cluster like distribution of the protein through the cell. The treatment of myoblasts overexpressing IQGAP1 with agrin seems to induce a clustering of the two proteins distributed throughout the cell surface while in control treated myoblasts the two proteins seem to be enriched at the plasma membrane (Figure 46-right panel).

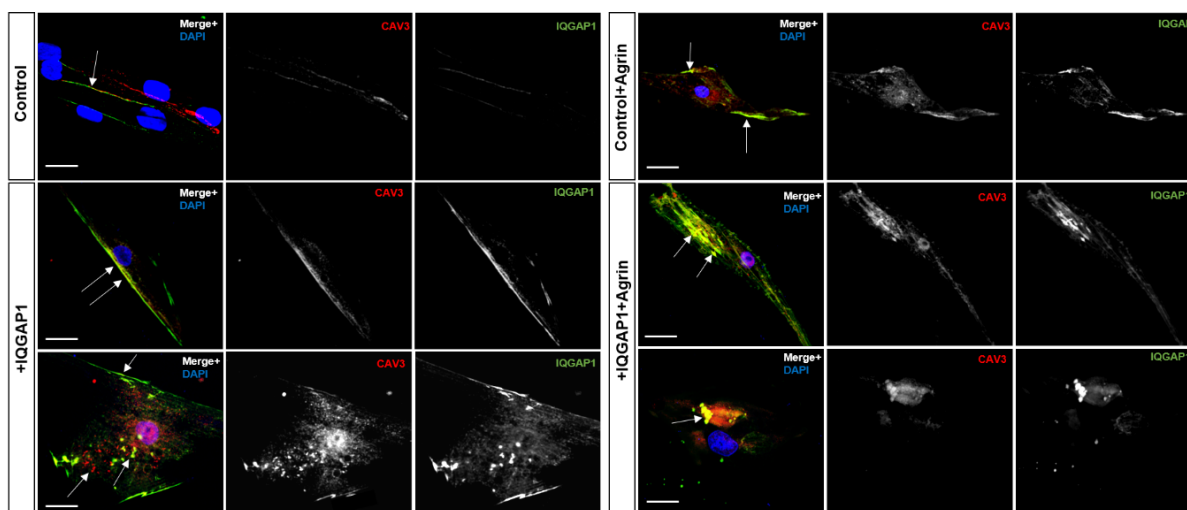


Figure 46. Immunostainings for CAV3 (red) and IQGAP1 (green) were carried out in primary control myoblasts and myoblasts transduced with *Adv.IQGAP1*. Cells were transduced with adenoviral vectors at multiplicities of infection (MOI) of 100 for 12 h. The medium containing the virus vector was removed and the cells were washed twice with fresh 10% FBS-DMEM. Subsequently, the cells were cultured for further 2 days. Some of the control and transduced myoblasts were treated as well with the synthetic agrin to induce the AChR receptor clustering. Scale bars: 20 μ m.

So far, in the current literature, there has been no report on a functional connection or molecular interplay between IQGAP1 and AChR. In the IQGAP1 overexpressing human muscle cells, staining against the receptor (red) and IQGAP1 (green) revealed that these two proteins co-localize either in a diffused pattern at the plasma membrane/ sarcolemma or in pre-assembled clusters at the surface of the cell (Figure 47, left panel). In contrast, in the control cells, the receptor shows a faint staining probably corresponding to pre-existing diffusely distributed AChR (Figure 47, left panel). The addition of agrin in the control myoblasts leads to the formation of the typical AChR clusters but also to highly dense linear AChR areas which co-localize with IQGAP1. In the IQGAP1-overexpressing cells, supplementation of the agrin

peptide seems to lead to the formation of bigger rounded clusters which also co-localize with IQGAP1 (Figure 47-right panel).

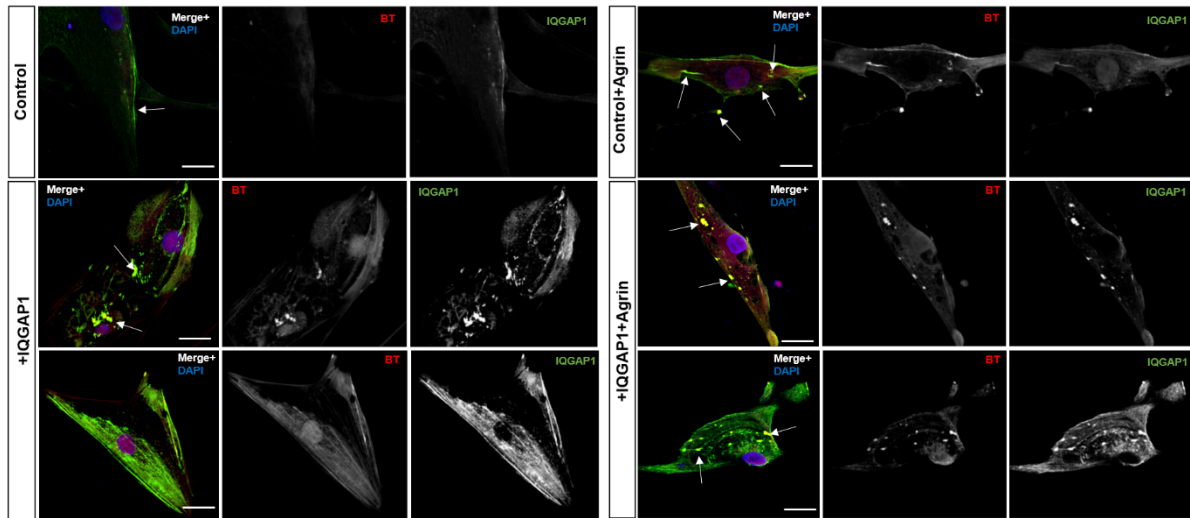


Figure 47. Immunostainings for bungarotoxin (red) and IQGAP1 (green) were carried out in myoblasts control and transduced with *AdV.IQGAP1* at a MOI of 100 for 12h. Then the medium containing the virus vector (*AdV.IQGAP1* or control) was removed and the cells were washed twice with fresh 10% FBS-DMEM and incubated for extra 2 days. Some of the control and transduced myoblasts were treated as well with the synthetic agrin in order to induce the AChR receptor clustering. Scale bars: 20 μ m.

As IQGAP1 promotes the remodelling of actin cytoskeleton, the effects of overexpressing this protein in primary myoblasts were verified (Figure 48). The architecture of the actin cytoskeleton changes dramatically upon the overexpression of IQGAP1. In the control myoblasts, typical actin fibers orientated along the predominant and longitudinal direction of cells are present while, the overexpression of IQGAP1 leads to the formation of cortical actin and to filopodia.

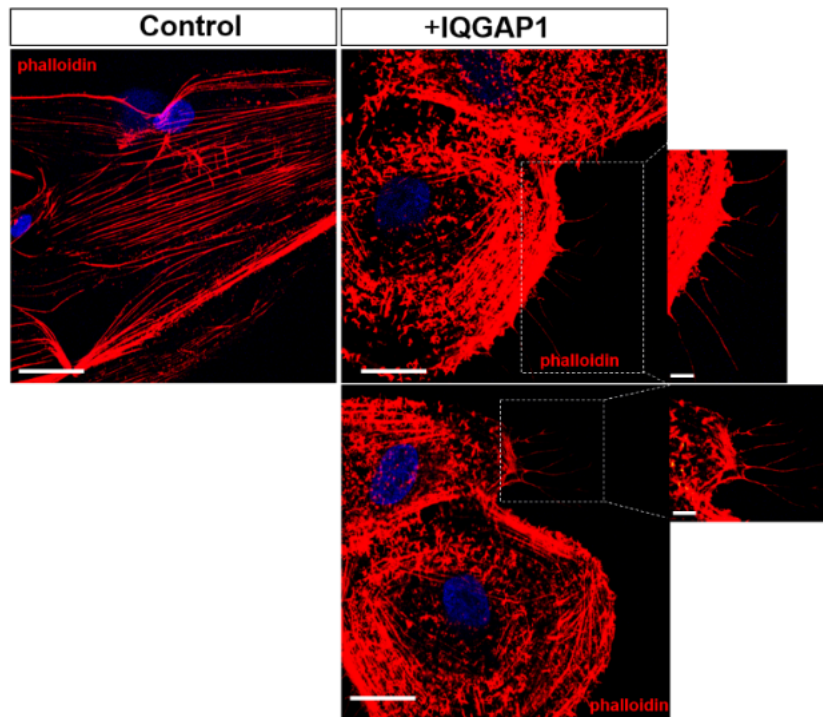


Figure 48. Immunostainings for phalloidin (red) in order to visualize the actin cytoskeleton in primary control myoblasts and primary myoblasts overexpressing IQGAP1. To achieve IQGAP1-overexpression, primary myoblasts were transduced with *AdV.IQGAP1* at a MOI of 100 for 12h. Then the medium containing the virus vector (*AdV.IQGAP1* or control) was removed and the cells were washed twice with fresh 10% FBS-DMEM and incubated for extra 2 days prior phalloidin staining was carried out revealing a rearrangement of the actin cytoskeleton in IQGAP1-overexpressing cells (right panel) compared to the controls (left panel). Scale bars: 20 μ m.

To obtain insights into the cellular consequences of IQGAP1 increase and its molecular role in NMJ function, proteomic signature of IQGAP1 overexpressing human primary muscle cells has been studied. A total of 2002 proteins were identified with more than 2 unique peptides and an FDR of 1% at protein and peptide level. IQGAP1 was identified with more than 50 unique peptides, amongst the top 10 most abundant proteins, thus confirming the overexpression of this protein in myoblasts. From the total proteins, 547 (27.3%) were statistically significant (p -Anova < 0.05) and 80 proteins were found to be altered in abundance: 34 down-regulated and 46 up-regulated (Figure 49A). As expected due to the subcellular localization of IQGAP1, 15 of the 80 regulated proteins are localizing at the plasma membrane (Figure 49B). Other proteins found to be affected are localizing to the nucleus, ER, to mitochondria or are regularly secreted (Figure 49B). Pathway analysis of all regulated proteins was performed using KEGG, DAVID and Reactome repositories (Figure 49C). Additionally, all statistically significant altered proteins (p -Anova < 0.05) were filtered for those belonging to 5 GO biological processes that play a crucial role in the postsynaptic NMJ formation, thus emphasizing the role of IQGAP1 in

this process (Figure 50). This *in silico* study indeed revealed that several pathways involved in the maintenance of the actin cytoskeleton (signaling by Rho GTPases), of the ECM or those of importance for axon guidance/PNS development are addressed by cellular increase of IQGAP1.

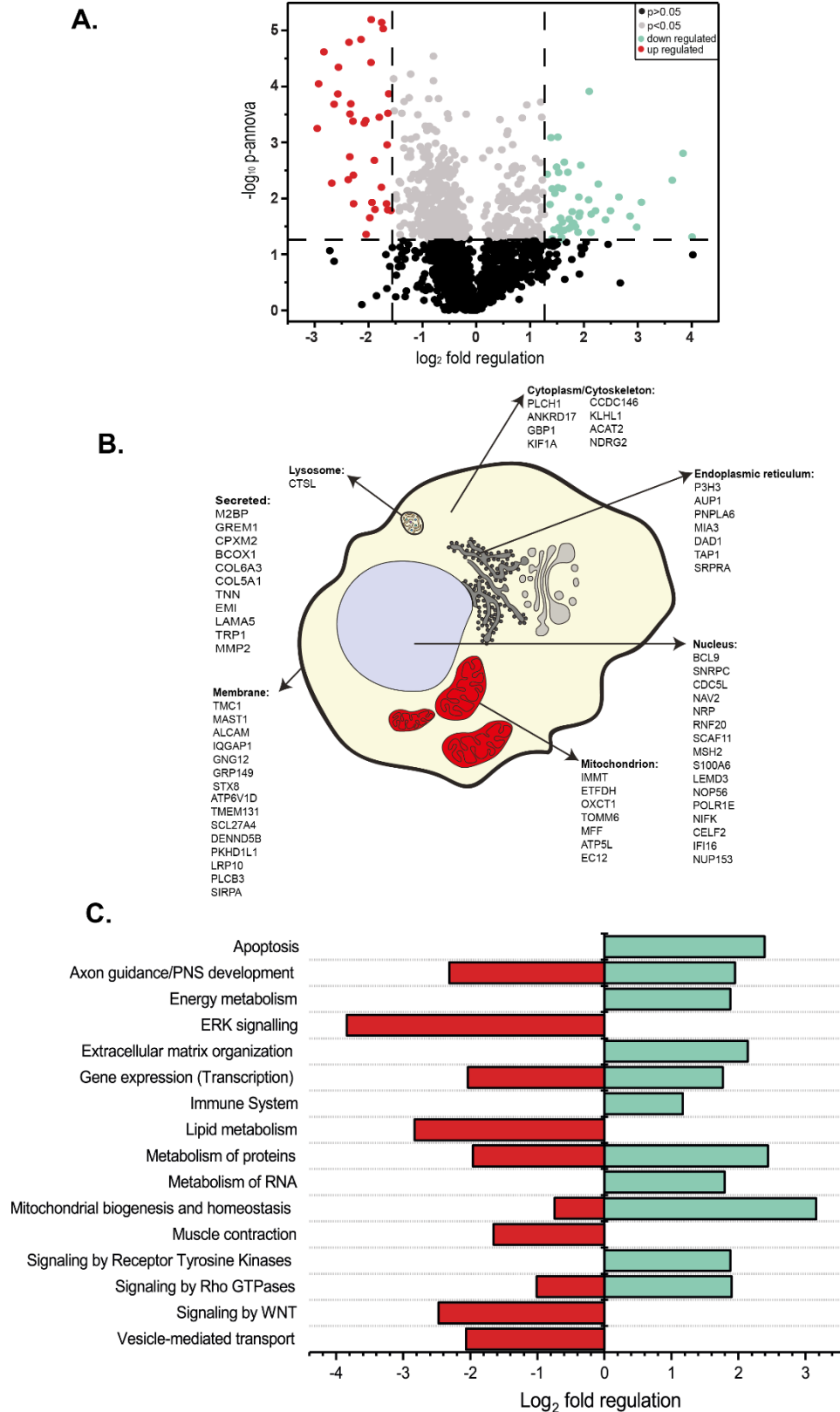


Figure 49. *In silico* analysis of proteomic data obtained in the IQGAP1 overexpressing myoblasts. (A) The volcano plot of myoblasts transduced with IQGAP1 were compared with control myoblast via proteomics which resulted in the identification of 2002 proteins. All identified proteins in the muscles are represented and a clear delimitation between the proteins with a p -Annova <0.05 (statistically significant) and the rest is made by a horizontal line. Proteins which are decreased are represented in red while the up regulated ones are in green. (B) Schematic overview of the subcellular compartments and respective proteins that showed a significant fold regulation. (C) Analysis of pathways (KEGG, DAVID and Reactome) associated either with up- or down-regulated proteins revealed by the proteome profiling where red labelling represents down-regulated proteins and green labelling up-regulated proteins.

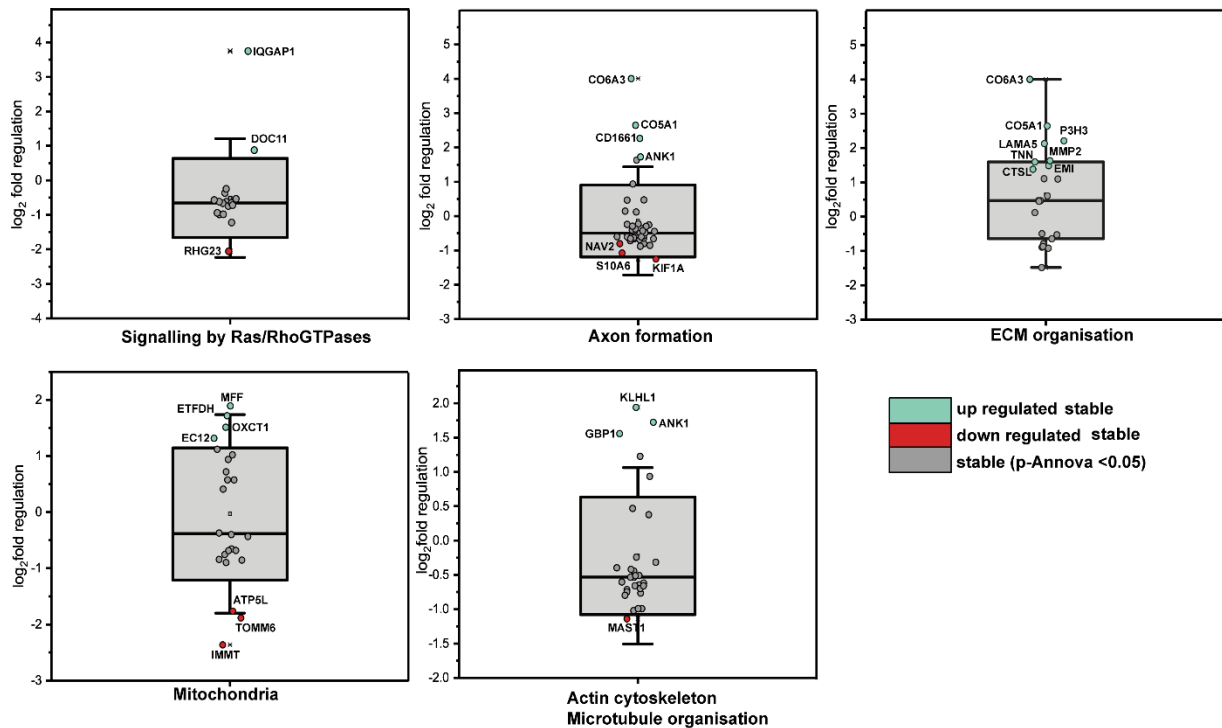


Figure 50. Analysis of proteins that are relevant for the NMJ in IQGAP1-overexpressing cells. The box plots depict the distribution of median \log_2 ratio of statistically significant proteins from the proteomic experiment for the indicated Uniprot keyword GO term. Proteins were filtered out just against 5 GO biological processes belonging to processes important for the NMJ. All up regulated proteins were represented with green while the down regulated ones with red while proteins with a stable expression are in grey.

3.2.2.3.7 Discussion

To expand the current understanding of the biological function of CAV3, the interactome of this protein was investigated, allowing the identification of IQGAP1 as a new binding partner. IQGAP1 is a scaffold protein that integrates multiple signalling pathways such as MAPK signalling, PI3K/Akt signalling and regulation of small GTPases due to its binding to RHO, RAC1 and CDC42²⁸⁴ and coordinates different cellular activities. Among these activities, regulation of the actin cytoskeleton is one of the best characterized functions²⁸⁴. Under regular

conditions, IQGAP1 co-localizes at the plasma membrane with CAV3 as seen in different cell lines (Figure 37 and 46). However, when pathogenic missense mutations (p.E34K, p.A93T, p.P104L) are present within the CAV3 protein, IQGAP1 seems to accumulate within the Golgi together with CAV3 (Figure 42), thus demonstrating an molecular interplay between these two proteins. Interestingly, IQGAP1 was recently described to interact with CAV1 (a protein having a high homology to CAV3) in adipocytes, modulating the insulin regulated interaction between caveolae and cytoskeletal elements of these cells²⁸⁵.

To gain further insights into the molecular connection between these two proteins, zebrafish models in which either *Iqgap1* or *Cav3* was depleted, were generated. The KD of *Iqgap1* impinges on the number of neuromuscular synapses formed in the dorsal region of the myotome segment, with a more pronounced effect on the pre-patterning of the AChR, a phenotype similar to the one seen in *cav3*-morphants (Figures 38 and 39). Notably, NMJs of the transgenic p.P104L CAV3 mouse model presented also a clear vulnerability of the postsynaptic part reflected by the changes in the morphology: smaller number of clusters, of AChR area, of the perimeter as well as diameter and compactness (Figure 43). Previously, it was reported that CAV3 is enriched at the NMJ and associated with the AChR in skeletal muscle²³⁰. The absence of the CAV3 protein in myotubes affects the AChR clustering as the receptor presents a more diffuse localization. It has been postulated that CAV3 modulates NMJ-integrity and -function via activation of MuSK/RAC1 pathways upon agrin treatment, which in turn initiates a complex signalling cascade that involves the distribution and reorganization of the AChR via cytoskeletal organization which eventually leads to the concentration of the AChR at the NMJ^{274,286}. Additionally, CAV3 might contribute to the AChR clustering via the DGC which has been described to be important for the maintenance of the postsynaptic NMJ given that defects in the endplate were seen in the *mdx* mouse²⁷⁶. Additionally, components of this complex have been described to be enriched at the NMJ, thus the destabilization of the DGC complex which can result also from loss of CAV3 can affect the AChR clustering^{276,287}.

The mechanism of AChR clustering, downstream of MuSK is poorly defined and understood. In skeletal muscle, clustering of the receptor induced by agrin depends on cytoskeletal actin and microtubule system. Upon the activation of MuSK, the dynamics of actin cytoskeleton changes via activation of small GTPases such as CDC42 and RAC1²⁸⁸. So far, the activation of these proteins was attributed to AbI and GGT, two interactors of MuSk^{288,289}. Then the activated Rho-GTPases target different proteins which regulate the actin dynamics namely PAK1, WASP and ROCK. IQGAP1 acts as a small GTPase scaffolding platform recruiting small GTPase regulator

and effectors to the leading edge of the cell²⁹⁰. *In vivo*, IQGAP1 was found to be particularly enriched at the NMJ (Figure 41) and also co-localizing with bungarotoxin in agrin treated myoblasts (Figure 47) suggesting a function in AChR clustering. In cultured primary human myoblasts, overexpression of IQGAP1 alone induces the formation of micro-AChR clusters, which fail to aggregate into larger ones. However, in the presence of agrin, IQGAP1 obviously promotes the formation of larger clusters, thus enhancing agrin activity. This phenomena was seen also in myotubes where the activation of RAC1 and CDC42 is sufficient for the formation of micro-clusters, independent of agrin²⁸⁸. Thus, the overexpression of IQGAP1 might lead to the activation of these two small GTPases. In the primary IQGAP1-overexpression cell line, CAV3 co-localizes with exogenous IQGAP1 at the plasma membrane also in clusters, a form similar to the AChR clusters while in the agrin treated IQGAP1-overexpressing primary myoblasts, the formation of bigger clusters and no diffuse membrane staining could be observed (Figure 46) suggesting that both proteins are recruited for NMJ-formation. Due to its known binding to CDC42, IQGAP1 might also contribute to the formation of actin containing muscle filopodia, also known as myopodia²⁷⁸. These postsynaptic myopodia are in intimate contact with innervating presynaptic axons thus dynamically modulating the synaptic matchmaking²⁹¹.

While previous literature has already provided evidence that the agrin-based activation of MuSK results in recruitment of CDC42 and RAC1 to the NMJs towards the clustering of the AChR²⁸⁸, it still questionable how this process is mediated on the molecular level. Here, based on the interaction of CAV3 (a known binding partner of MuSK) with IQGAP1, an effector for CDC42 and RAC1, a molecular model of their recruitment via IQGAP1 to the NMJs is provided (Figure 51). In the CAV3 p.P104L-diseased murine quadriceps muscle, CDC42 is unchanged in abundance while RAC1-GAP (activator of RAC1) is increased suggesting that the vulnerability of the NMJs seen in these mice is due to defects that appear along the CAV3-IQGAP1 and RAC1-axis. This hypothesis is also supported by the findings from the unbiased proteomic study of p.P104L-diseased murine quadriceps muscle where a vulnerability of the cytoskeleton was observed on the molecular level. This fact also accords with the known role of RAC1 in actin cytoskeletal remodelling which in turn notoriously affects AChR clustering²⁹², a process triggered by the overexpression of IQGAP1 *in vivo* as shown for the first time in this study. Consequently, the discovery of this interaction of IQGAP1 with CAV3 improves the current knowledge of how the assembly of the actin cytoskeleton impacts the AChR clustering. This, in turn, also offers the missing link between RAC1 and CAV3 as there is no clear description of how these proteins are interconnected at the sites of MuSK activation (Figure51).

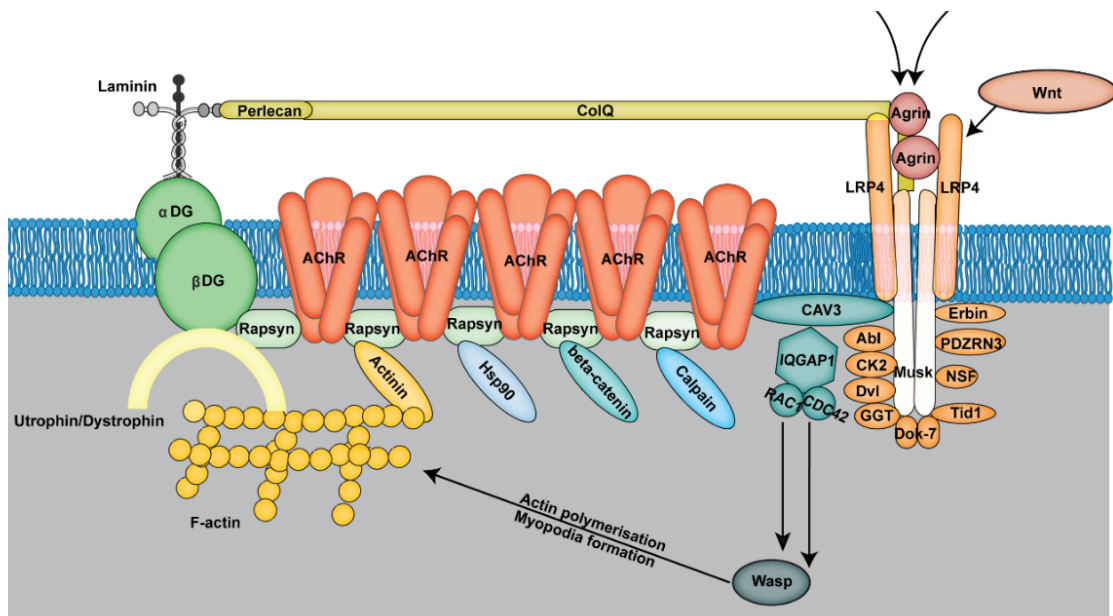


Figure 51. Schematic representation of the proposed mechanism for the clustering of the AChR receptor where IQGAP1 recruits RAC1 and CDC42 at the sites of MuSK activation.

To obtain a deeper understanding of how IQGAP1 promotes NMJ-function and integrity, proteomic signature of primary human muscle cells overexpressing IQGAP1 was determined. From the proteins affected by IQGAP1 overexpression, around 23 proteins belong to processes that are known to be involved in the formation of NMJs (Figure 50):

(I) the overexpression of IQGAP1 alters the abundance of Ras and Rho-GTPases such as dedicator of cytokinesis protein 11 (DOC11), a guanine exchange factor activating CDC42 by exchanging bound GDP for free GTP²⁹³. This suggests that increase of IQGAP1 induces the formation of filopodia (a process known to be controlled by CDC42), concomitant to the activation of RAC1 (Figure 48). Whereas the overexpression of IQGAP1 activates RAC1, which is necessary for the initial phase of AChR cluster formation (aggregation of diffuse AChR into micro-clusters), Rho is crucial for the subsequent condensation of these micro-clusters into full size²⁸⁹. Deactivation of Rho proteins can be observed in the IQGAP1-overexpressing myoblasts by a decrease of GTPase activator protein 23 (RHG23) and thus suggesting a shift to the RAC1 pathway with the concomitant deactivation of Rho proteins.

(II) overexpression of IQGAP1 in myoblasts leads to the up-regulation of proteins involved in the ECM organization. During the neuromuscular development each myofiber secretes and deposits around its ECM surface an assembly of proteins for the basal lamina, and in the case of the NMJ, the nerve contributes with additional factors²⁹⁴. Laminin proteins, especially $\alpha 4$ and $\alpha 5$ chains, appear to be responsible for the accumulation of dystroglycan

receptors at the plasma membrane and thus the up-regulation of LAMA5 might aid in the further maturation of the AChR clusters²⁹⁵. Other ECM proteins increased by the overexpression of IQGAP1 in myoblasts are collagen (CO6A3 and CO5A1) and collagen biosynthesis (MMP2), proteins which contribute as well to the formation of the basal lamina and bridge cells at the ECM²⁹⁴. Mutations in CO6A3 have been associated with Bethlem and Ullrich muscular dystrophies characterized by early childhood onset, muscle weakness and multiple joint contractures, however no reports regarding the NMJ were presented so far²⁹⁶.

(III) mitochondria related proteins are also changed upon the expression of IQGAP1. It is well known that mitochondria are highly enriched at the NMJ where these organelles provide energy for the actin assembly which leads to the formation of filopodia, lamellipodi and synaptic vesicles²⁹⁷. Proteins involved in energy production from fatty acids (EC12) and ketones (OXCT, THIC) are increased in the IQGAP1-overexpressing myoblasts, most likely to provide energy for the formation of CDC42 induced filopodia. In contrast, IMMT, a protein important for mitochondrial morphology, mtDNA organization and mitochondrial fission²⁹⁸ is down-regulated by the overexpression of IQGAP1 and down-regulation of IMMT was linked to the formation of enlarged and spherical mitochondria which are also known as “gigantic mitochondria”²⁹⁹. To fully clarify and understand the beneficial role of IQGAP1 for mitochondria morphology and function further studies would be necessary.

(IV) IQGAP1 together with the cytoplasmic linker protein CLIP170, cooperate in the establishment of proper dendritic morphology via the regulation of microtubule dynamics and actin cytoskeleton polymerization³⁰⁰. The overexpression of IQGAP1 leads to altered levels of proteins involved in axon genesis and nerve development in muscle cells. In the absence of innervation, ANK 1 links pro-neuregulin-3 or NRG to the spectrin based membrane cytoskeleton. Together, these proteins contribute to axonal and dendritic morphogenesis³⁰¹. Further increased proteins involved in axon extension and branching include collagens (CO6A3 and CO5A1), which can act as synapse organizers and CD1661, which also promotes axon guidance and neuronite extension^{294,302}. Elevation of these proteins might be correlated with the effect of IQGAP1-overexpression on increased formation of filopodia (Figure 48). In contrast, proteins involved in nerve development are down regulated in the IQGAP1 cells. One might hypothesize that IQGAP1 overexpression promotes the expression of proteins important for early NMJ-development (like proteins needed for the proper molecular communication between the nerve endplate and muscle) rather than of proteins involved in the later stages of the NMJ-maturation.

Additionally, to the NMJ phenotype, *iqgap1*-morphants present clearly with alterations of the skeletal muscle thus showing a phenotype similar to the one observed in the *cav3*-morphants (Figure 38), suggesting a vulnerability not only of the NMJs but also of the muscle fibres upon the reduction of Iqgap1 (Figure 39). The malfunction of CAV3, due to different mutations, has been associated with the development of several muscle disorders (muscle dystrophy, hyperCKnemia, distal myopathy and rippling muscle disease) with a great heterogeneity even amongst family members²³² and the reduction of CAV3 in muscle fibres has been linked multiple times to muscular phenotypes in different animal models of Caveolinopathy^{238,303}. However, this is the first report showing that reduction of IQGAP1 as a new binding partner of CAV3 also impinges on muscle fibre integrity. Based on the molecular function of IQGAP1, one might speculate that a reduction of this protein affects the actin cytoskeleton and thus the contractile apparatus within the T-tubules system together with the sarcoplasmic reticulum membranes³⁰⁴ having a massive impact on proper muscle fibre contraction. In this context, the presumed beneficial effect of IQGAP1 overexpression on the molecular level might suggest that IQGAP1 elevation (exogenous or via agonists) could open new avenues for the treatment of neuromuscular diseases affecting NMJs-integrity and/or regular actin cytoskeleton. Indeed, the proteomic profiling of intercostal muscles of the first animal model for GFPT1-related CMS-LGMD³⁰⁵ revealed an increase of IQGAP1 most likely to antagonize NMJ- and overall muscle fibre breakdown. This finding has been confirmed via immunofluorescence staining as shown in Figure 57. However, comprehensive studies on CMS and/or muscular dystrophy animal models would be needed to confirm the hypothesis of IQGAP1-elevation as a therapeutic approach in neuromuscular diseases.

To summarize, by identifying IQGAP1 as a new binding partner of CAV3, new evidence on the mechanism of the AChR clustering downstream of MuSK was given. Evidence reinforcing the role of CAV3 at the NMJ was brought about by the analysis of two *in vivo* models, which upon the down regulation of CAV3 show clear defects at the postsynaptic NMJ. The proposed mechanism by which IQGAP1 contributes to the AChR clustering is the recruitment of RAC1 and CDC42 to the sites of MuSK activation via its interaction with CAV3, thus leading to the remodelling of the actin cytoskeleton and the formation of myopodia. Additionally, the proteomic data revealed that the overexpression of IQGAP1 influences other cellular processes which are important for the formation of the postsynaptic NMJ.

3.2.3 Molecular pathophysiology in GFPT1-deficient muscles

3.2.3.1 *GFPT1* is a causative factor for LGMD-CMS

Congenital myasthenic syndromes (CMS) are a heterogeneous group of diseases characterized by impaired neuromuscular transmission as a result of a mutation that affects a constitutive protein of the NMJ⁹⁶. Most of the CMS subtypes are caused by defects in proteins belonging to the postsynaptic region of the NMJ (*CHRNA1*, *CHRN1*, *RAPSN*, *MUSK*, *DOK-7*, *LRP4*) however, recently new groups of genes affecting the glycosylation (*GFPT1*, *DPAGT1*, *ALG2*, *ALG14*) or the synthesis of propyl-oligopeptidase (PREPL) were associated with CMS^{96,306-309}.

Glutamine-fructose-6-phosphate aminotransferase 1 (GFPT1) catalyses the conversion of D-fructose 6-phosphate to D-glucosamide 6-phosphate and glutamate and is a major player in the hexosamine pathway which yields precursors for N and O glycosylation³⁰⁷. This protein is usually expressed in numerous tissues and its mRNA shows two specific splice variants: a long muscle (skeletal muscle and heart) specific isoform designated as GFPT1-L and a ubiquitous GFPT1 isoform⁹⁶. Several mutations (point mutation and deletions) affecting not only the muscle specific exon but spread along the whole coding sequence were described to affect GFPT1 (Figure 52)³¹⁰. These mutations impair the function of the muscle and of NMJs and are surprisingly not leading to multisystemic (metabolic) disorders.

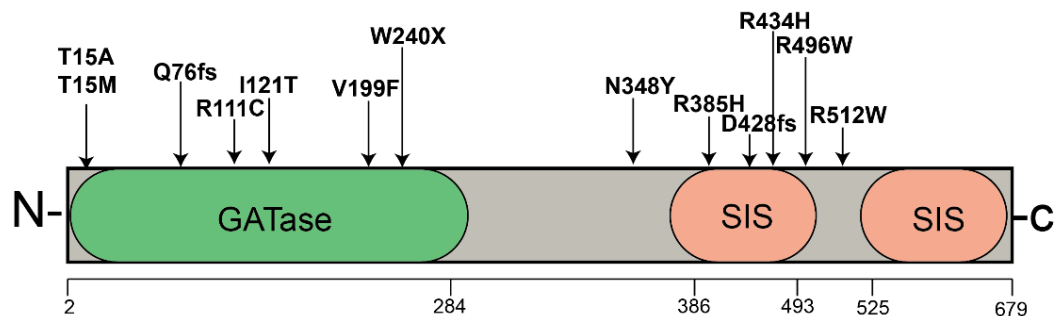


Figure 52. Schematic representation of the GFPT1 domains and the localization of some of the so far identified mutations which spread across the whole domains of the protein: GATase-glutamine amidotransferase type 2 domain and SIS-sugar isomerase domain.

The usual clinical presentation of the patients harbouring *GFPT1* mutations seems to be distinct and consists in a progressive limb-girdle pattern of weakness, normal eye movements, good response to esterase inhibitors and muscle biopsy with tubular aggregates³¹¹. Additionally, patients also present with alterations of the NMJs (reduction in the postsynaptic folds and an

increased fragmentation of the endplate). This morphological observation is also reflected by the abnormal response to electromyography and repetitive nerve stimulation^{309,310}.

To shed light into the underlying pathophysiological processes, a mouse model with a defective glycosylation caused by the muscle-specific knockout of GFPT1 was created and described by Issop and colleagues³⁰⁵. To generate this mouse model, homozygous mice harbouring two loxP sites flanking exon 7 of the *Gfpt1* gene were bred with mice having a *Ckm-Cre* transgene Ckm promoter thus resulting in the depletion of GFPT1 from muscle (*Gfpt1*^{tm1d/tm1d}). The depletion of GFPT1 seems to have no effect on the general and physical appearance when compared with the WT littermates, however mutant mice have lower muscle strength and are more susceptible to fatigue similar to other CMS mouse models³⁰⁵. The NMJs of these mice present changes in the endplate architecture (smaller and more fragmented endplates) as well as in the presynaptic part (axonal fragmentation, thinner myelin sheets)³⁰⁵. Investigation of muscle biopsies revealed an abnormal variance of fiber size, regenerating and necrotic fibers and tubular aggregates. Taking all these characteristics into account, this mouse model represents a good phenocopy of the human disease and is therefore a suitable model for studying the effects of GFPT1 depletion in muscle.

3.2.3.2 *GFPT1-deficiency alters the proteomic signature of intercostal muscle*

Proteomics is a powerful tool that can be successfully used to unravel the biochemical changes that can occur upon disease in either tissue or cells. To better understand the pathophysiology upon muscle-specific GFPT1 KO, intercostal muscles derived from 3 months old control and *Gfpt1*^{tm1d/tm1d} mice were analyzed using LC-MS/MS (label free) in an unbiased manner. A total of 1517 proteins were identified from which 12.5% were found to be statistically significant (p -Anova < 0.05) and 2.8% differentially regulated (39 proteins were up-regulated while 4 were down-regulated) (Figure 53). All quantified proteins were identified with a minimum of one unique peptide and an FDR of 1% at protein and peptide level.

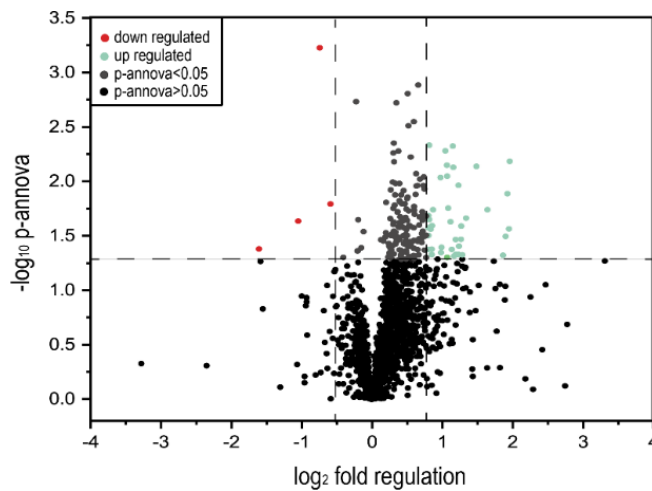


Figure 53. Volcano plot of the proteomics finding obtained by comparing intercostal muscle from the *Gfpt1^{tm1d/tm1d}* with WT littermates. All identified proteins in the muscles are represented and a clear delimitation between the proteins with a p-Anova<0.05 (statistically significant) and “the rest” is made by a horizontal line. Proteins which are decreased are represented in red while the up-regulated ones are in green.

Pathway analysis using KEGG, DAVID and Reactome repositories were performed for all regulated proteins. The absence of GFPT1 is expected to lead to a faulty glycosylation, a fact also mirrored by the results of pathway analysis as proteins (6 out of 39 regulated proteins) that are involved in N and O-glycosylation (N-GlcNAc) or harbour this kind of glycosylation sites are altered in abundance in the *Gfpt1^{tm1d/tm1d}* intercostal muscles (Figure 54A).

Golgi receives cargo-loaded transport molecules or vesicles which contain newly synthesized and folded proteins from the ER and the ERGIC. Interestingly, the pathway analyses revealed a compromised machinery for vesicular trafficking from the ER to the Golgi reflected by an up-regulation of LMAN2, SCFD1 and ARF4 (Figure 54A). The proteomic results also suggest that pathways involved in protein and energy metabolism or actin cytoskeleton organization (Rho GTPase signalling) are also impinged by the KO of GFPT1 in muscle. The subcellular localization of altered proteins is presented in Figure 54B. Approximately 26% of the affected proteins belong to the sarcoplasm and cytoskeleton. Proteins localizing to the myonucleus, SR, Golgi and sarcolemma seem to also be affected in the intercostal muscle of the *Gfpt1^{tm1d/tm1d}* mouse model.

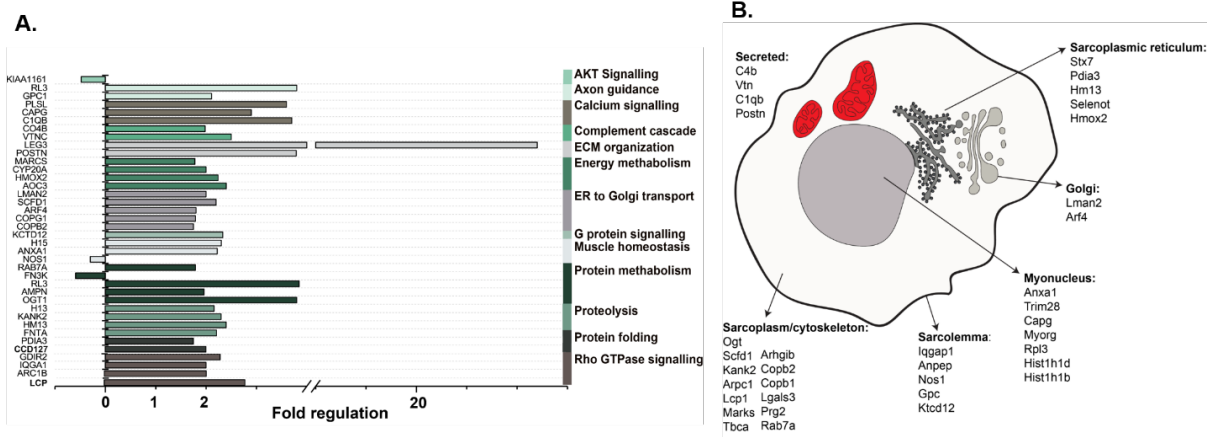


Figure 54. *In silico* analysis of proteomic findings obtained in murine intercostal muscle deficient for GFPT1. (A) Analysis of pathways (KEGG, DAVID and Reactome) associated either with up- or down-regulated proteins revealed by the proteome profiling. (B) Schematic overview of the subcellular compartments and respective proteins that showed a significant fold regulation.

Proteomic signature of GFPT1-deficient intercostal muscles showed an increase in glypcan-1, a heparin sulphate proteoglycan involved in axon guidance and growth³¹². This was further confirmed with the help of immunoblotting (Figure 55). Another protein of interest increased in the GFPT1 KO muscles is FNTA, which plays an active role in the NMJ development. Therefore MuSK, a downstream target of this protein³¹³, was also investigated via immunoblotting³⁰⁵ (Figure 55). The confirmation of the proteomic data was performed by our collaboration partner in the Institute of Genetic Medicine, at Newcastle University.

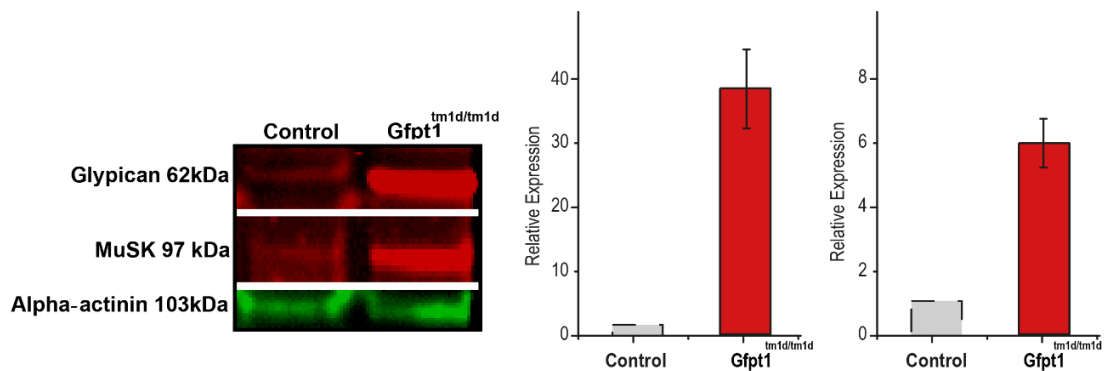


Figure 55. Verification of proteomic findings. Immunoblot analysis confirmed that glypican and MuSK are up-regulated in the intercostal muscles of the Gfpt1^{tm1d/tm1d} mouse. Alpha-actinin was used as a loading control. The expression levels resulted from the immunoblot studies were quantified and normalized to the loading control. For each condition, 3 biological replicates were used. All the immunoblot studies were performed at the Institute of Genetic Medicine, Newcastle³⁰⁵.

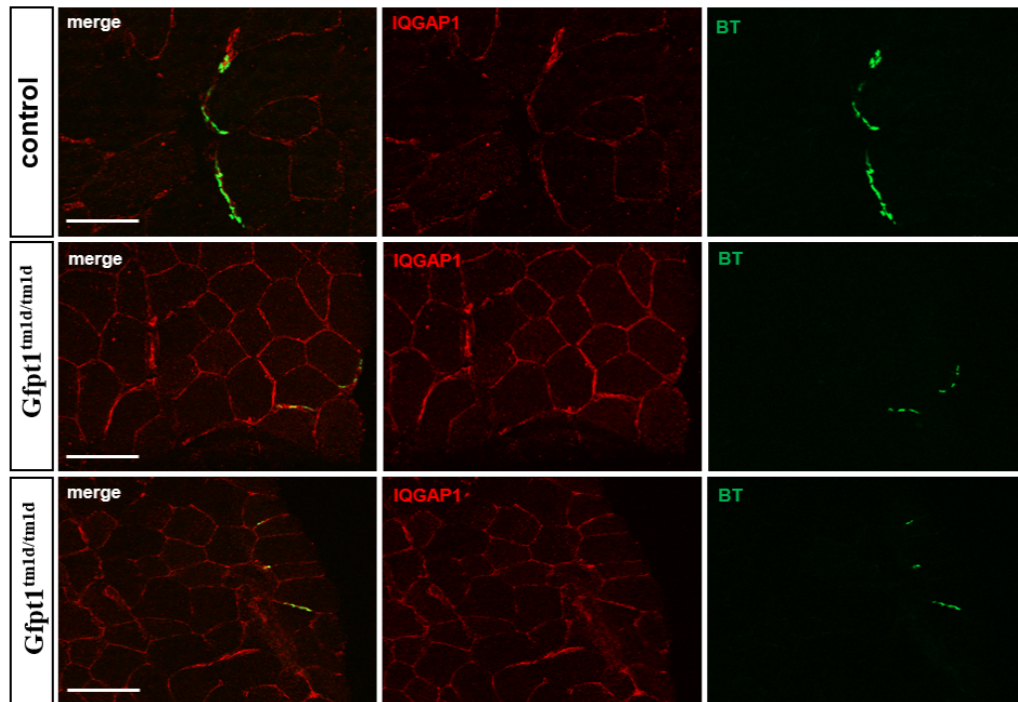


Figure 57. Immunofluorescence analysis of intercostal muscle derived from control and *Gfpt1*^{tm1d/tm1d} 3 months old animals. Muscles were stained against IQGAP1 (red) and bungarotoxin-AChR (green) showing an increase of IQGAP1 at the sarcolemma.

3.2.3.3 Proteomic profiling of *GFPT1*-deficient mice improves the knowledge of *LGMD-CMS*

The precise mechanisms by which mutations in *GFPT1* affect the skeletal muscle and the NMJs exclusively are so far poorly understood. Based on the phenotype described so far by Issop and colleagues, this mouse model resembles closely the one seen in patients harbouring the c.6862A>G mutation, which is responsible for the disruption of the muscle isoform^{140,309}. Glycosylation is a ubiquitous PTM and it is highly probable that *GFPT1* is involved in the glycosylation of a multitude of proteins besides the ones belonging to the NMJ. The proteomic analysis highlighted that 11 of the regulated proteins contain at least one N- or O- GlcNAc glycosylation sites (Table 15). All these proteins are involved in different pathways like protein metabolism, ER to Golgi transport and ECM organization (summarized in table 14).

Table 14. Regulated proteins with N- and O-glycosylation sites

Name	Gene	PTM
Aminopeptidase N	Anpep	N-linked (GlcNAc) asparagine(17)
Complement C4-B	C4b	N-linked (GlcNAc) asparagine (4)

Glypican-1	Gpc1	N-linked (GlcNAc) asparagine(2), O-linked (Xyl) (heparan sulfate) serine (3)
Membrane primary amine oxidase	Vap1	N-linked (GlcNAc) asparagine (4), O-linked (GalNAc)
Minor histocompatibility antigen H13	Hm13	N-linked (GlcNAc) asparagine (2)
Myogenesis-regulating glycosidase	Myorg	N-linked (GlcNAc) asparagine (3)
Periostin	Postn	N-linked (GlcNAc) asparagine
Protein disulfide-isomerase A3	Pdia2	N-linked (GlcNAc) asparagine (3)
UDP-N-acetylglucosamine-peptide N-acetylglucosaminyltransferase	Ogt	O-linked (GlcNAc) serine (2)
Vesicular integral-membrane protein VIP36	Lman2	N-linked (GlcNAc) asparagine
Vitronectin	Vtn	N-linked (GlcNAc) asparagine (3)

Muscle biopsies derived from patients harbouring GFPT1 mutations show the presence of tubular aggregates predominantly in type 2 fibers. Similar findings were also described for the *Gfpt1*^{tm1d/tm1d} animals^{140,311}. The culprit for these aggregates in GFPT1 and DPAGT1 myasthenia was considered to be a functionally deficient STIM1 protein (an ER glycosylated Ca²⁺ controlling protein)³⁰⁹. However, the proteomic data of intercostal muscle derived from the GFPT1 mouse shows unaffected levels of this protein. In contrast, larger sarcoplasmic deposits of CAV3 were described to be present in the muscles of the GFPT1 deficient mice¹⁴⁰. Additionally, proteins involved in the endosomal and vesicular transport like GPC1, LMAN2, SCFD1, ARF4, COPG1 and COPB2 are up regulated, most likely corresponding to a hindered ER to Golgi transport of proteins. GPC1 or glypican 1 is a heparan sulphate proteoglycan, involved in the modulation of growth factors, Schwann cell myelination and skeletal muscle differentiation^{314,315} and was described to localize with caveolin-positive endosomal structures especially upon the initiation of ER-Golgi stress³¹⁶. Another protein indicative of ER stress which is regulated in the proteomic profile is OGT. OGT catalyzes the transfer of an N-acetylglucosamine from UDP-GlcNAc to a serine or threonine and its regulation is highly dependent on the UDP and UDP-GlcNAc levels. Increased levels of this protein were previously associated with an increase of O-GlcNAc which in turn switches on the expression of heat shock proteins³¹⁷. Moreover, PDIA2, a chaperone that protects against misfolded protein aggregation, is also altered in the intercostal muscle proteome of the GFPT1 mouse model³¹⁸. Taking all these factors into consideration, it is plausible that the tubular aggregates detected in muscle biopsies

from GFPT1 deficient human and mice are due to an impaired SR-Golgi and SR associated glycosylation together with the changes in CAV3. An increase of endopeptidase (H13, HM13), responsible for chopping proteins into specific fragments³¹⁹, was also observed most likely as a result of the ER-stress.

As described previously, *Gfpt1*^{tm1d/tm1d} mice present with aberrant AChR clusters and changes in the endplate architecture¹⁴⁰, findings also supported by the proteomic results. Several proteins important in the AChR clustering were found to be altered in abundance. FNTA, a subunit of the GGT complex and a signalling component of the Agrin/MuSK pathway, was found to be upregulated most likely as a cellular attempt to recruit and cluster more AChR³¹³. MuSK was also found to be up-regulated in the muscle in contrast with the AChR clusters which were described as being smaller and fragmented¹⁴⁰. This suggests that the pathogenic mechanism by which the NMJ is affected in the muscle specific GFPT1 deficient mice actually occurs downstream of MuSK. One of the possible affected pathways involves the small guanosine triphosphates Rac1 and CDC42²⁸⁸. Although these proteins appear to be stable in the intercostal muscles of the *Gfpt1* deficient mice, IQGAP1 a direct interactor of these two proteins presents with a significant increase. This protein was described in the previous chapter as being essential for the clustering event and it is recruited by CAV3 at the NMJ where it interacts with MuSK. The increase of FNTA together with the increase of IQGAP1 might represent a cellular attempt to recruit and cluster more AChR. Additionally, other proteins belonging to the Rho GTPase family, which are involved in the cytoskeleton remodelling (important process in the AChR clustering), were also found to be up-regulated in the intercostal muscles of mutant animals probably as a secondary rescue mechanism.

The proteomic data also revealed alterations in other pathways. MYORG is considered to be a glycosylase that activates AKT signalling via the modulation of insulin growth factor 2 (IGF2) that triggers molecular events responsible for muscle growth and regeneration. The down regulation of MYORG leads to reduced activation of IGF2, which was associated with muscle growth³²⁰. This most likely reflects a compensatory mechanism, as an immature NMJ can lead to muscle wasting as described previously and also in the context of other CMS mouse models³²¹.

To summarize, the proteomic analysis of intercostal muscles derived from the GFPT1 mouse model gave insights into the underlying NMJ- and muscle-pathology. Interestingly, IQGAP1, a protein found to be crucial in the clustering of the AChR receptor via its binding to CAV3, was

found to be altered in the intercostal muscle of the *Gfpt1* mouse model, thus suggesting that the alterations seen in the NMJ might be due to the perturbation of pathways downstream of MuSK. Moreover, the proteomics analysis suggests that STIM1, a protein considered to be responsible for the presence of tubular aggregates, is actually not altered in abundance and that other mechanisms contribute to the formation of these aggregates, such as ER-Golgi stress due to impaired glycosylation.

3.2.4 Biochemical changes upon muscle denervation in neuropathies

Inherited degenerative disorders of the peripheral nervous system, or so-called Charcot-Marie-Tooth (CMT) neuropathies, are generally accompanied by progressive muscle loss in the extremities and represent one of the most common inherited neurological disorders affecting approximately 1 in 2,500 people³²². SH3TC2 (SH3 domain and tetratricopeptide repeat-containing protein 2) is a 145 kDa protein with diverse functions like myelination and myelin maintenance and thus regulation

of the proper function of the peripheral nervous system. This is achieved via the control of regular endosomal recycling through SH3TC2 in Schwann cells. In this context, regulation of intracellular protein transport and regulation of ERBB signalling pathway have been linked to SH3TC2 function³²³. The SH3TC2 protein is peripherally localized to the plasma membrane and to the membrane of recycling endosomes of the Schwann cells³²⁴. Mutations in the corresponding *SH3TC2* gene are causative for a demyelinating childhood onset progressive neuropathy called Charcot-Marie-Tooth type 4C (CMT4C). CMT4C is of autosomal recessive inheritance and clinically associated with scoliosis, severe muscle weakness, and atrophy affecting the arms and legs. Other clinical manifestations include delayed age of walking, areflexia and foot deformities^{141,325}. Electron microscopic studies of nerve biopsies revealed existence of abnormal protrusions in non-myelinating Schwann cells, de- and re-myelinated axons presenting as so called onion bulb formations^{326,327}. Arnaud and colleagues described a mouse model which represents a suitable phenocopy of the human disease¹⁴¹. To obtain this first CMT4C animal model, exon 1 of the murine *Sh3tc2* gene was replaced with a GFP cassette, thus leading to a premature stop codon. Mutant mice developed normally, were fertile, lived as long as the WT, and did not present with scoliosis unlike the patients¹⁴¹. Although the *Sh3tc2*^{ΔEx1/ΔEx1} mice appear similar to their WT littermates, they could be distinguished due to the abnormal clenching of toes and clasping of hind limbs upon suspension by tail suggesting

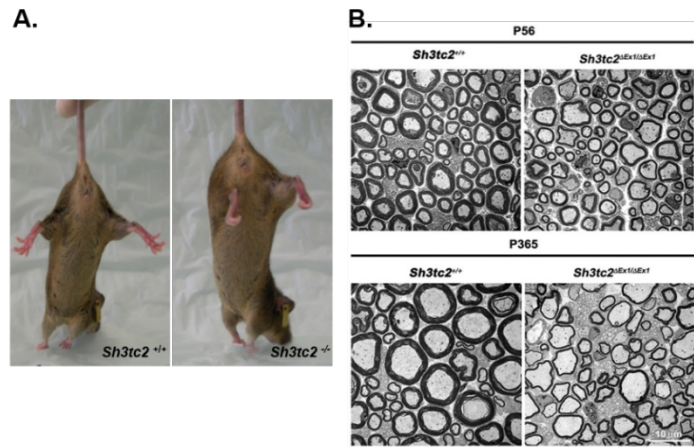


Figure 58. (A) Peripheral neuropathy phenotype in the 2 years old CMT4C mouse model, which presents abnormal clenching of toes and clasping upon tail suspension, suggesting a PNS defect. Electron micrographs of sciatic nerves isolated from WT and the *Sh3tc2*^{ΔEx1/ΔEx1} mice showing a reduced thickness of the myelin sheath.

the presence of a PNS defect (Figure 58A). Additionally, nerve conduction velocities were decreased in SH3TC2-deficient mice, suggesting abnormalities in the peripheral nervous system caused by perturbed myelination which is clearly seen at 56 days and progresses with time¹⁴¹ (Figure 58B). The depletion of SH3TC2 in mice has an impact on the myelination-related gene expression program as genes encoding for structural myelin proteins and cholesterol biosynthesis enzymes (play a role in the formation of the myelin membrane) are down regulated¹⁴¹.

Upon denervation, skeletal muscle undergoes a process of atrophy in which the protein degradation exceeds protein production, finally leading to the replacement of muscle with connective tissue and fat^{328,329}. Other factors that can lead to muscle atrophy include aging, long term immobilization, malnutrition, cancer, cachexia, diabetes, congenital heart failure, renal failure and exposure to toxic elements³³⁰. At the molecular level, upon denervation, several complex processes are triggered leading to a change in gene and respective protein expression affecting pathways that usually control fiber size and contractile performance³²⁹. The cellular shrinkage is mainly caused by the well-known activation of 2 molecular systems, the ubiquitin proteasome system and lysosomal autophagy^{329,330}, however the exact mechanisms which govern this phenomena are still elusive and not fully understood, especially with regard to the maintenance of the atrophied state and the prevention of a total tissue breakdown. The study of the atrophic muscle due to the most common demyelinating neuropathy can lead to the discovery of different mechanisms that prevent the muscle from a total breakdown. Thus, offering promising starting points for the development of therapeutic interventional concepts.

3.2.4.1 Proteomic signature of murine gastrocnemius muscle upon neuropathy related short and long-term denervation

To understand the molecular processes that occur during muscle atrophy upon long and short-term denervation in recessively inherited CMT neuropathies, muscle derived from the *Sh3tc2*^{ΔEx1/ΔEx1} mouse model was analyzed using label-free proteomics. The biochemical effects of short-term denervation of gastrocnemius muscle were identified via comparison of the proteomic signature in this distal muscle derived from 3 months animals with the muscle derived from respective littermates. This study led to the identification of 1391 different proteins. From these proteins just 52 (3.7%) presented with a p-Anova <0.05 from which 3 were up regulated and 6 were down regulated (with a ratio of 2.1>for a statistically significant increase and >0.4 for a statistically significant decrease) (Figure 59A). All quantified proteins had a minimum of two unique peptides and an FDR of 1%. The low number of statistically significant proteins

altered in abundances is most likely due to the lack of changes in the gastrocnemius proteome of these mice as they “solely” present with the first manifesting signs of peripheral neuropathy at 4 weeks after birth and with clear hypomyelination at 8 weeks¹⁴¹. Thus, denervation of gastrocnemius muscle in SH3TC2-deficient animals investigated here only occurred for a period of 4 weeks and is obviously associated with only subtle changes in protein composition.

To study the biochemical changes maintaining the atrophied phase and preventing fibers from break-down, proteomic signature of gastrocnemius muscle derived from 2 years old SH3TC2 deficient mice was compared with the signature of muscle derived from WT mice. To maximize the identifications, in this experiment peptides were measured using two instruments and the combined results led to the identification of 1244 proteins, from which 176 (14%) presented with a p-Anova<0.05 (Figure 59B and C). Out of these proteins, 6 were statistically significant increased and 20 decreased with a ratio of 1.8> for up-regulation and >0.6 for down-regulation.

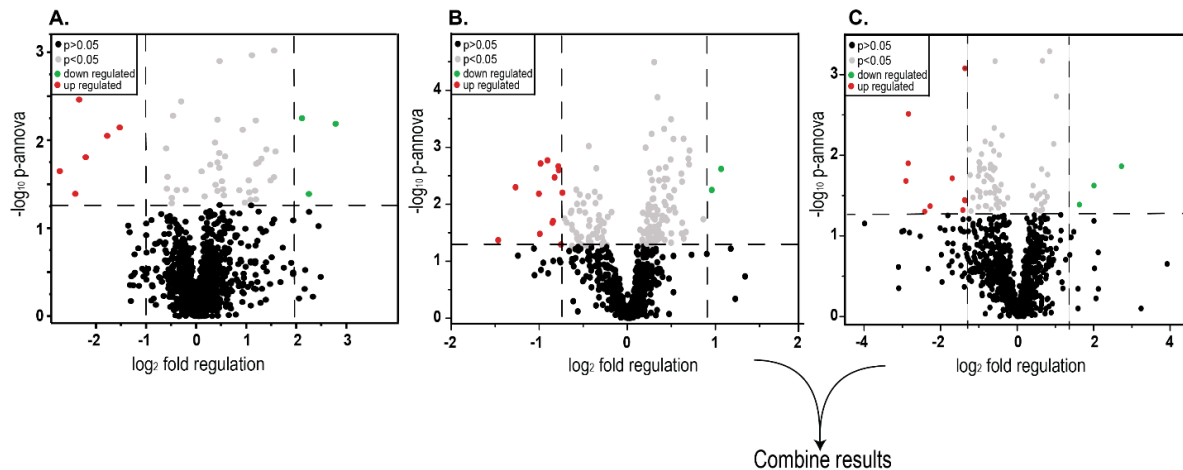


Figure 59. Volcano plot depicting the proteomics findings derived by comparing gastrocnemius muscle from the Sh3tc2 Δ Ex1/ Δ Ex1 (at 3 months-A and 2years old) with WT littermates. The volcano plot shows all the proteins identified in the muscles, making a clear delimitation between the proteins with a p-Anona<0.05 (statistically significant; horizontal line). Proteins, which are decreased, are represented in red while the up-regulated ones are in green. The fold regulation of each data set was determined based on the data distribution.

The subcellular localization of all regulated proteins was assessed using the Uniprot database (Figure 60A and B). For each protein, just one cellular localization was considered. In the muscles derived from 3 months old animals (Figure 60A), most of the altered proteins belong to the mitochondria and cytosol/cytoskeleton while in the muscle of 2 years old animals (Figure 60B) secreted proteins seem to be mostly affected together with the ones belonging to the sarcoplasm/cytoskeleton. In the progressed atrophy, no proteins belonging to mitochondrial functions are affected. Pathway analysis was conducted using Reactome, KEGG and DAVID

databases and revealed that the most perturbed cellular processes in the muscles derived from the 3 month old SH3TC2 deficient mice are related to calcium signalling, glycosylation and the metabolism of fatty acids (Figure 60C). In comparison, in the gastrocnemius muscle of 2 years old mice, multiple and completely different processes seem to be affected due to the long-term denervation (Figure 60-D). Even though some publications described a vast influence of AKT-signalling, FOXO-activation, NF-kappa-B and MAPK-pathways at transcript level during early muscle atrophy, this cannot be deduced from the unbiased proteomic profiling data of the 2 year old *Sh3tc2*^{ΔEx1/ΔEx1} mice^{329,330}. Cellular processes that seem to be the most affected by the long-term denervation belong to muscle contraction, membrane trafficking and extracellular matrix organization (Figure 60D).

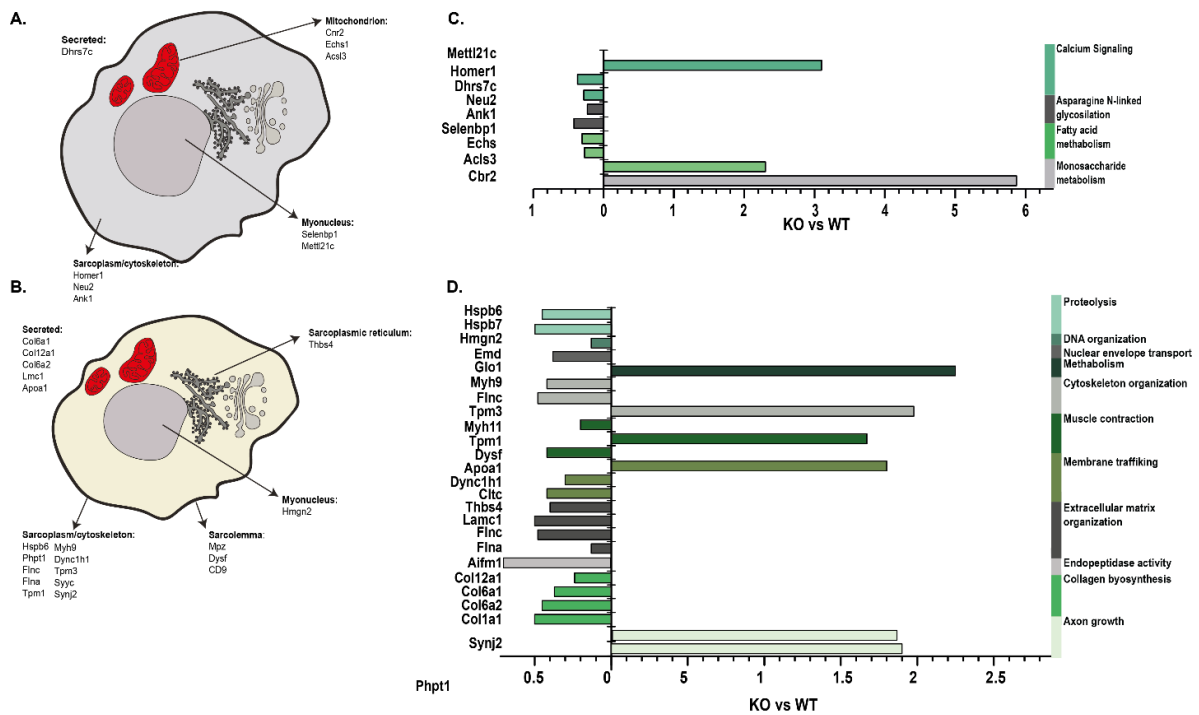


Figure 60. Overview of the molecular changes that result upon long- and short-term denervation in the *Sh3tc2*^{ΔEx1/ΔEx1} muscles. (A) and (B) Subcellular localization of proteins altered in abundance by the short and long-term denervation in the *Sh3tc2* mouse model was assessed using Uniprot database. (C) and (D) *In silico* pathway analysis using Reactome, KEGG and DAVID of all proteins altered in abundance.

3.2.4.2 Longitudinal proteomic profiling of denervated muscle provides insights into the dynamic molecular processes of neurogenic muscular atrophy

A number of publications have reported on the biochemical and molecular changes that occur in several stages of denervation using mouse or rat models in which the sciatic nerve was

sectioned³³¹⁻³³³. This leads to a severe and extremely rapid atrophy of the muscle with the peak being at 3 days post denervation, whereas at 28 days the atrophy process reaches a plateau^{332,333}. This kind of experiment is actually mimicking a muscle atrophy that would occur during acute injury, whereas in the case of peripheral neuropathies, the denervation is a more long-term process occurring gradually over time. To strengthen the knowledge in this field and get a glimpse of what biological processes are affected in muscle atrophy induced by denervation due to a peripheral demyelinating neuropathy, gastrocnemius muscles derived from 3 months and 2 years old SH3TC2-deficient mice were analysed using unbiased proteomic profiling. The *Sh3tc2*^{ΔEx1/ΔEx1} mice present the first signs of neuropathy at 4 weeks, indicated by the lower nerve conductivities; however, at approximately 2 months, hypomyelination is observed so that 3 months of age corresponds to 1 month of de-innervation. Following this, the neuropathy slowly progresses until the mice reach 1 year of age¹⁴¹.

Muscle atrophy is a complex process defined by three stages:

Stage 1 - takes place immediately after denervation with a continuous degradation of muscle fibers due to the activation of ubiquitin-proteasome or autophagy-lysosomal pathways.

Stage 2 - the lost muscle tissue is replaced with fat and collagen.

Stage 3 - maintenance of the atrophied state and activation of satellite cells^{330,333}.

Each of these stages is defined by expression of the so-called “atrogens”, which describe the molecular status of the muscle undergoing atrophy. The proteomics results of younger SH3TC2-deficient mouse could confirm the presence of some of these proteins which are involved in glycolysis (LDHA, TPI1, PGAM1, PGAM2) and ATP synthesis (ATP5A1); however, their expression was stable in the atrophic gastrocnemius muscle of the CMT4C mouse model. The overall protein composition of the denervated gastrocnemius muscle seems to undergo no major changes, as reflected in the low number of regulated proteins (Figure 60). This suggests that 1 month of denervation is not sufficient to trigger the expression of the “atrogenes”. Protein-lysine methyltransferase (Mettl21c) is required under conditions of intense stress and muscle fiber breakdown and its inactivation is linked to an impairment of the autophagy-lysosomal pathway as seen in the deficient *Mettl21c* mouse under denervation conditions³³⁴. This protein is up regulated in the gastrocnemius muscle of 3 months old SH3TC2-deficient mice indicating that at this stage there are markers that suggest a triggering of the autophagy-lysosomal pathway, however no alterations in these pathways were seen in the proteomics. Further immunoblotting analysis of autophagy markers can shed some light on this aspect as some of the proteins

involved in the formation of the autophagosomes like LC3 are not increased in abundance when autophagy is activated but are lipidated, thus not detectable via proteomics³³⁵. In this context, *Mettl21c* might be considered as a marker of early stage muscular atrophy and represents a therapeutic target as its moderation might delay or make the autophagy process milder in muscle atrophy. Sialidase-2 (*Neu2*) is an exoglycosidase that removes sialic acid from glycolipids and is also decreasing in the gastrocnemius muscles of the younger *Sh3tc2*^{ΔEx1/ΔEx1} mice suggesting that sialic acid might play a role in the muscle pathology during the first stages of induction of muscle atrophy. Notably, low amounts of free sialic acid were also linked to the possible muscle pathogenesis in GNE myopathy³³⁶. Other proteins affected in the younger animals are involved in the acylCoA metabolism and β -oxidation (Figure 60). Enoyl-CoA hydratase is an enzyme responsible for the second step in the fatty acid oxidation in the mitochondria, and deficiencies in this enzyme were linked to muscle weakness and with a severe neurodegenerative disorder³³⁷. Moreover, adipogenesis seems to be activated as increase in acylCoA synthase has been linked to the activation of several lipogenic transcription factors including PPAR- γ ³³⁸.

The global proteomic approaches led to the identification of 2 proteins (*Colla1* and *Col5a2*) as being regulated and overlapping with the so called “atrogenes” in the 2 years old *Sh3tc2*^{ΔEx1/ΔEx1} mice. Interestingly, collagen proteins were described as increased during the atrophy process³³² however, in the gastrocnemius muscles these proteins are down-regulated. Other proteins classified as “atrogenes” involved in protein degradation (*Ubb*), glycolysis (*Ldha*, *Phkg1*, *Pgam1*, *Pgam2*) are stable in the older mice. Thus, the results confirm the hypothesis of Satchek and colleagues which states that the expression of most “atrogenes” goes back to baseline with disease progression in order to stop the further loss of muscle mass³³². The spectrum of affected proteins is different in the muscles under continuous atrophy compared to the younger animals. *MPZ* and *LAMC1*, proteins crucial for the myelination of the peripheral nervous system^{141,339}, are decreased, thus reflecting the demyelinating neuropathy as a cause of muscle denervation in this mouse model. Additionally, mutations in *MPZ* are also associated with a demyelinating neuropathy, namely CMT1B³⁴⁰. In contrast, enhanced expression of *SYNJ2* and *PHPt1*, two proteins involved in the development of the nervous system and axonal outgrowth, might be required in order to recruit more vesicles at the synapse and to attenuate axon collapse^{341,342}.

Previous studies have demonstrated that during atrophy, contractile proteins, especially myosins are undergoing changes thus impinging on the number of force developing cross-bridges and are considered a hallmark of muscle wasting. Loss of filamins (*FLNC* and *FLNA*) can be associated with myofibrillar destruction³⁴³. The disruption of the sarcomere is also reflected by

the down-regulation of myosin proteins (Myh9, Myh11) in the SH3TC2-deficient mice of older age. In contrast, TPM1 and TPM3 proteins involved in actin filament organization are increased in abundance probably as a rescue mechanism as actin proteins, components of the Z-disk, are stable upon the maintenance of the atrophied state in the gastrocnemius muscle³⁴⁴. The proteomic results also revealed a down-regulation of dysferlin which is associated with muscle wasting, sarcolemma stability and contraction in LGMD³⁴⁵. Filamins undergo folding and refolding cycles during muscle contraction and have been described to be degraded during muscle atrophy by the ubiquitin-proteasome system³²⁹. FLNA and FLNC show decreased levels in the older animals thus reinforcing the alterations of the Z-disk, a component of the contractile apparatus. Previous studies of atrophic muscles showed at the transcript level that proteins, components of the ECM, especially collagens are up-regulated during the first phases of muscle atrophy³³². In contrast, these proteins are lower in abundance during the maintenance of the atrophied state as collagens are most likely no longer required.

Changes in contractile activity are translated into altered rates of protein production, thereby atrophy is associated with a decrease in protein production and processing³³². The proteome profiling of the *Sh3tc2*^{ΔEx1/ΔEx1} mice revealed a down-regulation of proteins involved in transcription (HMGN2) and in protein export from the nucleus (EMD)³⁴⁶. Moreover, the decrease of CLH1 and DYHC1 indicates that intracellular transport, an important process also for the delivery of newly synthesized proteins to their final subcellular localization, is part of the pathogenesis of muscle atrophy upon long-term denervation. Additionally, a proper vesicular transport depends strongly on the integrity of the cytoskeleton which is affected in the older mice³⁴⁷. During muscle atrophy, changes in metabolism including a shift towards glycolysis and a perturbed capacity of fatty acid oxidation were described^{329,330}. No proteins involved in these pathways seem to be affected during the maintenance of the atrophied state suggesting that the changes in expression of these enzymes occur only in the first phases of neurogenic muscular atrophy.

In conclusion, proteomics allowed the unbiased analysis of gastrocnemius muscle belonging to different stages of denervation in the context of a neurogenic muscular atrophy, utilizing a mouse model of a recessive form of demyelinating CMT neuropathy. This study demonstrated that the starting point of muscle atrophy in the case of a demyelinating neuropathy is quite mild at the biochemical level as only few proteins are affected while during long-term denervation, expression of the most common atrogens returns to baseline and together with several pro-survival proteins might prevent the muscle from a complete breakdown.

4. Final conclusions and remaining challenges

Muscle proteomics is considered to be particularly challenging due to the high dynamic range of the tissue making its analysis quite difficult. Multiple attempts have been made to characterize and provide insights not only into the molecular composition but also into the changes that occur due to disease to open the way for new therapeutic interventions.

This thesis puts forward the most comprehensive protein catalogue yet described. This catalogue not only provides insights into the individual proteome composition of myoblasts, myotubes and muscle tissue – thus providing detailed information regarding the most abundant biological processes – but also provides a useful platform for the muscle research community, which is currently lacking proper information regarding whether a protein is expressed only in a complex tissue or also in myoblasts and/or myotubes. This information will facilitate access to easier model systems to analyse for certain diseases.

By applying mass spectrometry to the study of neuromuscular diseases, insights into their molecularity could be gained. This technique allowed the linkage of INPP5K-CMD and MSS, two rare neuromuscular diseases, by identifying PHGDH as common denominator, and then by utilizing zebrafish models and functional assays the connection was further characterized. A pre-clinical therapeutic approach of this newly acquired knowledge was further demonstrated via the utilization of zebrafish models, where the addition of L-serine improved the brain phenotype in the MSS fish model and also aided in the understanding of why INPP5K disease animal models present with a rather milder vulnerability of the CNS and the NMJs. One of the limitations of this study is that the exact mechanism by which L-serine has a beneficial role on the nervous system is not described and investigated. Further studies on mice might be able to shed some light into this mechanism.

MS based proteomics was particularly helpful for the unravelling of new molecular functions of CAV3 by the identification of IQGAP1 as a new binding partner. This interconnection was further characterized by utilizing different zebrafish models, the p.P104L_CAV3 transgenic mouse model and a IQGAP1-overexpressing human primary myoblasts. This study reinforced the role of CAV3 at the NMJ and proposed a new mechanism by which IQGAP1 recruits RAC1 and CDC42 at the sites of MuSK activation via its interaction with CAV3. Moreover, defective CAV3 depending signalling at the NMJ might also contribute, in part, to the defects observed in muscle diseases characterized by mutations in the *CAV3* gene. A weakness of this study is

that the exact binding region of these two proteins could not be determined or inferred. Crosslinking studies coupled with MS might be able to shed some light into this aspect and event to provide a 3D-structure of these two proteins interacting.

Finally, the protein signature of the muscles derived from three distinct model systems p.P104L_CAV3 transgenic mice , GFPT1-KO mice and the SH3TC2-KO mouse were determined using label free MS based approaches:

- The analysis of gastrocnemius muscle derived from the transgenic p.P104L mouse enhanced the knowledge regarding the ER-Golgi pathology and demonstrated that components of the DGC are up-regulated upon the loss of functional CAV3 thus altering the ECM and the cytoskeleton. While it is hard to elucidate why the expression of these proteins is increased, further studies involving transcript analysis of the DGC components and co-immunofluorescence might shed some light into the underlying mechanism.
- The analysis of intercostal muscle derived from the GFPT1 mouse model gave further insights into the pathophysiology of the NMJs as the alterations seen in these mice might be due to the perturbation of the pathways downstream of MuSK as suggested by an increase of IQGAP1, a protein described in this thesis to be crucial in the postsynaptic NMJs. While it is still hard to define a clear mechanism, based solely on the results presented, by which the muscle and the NMJ in this mouse model are altered, proteomics offers good guidance as to the direction further studies should take.
- The analysis of gastrocnemius muscle belonging to different stages of denervation, as a result of a demyelinating CMT neuropathy, allowed the characterization of the molecular processes that occur in these muscles. During long term denervation very few proteins are affected while in the long term denervation the expression of the well known atrogens returns to baseline in order to prevent the muscle from further breakdown.

These kind of studies give insights into the different underlying pathophysiologies in the case of diseases and also offer a tool for the development of possible therapeutic approaches.

5. Acknowledgments

First and foremost, I would like to express my sincere gratitude to Dr. Andreas Roos for his ongoing support, advice, patience and enthusiasm towards me and my research topic. He has continually motivated me to think critically and independently, and had faith in me even when I did not. I would also like to thank Prof. Kristina Lorenz and Prof. Sickman not only for giving me the opportunity to undertake a PhD at ISAS but also for their ongoing support.

Secondly, I would like to offer my gratitude to the patients and healthy volunteers who agreed to undergo an invasive procedure, such as biopsy in order to donate tissue for this research.

Fortunately, I had the chance to carry out a part of this research in an incredibly friendly lab at ISAS. I would like to thank Vietxuan Phan for being such a great colleague throughout the four years of this PhD. I will forever be indebted to Dr. Raffael Kettler for the preparation of much needed constructs and plasmids and for introducing me to the world of cloning. Additionally, I would like to thank Sarah Waide for her help in cell culture and for always making it fun. My sincere thanks go to Dr. Erik Freier and Dr. Ute Münchberg for their kind help with the microscopy part conducted at ISAS.

It gives me great pleasure to thank all my past and present co-workers from different research groups from ISAS, especially from the Lipidomics CARS and Protein Dynamics, for all the coffee breaks, lunches, laughs and good times. Through your teasing, joking and high spirits, you all made being in the institute a fun experience.

A great experience for which I am very grateful was the one I had in Newcastle at the John Walton Muscular Dystrophy Research Center. I would like to thank Prof. Lochmüller for having me in his laboratory and for helping me to gain so much knowledge in the muscle field. Special thanks go to Dan Cox for introducing me to zebrafish research and for being so helpful and kind at all times – I will always remember the fish lab with great fondness. I would also like to extend special thanks to Emily O'Connor, for not only being a great colleague but also a friend, with an endless reserve of good mood. Regardless of her work load, Emily was always willing to stop what she was doing and answer my barrage of questions and offer great advice.

My sincere gratitude is also extended to Dr. Sally Spendiff for her kind help and support in the lab but also for her incredible endurance in reading through the draft of this thesis, and for always having the time and patience to help.

Additionally, I would like to express my gratitude to Prof. David Rubinzstein from the Institute of Medical Research, Cambridge for having me as a visiting scientist in his laboratory. Special thanks go to Dr. Mariana Pavel for her endless patience and willingness to teach me immunoblotting and immunofluorescence.

I have been so fortunate to be always surrounded by a great group of people that have been so supportive over this long and hard process. Last but by no means least; I would like to thank my boyfriend, Dominic, as well as my family for their ongoing love, support and encouragement. I could not have completed this PhD without them. To many other friends in and out of the institute, thank you for keeping me laughing, optimistic and for showing me that there is life outside the lab.

It has been a long way (literally there is a long way from Romania to Germany) since the first time I stepped into ISAS. I have experienced many things while doing my PhD: I have laughed, smiled, got angry, fell down and missed a lot of people. To be honest it is still hard to believe that THE DAY HAS COME!

6. References:

- 1 Hathaway, D. R., March, K. L., Lash, J. A., Adam, L. P. & Wilensky, R. L. Vascular smooth muscle. A review of the molecular basis of contractility. *Circulation* **83**, 382-390 (1991).
- 2 Tabebordbar, M., Wang, E. T. & Wagers, A. J. Skeletal muscle degenerative diseases and strategies for therapeutic muscle repair. *Annu Rev Pathol* **8**, 441-475, doi:10.1146/annurev-pathol-011811-132450 (2013).
- 3 Frontera, W. R. & Ochala, J. Skeletal muscle: a brief review of structure and function. *Calcif Tissue Int* **96**, 183-195, doi:10.1007/s00223-014-9915-y (2015).
- 4 Wolfe, R. R. The underappreciated role of muscle in health and disease. *Am J Clin Nutr* **84**, 475-482 (2006).
- 5 Jones, D., Round, J. & de Haan, A. in *Skeletal Muscle from Molecules to Movement* 1-8 (Churchill Livingstone, 2004).
- 6 Cooke, R. The sliding filament model: 1972-2004. *J Gen Physiol* **123**, 643-656, doi:10.1085/jgp.200409089 (2004).
- 7 E, H. H. in *Nature* Vol. 173 973-976 (1954).
- 8 Jones, D., Round, J. & de Haan, A. in *Skeletal Muscle from Molecules to Movement* vii (Churchill Livingstone, 2004).
- 9 Rebbeck, R. T. *et al.* Skeletal muscle excitation-contraction coupling: who are the dancing partners? *Int J Biochem Cell Biol* **48**, 28-38, doi:10.1016/j.biocel.2013.12.001 (2014).
- 10 Jones, D., Round, J. & de Haan, A. in *Skeletal Muscle from Molecules to Movement* 21-29 (Churchill Livingstone, 2004).
- 11 Hynes, T. R., Block, S. M., White, B. T. & Spudich, J. A. Movement of myosin fragments in vitro: domains involved in force production. *Cell* **48**, 953-963 (1987).
- 12 Gaitanos, G. C., Williams, C., Boobis, L. H. & Brooks, S. Human muscle metabolism during intermittent maximal exercise. *J Appl Physiol (1985)* **75**, 712-719, doi:10.1152/jappl.1993.75.2.712 (1993).
- 13 Spriet, L. L. Anaerobic metabolism in human skeletal muscle during short-term, intense activity. *Can J Physiol Pharmacol* **70**, 157-165 (1992).
- 14 Kunz, W. S. Control of oxidative phosphorylation in skeletal muscle. *Biochim Biophys Acta* **1504**, 12-19 (2001).
- 15 Schiaffino, S. & Reggiani, C. Fiber types in mammalian skeletal muscles. *Physiol Rev* **91**, 1447-1531, doi:10.1152/physrev.00031.2010 (2011).
- 16 Edstrom, L. & Kugelberg, E. Histochemical composition, distribution of fibres and fatiguability of single motor units. Anterior tibial muscle of the rat. *J Neurol Neurosurg Psychiatry* **31**, 424-433 (1968).
- 17 Close, R. Properties of motor units in fast and slow skeletal muscles of the rat. *J Physiol* **193**, 45-55 (1967).
- 18 Schiaffino, S., Hanzlikova, V. & Pierobon, S. Relations between structure and function in rat skeletal muscle fibers. *J Cell Biol* **47**, 107-119 (1970).
- 19 Schiaffino, S. *et al.* Three myosin heavy chain isoforms in type 2 skeletal muscle fibres. *J Muscle Res Cell Motil* **10**, 197-205 (1989).
- 20 Schiaffino, S. *et al.* Myosin heavy chain isoforms and velocity of shortening of type 2 skeletal muscle fibres. *Acta Physiol Scand* **134**, 575-576, doi:10.1111/j.1748-1716.1998.tb08539.x (1988).

- 21 Larsson, L., Edstrom, L., Lindegren, B., Gorza, L. & Schiaffino, S. MHC composition and enzyme-histochemical and physiological properties of a novel fast-twitch motor unit type. *Am J Physiol* **261**, C93-101, doi:10.1152/ajpcell.1991.261.1.C93 (1991).
- 22 Egan, B. & Zierath, J. R. Exercise metabolism and the molecular regulation of skeletal muscle adaptation. *Cell Metab* **17**, 162-184, doi:10.1016/j.cmet.2012.12.012 (2013).
- 23 Jones, D. A., Jackson, M. J., McPhail, G. & Edwards, R. H. Experimental mouse muscle damage: the importance of external calcium. *Clin Sci (Lond)* **66**, 317-322 (1984).
- 24 Hikida, R. S. Aging changes in satellite cells and their functions. *Curr Aging Sci* **4**, 279-297 (2011).
- 25 Charge, S. B. & Rudnicki, M. A. Cellular and molecular regulation of muscle regeneration. *Physiol Rev* **84**, 209-238, doi:10.1152/physrev.00019.2003 (2004).
- 26 Deshmukh, A. S. *et al.* Deep proteomics of mouse skeletal muscle enables quantitation of protein isoforms, metabolic pathways, and transcription factors. *Mol Cell Proteomics* **14**, 841-853, doi:10.1074/mcp.M114.044222 (2015).
- 27 Gelfi, C., Vasso, M. & Cerretelli, P. Diversity of human skeletal muscle in health and disease: contribution of proteomics. *J Proteomics* **74**, 774-795, doi:10.1016/j.jprot.2011.02.028 (2011).
- 28 Linke, W. A. Titin Gene and Protein Functions in Passive and Active Muscle. *Annu Rev Physiol*, doi:10.1146/annurev-physiol-021317-121234 (2017).
- 29 Ottenheijm, C. A. & Granzier, H. Lifting the nebula: novel insights into skeletal muscle contractility. *Physiology (Bethesda)* **25**, 304-310, doi:10.1152/physiol.00016.2010 (2010).
- 30 Gillies, A. R. & Lieber, R. L. Structure and function of the skeletal muscle extracellular matrix. *Muscle Nerve* **44**, 318-331, doi:10.1002/mus.22094 (2011).
- 31 Gelse, K., Poschl, E. & Aigner, T. Collagens--structure, function, and biosynthesis. *Adv Drug Deliv Rev* **55**, 1531-1546 (2003).
- 32 Kamga, C., Krishnamurthy, S. & Shiva, S. Myoglobin and mitochondria: a relationship bound by oxygen and nitric oxide. *Nitric Oxide* **26**, 251-258, doi:10.1016/j.niox.2012.03.005 (2012).
- 33 Davies, K. E. & Nowak, K. J. Molecular mechanisms of muscular dystrophies: old and new players. *Nat Rev Mol Cell Biol* **7**, 762-773, doi:10.1038/nrm2024 (2006).
- 34 Hackman, P. *et al.* Tibial muscular dystrophy is a titinopathy caused by mutations in TTN, the gene encoding the giant skeletal-muscle protein titin. *Am J Hum Genet* **71**, 492-500, doi:10.1086/342380 (2002).
- 35 Chauveau, C. *et al.* Recessive TTN truncating mutations define novel forms of core myopathy with heart disease. *Hum Mol Genet* **23**, 980-991, doi:10.1093/hmg/ddt494 (2014).
- 36 Bonne, G. *et al.* Mutations in the gene encoding lamin A/C cause autosomal dominant Emery-Dreifuss muscular dystrophy. *Nat Genet* **21**, 285-288, doi:10.1038/6799 (1999).
- 37 McNally, E. M. & Pytel, P. Muscle diseases: the muscular dystrophies. *Annu Rev Pathol* **2**, 87-109, doi:10.1146/annurev.pathol.2.010506.091936 (2007).
- 38 Hoogerwaard, E. M. *et al.* Signs and symptoms of Duchenne muscular dystrophy and Becker muscular dystrophy among carriers in The Netherlands: a cohort study. *Lancet* **353**, 2116-2119 (1999).
- 39 Koenig, M. & Kunkel, L. M. Detailed analysis of the repeat domain of dystrophin reveals four potential hinge segments that may confer flexibility. *J Biol Chem* **265**, 4560-4566 (1990).
- 40 Rybakova, I. N., Patel, J. R. & Ervasti, J. M. The dystrophin complex forms a mechanically strong link between the sarcolemma and costameric actin. *J Cell Biol* **150**, 1209-1214 (2000).

- 41 Murphy, A. P. & Straub, V. The Classification, Natural History and Treatment of the Limb Girdle Muscular Dystrophies. *J Neuromuscul Dis* **2**, S7-S19, doi:10.3233/JND-150105 (2015).
- 42 Bushby, K. M. Diagnostic criteria for the limb-girdle muscular dystrophies: report of the ENMC Consortium on Limb-Girdle Dystrophies. *Neuromuscul Disord* **5**, 71-74 (1995).
- 43 Hauser, M. A. *et al.* myotilin Mutation found in second pedigree with LGMD1A. *Am J Hum Genet* **71**, 1428-1432, doi:10.1086/344532 (2002).
- 44 Muchir, A. *et al.* Identification of mutations in the gene encoding lamins A/C in autosomal dominant limb girdle muscular dystrophy with atrioventricular conduction disturbances (LGMD1B). *Hum Mol Genet* **9**, 1453-1459 (2000).
- 45 Gazzo, E., Bonetto, A. & Minetti, C. Caveolinopathies: translational implications of caveolin-3 in skeletal and cardiac muscle disorders. *Handb Clin Neurol* **101**, 135-142, doi:10.1016/B978-0-08-045031-5.00010-4 (2011).
- 46 Sarparanta, J. *et al.* Mutations affecting the cytoplasmic functions of the co-chaperone DNAJB6 cause limb-girdle muscular dystrophy. *Nat Genet* **44**, 450-455, S451-452, doi:10.1038/ng.1103 (2012).
- 47 Richard, I. *et al.* Calpainopathy-a survey of mutations and polymorphisms. *Am J Hum Genet* **64**, 1524-1540, doi:10.1086/302426 (1999).
- 48 Liu, J. *et al.* Dysferlin, a novel skeletal muscle gene, is mutated in Miyoshi myopathy and limb girdle muscular dystrophy. *Nat Genet* **20**, 31-36, doi:10.1038/1682 (1998).
- 49 Valle, G. *et al.* Telethonin, a novel sarcomeric protein of heart and skeletal muscle. *FEBS Lett* **415**, 163-168 (1997).
- 50 Chardon, J. W. *et al.* LIMS2 mutations are associated with a novel muscular dystrophy, severe cardiomyopathy and triangular tongues. *Clin Genet* **88**, 558-564, doi:10.1111/cge.12561 (2015).
- 51 Gundesli, H. *et al.* Mutation in exon 1f of PLEC, leading to disruption of plectin isoform 1f, causes autosomal-recessive limb-girdle muscular dystrophy. *Am J Hum Genet* **87**, 834-841, doi:10.1016/j.ajhg.2010.10.017 (2010).
- 52 Bogershausen, N. *et al.* Recessive TRAPPC11 mutations cause a disease spectrum of limb girdle muscular dystrophy and myopathy with movement disorder and intellectual disability. *Am J Hum Genet* **93**, 181-190, doi:10.1016/j.ajhg.2013.05.028 (2013).
- 53 Bolduc, V. *et al.* Recessive mutations in the putative calcium-activated chloride channel Anoctamin 5 cause proximal LGMD2L and distal MMD3 muscular dystrophies. *Am J Hum Genet* **86**, 213-221, doi:10.1016/j.ajhg.2009.12.013 (2010).
- 54 Bertini, E., D'Amico, A., Gualandi, F. & Petrini, S. Congenital muscular dystrophies: a brief review. *Semin Pediatr Neurol* **18**, 277-288, doi:10.1016/j.spen.2011.10.010 (2011).
- 55 Wiessner, M. *et al.* Mutations in INPP5K, Encoding a Phosphoinositide 5-Phosphatase, Cause Congenital Muscular Dystrophy with Cataracts and Mild Cognitive Impairment. *Am J Hum Genet* **100**, 523-536, doi:10.1016/j.ajhg.2017.01.024 (2017).
- 56 Clarke, N. F. *et al.* Congenital muscular dystrophy type 1D (MDC1D) due to a large intragenic insertion/deletion, involving intron 10 of the LARGE gene. *Eur J Hum Genet* **19**, 452-457, doi:10.1038/ejhg.2010.212 (2011).
- 57 Vigliano, P., Dassi, P., Di Blasi, C., Mora, M. & Jarre, L. LAMA2 stop-codon mutation: merosin-deficient congenital muscular dystrophy with occipital polymicrogyria, epilepsy and psychomotor regression. *Eur J Paediatr Neurol* **13**, 72-76, doi:10.1016/j.ejpn.2008.01.010 (2009).
- 58 Fukuyama, Y., Osawa, M. & Suzuki, H. Congenital progressive muscular dystrophy of the Fukuyama type - clinical, genetic and pathological considerations. *Brain Dev* **3**, 1-29 (1981).

- 59 Lefeber, D. J. *et al.* Deficiency of Dol-P-Man synthase subunit DPM3 bridges the congenital disorders of glycosylation with the dystroglycanopathies. *Am J Hum Genet* **85**, 76-86, doi:10.1016/j.ajhg.2009.06.006 (2009).
- 60 Baker, N. L. *et al.* Molecular consequences of dominant Bethlem myopathy collagen VI mutations. *Ann Neurol* **62**, 390-405, doi:10.1002/ana.21213 (2007).
- 61 Mahjneh, I. *et al.* Merosin-positive congenital muscular dystrophy: a large inbred family. *Neuropediatrics* **30**, 22-28, doi:10.1055/s-2007-973452 (1999).
- 62 Chacon-Cabrera, A., Gea, J. & Barreiro, E. Short- and Long-Term Hindlimb Immobilization and Reloading: Profile of Epigenetic Events in Gastrocnemius. *J Cell Physiol* **232**, 1415-1427, doi:10.1002/jcp.25635 (2017).
- 63 Strasser, B., Volaklis, K., Fuchs, D. & Burtscher, M. Role of Dietary Protein and Muscular Fitness on Longevity and Aging. *Aging Dis* **9**, 119-132, doi:10.14336/AD.2017.0202 (2018).
- 64 Mary, P., Servais, L. & Vialle, R. Neuromuscular diseases: Diagnosis and management. *Orthop Traumatol Surg Res*, doi:10.1016/j.otsr.2017.04.019 (2017).
- 65 Fardeau, M. & Desguerre, I. Diagnostic workup for neuromuscular diseases. *Handb Clin Neurol* **113**, 1291-1297, doi:10.1016/B978-0-444-59565-2.00001-0 (2013).
- 66 Orrell, R. W., Habgood, J. J., de Belleruche, J. S. & Lane, R. J. The relationship of spinal muscular atrophy to motor neuron disease: investigation of SMN and NAIP gene deletions in sporadic and familial ALS. *J Neurol Sci* **145**, 55-61 (1997).
- 67 Tiriyaki, E. & Horak, H. A. ALS and other motor neuron diseases. *Continuum (Minneap Minn)* **20**, 1185-1207, doi:10.1212/01.CON.0000455886.14298.a4 (2014).
- 68 Zarei, S. *et al.* A comprehensive review of amyotrophic lateral sclerosis. *Surg Neurol Int* **6**, 171, doi:10.4103/2152-7806.169561 (2015).
- 69 Abhinav, K. *et al.* Amyotrophic lateral sclerosis in South-East England: a population-based study. The South-East England register for amyotrophic lateral sclerosis (SEALS Registry). *Neuroepidemiology* **29**, 44-48, doi:10.1159/000108917 (2007).
- 70 Logroscino, G. *et al.* Descriptive epidemiology of amyotrophic lateral sclerosis: new evidence and unsolved issues. *J Neurol Neurosurg Psychiatry* **79**, 6-11, doi:10.1136/jnnp.2006.104828 (2008).
- 71 Wijesekera, L. C. & Leigh, P. N. Amyotrophic lateral sclerosis. *Orphanet J Rare Dis* **4**, 3, doi:10.1186/1750-1172-4-3 (2009).
- 72 Schymick, J. C., Talbot, K. & Traynor, B. J. Genetics of sporadic amyotrophic lateral sclerosis. *Hum Mol Genet* **16 Spec No. 2**, R233-242, doi:10.1093/hmg/ddm215 (2007).
- 73 Siuda, J. *et al.* ALS-FTD complex disorder due to C9ORF72 gene mutation: description of first Polish family. *Eur Neurol* **72**, 64-71, doi:10.1159/000362267 (2014).
- 74 Maragakis, N. J. Motor neuron disease: progressive muscular atrophy in the ALS spectrum. *Nat Rev Neurol* **6**, 187-188, doi:10.1038/nrneurol.2010.29 (2010).
- 75 Kim, W. K. *et al.* Study of 962 patients indicates progressive muscular atrophy is a form of ALS. *Neurology* **73**, 1686-1692, doi:10.1212/WNL.0b013e3181c1dea3 (2009).
- 76 Kolb, S. J. & Kissel, J. T. Spinal muscular atrophy: a timely review. *Arch Neurol* **68**, 979-984, doi:10.1001/archneurol.2011.74 (2011).
- 77 Kolb, S. J. & Kissel, J. T. Spinal Muscular Atrophy. *Neurol Clin* **33**, 831-846, doi:10.1016/j.ncl.2015.07.004 (2015).
- 78 Monani, U. R. Spinal muscular atrophy: a deficiency in a ubiquitous protein; a motor neuron-specific disease. *Neuron* **48**, 885-896, doi:10.1016/j.neuron.2005.12.001 (2005).
- 79 Hughes, R. A. Peripheral neuropathy. *BMJ* **324**, 466-469 (2002).
- 80 Martyn, C. N. & Hughes, R. A. Epidemiology of peripheral neuropathy. *J Neurol Neurosurg Psychiatry* **62**, 310-318 (1997).

- 81 Rossor, A. M., Polke, J. M., Houlden, H. & Reilly, M. M. Clinical implications of genetic advances in Charcot-Marie-Tooth disease. *Nat Rev Neurol* **9**, 562-571, doi:10.1038/nrneurol.2013.179 (2013).
- 82 Pareyson, D. & Marchesi, C. Diagnosis, natural history, and management of Charcot-Marie-Tooth disease. *Lancet Neurol* **8**, 654-667, doi:10.1016/S1474-4422(09)70110-3 (2009).
- 83 Barisic, N. *et al.* Charcot-Marie-Tooth disease: a clinico-genetic confrontation. *Ann Hum Genet* **72**, 416-441, doi:10.1111/j.1469-1809.2007.00412.x (2008).
- 84 Szigeti, K. & Lupski, J. R. Charcot-Marie-Tooth disease. *Eur J Hum Genet* **17**, 703-710, doi:10.1038/ejhg.2009.31 (2009).
- 85 Pareyson, D. Differential diagnosis of Charcot-Marie-Tooth disease and related neuropathies. *Neurol Sci* **25**, 72-82, doi:10.1007/s10072-004-0233-4 (2004).
- 86 Sanes, J. R. & Lichtman, J. W. Induction, assembly, maturation and maintenance of a postsynaptic apparatus. *Nat Rev Neurosci* **2**, 791-805, doi:10.1038/35097557 (2001).
- 87 Wu, H. T., Xiong, W. C. & Mei, L. To build a synapse: signaling pathways in neuromuscular junction assembly. *Development* **137**, 1017-1033, doi:10.1242/dev.038711 (2010).
- 88 Kullberg, R. W., Lentz, T. L. & Cohen, M. W. Development of the myotomal neuromuscular junction in *Xenopus laevis*: an electrophysiological and fine-structural study. *Dev Biol* **60**, 101-129 (1977).
- 89 Unwin, N. Nicotinic acetylcholine receptor and the structural basis of neuromuscular transmission: insights from *Torpedo* postsynaptic membranes. *Q Rev Biophys* **46**, 283-322, doi:10.1017/S0033583513000061 (2013).
- 90 Keshishian, H., Broadie, K., Chiba, A. & Bate, M. The *Drosophila* neuromuscular junction: A model system for studying synaptic development and function. *Annual Review of Neuroscience* **19**, 545-575, doi:DOI 10.1146/annurev.ne.19.030196.002553 (1996).
- 91 Abicht, A., Kroger, S. & Schoser, B. Neuromuscular signal transmission in adulthood. Current facets of acquired and hereditary disorders. *Nervenarzt* **82**, 707-+, doi:10.1007/s00115-010-2969-9 (2011).
- 92 Alpern, R. J. The Physiological-Basis of Neuromuscular-Transmission Disorders. *Hosp Pract* **27**, 12-13 (1992).
- 93 Confalonieri, P., Antozzi, C., Mora, M. & Mantegazza, R. Disorders of neuromuscular transmission in childhood. *Mariani F P* **5**, 77-88 (1997).
- 94 Mahadeva, B., Phillips, L. H. & Juel, V. C. Autoimmune disorders of neuromuscular transmission. *Semin Neurol* **28**, 212-227, doi:10.1055/s-2008-1062260 (2008).
- 95 Darabid, H., Perez-Gonzalez, A. P. & Robitaille, R. Neuromuscular synaptogenesis: coordinating partners with multiple functions. *Nature Reviews Neuroscience* **15**, 703-718, doi:10.1038/nrn3821 (2014).
- 96 Evangelista, T., Hanna, M. & Lochmuller, H. Congenital Myasthenic Syndromes with Predominant Limb Girdle Weakness. *J Neuromuscul Dis* **2**, S21-S29, doi:10.3233/JND-150098 (2015).
- 97 Nicole, S. *et al.* Congenital Myasthenic Syndromes or Inherited Disorders of Neuromuscular Transmission: Recent Discoveries and Open Questions. *J Neuromuscul Dis* **4**, 269-284, doi:10.3233/JND-170257 (2017).
- 98 O'Connor, E. *et al.* Clinical and research strategies for limb-girdle congenital myasthenic syndromes. *Ann N Y Acad Sci* **1412**, 102-112, doi:10.1111/nyas.13520 (2018).
- 99 Muller, J. S. *et al.* Dok-7 promotes slow muscle integrity as well as neuromuscular junction formation in a zebrafish model of congenital myasthenic syndromes. *Human Molecular Genetics* **19**, 1726-1740, doi:10.1093/hmg/ddq049 (2010).

- 100 Chevessier, F. *et al.* MuSK, a new target for mutations causing congenital myasthenic syndromes. *Neuromuscular Disord* **16**, S147-S148 (2006).
- 101 Milone, M. *et al.* Myasthenic syndrome due to defects in rapsyn Clinical and molecular findings in 39 patients. *Neurology* **73**, 228-235, doi:10.1212/WNL.0b013e3181ae7cbc (2009).
- 102 Ohkawara, B. *et al.* LRP4 third beta-propeller domain mutations cause novel congenital myasthenia by compromising agrin-mediated MuSK signaling in a position-specific manner. *Hum Mol Genet* **23**, 1856-1868, doi:10.1093/hmg/ddt578 (2014).
- 103 O'Connor, E. *et al.* Identification of mutations in the MYO9A gene in patients with congenital myasthenic syndrome. *Brain* **139**, 2143-2153, doi:10.1093/brain/aww130 (2016).
- 104 Beeson, D. Congenital myasthenic syndromes: recent advances. *Curr Opin Neurol* **29**, 565-571, doi:10.1097/WCO.0000000000000370 (2016).
- 105 Hosp, F. & Mann, M. A Primer on Concepts and Applications of Proteomics in Neuroscience. *Neuron* **96**, 558-571, doi:10.1016/j.neuron.2017.09.025 (2017).
- 106 Dunkley, T. P. J., Watson, R., Griffin, J. L., Dupree, P. & Lilley, K. S. Localization of organelle proteins by isotope tagging (LOPIT). *Molecular & Cellular Proteomics* **3**, 1128-1134, doi:10.1074/mcp.T400009-MCP200 (2004).
- 107 Liu, F., Rijkers, D. T. S., Post, H. & Heck, A. J. R. Proteome-wide profiling of protein assemblies by cross-linking mass spectrometry. *Nat Methods* **12**, 1179+, doi:10.1038/nmeth.3603 (2015).
- 108 Hein, M. Y. *et al.* A human interactome in three quantitative dimensions organized by stoichiometries and abundances. *Cell* **163**, 712-723, doi:10.1016/j.cell.2015.09.053 (2015).
- 109 Olsen, J. V. *et al.* Global, in vivo, and site-specific phosphorylation dynamics in signaling networks. *Cell* **127**, 635-648, doi:10.1016/j.cell.2006.09.026 (2006).
- 110 Udeshi, N. D., Mertins, P., Svinkina, T. & Carr, S. A. Large-scale identification of ubiquitination sites by mass spectrometry. *Nat Protoc* **8**, 1950-1960, doi:10.1038/nprot.2013.120 (2013).
- 111 Ji, Y. *et al.* Direct detection of S-palmitoylation by mass spectrometry. *Anal Chem* **85**, 11952-11959, doi:10.1021/ac402850s (2013).
- 112 Parker, C. E., Mocanu, V., Mocanu, M., Dicheva, N. & Warren, M. R. in *Neuroproteomics Frontiers in Neuroscience* (ed O. Alzate) (2010).
- 113 Capitanio, D., Moriggi, M. & Gelfi, C. Mapping the human skeletal muscle proteome: progress and potential. *Expert Rev Proteomics* **14**, 825-839, doi:10.1080/14789450.2017.1364996 (2017).
- 114 Roos, A., Thompson, R., Horvath, R., Lochmuller, H. & Sickmann, A. Intersection of Proteomics and Genomics to "Solve the Unsolved" in Rare Disorders such as Neurodegenerative and Neuromuscular Diseases. *Proteomics Clin Appl* **12**, doi:10.1002/prca.201700073 (2018).
- 115 Canas, B., Lopez-Ferrer, D., Ramos-Fernandez, A., Camafeita, E. & Calvo, E. Mass spectrometry technologies for proteomics. *Brief Funct Genomic Proteomic* **4**, 295-320, doi:10.1093/bfgp/eli002 (2006).
- 116 Ong, S. E., Foster, L. J. & Mann, M. Mass spectrometric-based approaches in quantitative proteomics. *Methods* **29**, 124-130 (2003).
- 117 Whitehouse, C. M., Dreyer, R. N., Yamashita, M. & Fenn, J. B. Electrospray interface for liquid chromatographs and mass spectrometers. *Anal Chem* **57**, 675-679 (1985).
- 118 Davis, M. T., Stahl, D. C., Hefta, S. A. & Lee, T. D. A microscale electrospray interface for on-line, capillary liquid chromatography/tandem mass spectrometry of complex peptide mixtures. *Anal Chem* **67**, 4549-4556 (1995).

- 119 Aebersold, R. & Mann, M. Mass spectrometry-based proteomics. *Nature* **422**, 198-207, doi:10.1038/nature01511 (2003).
- 120 Hunt, D. F., Yates, J. R., 3rd, Shabanowitz, J., Winston, S. & Hauer, C. R. Protein sequencing by tandem mass spectrometry. *Proc Natl Acad Sci U S A* **83**, 6233-6237 (1986).
- 121 McLuckey, S. A. Principles of collisional activation in analytical mass spectrometry. *J Am Soc Mass Spectrom* **3**, 599-614, doi:10.1016/1044-0305(92)85001-Z (1992).
- 122 Old, W. M. *et al.* Comparison of label-free methods for quantifying human proteins by shotgun proteomics. *Mol Cell Proteomics* **4**, 1487-1502, doi:10.1074/mcp.M500084-MCP200 (2005).
- 123 Neilson, K. A. *et al.* Less label, more free: approaches in label-free quantitative mass spectrometry. *Proteomics* **11**, 535-553, doi:10.1002/pmic.201000553 (2011).
- 124 <http://www.nonlinear.com/progenesis/qi-for-proteomics/>.
- 125 Ishihama, Y. *et al.* Exponentially modified protein abundance index (emPAI) for estimation of absolute protein amount in proteomics by the number of sequenced peptides per protein. *Mol Cell Proteomics* **4**, 1265-1272, doi:10.1074/mcp.M500061-MCP200 (2005).
- 126 Braisted, J. C. *et al.* The APEX Quantitative Proteomics Tool: generating protein quantitation estimates from LC-MS/MS proteomics results. *BMC Bioinformatics* **9**, 529, doi:10.1186/1471-2105-9-529 (2008).
- 127 Zybaylov, B. *et al.* Statistical analysis of membrane proteome expression changes in *Saccharomyces cerevisiae*. *J Proteome Res* **5**, 2339-2347, doi:10.1021/pr060161n (2006).
- 128 <http://www.matrixscience.com/>.
- 129 Kim, S. & Pevzner, P. A. MS-GF+ makes progress towards a universal database search tool for proteomics. *Nat Commun* **5**, 5277, doi:10.1038/ncomms6277 (2014).
- 130 Wen, B. *et al.* The OMSSAPercolator: an automated tool to validate OMSSA results. *Proteomics* **14**, 1011-1014, doi:10.1002/pmic.201300393 (2014).
- 131 Vaudel, M. *et al.* PeptideShaker enables reanalysis of MS-derived proteomics data sets. *Nat Biotechnol* **33**, 22-24, doi:10.1038/nbt.3109 (2015).
- 132 <http://www.nonlinear.com/progenesis/qi-for-proteomics/>.
- 133 Vaudel, M., Barsnes, H., Berven, F. S., Sickmann, A. & Martens, L. SearchGUI: An open-source graphical user interface for simultaneous OMSSA and X!Tandem searches. *Proteomics* **11**, 996-999, doi:10.1002/pmic.201000595 (2011).
- 134 Diamant, B. J. & Noble, W. S. Faster SEQUEST searching for peptide identification from tandem mass spectra. *J Proteome Res* **10**, 3871-3879, doi:10.1021/pr101196n (2011).
- 135 Shannon, P. *et al.* Cytoscape: a software environment for integrated models of biomolecular interaction networks. *Genome Res* **13**, 2498-2504, doi:10.1101/gr.1239303 (2003).
- 136 Bindea, G. *et al.* ClueGO: a Cytoscape plug-in to decipher functionally grouped gene ontology and pathway annotation networks. *Bioinformatics* **25**, 1091-1093, doi:10.1093/bioinformatics/btp101 (2009).
- 137 Reza, M. *et al.* MRC Centre Neuromuscular Biobank (Newcastle and London): Supporting and facilitating rare and neuromuscular disease research worldwide. *Neuromuscul Disord* **27**, 1054-1064, doi:10.1016/j.nmd.2017.07.001 (2017).
- 138 Kuga, A. *et al.* Endoplasmic reticulum stress response in P104L mutant caveolin-3 transgenic mice. *Hum Mol Genet* **20**, 2975-2983, doi:10.1093/hmg/ddr201 (2011).
- 139 Sunada, Y. *et al.* Transgenic mice expressing mutant caveolin-3 show severe myopathy associated with increased nNOS activity. *Hum Mol Genet* **10**, 173-178 (2001).

- 140 Yasmin Issop, D. H., Muzamil Majid Khan, Rudiger Rudolf, Joachim Weis, Sally
Spendiff, Clarke Slater, Andreas Roos, Hans Lochmuller. GFPT1 deficiency in muscle
leads to myasthenia and myopathy in mice. *Human Molecular Genetics* **Under review**
(2018).
- 141 Arnaud, E. *et al.* SH3TC2/KIAA1985 protein is required for proper myelination and the
integrity of the node of Ranvier in the peripheral nervous system. *Proc Natl Acad Sci U*
S A **106**, 17528-17533, doi:10.1073/pnas.0905523106 (2009).
- 142 Puig, O. *et al.* The tandem affinity purification (TAP) method: a general procedure of
protein complex purification. *Methods* **24**, 218-229, doi:10.1006/meth.2001.1183
(2001).
- 143 Manza, L. L., Stamer, S. L., Ham, A. J., Codreanu, S. G. & Liebler, D. C. Sample
preparation and digestion for proteomic analyses using spin filters. *Proteomics* **5**, 1742-
1745, doi:10.1002/pmic.200401063 (2005).
- 144 Wisniewski, J. R., Zougman, A., Nagaraj, N. & Mann, M. Universal sample preparation
method for proteome analysis. *Nat Methods* **6**, 359-362, doi:10.1038/nmeth.1322
(2009).
- 145 Olsen, J. V. *et al.* Parts per million mass accuracy on an Orbitrap mass spectrometer via
lock mass injection into a C-trap. *Mol Cell Proteomics* **4**, 2010-2021,
doi:10.1074/mcp.T500030-MCP200 (2005).
- 146 Olsen, J. V. *et al.* Parts per Million Mass Accuracy on an Orbitrap Mass Spectrometer
via Lock Mass Injection into a C-trap. *Molecular & Cellular Proteomics* **4**, 2010-2021
(2005).
- 147 Ogata, H. *et al.* KEGG: Kyoto Encyclopedia of Genes and Genomes. *Nucleic Acids Res*
27, 29-34 (1999).
- 148 Croft, D. *et al.* Reactome: a database of reactions, pathways and biological processes.
Nucleic Acids Res **39**, D691-697, doi:10.1093/nar/gkq1018 (2011).
- 149 Higashijima, S., Hotta, Y. & Okamoto, H. Visualization of cranial motor neurons in live
transgenic zebrafish expressing green fluorescent protein under the control of the islet-1
promoter/enhancer. *J Neurosci* **20**, 206-218 (2000).
- 150 Kimmel, C. B., Ballard, W. W., Kimmel, S. R., Ullmann, B. & Schilling, T. F. Stages of
embryonic development of the zebrafish. *Dev Dyn* **203**, 253-310,
doi:10.1002/aja.1002030302 (1995).
- 151 Kawahara, G. & Hayashi, Y. K. Characterization of Zebrafish Models of Marinesco-
Sjogren Syndrome. *PLoS One* **11**, e0165563, doi:10.1371/journal.pone.0165563 (2016).
- 152 Muller, T. *et al.* Non-muscle myosin IIA is required for the development of the zebrafish
glomerulus. *Kidney Int* **80**, 1055-1063, doi:10.1038/ki.2011.256 (2011).
- 153 Jones, R. A. *et al.* NMJ-morph reveals principal components of synaptic morphology
influencing structure-function relationships at the neuromuscular junction. *Open Biol* **6**,
doi:ARTN 16024010.1098/rsob.160240 (2016).
- 154 Kollipara, L. *et al.* Proteome Profiling and Ultrastructural Characterization of the Human
RCMH Cell Line: Myoblastic Properties and Suitability for Myopathological Studies. *J*
Proteome Res **15**, 945-955, doi:10.1021/acs.jproteome.5b00972 (2016).
- 155 Drexler, H. C. *et al.* On marathons and Sprints: an integrated quantitative proteomics
and transcriptomics analysis of differences between slow and fast muscle fibers. *Mol*
Cell Proteomics **11**, M111 010801, doi:10.1074/mcp.M111.010801 (2012).
- 156 Murgia, M. *et al.* Single muscle fiber proteomics reveals unexpected mitochondrial
specialization. *EMBO Rep* **16**, 387-395, doi:10.15252/embr.201439757 (2015).
- 157 Hu, X., Charles, J. P., Akay, T., Hutchinson, J. R. & Blemker, S. S. Are mice good
models for human neuromuscular disease? Comparing muscle excursions in walking
between mice and humans. *Skelet Muscle* **7**, 26, doi:10.1186/s13395-017-0143-9 (2017).

- 158 Pan, C., Kumar, C., Bohl, S., Klingmueller, U. & Mann, M. Comparative proteomic phenotyping of cell lines and primary cells to assess preservation of cell type-specific functions. *Mol Cell Proteomics* **8**, 443-450, doi:10.1074/mcp.M800258-MCP200 (2009).
- 159 Altelaar, A. F., Munoz, J. & Heck, A. J. Next-generation proteomics: towards an integrative view of proteome dynamics. *Nat Rev Genet* **14**, 35-48, doi:10.1038/nrg3356 (2013).
- 160 Nagaraj, N. *et al.* Deep proteome and transcriptome mapping of a human cancer cell line. *Mol Syst Biol* **7**, 548, doi:10.1038/msb.2011.81 (2011).
- 161 Ohlendieck, K. Proteomics of skeletal muscle differentiation, neuromuscular disorders and fiber aging. *Expert Rev Proteomics* **7**, 283-296, doi:10.1586/epr.10.2 (2010).
- 162 Liebermeister, W. *et al.* Visual account of protein investment in cellular functions. *Proc Natl Acad Sci U S A* **111**, 8488-8493, doi:10.1073/pnas.1314810111 (2014).
- 163 Brancaccio, P., Lippi, G. & Maffulli, N. Biochemical markers of muscular damage. *Clin Chem Lab Med* **48**, 757-767, doi:10.1515/CCLM.2010.179 (2010).
- 164 Chaillou, T., Kirby, T. J. & McCarthy, J. J. Ribosome biogenesis: emerging evidence for a central role in the regulation of skeletal muscle mass. *J Cell Physiol* **229**, 1584-1594, doi:10.1002/jcp.24604 (2014).
- 165 Carlisle, C., Prill, K. & Pilgrim, D. Chaperones and the Proteasome System: Regulating the Construction and Demolition of Striated Muscle. *Int J Mol Sci* **19**, doi:10.3390/ijms19010032 (2017).
- 166 Afroze, D. & Kumar, A. ER stress in skeletal muscle remodeling and myopathies. *FEBS J*, doi:10.1111/febs.14358 (2017).
- 167 Yang, W. & Paschen, W. The endoplasmic reticulum and neurological diseases. *Exp Neurol* **219**, 376-381, doi:10.1016/j.expneurol.2009.07.009 (2009).
- 168 Pajalunga, D. *et al.* DNA Replication Is Intrinsically Hindered in Terminally Differentiated Myotubes. *Plos One* **5**, doi:ARTN e1155910.1371/journal.pone.0011559 (2010).
- 169 Rochlin, K., Yu, S., Roy, S. & Baylies, M. K. Myoblast fusion: When it takes more to make one. *Developmental Biology* **341**, 66-83, doi:10.1016/j.ydbio.2009.10.024 (2010).
- 170 Buckingham, M. & Rigby, P. W. Gene regulatory networks and transcriptional mechanisms that control myogenesis. *Dev Cell* **28**, 225-238, doi:10.1016/j.devcel.2013.12.020 (2014).
- 171 Leroy, M. C., Perroud, J., Darbellay, B., Bernheim, L. & Konig, S. Epidermal growth factor receptor down-regulation triggers human myoblast differentiation. *PLoS One* **8**, e71770, doi:10.1371/journal.pone.0071770 (2013).
- 172 Sartori, R., Gregorevic, P. & Sandri, M. TGF beta and BMP signaling in skeletal muscle: potential significance for muscle-related disease. *Trends Endocrin Met* **25**, 464-471, doi:10.1016/j.tem.2014.06.002 (2014).
- 173 Ono, Y. *et al.* BMP signalling permits population expansion by preventing premature myogenic differentiation in muscle satellite cells. *Cell Death Differ* **18**, 222-234, doi:10.1038/cdd.2010.95 (2011).
- 174 Yamamoto, N. *et al.* Smad1 and Smad5 act downstream of intracellular signalings of BMP-2 that inhibits myogenic differentiation and induces osteoblast differentiation in C2C12 myoblasts. *Biochem Bioph Res Co* **238**, 574-580, doi:DOI 10.1006/bbrc.1997.7325 (1997).
- 175 Charrasse, S., Meriane, M., Comunale, F., Blangy, A. & Gauthier-Rouviere, C. N-cadherin-dependent cell-cell contact regulates Rho GTPases and beta-catenin localization in mouse C2C12 myoblasts. *Journal of Cell Biology* **158**, 953-965, doi:10.1083/jcb.200202034 (2002).

- 176 Castellani, L., Salvati, E., Alema, S. & Falcone, G. Fine regulation of RhoA and rock is required for skeletal muscle differentiation. *Journal of Biological Chemistry* **281**, 15249-15257, doi:10.1074/jbc.M601390200 (2006).
- 177 Ho, A. T. V. *et al.* Prostaglandin E2 is essential for efficacious skeletal muscle stem-cell function, augmenting regeneration and strength. *P Natl Acad Sci USA* **114**, 6675-6684, doi:10.1073/pnas.1705420114 (2017).
- 178 Fu, W. X., Asp, P., Canter, B. & Dynlacht, B. D. Primary cilia control hedgehog signaling during muscle differentiation and are deregulated in rhabdomyosarcoma. *P Natl Acad Sci USA* **111**, 9151-9156, doi:10.1073/pnas.1323265111 (2014).
- 179 White, J. P. Control of Skeletal Muscle Cell Growth and Size Through Adhesion GPCRs. *Handb Exp Pharmacol* **234**, 299-308, doi:10.1007/978-3-319-41523-9_13 (2016).
- 180 Suzuki, A., Pelikan, R. C. & Iwata, J. WNT/beta-Catenin Signaling Regulates Multiple Steps of Myogenesis by Regulating Step-Specific Targets. *Mol Cell Biol* **35**, 1763-1776, doi:10.1128/Mcb.01180-14 (2015).
- 181 Saada, Y. B. *et al.* Control of DNA integrity in skeletal muscle under physiological and pathological conditions. *Cellular and Molecular Life Sciences* **74**, 3439-3449, doi:10.1007/s00018-017-2530-0 (2017).
- 182 Lefta, M., Wolff, G. & Esser, K. A. Circadian Rhythms, the Molecular Clock, and Skeletal Muscle. *Curr Top Dev Biol* **96**, 231-271, doi:10.1016/B978-0-12-385940-2.00009-7 (2011).
- 183 Perrin, L. *et al.* Transcriptomic analyses reveal rhythmic and CLOCK-driven pathways in human skeletal muscle. *Elife* **7**, doi:ARTN e3411410.7554/eLife.34114 (2018).
- 184 Brunelli, S. & Rovere-Querini, P. The immune system and the repair of skeletal muscle. *Pharmacol Res* **58**, 117-121, doi:10.1016/j.phrs.2008.06.008 (2008).
- 185 Vandenboom, R. Modulation of Skeletal Muscle Contraction by Myosin Phosphorylation. *Compr Physiol* **7**, 171-212, doi:10.1002/cphy.c150044 (2017).
- 186 Partridge, T. A. Cells that participate in regeneration of skeletal muscle. *Gene Ther* **9**, 752-753, doi:DOI 10.1038/sj.gt.3301764 (2002).
- 187 Ijuin, T. *et al.* Identification and characterization of a novel inositol polyphosphate 5-phosphatase. *J Biol Chem* **275**, 10870-10875 (2000).
- 188 Odorizzi, G., Babst, M. & Emr, S. D. Phosphoinositide signaling and the regulation of membrane trafficking in yeast. *Trends Biochem Sci* **25**, 229-235 (2000).
- 189 Osborn, D. P. S. *et al.* Mutations in INPP5K Cause a Form of Congenital Muscular Dystrophy Overlapping Marinesco-Sjogren Syndrome and Dystroglycanopathy. *Am J Hum Genet* **100**, 537-545, doi:10.1016/j.ajhg.2017.01.019 (2017).
- 190 Denisa Hathazi, D. C., Richard Charlton, Adele D'Amico, Robert-Yves Carlier, René Zahedi, Laxmikanth Kollipara, Jennifer Baumann, Jan Senderek, Emily O'Connor, Rita Barresi, Hanns Lochmüller, Andoni Urtizberea, Marie-Line Jacquemont, Isabelle Nelson, Laura Swan, Gisele Bonne, Andreas Roos. Molecular linkage of rare neuromuscular diseases allows the definition of a treatment strategy for Marinesco-Sjögren and Marinesco-Sjögren-like syndromes. *In preparation* (2018).
- 191 Marinesco G, D. S., D V. Nouvelle maladie familiale caractérisée par une cataracte congénitale et un arrêt du développement somato-neuro-psychique. *Encephale* **26**, 97-109 (1931).
- 192 Krieger, M. *et al.* SIL1 mutations and clinical spectrum in patients with Marinesco-Sjogren syndrome. *Brain* **136**, 3634-3644, doi:10.1093/brain/awt283 (2013).
- 193 Roos, A. *et al.* Cellular Signature of SIL1 Depletion: Disease Pathogenesis due to Alterations in Protein Composition Beyond the ER Machinery. *Mol Neurobiol* **53**, 5527-5541, doi:10.1007/s12035-015-9456-z (2016).

- 194 Varon, R. *et al.* Partial deficiency of the C-terminal-domain phosphatase of RNA polymerase II is associated with congenital cataracts facial dysmorphism neuropathy syndrome. *Nature Genetics* **35**, 185-189, doi:10.1038/ng1243 (2003).
- 195 Kollipara, L. *et al.* In-depth phenotyping of lymphoblastoid cells suggests selective cellular vulnerability in Marinesco-Sjogren syndrome. *Oncotarget* **8**, 68493-68516, doi:10.18632/oncotarget.19663 (2017).
- 196 Napolitano, G., Licciardo, P., Carbone, R., Majello, A. & Lania, L. CDK9 has the intrinsic property to shuttle between nucleus and cytoplasm, and enhanced expression of CyclinT1 promotes its nuclear localization. *Journal of Cellular Physiology* **192**, 209-215, doi:10.1002/jcp.10130 (2002).
- 197 Gibert, Y., Trengove, M. C. & Ward, A. C. Zebrafish As a Genetic Model in Pre-Clinical Drug Testing and Screening. *Curr Med Chem* **20**, 2458-2466, doi:Doi 10.2174/0929867311320190005 (2013).
- 198 Filezac LÉtang, V. P., Dan Cox, Silvia Cipriani, Sally Spendiff, Stephan Buchkremer, Emily O'Connor, Rita Horvath, Hans Hilmar Göbel, Denisa Hathazi, Hanns Lochmüller, Tatjana Straka, Rüdiger Rudolf, Joachim Weis, Andreas Roos. *Elucidation of SIL1-related peripheral nerve and neuromuscular junction pathology: a morphological and biochemical study* (2018).
- 199 Tabatabaie, L., Klomp, L. W., Berger, R. & de Koning, T. J. L-serine synthesis in the central nervous system: a review on serine deficiency disorders. *Mol Genet Metab* **99**, 256-262, doi:10.1016/j.ymgme.2009.10.012 (2010).
- 200 Kawakami, Y. *et al.* Impaired neurogenesis in embryonic spinal cord of Phgdh knockout mice, a serine deficiency disorder model. *Neurosci Res* **63**, 184-193, doi:10.1016/j.neures.2008.12.002 (2009).
- 201 Furuya, S. *et al.* Inactivation of the 3-phosphoglycerate dehydrogenase gene in mice: changes in gene expression and associated regulatory networks resulting from serine deficiency. *Funct Integr Genomics* **8**, 235-249, doi:10.1007/s10142-007-0072-5 (2008).
- 202 Yoshida, K. *et al.* Targeted disruption of the mouse 3-phosphoglycerate dehydrogenase gene causes severe neurodevelopmental defects and results in embryonic lethality. *J Biol Chem* **279**, 3573-3577, doi:10.1074/jbc.C300507200 (2004).
- 203 de Koning, T. J. *et al.* L-serine in disease and development. *Biochem J* **371**, 653-661, doi:10.1042/BJ20021785 (2003).
- 204 Levine, T. D. *et al.* Phase I clinical trial of safety of L-serine for ALS patients. *Amyotroph Lateral Scler Frontotemporal Degener* **18**, 107-111, doi:10.1080/21678421.2016.1221971 (2017).
- 205 MacRae, C. A. & Peterson, R. T. Zebrafish as tools for drug discovery. *Nat Rev Drug Discov* **14**, 721-731, doi:10.1038/nrd4627 (2015).
- 206 Eliceiri, B. P., Gonzalez, A. M. & Baird, A. Zebrafish model of the blood-brain barrier: morphological and permeability studies. *Methods Mol Biol* **686**, 371-378, doi:10.1007/978-1-60761-938-3_18 (2011).
- 207 Chen, X. G., Wang, Y. H., Wen, C. C. & Chen, Y. H. Overdose of D-serine Induces Movement Disorder and Neuromuscular Changes of Zebrafish Larvae. *J Toxicol Pathol* **27**, 19-24, doi:10.1293/tox.2013-0032 (2014).
- 208 Menelaou, E. *et al.* Embryonic motor activity and implications for regulating motoneuron axonal pathfinding in zebrafish. *Eur J Neurosci* **28**, 1080-1096, doi:10.1111/j.1460-9568.2008.06418.x (2008).
- 209 Jauhari, P. *et al.* SIL1-negative Marinesco-Sjogren syndrome: First report of two sibs from India. *J Pediatr Neurosci* **9**, 291-292, doi:10.4103/1817-1745.147597 (2014).
- 210 Ohnuma, S. & Harris, W. A. Neurogenesis and the cell cycle. *Neuron* **40**, 199-208 (2003).

- 211 Furuya, S. *et al.* L-serine and glycine serve as major astroglia-derived trophic factors for cerebellar Purkinje neurons. *Proc Natl Acad Sci U S A* **97**, 11528-11533, doi:10.1073/pnas.200364497 (2000).
- 212 Buchkremer, S., Gonzalez Coraspe, J. A., Weis, J. & Roos, A. Sill1-Mutant Mice Elucidate Chaperone Function in Neurological Disorders. *J Neuromuscul Dis* **3**, 169-181, doi:10.3233/JND-160152 (2016).
- 213 Poli, A. *et al.* Phosphoglycerate dehydrogenase (PHGDH) deficiency without epilepsy mimicking primary microcephaly. *Am J Med Genet A* **173**, 1936-1942, doi:10.1002/ajmg.a.38217 (2017).
- 214 Brown, D. M. *et al.* Mitochondrial phosphoenolpyruvate carboxykinase (PEPCK-M) and serine biosynthetic pathway genes are co-ordinately increased during anabolic agent-induced skeletal muscle growth. *Sci Rep-Uk* **6**, doi:ARTN 2869310.1038/srep28693 (2016).
- 215 Brassier, A. *et al.* Two new cases of serine deficiency disorders treated with L-serine. *Eur J Paediatr Neuro* **20**, 53-60, doi:10.1016/j.ejpn.2015.10.007 (2016).
- 216 Dunlop, R. A., Powell, J., Guillemain, G. J. & Cox, P. A. Mechanisms of L-Serine Neuroprotection in vitro Include ER Proteostasis Regulation. *Neurotox Res* **33**, 123-132, doi:10.1007/s12640-017-9829-3 (2018).
- 217 Giacinti, C. *et al.* Cdk9-55: a new player in muscle regeneration. *J Cell Physiol* **216**, 576-582, doi:10.1002/jcp.21361 (2008).
- 218 Lagier-Tourenne, C. *et al.* Linkage to 18qter differentiates two clinically overlapping syndromes: congenital cataracts-facial dysmorphism-neuropathy (CCFDN) syndrome and Marinesco-Sjogren syndrome. *J Med Genet* **39**, 838-843 (2002).
- 219 Hagiwara, Y., Nishina, Y., Yorifuji, H. & Kikuchi, T. Immunolocalization of caveolin-1 and caveolin-3 in monkey skeletal, cardiac and uterine smooth muscles. *Cell structure and function* **27**, 375-382 (2002).
- 220 Razani, B. *et al.* Caveolin-1 regulates transforming growth factor (TGF)-beta/SMAD signaling through an interaction with the TGF-beta type I receptor. *The Journal of biological chemistry* **276**, 6727-6738, doi:10.1074/jbc.M008340200 (2001).
- 221 Schlegel, A. & Lisanti, M. P. The caveolin triad: caveolae biogenesis, cholesterol trafficking, and signal transduction. *Cytokine & growth factor reviews* **12**, 41-51 (2001).
- 222 Song, K. S. *et al.* Expression of caveolin-3 in skeletal, cardiac, and smooth muscle cells. Caveolin-3 is a component of the sarcolemma and co-fractionates with dystrophin and dystrophin-associated glycoproteins. *J Biol Chem* **271**, 15160-15165 (1996).
- 223 Way, M. & Parton, R. G. M-caveolin, a muscle-specific caveolin-related protein. *FEBS letters* **378**, 108-112 (1996).
- 224 Brauers, E. *et al.* Differential effects of myopathy-associated caveolin-3 mutants on growth factor signaling. *Am J Pathol* **177**, 261-270, doi:10.2353/ajpath.2010.090741 (2010).
- 225 Parton, R. G. Caveolae and caveolins. *Current opinion in cell biology* **8**, 542-548 (1996).
- 226 Galbiati, F., Razani, B. & Lisanti, M. P. Caveolae and caveolin-3 in muscular dystrophy. *Trends in molecular medicine* **7**, 435-441 (2001).
- 227 Minetti, C. *et al.* Impairment of caveolae formation and T-system disorganization in human muscular dystrophy with caveolin-3 deficiency. *Am J Pathol* **160**, 265-270, doi:10.1016/S0002-9440(10)64370-2 (2002).
- 228 Razani, B. & Lisanti, M. P. Caveolins and caveolae: molecular and functional relationships. *Experimental cell research* **271**, 36-44, doi:10.1006/excr.2001.5372 (2001).
- 229 Williams, T. M. & Lisanti, M. P. The Caveolin genes: from cell biology to medicine. *Annals of medicine* **36**, 584-595 (2004).

- 230 Hezel, M., de Groat, W. C. & Galbiati, F. Caveolin-3 promotes nicotinic acetylcholine
receptor clustering and regulates neuromuscular junction activity. *Mol Biol Cell* **21**, 302-
310, doi:10.1091/mbc.E09-05-0381 (2010).
- 231 Wang, Y. *et al.* Hypoxia promotes ligand-independent EGF receptor signaling via
hypoxia-inducible factor-mediated upregulation of caveolin-1. *Proceedings of the
National Academy of Sciences of the United States of America* **109**, 4892-4897,
doi:10.1073/pnas.1112129109 (2012).
- 232 Gazzo, E., Sotgia, F., Bruno, C., Lisanti, M. P. & Minetti, C. Caveolinopathies: from
the biology of caveolin-3 to human diseases. *Eur J Hum Genet* **18**, 137-145,
doi:10.1038/ejhg.2009.103 (2010).
- 233 McNally, E. M. *et al.* Caveolin-3 in muscular dystrophy. *Hum Mol Genet* **7**, 871-877
(1998).
- 234 Guglieri, M., Straub, V., Bushby, K. & Lochmuller, H. Limb-girdle muscular
dystrophies. *Curr Opin Neurol* **21**, 576-584, doi:10.1097/WCO.0b013e32830efdc2
(2008).
- 235 Traverso, M. *et al.* Caveolin-3 T78M and T78K missense mutations lead to different
phenotypes in vivo and in vitro. *Lab Invest* **88**, 275-283, doi:10.1038/labinvest.3700713
(2008).
- 236 Betz, R. C. *et al.* Mutations in CAV3 cause mechanical hyperirritability of skeletal
muscle in rippling muscle disease. *Nat Genet* **28**, 218-219, doi:10.1038/90050 (2001).
- 237 Gonzalez-Perez, P. *et al.* Phenotypic variability in a Spanish family with a Caveolin-3
mutation. *J Neurol Sci* **276**, 95-98, doi:10.1016/j.jns.2008.09.009 (2009).
- 238 Ohsawa, Y. *et al.* Overexpression of P104L mutant caveolin-3 in mice develops
hypertrophic cardiomyopathy with enhanced contractility in association with increased
endothelial nitric oxide synthase activity. *Hum Mol Genet* **13**, 151-157,
doi:10.1093/hmg/ddh014 (2004).
- 239 Galbiati, F., Volonte, D., Minetti, C., Chu, J. B. & Lisanti, M. P. Phenotypic behavior of
caveolin-3 mutations that cause autosomal dominant limb girdle muscular dystrophy
(LGMD-1C). Retention of LGMD-1C caveolin-3 mutants within the golgi complex. *J
Biol Chem* **274**, 25632-25641 (1999).
- 240 DeChiara, T. M. *et al.* The receptor tyrosine kinase MuSK is required for neuromuscular
junction formation in vivo. *Cell* **85**, 501-512 (1996).
- 241 Iwasa, K., Furukawa, Y., Yoshikawa, H. & Yamada, M. Caveolin-3 is aberrantly
expressed in skeletal muscle cells in myasthenia gravis. *J Neuroimmunol* **301**, 30-34,
doi:10.1016/j.jneuroim.2016.10.011 (2016).
- 242 Karlsson, M., Thorn, H., Parpal, S., Stralfors, P. & Gustavsson, J. Insulin induces
translocation of glucose transporter GLUT4 to plasma membrane caveolae in
adipocytes. *FASEB J* **16**, 249-251, doi:10.1096/fj.01-0646fje (2002).
- 243 Augustus, A. S. *et al.* Substrate uptake and metabolism are preserved in hypertrophic
caveolin-3 knockout hearts. *Am J Physiol Heart Circ Physiol* **295**, H657-666,
doi:10.1152/ajpheart.00387.2008 (2008).
- 244 Brauers, E. *et al.* The Caveolin-3 G56S sequence variant of unknown significance:
Muscle biopsy findings and functional cell biological analysis. *Proteomics Clin Appl* **11**,
doi:10.1002/prca.201600007 (2017).
- 245 José Andrés González Coraspe, J. W., Mary E Anderson, Ute Münchberg, Kristina
Lorenz, Stephan Buchkremer, Stephanie Carr, René Peiman Zahedi,, Eva Brauers,
Hannah Michels, Yoshihide Sunada, Hanns Lochmüller, Kevin P Campbell, Erik Freier,
Denisa Hathazi, Andreas Roos. Biochemical and pathological changes result from
mutated Caveolin-3 in muscle. *Skeletal muscle* **just accepted** (2018).

- 246 Kennedy, D., Mnich, K. & Samali, A. Heat shock preconditioning protects against ER
stress-induced apoptosis through the regulation of the BH3-only protein BIM. *FEBS*
Open Bio **4**, 813-821, doi:10.1016/j.fob.2014.09.004 (2014).
- 247 Chang, H. Y. & Yang, X. Proteases for cell suicide: functions and regulation of caspases.
Microbiol Mol Biol Rev **64**, 821-846 (2000).
- 248 Soheili, T. *et al.* Rescue of sarcoglycan mutations by inhibition of endoplasmic reticulum
quality control is associated with minimal structural modifications. *Hum Mutat* **33**, 429-
439, doi:10.1002/humu.21659 (2012).
- 249 de Baaij, J. H. *et al.* Identification of SLC41A3 as a novel player in magnesium
homeostasis. *Sci Rep* **6**, 28565, doi:10.1038/srep28565 (2016).
- 250 Hayashi, Y. K. *et al.* Human PTRF mutations cause secondary deficiency of caveolins
resulting in muscular dystrophy with generalized lipodystrophy. *J Clin Invest* **119**, 2623-
2633, doi:10.1172/JCI38660 (2009).
- 251 Dunn, J. F., Burton, K. A. & Dauncey, M. J. Ouabain sensitive Na⁺/K⁺-ATPase
content is elevated in mdx mice: implications for the regulation of ions in dystrophic
muscle. *J Neurol Sci* **133**, 11-15 (1995).
- 252 Carberry, S., Zweyer, M., Swandulla, D. & Ohlendieck, K. Proteomics reveals drastic
increase of extracellular matrix proteins collagen and dermatopontin in the aged mdx
diaphragm model of Duchenne muscular dystrophy. *Int J Mol Med* **30**, 229-234,
doi:10.3892/ijmm.2012.1006 (2012).
- 253 Izadi, M. *et al.* Cobl-like promotes actin filament formation and dendritic branching
using only a single WH2 domain. *J Cell Biol* **217**, 211-230, doi:10.1083/jcb.201704071
(2018).
- 254 Mangan, M. E. & Olmsted, J. B. A muscle-specific variant of microtubule-associated
protein 4 (MAP4) is required in myogenesis. *Development* **122**, 771-781 (1996).
- 255 Tobin, S. W. *et al.* Regulation of Hspb7 by MEF2 and AP-1: implications for Hspb7 in
muscle atrophy. *J Cell Sci* **129**, 4076-4090, doi:10.1242/jcs.190009 (2016).
- 256 Smith, L. R., Hammers, D. W., Sweeney, H. L. & Barton, E. R. Increased collagen cross-
linking is a signature of dystrophin-deficient muscle. *Muscle Nerve* **54**, 71-78,
doi:10.1002/mus.24998 (2016).
- 257 Bizzarro, V., Petrella, A. & Parente, L. Annexin A1: novel roles in skeletal muscle
biology. *J Cell Physiol* **227**, 3007-3015, doi:10.1002/jcp.24032 (2012).
- 258 Demonbreun, A. R. *et al.* An actin-dependent annexin complex mediates plasma
membrane repair in muscle. *J Cell Biol* **213**, 705-718, doi:10.1083/jcb.201512022
(2016).
- 259 Charrin, S. *et al.* Normal muscle regeneration requires tight control of muscle cell fusion
by tetraspanins CD9 and CD81. *Nat Commun* **4**, 1674, doi:10.1038/ncomms2675
(2013).
- 260 Deng, Y. F. *et al.* The Caveolin-3 P104L mutation of LGMD-1C leads to disordered
glucose metabolism in muscle cells. *Biochem Biophys Res Commun* **486**, 218-223,
doi:10.1016/j.bbrc.2017.02.072 (2017).
- 261 Olson, A. L. & Pessin, J. E. Structure, function, and regulation of the mammalian
facilitative glucose transporter gene family. *Annu Rev Nutr* **16**, 235-256,
doi:10.1146/annurev.nu.16.070196.001315 (1996).
- 262 Streeter, A., Menzies, F. M. & Rubinsztein, D. C. LC3-II Tagging and Western Blotting
for Monitoring Autophagic Activity in Mammalian Cells. *Methods Mol Biol* **1303**, 161-
170, doi:10.1007/978-1-4939-2627-5_8 (2016).
- 263 Head, B. P. *et al.* Microtubules and actin microfilaments regulate lipid raft/caveolae
localization of adenylyl cyclase signaling components. *J Biol Chem* **281**, 26391-26399,
doi:10.1074/jbc.M602577200 (2006).

- 264 Sugie, K. *et al.* Two novel CAV3 gene mutations in Japanese families. *Neuromuscul Disord* **14**, 810-814, doi:10.1016/j.nmd.2004.08.008 (2004).
- 265 Tang, Z. *et al.* Molecular cloning of caveolin-3, a novel member of the caveolin gene family expressed predominantly in muscle. *J Biol Chem* **271**, 2255-2261 (1996).
- 266 Bischoff, R. & Schluter, H. Amino acids: chemistry, functionality and selected non-enzymatic post-translational modifications. *J Proteomics* **75**, 2275-2296, doi:10.1016/j.jprot.2012.01.041 (2012).
- 267 Sengupta, P. *et al.* ER trapping reveals Golgi enzymes continually revisit the ER through a recycling pathway that controls Golgi organization. *Proc Natl Acad Sci U S A* **112**, E6752-6761, doi:10.1073/pnas.1520957112 (2015).
- 268 Fossati, M., Colombo, S. F. & Borgese, N. A positive signal prevents secretory membrane cargo from recycling between the Golgi and the ER. *EMBO J* **33**, 2080-2097, doi:10.15252/embj.201488367 (2014).
- 269 Gawor, M. & Proszynski, T. J. The molecular cross talk of the dystrophin-glycoprotein complex. *Ann Ny Acad Sci* **1412**, 62-72, doi:10.1111/nyas.13500 (2018).
- 270 Ricci, G. *et al.* Rippling muscle disease and facioscapulohumeral dystrophy-like phenotype in a patient carrying a heterozygous CAV3 T78M mutation and a D4Z4 partial deletion: Further evidence for "double trouble" overlapping syndromes. *Neuromuscul Disord* **22**, 534-540, doi:10.1016/j.nmd.2011.12.001 (2012).
- 271 Smith, J. M., Hedman, A. C. & Sacks, D. B. IQGAPs choreograph cellular signaling from the membrane to the nucleus. *Trends Cell Biol* **25**, 171-184, doi:10.1016/j.tcb.2014.12.005 (2015).
- 272 Nixon, S. J. *et al.* Zebrafish as a model for caveolin-associated muscle disease; caveolin-3 is required for myofibril organization and muscle cell patterning. *Human Molecular Genetics* **14**, 1727-1743, doi:10.1093/hmg/ddi179 (2005).
- 273 Arimura, S. *et al.* Neuromuscular disease. DOK7 gene therapy benefits mouse models of diseases characterized by defects in the neuromuscular junction. *Science* **345**, 1505-1508, doi:10.1126/science.1250744 (2014).
- 274 Glass, D. J. *et al.* Agrin acts via a MuSK receptor complex. *Cell* **85**, 513-523 (1996).
- 275 Lefebvre, J. L., Jing, L. L., Becaficco, S., Franzini-Armstrong, C. & Granato, M. Differential requirement for MuSK and dystroglycan in generating patterns of neuromuscular innervation. *P Natl Acad Sci USA* **104**, 2483-2488, doi:10.1073/pnas.0610822104 (2007).
- 276 Pratt, S. J. P., Valencia, A. P., Le, G. K., Shah, S. B. & Lovering, R. M. Pre- and postsynaptic changes in the neuromuscular junction in dystrophic mice. *Front Physiol* **6**, doi:ARTN 252
10.3389/fphys.2015.00252 (2015).
- 277 Sotgia, F. *et al.* Caveolin-3 directly interacts with the C-terminal tail of beta-dystroglycan - Identification of a central WW-like domain within caveolin family members. *Journal of Biological Chemistry* **275**, 38048-38058, doi:DOI 10.1074/jbc.M005321200 (2000).
- 278 Owen, D. *et al.* The IQGAP1-Rac1 and IQGAP1-Cdc42 interactions - Interfaces differ between the complexes. *Journal of Biological Chemistry* **283**, 1692-1704, doi:10.1074/jbc.M707257200 (2008).
- 279 Su, X., Berman, S. A., Sullivan, T. & Bursztajn, S. Myoblast and myotube nuclei display similar patterns of heterogeneous acetylcholine receptor subunit mRNA expression. *J Cell Biochem* **58**, 22-38, doi:10.1002/jcb.240580105 (1995).
- 280 Schoneich, C., Dremina, E., Galeva, N. & Sharov, V. Apoptosis in differentiating C2C12 muscle cells selectively targets Bcl-2-deficient myotubes. *Apoptosis* **19**, 42-57, doi:10.1007/s10495-013-0922-7 (2014).

- 281 Jackson, M. F., Hoversten, K. E., Powers, J. M., Trobridge, G. D. & Rodgers, B. D. Genetic manipulation of myoblasts and a novel primary myosatellite cell culture system: comparing and optimizing approaches. *Febs Journal* **280**, 827-839, doi:10.1111/febs.12072 (2013).
- 282 Hettwer, S. *et al.* Injection of a soluble fragment of neural agrin (NT-1654) considerably improves the muscle pathology caused by the disassembly of the neuromuscular junction. *PLoS One* **9**, e88739, doi:10.1371/journal.pone.0088739 (2014).
- 283 O'Connor, E. *et al.* MYO9A deficiency in motor neurons is associated with reduced neuromuscular agrin secretion. *Hum Mol Genet*, doi:10.1093/hmg/ddy054 (2018).
- 284 White, C. D., Erdemir, H. H. & Sacks, D. B. IQGAP1 and its binding proteins control diverse biological functions. *Cell Signal* **24**, 826-834, doi:10.1016/j.cellsig.2011.12.005 (2012).
- 285 Jufvas, A., Rajan, M. R., Jonsson, C., Stralfors, P. & Turkina, M. V. Scaffolding protein IQGAP1: an insulin-dependent link between caveolae and the cytoskeleton in primary human adipocytes? *Biochemical Journal* **473**, 3177-3188, doi:10.1042/Bcj20160581 (2016).
- 286 Ruegg, M. A. & Bixby, J. L. Agrin orchestrates synaptic differentiation at the vertebrate neuromuscular junction. *Trends Neurosci* **21**, 22-27 (1998).
- 287 Grady, R. M. *et al.* Maturation and maintenance of the neuromuscular synapse: genetic evidence for roles of the dystrophin--glycoprotein complex. *Neuron* **25**, 279-293 (2000).
- 288 Weston, C., Yee, B., Hod, E. & Prives, J. Agrin-induced acetylcholine receptor clustering is mediated by the small guanosine triphosphatases Rac and Cdc42. *Journal of Cell Biology* **150**, 205-212, doi:DOI 10.1083/jcb.150.1.205 (2000).
- 289 Weston, C. *et al.* Cooperative regulation by Rac and Rho of agrin-induced acetylcholine receptor clustering in muscle cells. *J Biol Chem* **278**, 6450-6455, doi:10.1074/jbc.M210249200 (2003).
- 290 Jacquemet, G. *et al.* Rac1 is deactivated at integrin activation sites through an IQGAP1-filamin-A-RacGAP1 pathway. *J Cell Sci* **126**, 4121-4135, doi:10.1242/jcs.121988 (2013).
- 291 Ritzenthaler, S., Suzuki, E. & Chiba, A. Postsynaptic filopodia in muscle cells interact with innervating motoneuron axons. *Nat Neurosci* **3**, 1012-1017 (2000).
- 292 Guo, F., Debidda, M., Yang, L., Williams, D. A. & Zheng, Y. Genetic deletion of Rac1 GTPase reveals its critical role in actin stress fiber formation and focal adhesion complex assembly. *J Biol Chem* **281**, 18652-18659, doi:10.1074/jbc.M603508200 (2006).
- 293 Meller, N., Irani-Tehrani, M., Ratnikov, B. I., Paschal, B. M. & Schwartz, M. A. The novel Cdc42 guanine nucleotide exchange factor, zizimin1, dimerizes via the Cdc42-binding CZH2 domain. *J Biol Chem* **279**, 37470-37476, doi:10.1074/jbc.M404535200 (2004).
- 294 Singhal, N. & Martin, P. T. Role of Extracellular Matrix Proteins and Their Receptors in the Development of the Vertebrate Neuromuscular Junction. *Dev Neurobiol* **71**, 982-1005, doi:10.1002/dneu.20953 (2011).
- 295 Rogers, R. S. & Nishimune, H. The role of laminins in the organization and function of neuromuscular junctions. *Matrix Biol* **57-58**, 86-105, doi:10.1016/j.matbio.2016.08.008 (2017).
- 296 Bonnemann, C. G. The collagen VI-related myopathies Ullrich congenital muscular dystrophy and Bethlem myopathy. *Handb Clin Neurol* **101**, 81-96, doi:10.1016/B978-0-08-045031-5.00005-0 (2011).
- 297 Lee, C. W. & Peng, H. B. Mitochondrial clustering at the vertebrate neuromuscular junction during presynaptic differentiation. *J Neurobiol* **66**, 522-536, doi:10.1002/neu.20245 (2006).

- 298 Kozjak-Pavlovic, V. The MICOS complex of human mitochondria. *Cell Tissue Res* **367**, 83-93, doi:10.1007/s00441-016-2433-7 (2017).
- 299 Li, H. *et al.* Mic60/Mitofilin determines MICOS assembly essential for mitochondrial dynamics and mtDNA nucleoid organization. *Cell Death Differ* **23**, 380-392, doi:10.1038/cdd.2015.102 (2016).
- 300 Swiech, L. *et al.* CLIP-170 and IQGAP1 Cooperatively Regulate Dendrite Morphology. *Journal of Neuroscience* **31**, 4555-4568, doi:10.1523/Jneurosci.6582-10.2011 (2011).
- 301 Yamamoto, M., Ueda, R., Takahashi, K., Saigo, K. & Uemura, T. Control of axonal sprouting and dendrite branching by the Nrg-Ank complex at the neuron-glia interface. *Curr Biol* **16**, 1678-1683, doi:10.1016/j.cub.2006.06.061 (2006).
- 302 Iolyeva, M. *et al.* Novel role for ALCAM in lymphatic network formation and function. *Faseb Journal* **27**, 978-990, doi:10.1096/fj.12-217844 (2013).
- 303 Galbiati, F. *et al.* Caveolin-3 null mice show a loss of caveolae, changes in the microdomain distribution of the dystrophin-glycoprotein complex, and T-tubule abnormalities. *Journal of Biological Chemistry* **276**, 21425-21433, doi:DOI 10.1074/jbc.M100828200 (2001).
- 304 Kee, A. J., Gunning, P. W. & Hardeman, E. C. Diverse roles of the actin cytoskeleton in striated muscle. *J Muscle Res Cell M* **30**, 187-197, doi:10.1007/s10974-009-9193-x (2009).
- 305 Issop, Y. *et al.* GFPT1 deficiency in muscle leads to myasthenia and myopathy in mice. *Hum Mol Genet*, doi:10.1093/hmg/ddy225 (2018).
- 306 Belaya, K. *et al.* Identification of DPAGT1 as a new gene in which mutations cause a congenital myasthenic syndrome. *Ann N Y Acad Sci* **1275**, 29-35, doi:10.1111/j.1749-6632.2012.06790.x (2012).
- 307 Senderek, J. *et al.* Hexosamine biosynthetic pathway mutations cause neuromuscular transmission defect. *Am J Hum Genet* **88**, 162-172, doi:10.1016/j.ajhg.2011.01.008 (2011).
- 308 Cossins, J. *et al.* Congenital myasthenic syndromes due to mutations in ALG2 and ALG14. *Brain* **136**, 944-956, doi:10.1093/brain/awt010 (2013).
- 309 Selcen, D. *et al.* GFPT1-myasthenia: clinical, structural, and electrophysiologic heterogeneity. *Neurology* **81**, 370-378, doi:10.1212/WNL.0b013e31829c5e9c (2013).
- 310 Zoltowska, K. *et al.* Mutations in GFPT1 that underlie limb-girdle congenital myasthenic syndrome result in reduced cell-surface expression of muscle AChR. *Hum Mol Genet* **22**, 2905-2913, doi:10.1093/hmg/ddt145 (2013).
- 311 Guergueltcheva, V. *et al.* Congenital myasthenic syndrome with tubular aggregates caused by GFPT1 mutations. *J Neurol* **259**, 838-850, doi:10.1007/s00415-011-6262-z (2012).
- 312 Blanchette, C. R., Perrat, P. N., Thackeray, A. & Benard, C. Y. Glypican Is a Modulator of Netrin-Mediated Axon Guidance. *Plos Biol* **13**, doi:ARTN e100218310.1371/journal.pbio.1002183 (2015).
- 313 Luo, Z. G. *et al.* Implication of geranylgeranyltransferase I in synapse formation. *Neuron* **40**, 703-717 (2003).
- 314 Chernousov, M. A. *et al.* Glypican-1 and alpha4(V) collagen are required for Schwann cell myelination. *J Neurosci* **26**, 508-517, doi:10.1523/JNEUROSCI.2544-05.2006 (2006).
- 315 Casar, J. C. *et al.* Heparan sulfate proteoglycans are increased during skeletal muscle regeneration: requirement of syndecan-3 for successful fiber formation. *Journal of Cell Science* **117**, 73-84, doi:DOI 10.1242/jcs.00828 (2004).

- 316 Cheng, F. *et al.* Nitric oxide-dependent processing of heparan sulfate in recycling S-nitrosylated glypican-1 takes place in caveolin-1-containing endosomes. *J Biol Chem* **277**, 44431-44439, doi:10.1074/jbc.M205241200 (2002).
- 317 Kazemi, Z., Chang, H., Haserodt, S., McKen, C. & Zachara, N. E. O-linked beta-N-acetylglucosamine (O-GlcNAc) regulates stress-induced heat shock protein expression in a GSK-3beta-dependent manner. *J Biol Chem* **285**, 39096-39107, doi:10.1074/jbc.M110.131102 (2010).
- 318 Zhao, G., Lu, H. & Li, C. Proapoptotic activities of protein disulfide isomerase (PDI) and PDIA3 protein, a role of the Bcl-2 protein Bak. *J Biol Chem* **290**, 8949-8963, doi:10.1074/jbc.M114.619353 (2015).
- 319 Wei, J. W. *et al.* Signal Peptide Peptidase, Encoded by HM13, Contributes to Tumor Progression by Affecting EGFRvIII Secretion Profiles in Glioblastoma. *CNS Neurosci Ther* **23**, 257-265, doi:10.1111/cns.12672 (2017).
- 320 Clark, D. L., Clark, D. I., Hogan, E. K., Kroscher, K. A. & Dilger, A. C. Elevated insulin-like growth factor 2 expression may contribute to the hypermuscular phenotype of myostatin null mice. *Growth Horm Igf Res* **25**, 207-218, doi:10.1016/j.ghir.2015.06.007 (2015).
- 321 Sigoillot, S. M. *et al.* Neuromuscular junction immaturity and muscle atrophy are hallmarks of the ColQ-deficient mouse, a model of congenital myasthenic syndrome with acetylcholinesterase deficiency. *Faseb Journal* **30**, 2382-2399, doi:10.1096/fj.201500162 (2016).
- 322 Rudnik-Schoneborn, S. *et al.* Diagnostic algorithms in Charcot-Marie-Tooth neuropathies: experiences from a German genetic laboratory on the basis of 1206 index patients. *Clin Genet* **89**, 34-43, doi:10.1111/cge.12594 (2016).
- 323 Gouttenoire, E. A. *et al.* Sh3tc2 deficiency affects neuregulin-1/ErbB signaling. *Glia* **61**, 1041-1051, doi:10.1002/glia.22493 (2013).
- 324 Stendel, C. *et al.* SH3TC2, a protein mutant in Charcot-Marie-Tooth neuropathy, links peripheral nerve myelination to endosomal recycling. *Brain : a journal of neurology* **133**, 2462-2474, doi:10.1093/brain/awq168 (2010).
- 325 Senderek, J. *et al.* Mutations in a gene encoding a novel SH3/TPR domain protein cause autosomal recessive Charcot-Marie-Tooth type 4C neuropathy. *Am J Hum Genet* **73**, 1106-1119, doi:10.1086/379525 (2003).
- 326 Jerath, N. U. *et al.* Charcot-Marie-Tooth Disease type 4C: Novel mutations, clinical presentations, and diagnostic challenges. *Muscle Nerve* **57**, 749-755, doi:10.1002/mus.25981 (2018).
- 327 Houlden, H. *et al.* The phenotype of Charcot-Marie-Tooth disease type 4C due to SH3TC2 mutations and possible predisposition to an inflammatory neuropathy. *Neuromuscul Disord* **19**, 264-269, doi:10.1016/j.nmd.2009.01.006 (2009).
- 328 Carlson, B. M. The Biology of Long-Term Denervated Skeletal Muscle. *Eur J Transl Myol* **24**, 3293, doi:10.4081/ejtm.2014.3293 (2014).
- 329 Bonaldo, P. & Sandri, M. Cellular and molecular mechanisms of muscle atrophy. *Dis Model Mech* **6**, 25-39, doi:10.1242/dmm.010389 (2013).
- 330 Fanzani, A., Conraads, V. M., Penna, F. & Martinet, W. Molecular and cellular mechanisms of skeletal muscle atrophy: an update. *J Cachexia Sarcopenia Muscle* **3**, 163-179, doi:10.1007/s13539-012-0074-6 (2012).
- 331 Schiaffino, S., Dyar, K. A., Ciciliot, S., Blaauw, B. & Sandri, M. Mechanisms regulating skeletal muscle growth and atrophy. *FEBS J* **280**, 4294-4314, doi:10.1111/febs.12253 (2013).

- 332 Sacheck, J. M. *et al.* Rapid disuse and denervation atrophy involve transcriptional changes similar to those of muscle wasting during systemic diseases. *FASEB J* **21**, 140-155, doi:10.1096/fj.06-6604com (2007).
- 333 Lang, F. *et al.* Dynamic changes in the mouse skeletal muscle proteome during denervation-induced atrophy. *Dis Model Mech* **10**, 881-896, doi:10.1242/dmm.028910 (2017).
- 334 Wiederstein, J. L. *et al.* Skeletal Muscle-Specific Methyltransferase METTL21C Trimethylates p97 and Regulates Autophagy-Associated Protein Breakdown. *Cell Rep* **23**, 1342-1356, doi:10.1016/j.celrep.2018.03.136 (2018).
- 335 Rubinsztein, D. C. *et al.* In search of an "autophagometer". *Autophagy* **5**, 585-589 (2009).
- 336 Pogoryelova, O., Coraspe, J. A. G., Nikolenko, N., Lochmuller, H. & Roos, A. GNE myopathy: from clinics and genetics to pathology and research strategies. *Orphanet Journal of Rare Diseases* **13**, doi:ARTN 7010.1186/s13023-018-0802-x (2018).
- 337 Sharpe, A. J. & McKenzie, M. Mitochondrial Fatty Acid Oxidation Disorders Associated with Short-Chain Enoyl-CoA Hydratase (ECHS1) Deficiency. *Cells* **7**, doi:10.3390/cells7060046 (2018).
- 338 Yan, S. *et al.* Long-chain acyl-CoA synthetase in fatty acid metabolism involved in liver and other diseases: an update. *World J Gastroenterol* **21**, 3492-3498, doi:10.3748/wjg.v21.i12.3492 (2015).
- 339 Mckee, K. K. *et al.* Schwann cell myelination requires integration of laminin activities. *Journal of Cell Science* **125**, 4609-4619, doi:10.1242/jcs.107995 (2012).
- 340 Magot, A. *et al.* A new MPZ mutation associated with a mild CMT1 phenotype presenting with recurrent nerve compression. *Muscle & Nerve* **38**, 1055-1059, doi:10.1002/mus.21050 (2008).
- 341 Verstreken, P. *et al.* Synaptojanin is recruited by Endophilin to promote synaptic vesicle uncoating. *Neuron* **40**, 733-748, doi:Doi 10.1016/S0896-6273(03)00644-5 (2003).
- 342 Brauer, A. U. *et al.* A new phospholipid phosphatase, PRG-1, is involved in axon growth and regenerative sprouting. *Nat Neurosci* **6**, 572-578, doi:10.1038/nn1052 (2003).
- 343 Kley, R. A. *et al.* Clinical and morphological phenotype of the filamin myopathy: a study of 31 German patients. *Brain* **130**, 3250-3264, doi:10.1093/brain/awm271 (2007).
- 344 Lehman, W., Galinska-Rakoczy, A., Hatch, V., Tobacman, L. S. & Craig, R. Structural Basis for the Activation of Muscle Contraction by Troponin and Tropomyosin. *J Mol Biol* **388**, 673-681, doi:10.1016/j.jmb.2009.03.060 (2009).
- 345 Fanin, M., Nascimbeni, A. C. & Angelini, C. Muscle Atrophy, Ubiquitin-Proteasome, and Autophagic Pathways in Dysferlinopathy. *Muscle & Nerve* **50**, 340-347, doi:10.1002/mus.24167 (2014).
- 346 Lei, E. P. & Silver, P. A. Protein and RNA export from the nucleus. *Developmental Cell* **2**, 261-272, doi:Doi 10.1016/S1534-5807(02)00134-X (2002).
- 347 Klann, M., Koeppl, H. & Reuss, M. Spatial Modeling of Vesicle Transport and the Cytoskeleton: The Challenge of Hitting the Right Road. *Plos One* **7**, doi:ARTN e2964510.1371/journal.pone.0029645 (2012).

7. Appendices

9.1 Appendix 1

Regulated proteins in the chapter 3.2.1 entitled molecular linkage of rare neuromuscular diseases

Gene name	Protein name	Fold regulation	Function (according to uniprot, July. 2018)
<i>ARPC5L</i>	Actin-related protein 2/3 complex subunit 5-like protein	2.71	Regulation of actin polymerization formation of branched actin networks
<i>F3</i>	Tissue factor	2.4	Cell-surface assembly and propagation of the coagulation protease cascade
<i>TNC</i>	Tenascin	2.36	Migrating neurons as well as axons during development
<i>SERPINE 1</i>	Plasminogen activator inhibitor 1	1.98	Serine protease inhibitor
<i>PHGDH</i>	D-3-phosphoglycerate dehydrogenase	1.93	synthesis of L-serine from 3-phospho-D-glycerate
<i>PALM2</i>	Paralemmin-2	1.92	Regulation of cell shape
<i>FKBP11</i>	Peptidyl-prolyl cis-trans isomerase	1.9	folding of proteins during protein synthesis
<i>BID</i>	BH3-interacting domain death agonist	1.87	ICE-like proteases and apoptosis
<i>ITPA</i>	Inosine triphosphate pyrophosphatase	1.84	Hydrolyzes the non-canonical purine nucleotides inosine triphosphate (ITP)
<i>RBPM5</i>	RNA-binding protein with multiple splicing	1.78	Coactivator of transcriptional activity
<i>CTSC</i>	Dipeptidyl peptidase 1	1.75	Thiol protease that activates serine proteases and neuraminidase
<i>NNMT</i>	Nicotinamide N-methyltransferase	1.75	Catalyzes the N-methylation of nicotinamide and other pyridines to form pyridinium ions
<i>PCK2</i>	Phosphoenolpyruvate carboxykinase	1.73	Catalyzes the conversion of oxaloacetate (OAA) to phosphoenolpyruvate (PEP)
<i>BTF3L4</i>	Transcription factor BTF3 homolog 4	1.71	Transcription factor
<i>PPME1</i>	Protein phosphatase methylesterase 1	1.7	RK pathway through dephosphorylation of regulatory proteins
<i>MXRA7</i>	Matrix-remodeling-associated protein 7	1.66	
<i>HSPB1</i>	Heat shock protein beta-1	1.65	Involved in stress resistance and actin organization

<i>TLL12</i>	Tubulin-tyrosine ligase-like protein 12	1.65	Catalyses posttranslational modification of tubulins
<i>ITSN1</i>	Intersectin-1	1.63	Acts as guanine nucleotide exchange factor (GEF) specific for the CDC42 GTPase
<i>STAT3</i>	Signal transducer and activator of transcription 3	1.62	Transcription factor (activated through EGF)
<i>SASH1</i>	SAM and SH3 domain-containing protein 1	1.61	Co-distributes with the actin cytoskeleton
<i>SLC1A5</i>	Neutral amino acid transporter B(0)	1.59	Sodium-dependent amino acids transporter
<i>GPNMB</i>	Transmembrane glycoprotein NMB	0.61	Melanogenic enzyme; regulates cell proliferation
<i>PI4K2A</i>	Phosphatidylinositol 4-kinase type 2-alpha	0.61	Membrane trafficking and is required for prolonged survival of neurons
<i>RAP2B</i>	Ras-related protein Rap-2b	0.6	Involved in EGFR and CHRM3 signalling pathways
<i>EPS8L2</i>	Epidermal growth factor receptor kinase substrate 8-like protein 2	0.58	Membrane ruffling and remodelling of the actin cytoskeleton
<i>BCAP29</i>	B-cell receptor-associated protein 29	0.57	Transport of membrane proteins from the endoplasmic reticulum to the Golgi
<i>TSPAN3</i>	Tetraspanin-3	0.56	Proliferation and migration of oligodendrocytes
<i>BDH2</i>	3-hydroxybutyrate dehydrogenase type 2	0.56	Mediates the formation of 2,5-dihydroxybenzoic acid (2,5-DHBA)
<i>NCEH1</i>	Neutral cholesterol ester hydrolase 1	0.55	Hydrolyzes 2-acetyl monoalkylglycerol ether and promotes tumour cell migration
<i>KPNA2</i>	Importin subunit alpha-1	0.55	Functions in nuclear protein import as an adapter protein for nuclear receptor KPNB1
<i>SIRPA</i>	Tyrosine-protein phosphatase non-receptor type substrate 1	0.54	Supports adhesion of cerebellar neurons, neurite outgrowth and glial cell attachment
<i>PUDP</i>	Pseudouridine-5'-phosphatase	0.53	Potential intermediate in rRNA degradation
<i>TYMS</i>	Thymidylate synthase	0.52	Contributes to the de novo mitochondrial thymidylate biosynthesis pathway
<i>CD68</i>	Macrosialin	0.51	Phagocytic activities including intracellular lysosomal metabolism
<i>SLC25A2</i> <i>0</i>	Mitochondrial carnitine/acylcarnitine carrier protein	0.5	Transport of acylcarnitines across the mitochondrial inner membrane
<i>GABARA</i> <i>PL2</i>	Gamma-aminobutyric acid receptor-associated protein-like 2	0.49	Ubiquitin-like modifier involved in intra-Golgi traffic

<i>ZHX3</i>	Zinc fingers and homeoboxes protein 3	0.48	Transcriptional repressor
<i>ALB</i>	Serum albumin	0.48	Regulation of the colloidal osmotic pressure of blood
<i>JUN</i>	Transcription factor AP-1	0.48	Transcription factor
<i>CDK9</i>	Cyclin-dependent kinase 9	0.45	The CDK9/cyclin-K complex has also a kinase activity towards CTD of RNAP II
<i>ADIRF</i>	Adipogenesis regulatory factor	0.44	Cell development; promotes adipogenic differentiation
<i>TOP2A</i>	DNA topoisomerase 2-alpha	0.31	Control of topological states of DNA
<i>CES1</i>	Liver carboxylesterase 1	0.17	Detoxification of xenobiotics and in the activation of ester and amide prodrugs

9.2 Appendix 2

Regulated proteins in the chapter 3.2.2.1 entitled proteomic signature of the CAV3 p.P104L mutant muscle

Gene name	Protein name	Fold regulation	Function (according to uniprot, Sept. 2018)
<i>SERPINB1A</i>	Leukocyte elastase inhibitor A	2.64	Protein catabolic process
<i>COL6A6</i>	Collagen alpha-6(VI) chain	2.39	cell adhesion [GO:0007155]
<i>COL1A1</i>	Collagen alpha-1(I) chain	2.32	Collagen biosynthetic process
<i>SYNC</i>	Syncoilin	2.16	Intermediate filament-based process
<i>SERPINB6</i>	Serpin B6	2.13	Cellular response to osmotic stress
<i>MVP</i>	Major vault protein	2.03	Cell proliferation
<i>S100A13</i>	Protein S100-A13	1.85	Cell proliferation
<i>COL3A1</i>	Collagen alpha-1(III) chain	1.82	Collagen fibril organization
<i>YWHAH</i>	14-3-3 protein eta	1.80	Cytoskeleton organization
<i>TXN2</i>	Thioredoxin, mitochondrial	1.79	Cell redox homeostasis
<i>DPT</i>	Dermatopontin	1.77	Collagen fibril organization
<i>COBL</i>	Protein cordon-bleu	1.75	Actin filament network formation
<i>UGGT1</i>	UDP-glucose:glycoprotein glucosyltransferase 1	1.74	Endoplasmic reticulum unfolded protein response
<i>COL1A2</i>	Collagen alpha-2(I) chain	1.70	Collagen fibril organization

<i>TSPAN8</i>	Tetraspanin-8	1.67	Cell surface receptor signalling pathway
<i>TTR</i>	Transthyretin	1.63	Retinol metabolic process
<i>HSPB7</i>	Heat shock protein beta-7	1.63	heart development
<i>APOH</i>	Beta-2-glycoprotein 1	1.62	animal organ regeneration
<i>TMEM43</i>	Transmembrane protein 43	1.62	nuclear membrane organization
<i>SGCA</i>	Alpha-sarcoglycan	1.62	Skeletal muscle tissue regeneration
<i>ATPIA1</i>	Sodium/potassium-transporting ATPase subunit alpha-1	1.61	ATP hydrolysis coupled transmembrane transport
<i>GAMT</i>	Guanidinoacetate N-methyltransferase	1.60	Organ morphogenesis
<i>PACSIN3</i>	Protein kinase C and casein kinase II substrate protein 3	1.60	Negative regulation of calcium ion transport
<i>MUG1</i>	Murinoglobulin-1 (MuG1)	1.60	Embryo implantation
<i>COL6A2</i>	Collagen alpha-2(VI) chain	1.59	Cell adhesion
<i>HSPB1</i>	Heat shock protein beta-1	1.59	chaperone-mediated protein folding
<i>ANXA4</i>	Annexin A4	1.55	Negative regulation of NF-kappaB transcription factor activity
<i>SI00A4</i>	Protein S100-A4	1.53	regulation of I-kappaB kinase/NF-kappaB signaling
<i>GPX1</i>	Glutathione peroxidase 1	1.52	Apoptotic process
<i>DLST</i>	Dihydropyridyllysine-residue succinyltransferase component of 2-oxoglutarate dehydrogenase complex, mitochondrial	1.52	2-oxoglutarate metabolic process
<i>NID2</i>	Nidogen-2	1.52	Cell-matrix adhesion
<i>ASPN</i>	Asporin	1.51	Negative regulation of JAK-STAT cascade
<i>HK2</i>	Hexokinase-2	1.51	Apoptotic mitochondrial changes
<i>CYB5R3</i>	NADH-cytochrome b5 reductase 3	1.49	Cholesterol biosynthetic process
<i>CAPN1</i>	Calpain-1 catalytic subunit	1.44	Protein autoprocessing
<i>SGCB</i>	Beta-sarcoglycan	1.44	Membrane organization
<i>ERH</i>	Enhancer of rudimentary homolog (Mer)	1.43	Cell cycle
<i>DYSF</i>	Dysferlin	1.42	Membrane organization
<i>GSN</i>	Gelsolin	1.39	Actin filament capping

<i>SERPINAID</i>	Alpha-1-antitrypsin 1-4	1.39	Response to cytokine
<i>PZP</i>	Pregnancy zone protein	1.38	Embryo implantation
<i>SNTAI</i>	Alpha-1-syntrophin	1.38	Neuromuscular junction development
<i>DCN</i>	Decorin	1.37	Aging
<i>MARCKS</i>	Myristoylated alanine-rich C-kinase substrate	1.36	Actin crosslink formation
<i>SFPQ</i>	Splicing factor, proline- and glutamine-rich	1.35	Activation of innate immune response
<i>TPD52I2</i>	Tumor protein D54	1.34	Actin crosslink formation
<i>ANXA7</i>	Annexin A7	1.33	Alternative mRNA splicing, via spliceosome
<i>CD81</i>	CD81 antigen	1.33	activation of MAPK activity
<i>APOA2</i>	Apolipoprotein A-II	1.33	Cholesterol metabolic process
<i>TUBA4A</i>	Tubulin alpha-4A chain	1.33	microtubule-based process
<i>PURA</i>	Transcriptional activator protein Pur-alpha (Purine-rich single-stranded DNA-binding protein alpha)	1.32	Apoptotic process
<i>SGCG</i>	Gamma-sarcoglycan	1.32	Membrane organization
<i>APOA1</i>	Apolipoprotein A-I	1.32	Cholesterol biosynthetic process
<i>ANXA11</i>	Annexin A11	1.32	Response to calcium ion
<i>DPYSL2</i>	Dihydropyrimidinase-related protein 2	1.31	Cytoskeleton organization
<i>CAPNS1</i>	Calpain small subunit 1	1.31	
<i>HSPB2</i>	Heat shock protein beta-2	1.31	somatic muscle development
<i>SYNM</i>	Synemin	1.30	Intermediate filament cytoskeleton organization
<i>RNHI</i>	Ribonuclease inhibitor	1.30	Angiogenesis
<i>PUNE1</i>	Exopolyphosphatase	1.30	Regulation of microtubule polymerization
<i>SERPINC1</i>	Antithrombin-III	1.29	Acute inflammatory response to antigenic stimulus
<i>TCNDC17</i>	Thioredoxin domain-containing protein 17	1.29	Tumor necrosis factor-mediated signaling pathway
<i>VWA5A</i>	von Willebrand factor A domain-containing protein 5A	1.29	
<i>TXN</i>	Thioredoxin	1.29	Cellular response to oxidative stress

MAP4	Microtubule-associated protein 4	1.28	Cell division
CAPN2	Calpain-2 catalytic subunit	1.28	Myoblast fusion
ASNA1	ATPase Asna1	1.28	Tail-anchored membrane protein insertion into ER membrane
GSTP1	Glutathione S-transferase P 1	1.27	Negative regulation of MAP kinase activity
DMD	Dystrophin	1.27	Muscle contraction
PKIA	cAMP-dependent protein kinase inhibitor alpha	1.26	Negative regulation of cAMP-dependent protein kinase activity
TUBA8	Tubulin alpha-8 chain	1.25	Microtubule cytoskeleton organization
EEF1B	Elongation factor 1-beta	1.25	Response to ethanol
LUM	Lumican	1.25	Collagen fibril organization
ANXA5	Annexin A5	1.24	Response to calcium ion
RCN2	Reticulocalbin-2	1.24	
PSMA5	Proteasome subunit alpha type-5	1.24	Proteasome-mediated ubiquitin-dependent protein catabolic process
PDIM3	PDZ and LIM domain protein 3	1.24	Actin filament organization
TMOD4	Tropomodulin-4	0.83	actin filament organization
SMYD1	Histone-lysine N-methyltransferase Smyd1	0.83	Positive regulation of myoblast differentiation
PITPNA	Phosphatidylinositol transfer protein alpha isoform	0.83	Axonogenesis
RTN2	Reticulon-2	0.83	Intracellular protein transmembrane transport
EDF1	Endothelial differentiation-related factor 1	0.83	Cell differentiation
UBE2I3	Ubiquitin-conjugating enzyme E2 L3	0.83	Cell proliferation
PDIM5	PDZ and LIM domain protein 5	0.82	Synapse assembly
PGM1	Phosphoglucomutase-1	0.82	Glucose metabolic process
PGAM2	Phosphoglycerate mutase 2	0.82	Gluconeogenesis
PYGM	Glycogen phosphorylase, muscle form	0.82	Glycogen catabolic process
FITM1	Fat storage-inducing transmembrane protein 1	0.82	Lipid storage

<i>SYPL1</i>	Synaptophysin-like protein 1	0.81	
<i>GRPEL1</i>	GrpE protein homolog 1, mitochondrial	0.81	Protein folding
<i>NEXN</i>	Nexilin	0.81	Regulation of cytoskeleton organization
<i>GPB2</i>	Glycerol-3-phosphate dehydrogenase, mitochondrial	0.80	Gluconeogenesis
<i>SEC61B</i>	Protein transport protein Sec61 subunit beta	0.80	Protein import into nucleus, translocation
<i>PPP1R12B</i>	Protein phosphatase 1 regulatory subunit 12B	0.80	signal transduction
<i>ATL2</i>	Atlastin-2	0.80	Endoplasmic reticulum organization
<i>GLUL</i>	Glutamine synthetase	0.77	Cell proliferation
<i>MYH8</i>	Myosin-8	0.76	Skeletal muscle contraction
<i>PAICS</i>	Multifunctional protein ADE2	0.76	De novo' IMP biosynthetic process
<i>CMBL</i>	Carboxymethylenebutenolidase homolog	0.76	
<i>PADI2</i>	Protein-arginine deiminase type-2	0.74	Chromatin-mediated maintenance of transcription
<i>COPS3</i>	COP9 signalosome complex subunit 3	0.71	Protein deneddylation
<i>CDH13</i>	Cadherin-13	0.71	Positive regulation of cell-matrix adhesion
<i>SLC41A3</i>	Solute carrier family 41 member 3	0.69	Transmembrane transport
<i>GSTM2</i>	Glutathione S-transferase Mu 2	0.66	Glutathione metabolic process
<i>PC</i>	Pyruvate carboxylase, mitochondrial	0.64	Gluconeogenesis
<i>AMPD1</i>	AMP deaminase 1	0.62	IMP salvage
<i>CA3</i>	Carbonic anhydrase 3	0.60	Response to oxidative stress
<i>RPL12</i>	60S ribosomal protein L12	0.55	Translation
<i>CAVIN4</i>	Caveolae-associated protein 4	0.54	Muscle organ development
<i>CES1D</i>	Carboxylesterase 1D	0.40	Cholesterol biosynthetic process
<i>FASN</i>	Fatty acid synthase	0.39	Acetyl-CoA metabolic process

9.3 Appendix 3

Regulated proteins in in the chapter 3.2.2.4 entitled unraveling new CAV3 function at the NMJ via identification of IQGAP1 via identification of IQGAP1 as a new binding partner

Gene name	Protein name	Fold regulation	Function (according to uniprot, Sept. 2018)
<i>COL6A3</i>	Collagen alpha-3(VI) chain	16.08	Extracellular matrix organization
<i>MSH2</i>	DNA mismatch repair protein Msh2	14.33	Double-strand break repair
<i>NIFK</i>	MKI67 FHA domain-interacting nucleolar phosphoprotein	12.45	rRNA metabolic process
<i>GREM1</i>	Gremlin-1	8.38	Apoptotic process
<i>CPXM2</i>	Inactive carboxypeptidase-like protein X2	7.88	Proteolysis
<i>LRRC4C</i>	Leucine-rich repeat-containing protein 4C	7.24	Regulation of axonogenesis
<i>COL5A1</i>	Collagen alpha-1(V) chain	6.26	Collagen biosynthetic process
<i>PNPLA6</i>	Neuropathy target esterase	5.62	developmental process
<i>ECI2</i>	Enoyl-CoA delta isomerase 2, mitochondrial	5.29	Fatty acid beta-oxidation using acyl-CoA oxidase
<i>ALCAM</i>	CD166 antigen	4.81	Axon extension involved in axon guidance
<i>P3H3</i>	Prolyl 3-hydroxylase 3	4.64	Collagen biosynthetic process
<i>LAMA5</i>	Laminin subunit alpha-5	4.39	Cytoskeleton organization
<i>TMEM131</i>	Transmembrane protein 131	4.38	
<i>SIRPA</i>	Tyrosine-protein phosphatase non-receptor type substrate 1	4.29	Cell adhesion
<i>CDC5L</i>	Cell division cycle 5-like protein	4.25	Cell differentiation
<i>KLHL1</i>	Kelch-like protein 1	3.84	Actin cytoskeleton organization
<i>EMC10</i>	ER membrane protein complex subunit 10	3.79	
<i>IQGAP1</i>	Ras GTPase-activating-like protein	3.75	Positive regulation of actin assembly
<i>IL6ST</i>	Interleukin-6 receptor subunit beta	3.74	Ciliary neurotrophic factor-mediated signaling pathway

<i>MTF1</i>	Mitochondrial fission factor	3.71	Mitochondrial fission
<i>LEMD3</i>	Inner nuclear membrane protein Man1	3.58	Nuclear envelope organization
<i>NOP56</i>	Nucleolar protein 56	3.51	rRNA processing
<i>AUPI1</i>	Ancient ubiquitous protein 1	3.43	retrograde protein transport, ER to cytosol
<i>STX8</i>	Syntaxin-8	3.43	Early endosome to late endosome transport
<i>DKC1</i>	H/ACA ribonucleoprotein complex subunit DKC1	3.37	Box H/ACA snoRNA 3'-end processing
<i>ANK1</i>	Ankyrin-1	3.31	Cytoskeleton organization
<i>ETFDH</i>	Electron transfer flavoprotein-ubiquinone oxidoreductase, mitochondrial	3.29	Electron transport chain
<i>IFI16</i>	Gamma-interferon-inducible protein 16	3.25	Activation of cysteine-type endopeptidase activity
<i>MMP2</i>	72 kDa type IV collagenase	3.11	Collagen catabolic process
<i>ATP6V1D</i>	V-type proton ATPase subunit D	3.10	Cilium assembly
<i>SRPRA</i>	Signal recognition particle receptor subunit alpha	3.04	IRE1-mediated unfolded protein response
<i>TNN</i>	Tenascin-N	3.03	Axonogenesis
<i>NUP153</i>	Nuclear pore complex protein Nup153	3.00	mRNA export from nucleus
<i>GBPI1</i>	Guanylate-binding protein 1	2.96	Regulation of calcium-mediated signaling
<i>ACAT2</i>	Acetyl-CoA acetyltransferase, cytosolic	2.96	Cholesterol biosynthetic process
<i>SNRPC</i>	U1 small nuclear ribonucleoprotein C	2.89	mRNA 5'-splice site recognition
<i>DOCK11</i>	Dedicator of cytokinesis protein 11	2.89	Positive regulation of GTPase activity
<i>NIPSNAP1</i>	Protein NipSnap homolog 1	2.86	Sensory perception of pain
<i>OXCT1</i>	Succinyl-CoA:3-ketoacid coenzyme A transferase 1, mitochondrial	2.86	Brain development
<i>CTSL</i>	Cathepsin L1	2.81	Collagen catabolic process
<i>CELF2</i>	CUGBP Elav-like family member 2	2.75	mRNA splice site selection
<i>TAP1</i>	Antigen peptide transporter 1	2.73	Protein transport

<i>LGALS3BP</i>	Galectin-3-binding protein	2.66	Cell adhesion
<i>EMILIN1</i>	Emilin-1	2.62	Cell adhesion
<i>SLC27A4</i>	Long-chain fatty acid transport protein 4	2.58	Fatty acid transport
<i>MYL1</i>	Myosin light chain 1/3, skeletal muscle isoform	0.32	Muscle contraction
<i>LRMP</i>	Lymphoid-restricted membrane protein	0.32	Neutrophil degranulation
<i>RNF20 BRE1A</i>	E3 ubiquitin-protein ligase BRE1A	0.30	Histone H2B ubiquitination
<i>MIA3</i>	Transport and Golgi organization protein 1 homolog	0.30	ER to Golgi vesicle-mediated transport
<i>ATP5L</i>	ATP synthase subunit g, mitochondrial	0.30	ATP biosynthetic process
<i>CCDC28A</i>	Coiled-coil domain-containing protein 28A	0.29	
<i>TOMM6</i>	Mitochondrial import receptor subunit TOM6 homolog	0.27	Protein transport
<i>PRSS1</i>	Trypsin-1	0.27	Digestion
<i>SCAF11</i>	Protein SCAF11	0.26	mRNA processing
<i>PLCB3</i>	1-phosphatidylinositol 4,5-bisphosphate phosphodiesterase beta-3	0.26	Wnt signaling pathway
<i>NAV2</i>	Neuron navigator 2	0.26	Vagus nerve development
<i>PSMD3</i>	26S proteasome non-ATPase regulatory subunit 3	0.25	Post-translational protein modification
<i>DENND5B</i>	DENN domain-containing protein 5B	0.24	Detection of mechanical stimulus
<i>ARHGAP23</i>	Rho GTPase-activating protein 23	0.24	Positive regulation of GTPase activity
<i>KIF1A</i>	Kinesin-like protein	0.24	Anterograde axonal transport
<i>POLR1E</i>	DNA-directed RNA polymerase I subunit RPA49	0.23	Positive regulation of gene expression
<i>DAD1</i>	Dolichyl-diphosphooligosaccharide--protein glycosyltransferase subunit	0.21	Apoptotic process
<i>ANKRD17</i>	Ankyrin repeat domain-containing protein 17	0.21	Blood vessel maturation
<i>S100A6</i>	Protein S100-A6	0.20	Axonogenesis

<i>CCDC146</i>	Coiled-coil domain-containing protein 146	0.20	
<i>GNG12</i>	Guanine nucleotide-binding protein G(I)/G(S)/G(O) subunit gamma-12	0.20	G-protein coupled receptor signaling pathway
<i>PKHD1L1</i>	Fibrocystin-L	0.20	Immune response
<i>IMMT</i>	MICOS complex subunit MIC60	0.19	Cristae formation
<i>HBA1</i>	Hemoglobin subunit alpha	0.19	Oxygen transport
<i>MAST1</i>	Microtubule-associated serine/threonine-protein kinase 1	0.17	Cytoskeleton organization
<i>NAPIL1</i>	Nucleosome assembly protein 1-like 1	0.17	Positive regulation of cell proliferation
<i>LRP10</i>	Low-density lipoprotein receptor-related protein 10	0.16	Lipid metabolic process
<i>GPR149</i>	Probable G-protein coupled receptor 149	0.16	G-protein coupled receptor signaling pathway
<i>BCOX1</i>	Protein KIAA0100	0.14	
<i>PLCH1</i>	1-phosphatidylinositol 4,5-bisphosphate phosphodiesterase eta-1	0.13	Lipid catabolic process
<i>OSBPL8</i>	Oxysterol-binding protein-related protein 8	0.13	Fat cell differentiation
<i>TMCI</i>	Transmembrane channel-like protein 1	0.09	Regulation of calcium ion transmembrane transport
<i>BCL9</i>	B-cell CLL/lymphoma 9 protein	0.08	Canonical Wnt signaling pathway
<i>NDRG2</i>	Protein NDRG2	0.03	Cell differentiation

9.4 Appendix 4

Regulated proteins from the chapter 3.2.3 entitled molecular pathophysiology in GFPT1 deficient mouse

<i>Gene name</i>	Protein name	Fold regulation	Function (according to uniprot, Sept. 2018)
<i>LGALS3</i>	Galectin-3	22.48	Cell differentiation
<i>OGT</i>	UDP-N-acetylglucosamine-peptide N-acetylglucosaminyltransferase 110 kDa subunit	3.88	Apoptotic process
<i>RPL3</i>	60S ribosomal protein L3	3.85	Cellular response to interleukin-4
<i>POSTN</i>	Periostin	3.79	Cell adhesion

<i>C1QB</i>	Complement C1q subcomponent subunit B	3.72	Complement activation
<i>CCDC127</i>	Coiled-coil domain-containing protein 127	3.63	
<i>LCPI</i>	Plastin-2	3.11	Actin crosslink formation
<i>PRG2</i>	Bone marrow proteoglycan	3.10	Immune response
<i>ARPC1B</i>	Actin-related protein 2/3 complex subunit 1B	2.79	Arp2/3 complex-mediated actin nucleation
<i>VTN</i>	Vitronectin	2.52	Cell-matrix adhesion
<i>HMI3</i>	Minor histocompatibility antigen H13	2.43	Membrane protein proteolysis
<i>AOC3</i>	Membrane primary amine oxidase	2.41	Cell adhesion
<i>HIST1H1B</i>	Histone H1.5	2.40	Muscle organ development
<i>SH3BRGL</i>	SH3 domain-binding glutamic acid-rich-like protein	2.35	
<i>KCTD12</i>	BTB/POZ domain-containing protein KCTD12	2.34	Regulation of G-protein coupled receptor protein signalling pathway
<i>KANK2</i>	KN motif and ankyrin repeat domain-containing protein 2	2.34	Apoptotic process
<i>ARCHDIB</i>	Rho GDP-dissociation inhibitor 2	2.28	Regulation of actin cytoskeleton reorganization
<i>SCFD1</i>	Sec1 family domain-containing protein 1	2.28	Regulation of ER to Golgi vesicle-mediated transport
<i>HMOX2</i>	Heme oxygenase 2	2.24	Response to hypoxia
<i>ANXA1</i>	Annexin A1	2.22	Actin cytoskeleton reorganization
<i>FNTA</i>	Protein farnesyltransferase/geranyl geranyltransferase type-1 subunit alpha	2.21	Negative regulation of nitric-oxide synthase biosynthetic process
<i>CAPG</i>	Macrophage-capping protein	2.19	Cell projection assembly
<i>HIST1A1</i>	Histone H1.3	2.17	Regulation of transcription by RNA polymerase II
<i>GPC1</i>	Glypican-1	2.11	Myelin assembly
<i>CRIP1</i>	Cysteine-rich protein 1	2.09	Response to zinc ion
<i>CYP20A1</i>	Cytochrome P450	2.09	
<i>IQGAP1</i>	Ras GTPase-activating-like protein	2.09	Regulation of actin cytoskeleton
<i>LMAN2</i>	Vesicular integral-membrane protein VIP36	2.06	Retrograde vesicle-mediated transport, Golgi to ER
<i>C4B</i>	Complement C4-B	1.98	Complement activation

<i>TBCA</i>	Tubulin-specific chaperone A	1.97	Tubulin complex assembly
<i>ANPEP</i>	Aminopeptidase N	1.96	Proteolysis
<i>STX7</i>	Syntaxin-7	1.82	Intracellular protein transport
<i>ARF4</i>	ADP-ribosylation factor 4	1.80	Cell migration
<i>COPG1</i>	Coatomer subunit gamma-1	1.80	Intracellular protein transport
<i>RAB7A</i>	Ras-related protein	1.80	Autophagosome assembly
<i>MARCKS</i>	Myristoylated alanine-rich C-kinase substrate	1.78	Actin crosslink formation
<i>TRIM28</i>	Transcription intermediary factor 1-beta	1.77	Chromatin organization
<i>COPB2</i>	Coatomer subunit beta' (Beta'-coat protein)	1.75	ER to Golgi vesicle-mediated transport
<i>PDIA3</i>	Protein disulfide-isomerase	1.75	Response to endoplasmic reticulum stress
<i>SELENOT</i>	Thioredoxin reductase-like selenoprotein T	0.66	Cell redox homeostasis
<i>FNK3</i>	Fructosamine-3-kinase	0.60	Fructosamine metabolic process
<i>MYORG</i>	Myogenesis-regulating glycosidase	0.48	Skeletal muscle fiber development
<i>NOS1</i>	Nitric oxide synthase, brain	0.33	Striated muscle contraction

9.5 Appendix 5

Regulated proteins from the chapter 3.2.4 entitled biochemical changes upon muscle denervation in neuropathies for the 2 years old animals

Gene name	Protein name	Fold regulation	Function (according to uniprot, Sept. 2018)
<i>GLO1</i>	Lactoylglutathione lyase	2.10	Carbohydrate metabolic process
<i>TOM3</i>	Tropomyosin alpha-3 chain	1.95	Actin filament organization
<i>APOA1</i>	Apolipoprotein A-I	1.95	Cholesterol biosynthetic process
<i>PHPT1</i>	14 kDa phosphohistidine phosphatase	1.63	Negative regulation of ATP citrate synthase activity
<i>TPM1</i>	Tropomyosin alpha-1 chain	1.62	Actin filament organization
<i>SYNJ2</i>	Synaptojanin-2	1.82	Intracellular distribution of mitochondria
<i>HSPB6</i>	Heat shock protein beta-6	0.65	Chaperone-mediated protein folding

<i>FLNC</i>	Filamin-C	0.65	Muscle fiber development
<i>LAMC1</i>	Laminin subunit gamma-1	0.64	Extracellular matrix disassembly
<i>COL6A2</i>	Collagen alpha-2(VI) chain	0.60	Cell adhesion
<i>DYSF</i>	Dysferlin	0.58	Vesicle fusion
<i>THBS4</i>	Thrombospondin-4	0.56	Extracellular matrix organization
<i>IGKC</i>	Immunoglobulin kappa constant	0.56	B cell differentiation
<i>COL6A1</i>	Collagen alpha-1(VI) chain	0.53	Cell adhesion
<i>MPZ P0</i>	Myelin protein P0	0.50	cell aggregation
<i>CLTC</i>	Clathrin heavy chain 1	0.42	Autophagy
<i>COL12A1</i>	Collagen alpha-1(XII) chain	0.42	Cell adhesion
<i>CD9</i>	CD antigen 9	0.39	Cell adhesion
<i>DYNC1H1</i>	Cytoplasmic dynein 1 heavy chain 1	0.31	Cell division
<i>MYH11</i>	Myosin-11	0.21	Microtubule-based movement
<i>HMGN2</i>	Non-histone chromosomal protein HMG-17	0.14	Regulation of transcription by RNA polymerase II [GO:0006357]
<i>FLNA</i>	Filamin-A	0.13	Actin crosslink formation
<i>EE1F1</i>	Elongation factor 1-alpha 1	0.58	Cellular response to epidermal growth factor stimulus
<i>FGB</i>	Fibrinogen beta chain	0.56	Cell-matrix adhesion
<i>AIFM1</i>	Apoptosis-inducing factor 1, mitochondrial	0.65	Apoptotic mitochondrial changes
<i>FGG</i>	Fibrinogen gamma chain	0.61	Cell-matrix adhesion

9.6 Appendix 6

Regulated proteins from the chapter 3.2.4 entitled biochemical changes upon muscle denervation in neuropathies for the 3 months old animals

Gene name	Protein name	Fold regulation	Function (according to uniprot, Sept. 2018)
<i>CBR2</i>	Carbonyl reductase	5.87	NADH oxidation
<i>METTL21C</i>	Protein-lysine methyltransferase	3.14	Skeletal muscle tissue development
<i>ACSL3</i>	Long-chain-fatty-acid--CoA ligase 3	2.37	Fatty acid biosynthetic process

<i>ANK1</i>	Ankyrin-1	0.42	ER to Golgi vesicle-mediated transport
<i>HOMER1</i>	Homer protein homolog 1	0.37	G-protein coupled glutamate receptor signalling pathway
<i>SELENBP1</i>	Methanethiol oxidase	0.3	Protein transport
<i>DHRS7C</i>	Dehydrogenase/reductase SDR family member 7C	0.28	Regulation of release of sequestered calcium ion into cytosol by sarcoplasmic reticulum
<i>ECHS1</i>	Enoyl-CoA hydratase, mitochondrial	0.27	Fatty acid beta-oxidation
<i>NEU2</i>	Sialidase-2	0.23	

8. Curriculum vitae

The Curriculum vitae is not available in the online version due to data-legal reasons

The Curriculum vitae is not available in the online version due to data-legal reasons

9. List of publications and conferences

List of publications, trainings and conferences obtained during my doctoral studies:

Papers related to the thesis:

1. José Andrés González Coraspe, Joachim Weis, Mary E Anderson, Ute Münchberg, Kristina Lorenz, Stephan Buchkremer, Stephanie Carr, René Peiman Zahedi, Eva Brauers, Hannah Michels, Yoshihide Sunada, Hanns Lochmüller, Kevin P Campbell Erik Freier, Denisa Hathazi*, Andreas Roos*. Biochemical and pathological changes result from mutated Caveolin-3 in muscle, *Skeletal Muscle*, 2018, accepted for publication.
2. Yasmin Issop, Denisa Hathazi, Muzamil Khan, Rüdiger Rudolf, Joachim Weis, Sally Spendiff, Clarke Slater, Andreas Roos, Hanns Lochmüller. GFPT1 deficiency in muscle leads to myasthenia and myopathy in mice, *Human Molecular Genetics*, 2018, E version ahead of print.
3. Manuela Wiessner, Andreas Roos, Christopher Munn, Ranjith Viswanathan, Tamiaka Whyte, Daniel Cox, Benedikt Schoser, Caroline Sewry, Helen Roper, Rahul Phadke, Chiara Berttolo, Rita Baressi, Richard, Charlton, Carsten Bönnemann, Osorio Abath Neto, Umbertina Reed, Edmanr Zanotelli, Cristaine De Araujo Martins Moreno, Ertl-Wagner Birgit, Rolf Stucka, Christian De Goede, Tamiris Borges da Silva, Denisa Hathazi, Margherita Dell Aica, René Peiman Zahedi, Sebastian Thiele, Juliane Müller, Helen Kingston, Susanna Müller, Elizabeth Curtis, Maggie Walter, Tim Sorm, Volker Straub, Kate Bushby, Francesco Muntoni, Laura Swan, Hanns Lochmüller, Jan Senderek, Mutations in INPP5K, encoding a phosphoinositide 5-phosphatase, cause congenital muscular dystrophy with cataracts and mild cognitive impairment, *The American Journal of Human Genetics*, 2017, 2, 100(3):523-536.
4. Denisa Hathazi, Dan Cox, Richard Charlton, Adele D'Amico, Robert-Yves Carlier, René Zahedi, Laxmikanth Kollipara, Jennifer Baumann, Jan Senderek, Emily O'Connor, Rita Barresi, Hanns Lochmüller, Andoni Urtizberea, Marie-Line Jacquemont, Isabelle Nelson, Laura Swan, Gisele Bonne, Andreas Roos. Molecular linkage of rare neuromuscular diseases allows the definition of a treatment strategy for Marinesco-Sjögren and Marinesco-Sjögren like syndromes. In preparation.

5. Denisa Hathazi, Bernhard Blank-Landeshammer, Laxmikanth Kollipara, Werner Stenzel, Corinna Preusse, Dan Cox, René Zahedi, Hanns Lochmuller, Andreas Roos. Mass spectrometry-based protein identification to understand the proteomic signature of human skeletal muscle. In preparation.
6. Denisa Hathazi, Emily O'Connor, Dan Cox, José Andrés González Coraspe, Sally Spendiff, Silvia Cipriani, Hanns Lochmüller, Andreas Roos. CAV3 is promoting the NMJ formation via binding to IQGAP1. In preparation.

Papers not related to the thesis:

1. Leonardo Ladislau, Xavier Suarez-Calvet, Ségolène Roquet, Océane Landon-Cardinal, Damien Amelin, Marine Depp, Mathieu Rodero, Denisa Hathazi, Darragh Duffy, Bondet Vincent, Corinna Preusse, Boris Bienvenu, Flore Rozenberg, Andreas Roos, Claudia Benjamin, Eduardo Gallardo, Isabeli Illa, Vincent Mouly, Werner Stenzel, Gillian Butler-Browne, Olivier Beneviste, Yves Allenbach. JAK inhibitor improves type I interferon induced damage: proof of concept in dermatomyositis, *Brain*, 2018 1;141(6):1609-1621.
2. Laxmikanth Kollipara, Stephen Buchkremer, José Andrés González Coraspe, Denisa Hathazi, Jan Senderek, Joachim Weis, René Peimann Zahedi, Andreas Roos. In-depth phenotyping of lymphoblastoid cells suggests selective cellular vulnerability in Marinesco-Sjögren syndrome, *Oncotarget*, 2017, 15; 8(40): 68493-68516.

List of conferences and trainings at which I attended during my doctoral studies:

1. 46th European Muscle Conference, September 2017, in Potsdam, Germany, with a poster presentation. Title: Mass spectrometry-based protein identification to understand the proteomic signature of human skeletal muscle. Authors: Denisa Hathazi, Bernhard Blank-Landeshammer, Laxmikanth Kollipara, Werner Stenzel, Corinna Preusse, Dan Cox, René Zahedi, Andreas Roos.
2. Summer School of Myology at the Institut de Myologie, July 2017, Paris, France

Erklärung:

Hiermit erkläre ich, gem. § 6 Abs. (2) g) der Promotionsordnung der Fakultät für Biologie zur Erlangung der Dr. rer. nat., dass ich das Arbeitsgebiet, dem das Thema „*Tracking the nature of neromuscular diseases via combined proteomics and functional analyses*“ zuzuordnen ist, in Forschung und Lehre vertrete und den Antrag von *Denisa Hathazi* befürworte und die Betreuung auch im Falle eines Weggangs, wenn nicht wichtige Gründe dem entgegenstehen, weiterführen werde.

Essen, den _____
Unterschrift eines Mitglieds der Universität Duisburg-Essen

Erklärung:

Hiermit erkläre ich, gem. § 7 Abs. (2) d) + f) der Promotionsordnung der Fakultät für Biologie zur Erlangung des Dr. rer. nat., dass ich die vorliegende Dissertation selbständig verfasst und mich keiner anderen als der angegebenen Hilfsmittel bedient, bei der Abfassung der Dissertation nur die angegeben Hilfsmittel benutzt und alle wörtlich oder inhaltlich übernommenen Stellen als solche gekennzeichnet habe.

Essen, den _____
Unterschrift des/r Doktoranden/in

Erklärung:

Hiermit erkläre ich, gem. § 7 Abs. (2) e) + g) der Promotionsordnung der Fakultät für Biologie zur Erlangung des Dr. rer. nat., dass ich keine anderen Promotionen bzw. Promotionsversuche in der Vergangenheit durchgeführt habe und dass diese Arbeit von keiner anderen Fakultät/Fachbereich abgelehnt worden ist.

Essen, den _____
Unterschrift des Doktoranden